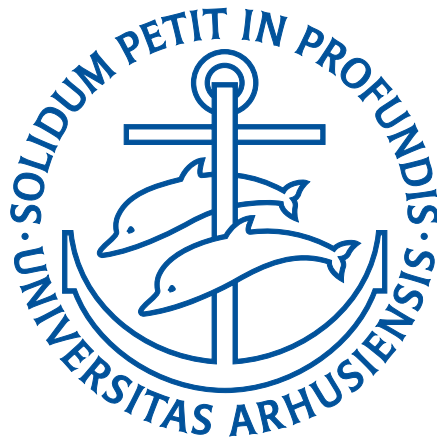


COOLING AND MANIPULATING  
IONS IN TRAPS WITH  
INTEGRATED OPTICAL CAVITIES



PHD THESIS

HANS HARHOFF ANDERSEN

AUGUST 2015

DEPARTMENT OF PHYSICS AND ASTRONOMY  
AARHUS UNIVERSITY

This thesis is submitted to the Faculty of Science at Aarhus University, Denmark, in order to fulfill the requirements for obtaining the PhD degree in Physics.

The studies have been carried out under the supervision of Prof. Michael Drewsen in the Ion Trap Group at the Department of Physics and Astronomy at Aarhus University from July 2011 to July 2015.

© Hans Harhoff Andersen 2015

[hha07@phys.au.dk](mailto:hha07@phys.au.dk)

Layout and typography by the author with L<sup>A</sup>T<sub>E</sub>X. Figures are made using Inkscape, Matplotlib, and Tikz.

# Preface

This thesis summarizes the work I have done, with numerous collaborators, as part of my PhD studies in the Ion trap group of Michael Drewsen at the Department of Physics and Astronomy at Aarhus University. The work presented here was performed partly in Aarhus and partly during two visits to the Quanta group of Isaac Chuang at Massachusetts Institute of Technology (MIT).

The work actually started a bit earlier than this, since I did my bachelor's thesis project in the Ion Trap Group in Aarhus as well. In the summer of 2010, while I was finishing my bachelor's thesis, Michael Drewsen suggested that I contact a former student of his at MIT, Peter Herskind. Peter had contacted Michael to establish an exchange of students with his previous group.

I did not hesitate long to accept this chance to visit the MIT group and perform experiments there. I traveled to Cambridge, Ma on November 2nd 2010 to do my master's thesis. At MIT I learned about ion trapping, lasers, and cavities, while performing cavity cooling experiments. I benefited from the help and teaching I received from the people there including, but not limited to, Michael Gutierrez, Peter Herskind, Isaac Chuang, Shannon Wang, Marko Cetina, and Tony Kim. Tony and Marko especially took the time needed to teach a novice about lasers and electronics, while Peter taught me most of what doing experiments is about.

While I was at MIT, Michael Drewsen suggested that I apply for a PhD position at Aarhus University, which I did. The experiments performed at MIT then became the basis for the first part of my PhD studies. I was accepted and officially started and returned to Aarhus in the summer of 2011.

From 2011 to 2012, I was mostly working on the design and preparation for a new trap setup while fulfilling the course requirements for both the master's and PhD simultaneously.

Between April and July 2012 I was at MIT again. The plan was to continue with cavity cooling experiments, but, as so often happens, other experimental paths were taken, specifically experiments on cavity thermometry.

Upon my return to Aarhus, the design of the new experiment, the Blue Cavity trap, was finalized and sent to the workshop to be machined. Then, in the early months of 2013, we were ready to assemble the cavity, test mirrors, etc. In the summer of 2013 I wrote and handed in my Part A progress report. During the following year, the cavity was characterized and various locking schemes were investigated.

In the summer of 2014 the trap was assembled, aligned with the cavity, and installed in our vacuum chamber. The fall of 2014 and the first months of 2015 were spent relocating all the

laboratories of the Ion Trap Group.

In the spring of 2015 the trap was commissioned, and ions were trapped for the first time on April 7th 2015 (late at night). For the next months the remainder of the setup was installed and trapping was improved. Finally, for the last few months I have been writing the thesis you are about to read.

The work as a PhD student involves much more than described above. During the last four years I have attended several summer schools, conferences, meetings, and attended courses. I have been an instructor for a number of courses and corrected what seems like an infinite number of reports. I have learned how to use a milling machine and a lathe and how to order stuff from around the world. A PhD student might also learn how to program in multiple languages, how electronics works (or doesn't) in practice, what kinds of glue are suitable for vacuum, what types of steel are suitable for which purposes, how to set up web-servers, etc. . . .

Suddenly you also find yourself being a senior person in the group, charged with helping the new students find their way. Instructing students is an interesting part of being a PhD student, which helps you figure out whether you yourself understand the matter at hand.

You also meet a lot of people who are pleasant company and who help you move your research forward. For me, these include Michael Drewsen (without whom there would be no Ion Trap Group), Aurelien Dantan (whose time I have spent a lot of), Ian Leroux (who always had time for any question big or small), Gregers Poulsen (who showed me that there are smart ways to do things), and fellow students who are always available to discuss problems.

We are blessed with a very good technical support at the Department of Physics and Astronomy, where the electronics department and the mechanical workshops are always there to help you make the right technical decisions. I would especially like to thank Torben Hyltoft (who taught me how to use the workshop), Henrik Bechtold (who helped design the trap), Anders Petersen (who machined the trap), Erik Søndergaard and Frank Mikkelsen (who designed much of the electronics used for the experiments).

I would like to thank Jacob Bisgaard Andersen, who read select chapters and gave thorough feedback and Io Odderskov, who read other chapters and helped with the layout and figures in this thesis. Special thanks go to Aurélien Dantan who read the whole thesis (some parts multiple times) and helped make it into a (hopefully) coherent work. Any problems that remain are my responsibility.

Lastly I would like to thank my family and friends who were understanding during the last four years and especially in the last few months where they knew how to be supportive even when I was too busy to talk to them.

Hans Harhoff Andersen, July 2015

# Abstract (English)

The work presented in this thesis, in the context of cavity Quantum Electrodynamics (CQED) with trapped ions, focuses on the interaction between ions trapped and laser-cooled in linear rf traps and light fields in optical resonators.

This work reports on experiments performed in two locations: 1) the Quanta Group at Massachusetts Institute of Technology and 2) in the Ion Trap Group at Aarhus University.

At MIT the interaction between a single  $^{88}\text{Sr}^+$  ion and an intracavity standing wave field was investigated. First, sub-Doppler resolved sideband cavity cooling of the ion motion along the cavity axis was demonstrated. Second, a novel method for measuring the temperature of a single, laser cooled ion using the scattering into a narrow linewidth optical resonator was investigated and compared to standard sideband spectroscopy methods<sup>1</sup>.

In Aarhus a new linear rf trap with an integrated optical resonator has been constructed. This larger trap should allow for trapping of single or large ensembles of ions and incorporates an optical resonator whose mirrors are highly reflective at the wavelength of the  $S$  to  $P$  transitions of the  $\text{Ca}^+$  ion. The assembly and alignment of this cavity trap are described and the trapping of its first ions is reported. The prospects for future experiments in this trap are discussed. These include: A novel laser cooling scheme, investigation and control of the structure of so-called ion Coulomb crystals, and investigations of the dynamics of ions in intracavity generated optical potentials.

---

<sup>1</sup>Manuscript in preparation: Hans Harhoff Andersen, Michael Gutierrez, Peter F. Herskind, Isaac L. Chuang, "Single-ion thermometry with an optical resonator".

# Abstract (dansk)

I denne afhandling præsenteres arbejde inden for kavitetskvanteelektrodynamik (CQED) med indfangede ioner. Der fokuseres på vekselvirkningen mellem ioner fanget i lineære rf-fælder og lysfelter i optiske resonatorer.

Der rapporteres om eksperimenter foretaget to forskellige steder: 1) i Quanta Group ved Massachusetts Institute of Technology (MIT) og 2) i Ionfældegruppen ved Aarhus Universitet.

På MIT blev vekselvirkningen mellem en enkelt  $^{88}\text{Sr}^+$ -ion og feltet fra en stående bølge i en kavitet undersøgt. Først demonstreredes sub-Doppler kavitetskøling med opløste sidebånd langs kavitetsaksen. Dernæst undersøgte en ny metode til at måle temperaturen af en enkelt, laser-kølet ion ved hjælp af det spredte lys i en optisk resonator med smal linjebredde; denne metode sammenlignedes med standard sidebåndsspektroskopimetoder<sup>2</sup>.

I Aarhus er en ny lineær rf-fælde med integreret optisk resonator blevet konstrueret. Denne større fælde burde tillade indfangning af enkelte eller store ensembler af ioner, og inkorporerer en optisk resonator, hvis spejle er højreflektive ved bølgelængderne for overgangene fra  $S$  til  $P$  tilstandene i  $\text{Ca}^+$ -ionen. Samling og oplining af denne kavitetsfælde er beskrevet, og indfangning af de første ioner rapporteres. Mulighederne for fremtidige eksperimenter med denne kavitetsfælde diskuteres. Disse omfatter: En ny metode til laserkøling, undersøgelser og kontrol af såkaldte ion-Coulomb-krystaller, samt undersøgelser af dynamikken af ioner i intrakavitetsgenererede optiske potentialer.

---

<sup>2</sup>Manuskript under udarbejdelse: Hans Harhoff Andersen, Michael Gutierrez, Peter F. Herskind, Isaac L. Chuang, "Single-ion thermometry with an optical resonator".

# Chapter 1

## Introduction

In the beginning of the 20th century, experiments on the photoelectric effect and absorption and emission spectra were pointing to the necessity of a quantum description of Nature.

The quantum theory of light, as pioneered by Planck and Einstein and irrevocably confirmed by the Hanbury Brown and Twiss experiment in 1956 [1], suggests that the electromagnetic field is quantized and that the quantized nature of it will lead to novel dynamics not predicted by semi-classical theories. From these developments the field of quantum optics arose. Quantum optics describes light-matter interactions in well-controlled settings, and experiments are probing the realm of single photons and single atoms. A requirement for these experiments was the development of monochromatic light sources and the application of these for laser cooling. The idea of optical cooling was envisioned as early as 1950 by Alfred Kastler [2], and developed further by Zel'Dovich [3]. Independent proposals from Wineland and Dehmelt [4] and Hänsch and Schawlow [5] suggested cooling of trapped and free particles, respectively. The first atomic laser cooling experiments of  $\text{Mg}^+$  by Wineland et al. [6] and  $\text{Ba}^+$  by Neuhauser et al. [7] were published in 1978 soon followed by the cooling and trapping of neutrals [8]. Ground state cooling of a trapped ion was first demonstrated by Diedrich et al. in 1989 [9]. Laser cooling is now an invaluable tool in many physics laboratories.

By combining laser cooling and optical pumping, all degrees of freedom of atoms can be controlled. This detailed control enables probes of the fundamentals of the theory at an incredible precision [10, 11], and amazing applications such as ultra-precise spectroscopy and atomic clocks [12, 13, 14, 15]. For these reasons the Nobel Prize in Physics have been awarded to pioneers in these fields on several occasions [16, 8, 17, 18, 19] and the applications of atomic clock techniques serve as the definition of time itself<sup>1</sup>.

In 1959 Richard Feynman gave a talk suggesting that *There's plenty of room at the bottom*, where he hypothesized great innovations in the microscopic realm of atom and quantum mechanics [21]. The talk was largely forgotten, but in 1982 he followed up with *Simulating physics with*

---

<sup>1</sup>The unit of time in the SI system is the second, defined as: *The second is the duration of 9 192 631 770 periods of the radiation corresponding to the transition between the two hyperfine levels of the ground state of the caesium 133 atom.* [20]

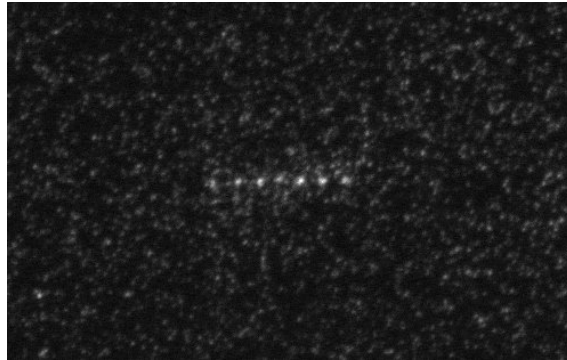


Figure 1.1: A string of 7 ions confined in the Blue Cavity trap discussed in part 3. The distance between the ions is  $\sim 25 \mu\text{m}$ .

*computers*, where an idea similar to the modern concept of quantum simulations was proposed [22]. Feynman conjectured that quantum computers can be programmed to simulate any local quantum system, which was shown to be correct by Seth Lloyd in 1996 [23]. The idea of quantum simulations is to find analogue systems, that is, systems governed by similar Hamiltonians, but where one of the systems is more amenable to control and measurement [24].

The first concept of a universal quantum computer was developed by David Deutsch in 1985 [25], while the first major algorithm breakthrough was due to Peter Shor in 1994, who proposed a polynomial time quantum algorithm for factoring integers (first demonstrated in 2001 [26]) [27]. This is faster than any known classical algorithm, and suggested the large advantage of using the properties of quantum mechanics for computing. Other proposed algorithms are Grover's search algorithm [28][29] and several variants of the Deutsch-Jozsa algorithm; for details see [30] and references therein.

Trapped ions have many desirable qualities for these applications, as demonstrated by the seminal works performed since the 1990s in the groups of David Wineland and Rainer Blatt [31][32]. Both the internal and external degrees of freedom of trapped ions can indeed be controlled with exquisite precision; ions can be kept in the traps for days, enabling extended measurements; they also offer long coherence times, i.e. the time over which quantum superpositions will survive. Detection schemes based on the fluorescence of the ions make it possible to obtain resolved images of single ions, and shelving techniques enable efficient state detection [33, 34, 35]. This makes them ideal candidates for quantum optics experiments.

Several schemes for trapping ions exist [36, 37] and the 1989 Nobel Prize was awarded jointly for these efforts to Wolfgang Paul and Hans Dehmelt [16]. In this thesis we will be discussing rf traps [38], specifically Linear Paul traps developed in 1989 [39].

It is both possible to load single and ensembles of ions into these traps. By confining more strongly in the radial directions in linear Paul traps, one dimensional strings of ions can be formed. The ions will mutually repulse each other due to the Coulomb interaction, but the confinement of

the trap will keep them together, see figure 1.1.

The concept of trapped ion quantum computing was first proposed by Ignacio Cirac and Peter Zoller [40] and later improved by Sørensen and Mølmer [41] and many others. In the late 1990s and 2000s, implementations of quantum gates [42, 43, 44, 45], demonstrations of detailed quantum control and generation of exotic quantum states [46, 47, 48], teleportation [49, 50], implementations of the Deutsch-Jozsa algorithm [51], Shor’s algorithm [52], entanglement [53, 31, 54], and error-correction codes [55] were presented.

Trapped ions have also been proposed as testbeds for quantum simulations [56][57]. There are many proposals and experiments e.g. of Ising spin models [58, 59, 60, 61, 62, 63], Kibble-Zurek laws for defect formation [64, 65], and Dicke models [66]. Several demonstrations have been performed, and simulations have emerged that are nearing the limit of tractability of classical computers [67].

All these experiments benefit from the good control of the light-matter interaction, and the possibility of coherent quantum dynamics, e.g. exchange of excitations between ions and photons.

Cavity Quantum Electrodynamics (CQED) is a subset of quantum optics which emerged in the 1970s, that investigates the interaction between atoms and the electromagnetic field of a resonator [68, p. 19][69]. The origins of CQED trace back to 1946, when Purcell noted the effect of increasing the decay rate of an atom, by increasing the density of states of the electromagnetic field it. This can be done by limiting the volume of the field modes, by e.g. placing the atoms in an optical resonator. In 1981, the reverse effect of decreasing the decay rate was proposed by Daniel Kleppner. This was done by limiting the density of states around the atom and was demonstrated a few years later [70, 71, 72]. CQED thus offers the possibility of tailoring light-matter interactions at the fundamental level [73].

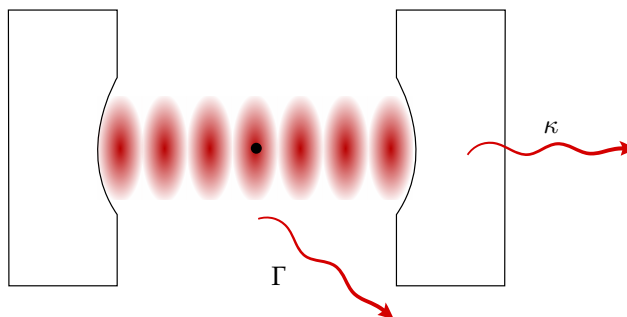


Figure 1.2: Two level atom in the field of linear Fabry-Perot resonator.

The generic model of an optical CQED experiment, see figure 1.2, consists of one or more atoms coherently coupling to a single mode of an optical resonator (single excitation exchange rate  $g$ ). The atoms also couple to the other modes of the quantized electromagnetic field via spontaneous emission (rate  $\Gamma$ ) and photons can leak out of the cavity at a rate  $\kappa$ .

The ratio of these dissipation rates to the coupling strength  $g$  determines the regime of the dynamics. For a weak coupling strength,  $g < \Gamma, \kappa$ , the system is in the weak coupling regime, while for  $g > \Gamma, \kappa$  the system is in the so-called strong coupling regime where excitations between

the cavity and the atom can occur faster than the decay and decoherence of the system [69]. In the case of many atoms the collective coupling strength is  $g\sqrt{N}$ , where  $N$  is the number of atoms. If  $g\sqrt{N} > \Gamma, \kappa$ , the regime is referred to as the collective strong coupling regime.

Strong coupling can be achieved by making the mode volume of the light field small. In this way the photons are less "diluted" and the amplitude of the field is larger. Strongly coupled experiments with optically trapped atoms have been performed both for ensembles and for single atoms [74, 75, 76]. Unfortunately, for ions, this requires placement of dielectric mirrors very close to the ions. Since the ions are confined electrically, the presence of the dielectrics in the trapping region will in general disturb the trapping potentials. Thus the cavities for trapped ions are typically much larger than those used for neutral atoms. The strong coupling regime has therefore not yet been achieved with trapped ions, although the collective strong coupling regime has been reached in Aarhus [77, 78]. Considerable efforts are made to reach the single ion strong coupling regime [79][80][81][82]. Many remarkable CQED experiments have already been performed in the weak or close to strong coupling regime with ions, due to their long trapping and coherence times and excellent localization [83, 84, 85, 86, 87, 88, 89, 90, 91].

The applications of the interaction between cavities and atoms are many. One of them is to use the interaction between cavity and atom as a means to cool down the atoms [92, 93]. These ideas have been treated theoretically in various regimes [94, 95, 96, 97, 98]. Experimental demonstrations have been performed for single neutral atoms [99, 100]. The interest in this so-called cavity cooling is due to it not requiring a closed optical transition, so that the range of particles that can be cooled is much larger. It has been suggested, for instance, that cooling be applied to molecules [92] or Bose-Einstein condensates [101]. Cavity cooling with trapped ions have been performed, but due to a generally lower coupling strength than for neutrals, progress has been slower. Experimental demonstrations are presented in [102], [103], and in this work.

The interaction between the cavity field and the motional degrees of freedom of the atoms can also be used for generating optical potentials [104]. Such experiments have opened up new avenues in the field, and many proposals about investigating thermal, structural and other properties of strings of trapped ions have been presented. Optical trapping of ions [105, 106] and pinning of trapped ions in optical potentials have recently been demonstrated [107][108][109].

Strings of ions trapped in linear Paul traps with periodic optical potentials have been suggested, among others, [110, 111] as candidates for investigations of a version of the Frenkel-Kontorova model of dry friction [112]. This model has been treated extensively in the literature [113, 114] and the first implementations with trapped ions have very recently been published by the group of Vladan Vuletić [115, 116].

## Outline of this thesis

In this thesis we work with single ions and ion Coulomb crystals in Linear Paul traps with integrated optical cavities. This thesis is divided into three parts. Part 1 introduces the basics of ion trapping and cooling in linear Paul traps and discusses the interaction with optical cavity fields. Part 2

presents ion cavity experiments performed in the group of Isaac Chuang at MIT with single ions. In particular, the demonstration of new scheme for cavity-assisted ion thermometry as well as the results of cavity cooling experiments is described. Part 3 discusses the development of a new cavity ion trap in Aarhus for studying the dynamics of ions in cavity fields. We will present the construction and commissioning of this *Blue Cavity trap* and discuss possible future experiments.

### Part 1: Theory

**Chapter 2** The theory of Linear Paul traps and the motion of ions within them. Ion Coulomb crystals will be discussed.

**Chapter 3** The theory of the interaction between quantized light and matter, with some examples.

**Chapter 4** The theory of Doppler cooling is presented. The effect of micromotion is modeled and a new pulsed cooling scheme is presented. Cooling of multilevel atoms is briefly discussed. Sideband cooling in the Lamb-Dicke regime is outlined.

**Chapter 5** The theory of Fabry-Perot cavities and their interaction with atoms.

**Chapter 6** The theory of optical dipole potentials is briefly presented.

### Part 2: Ion cavity experiments at MIT

**Chapter 7** MIT experimental setup description and characterization.

**Chapter 8** Derivations of the relevant scatterings rates for light incident on the ions in the cavity (side drive) or injected into the cavity (axial drive). Presentation of a model for cavity cooling with axial drive.

**Chapter 9** Results of investigations of the cavity-ion interactions including cavity thermometry and cooling.

### Part 3: Ion cavity experiments in Aarhus

**Chapter 10** The design, assembly, and characterization of the Blue Cavity trap.

**Chapter 11** The experimental setup for the Blue Cavity trap.

**Chapter 12** A description of the procedure for the initial trapping and cooling of ions. Future optimizations are discussed.

**Chapter 13** Perspectives for the Blue Cavity trap.

**Chapter 14** Conclusion.

**Part I**

**Theory**

## Chapter 2

# Ion trapping

This chapter introduces the basic theory of ion trapping. Firstly, the linear Paul trap is introduced and relevant approximations are made to give a simple picture for the dynamics of single ions. The thermodynamical properties of ensembles of ions trapped simultaneously and forming Coulomb crystals are then briefly introduced.

For neutral particles many types of traps exist essentially based on three different interactions [104, p. 1].

Firstly, Magneto-Optical Traps (MOT) are based on the scattering of near-resonance light from several counter-propagating beams in an inhomogeneous magnetic field. The beams serve as *optical molasses* in which the scattering induced friction cools down the atoms while the inhomogeneous magnetic field generates the position dependence of the trapping field. In this way traps with an effective depth of  $\sim 1$  kelvin can be realized [117].

Secondly, the interaction between a magnetic dipole moment and an inhomogeneous magnetic field can be used to generate a conservative *magnetic trap*. Such traps, with depths of typically  $100 \mu\text{K}$ , are often used as a second stage after trapping in a MOT. From here evaporative cooling, can be utilized to reach Bose-Einstein Condensation (BEC) [104, p. 2].

Thirdly, atoms with a permanent dipole moment or with a finite polarizability can be trapped in the conservative potential generated by far off-resonant light fields [104]. These are called dipole traps and are typically less than one millikelvin deep, and trapping times are limited by far off-resonance scattering. See chapter 6 for further details.

The types of traps mentioned above for neutral particles will also work in general for charged particles. However, charged particles have an additional *effective handle* due to their charge and the possibility to use the strong Coulomb interaction with low frequency electromagnetic fields. This implies that their trapping can be based solely on the net charge, thus leaving the internal degrees of freedom undisturbed and free for other manipulations with e.g. optical fields.

## 2.1 Earnshaw's theorem

As first shown by Earnshaw in 1839 it is impossible to confine a charged particle electrostatically in 3 dimensions [118]. The argument relates to Laplace's law which describes the electrical potential,  $\phi$ , in empty space

$$\nabla^2\phi(x, y, z) = \frac{\partial^2\phi(x, y, z)}{\partial x^2} + \frac{\partial^2\phi(x, y, z)}{\partial y^2} + \frac{\partial^2\phi(x, y, z)}{\partial z^2} = 0. \quad (2.1)$$

For confinement we require a point in space where  $\phi$  has positive second derivatives with respect to  $x$ ,  $y$ , and  $z$ . If all three terms in equation 2.1 are strictly larger than 0 the equation cannot be fulfilled. Earnshaw's theorem thus disallows 3D confinement using purely electrostatic fields for which Laplace's law applies.

For quantum optics experiments with ions two types of traps are mainly used [37]. The Penning trap is based on a combination of electrostatic fields and magnetic fields [36]. In this configuration the ions are not trapped in a 3D potential minimum; rather they are trapped in orbits defined by the applied electric and magnetic fields [119, Sec. 2][120].

The other major type of trap is the radio frequency (rf) or Paul trap, which relies on the application of both static and time-varying electric fields. Hans Dehmelt and Wolfgang Paul shared the 1989 Nobel Prize in Physics for their work on these traps.

## 2.2 The linear Paul trap

In 1953-54 Wolfgang Paul and colleagues published a number of papers on rf based mass spectrometers and ion traps<sup>1</sup> [38][37][16].

The working principle of the Paul traps is the generation of a saddle potential due to the application of both static and time-varying electric fields by suitably arranged electrodes. The sign of the potential is then periodically switched at rf frequencies to generate an effective confining harmonic potential. The stability of the trap then depends on the charge-to-mass ratio of the trapped particles and the frequency of switching.

The first Paul traps all used hyperbolically shaped electrodes since this shape generates a harmonic pseudopotential. Paul's original design has gone through some iterations and in this thesis we will be discussing the linear Paul trap invented in 1989 which combines rf and dc potentials [39]. The advantages of the linear Paul trap include increased capacity for ion number due to a lower second order Doppler shift<sup>2</sup> sensitivity and a line of zero rf potentials instead of a point [39][121]. In the following we will describe a variation on this design that was developed in the Ion Trap Group at Aarhus University. The theory developed here will also be relevant for the trap design used in section 7.1 with only slight modifications.

Consider four parallel rods aligned and segmented as in figure 2.1. A time varying potential is applied to all segments of diagonally opposite rods while a potential 180° out of phase is applied

---

<sup>1</sup>Initially called "Ionenkäfig".

<sup>2</sup>See section 4.2.

to adjacent rods, see figure 2.1. The rf voltage applied will be

$$\pm \frac{1}{2} U_{\text{rf}} \cos(\Omega_{\text{rf}} t), \quad (2.2)$$

where  $\Omega_{\text{rf}}$  is the drive frequency of the trap and  $U_{\text{rf}}$  is the peak to peak voltage of the rf-component. Note that in this configuration none of the electrodes are grounded as opposed to the configuration used in many other traps, e.g. in ref. [122]. The advantage of applying rf potentials to all electrodes is that the center of the trap will be at a constant zero potential with respect to other parts of the chamber. This makes this trap less sensitive to the presence of a ground conductor in the vicinity of the trapping area.

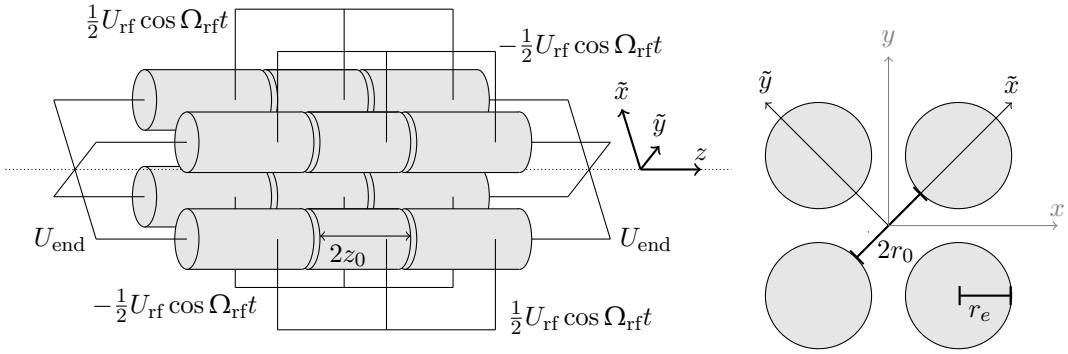


Figure 2.1: **Left)** Linear Paul trap with applied voltages. The  $z$ -axis will also be denoted as trap axis or cavity axis in the following (dotted line). **Right)** End-view of the Paul trap with trap axes defined.

To achieve a perfect harmonic potential the electrodes should have a hyperbolic shape as in the original Paul trap. It is however possible to achieve traps with very low anharmonicity with cylindrical electrodes by choosing the correct ratio between the electrode radius,  $r_e$ , and the inscribed radius between the cylinders,  $r_0$ , see figure 2.1b).

In the general case of infinitely long cylindrical rods we would have translational symmetry along the trap axis,  $z$ . In this case the potential can be described in polar coordinates by the distance from the trap center,  $r$ , and the angle to the  $\tilde{x}$ -axis,  $\theta$ , in a multipole expansion [123]

$$\phi_{\text{rf}}(r, \theta, t) = -\frac{1}{2} U_{\text{rf}} \cos(\Omega_{\text{rf}} t) \sum C_m \left( \frac{r}{r_0} \right)^m \cos(m\theta), \quad (2.3)$$

where  $r_0$  is the inter-electrode inscribed radius and  $C_m$  is the  $m$ th multipole expansion coefficient. Due to the symmetry of the four cylinders we get the requirement that  $m = 2, 6, 10, \dots$  since  $\cos m\pi/2 = -1$ . Re-indexing eq. 2.3 we get

$$\phi_{\text{rf}}(r, \theta, t) = -\frac{1}{2} U_{\text{rf}} \cos \Omega_{\text{rf}} t \sum_{n=0}^{\infty} C_n \left( \frac{r}{r_0} \right)^{2(2n+1)} \cos[2(2n+1)\theta], \quad (2.4)$$

where the first term is a quadrupole term, the second is 12-pole term, the third is a 20-pole term, etc. To have a harmonic potential all, but the quadrupole term must be eliminated or minimized.

In ref. [123] this is done numerically by varying the ratio  $r_e/r_0$  for  $C_1 = 0$ . The higher order terms are then presumed much smaller than the quadrupole term so that  $C_0 \sim 1 - C_1 \sim 1$ . They find that the optimal ratio is  $r_e/r_0 = 1.1468$ . In this case, the potential from the applied rf voltages will have the form

$$\phi_{\text{rf}}(\tilde{x}, \tilde{y}, t) = -\frac{1}{2}U_{\text{rf}} \cos(\Omega_{\text{rf}}t) \frac{\tilde{x}^2 - \tilde{y}^2}{r_0^2}, \quad (2.5)$$

near the trap axis. A dc potential,  $U_{\text{end}}$ , is applied to the 8 endcap electrodes and will generate a potential of the form

$$\phi_{\text{dc}}(\tilde{x}, \tilde{y}, z, t) = \eta U_{\text{end}} \frac{z^2}{z_0^2} - \frac{1}{2} \eta U_{\text{end}} \frac{\tilde{x}^2 + \tilde{y}^2}{z_0^2}, \quad (2.6)$$

where the second term defocuses the potential due to Laplace's law. Here  $\eta$  is a constant depending on the trap geometry and  $2z_0$  the length of the center electrode. In addition to these potentials it is in general possible to add other dc-potentials to compensate for other electric fields and to move the zero point of the trap [37], see e.g. section 12.2.

The equation of motion for a single charged particle in this potential can be separated into three modes. Firstly, the motion along the z-axis which is just a harmonic motion due to the potential

$$\Phi(z) = \frac{1}{2} M \omega_z^2 z^2, \quad (2.7)$$

where we have defined the axial secular frequency

$$\omega_z \equiv \sqrt{\frac{2\eta Q U_{\text{end}}}{M z_0^2}}. \quad (2.8)$$

In the radial directions the equations of motion can be put in a standard form

$$\frac{\partial^2 u}{\partial \tau^2} + [a - 2q_u \cos(2\tau)]u = 0 \quad \text{where } u = \tilde{x}, \tilde{y}. \quad (2.9)$$

This is called the Mathieu equation after Émile Mathieu [124, p. 721ff]. In eq. 2.9 we have defined the dimensionless parameters:

$$\tau = \frac{\Omega_{\text{rf}} t}{2}, \quad a = -4 \frac{\eta Q U_{\text{end}}}{M z_0^2 \Omega_{\text{rf}}^2}, \quad q_{\tilde{x}} = -q_{\tilde{y}} = 2 \frac{Q U_{\text{rf}}}{M r_0^2 \Omega_{\text{rf}}^2}, \quad (2.10)$$

where  $Q$  and  $M$  are the charge and mass of the particle, respectively.

For ion trapping the relevant solutions to eq. 2.9 are the stable (i.e. not diverging) solutions. Figure 2.2 shows a plot of the regions of stable solutions to the Mathieu equation in terms of the parameters  $a$  and  $q$  for radial confinement (a) and axial as well as radial confinement (b) [121].

Note that the stability parameters depend on the dimensionless parameters  $a$ ,  $q$ , which in turn depend only on the charge-to-mass ratio,  $Q/M$ , of the particles. In the stability diagram there is a range of  $q$  and  $a$  values such that different ion species with different  $Q/M$  can be trapped

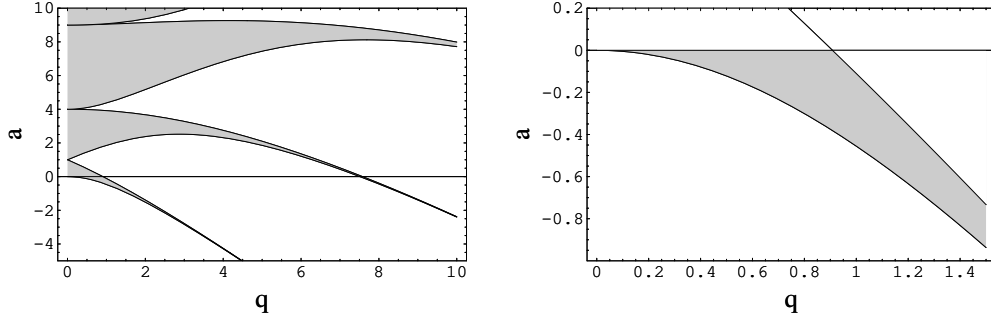


Figure 2.2: Single-ion stability diagrams for linear Paul trap. a) Shaded areas indicate radial stability. b) First stability zone: For axial as well as radial stability,  $a < 0$  is required if  $Q > 0$ , as indicated by the shaded area [121].

simultaneously if the ratio  $Q/M$  falls within the stability region for both species. Inspecting the stability diagram the regions are broader for lower  $a$  and  $q$ .

The typical operating range of ion traps are  $|a|, |q| \ll 1$ . In this limit approximate solutions to equation 2.9 can be written as

$$u(t) = u_0 \left[ 1 - \frac{q_u}{2} \cos(\Omega_{\text{rf}} t) \right] \cos(\omega_u t), \quad (2.11)$$

where we have introduced the secular frequency

$$\omega_u = \frac{\sqrt{q_u^2/2 + a_u}}{2} \Omega_{\text{rf}}. \quad (2.12)$$

The ion motion occurs on two timescales (eq. 2.11), one set by the secular frequency called secular motion, and one at the rf-frequency called micromotion. Typically we will consider the symmetric case where  $\omega_x = \omega_y = \omega_r$ . Since  $\omega_r \ll \Omega_{\text{rf}}$  and  $|q| \ll 1$  the secular motion will be much slower than the micromotion, and the amplitude of the micromotion will be much smaller, hence its name.

Since the micromotion is much faster and much smaller in amplitude than the secular motion it can be averaged out and we can define a pseudopotential corresponding to the secular motion. The pseudopotential in the radial direction in a symmetric situation is

$$\Phi_r(r) = \frac{1}{2} M \omega_r^2 r^2, \quad (2.13)$$

The secular frequency in the radial direction is, in terms of the applied voltages, given by

$$\omega_r^2 = \frac{Q^2 U_{\text{rf}}^2}{2M^2 r_0^4 \Omega_{\text{rf}}^2} - \frac{1}{2} \omega_z^2, \quad (2.14)$$

Note that for trapping positively charged ions the endcap potentials are always positive, which implies  $a < 0$ .

### 2.3 Micromotion

As will be shown later it is in general desirable to minimize the effect of micromotion since it interferes with efficient laser cooling. By inspection of equation 2.11 it is clear that the micromotion amplitude is proportional to  $q_u$  and  $u_0$ . Per assumption about the trap driving parameters,  $q_u \ll 1$  (typically 0.1) this limits the amplitude of the micromotion to  $u_0 q_u / 2$ . If the ion is near the trap center line (i.e.  $u_0$  small) then micromotion is also accordingly small. Thus a colder ion would experience less micromotion, because it spends more time close to the center axis. Note that this concerns the radial, not the axial direction, since there is in principle no micromotion along the axial (trap) axis, as only the dc endcap voltage is applied in this direction. This means that there exists a line parallel with the trap axis for which the rf amplitudes cancel which we will call the rf null line. If the trap is perfectly symmetric the trap axis and the rf null line will be the same. If, however, there is some asymmetry in the rf potentials the rf null line can be displaced from the geometric center of the trap, see section 12.2.1.

For single trapped ions the micromotion will be small and can be almost entirely eliminated by making sure that the ion sits on the rf nodal line [122]. For large crystals ions away from the rf node will always experience micromotion, and micromotion-related effects, such as rf-heating, can become important as will be described in section 4.2.

The estimate of micromotion given in the previous section is a best case scenario. In a real trap stray electric fields or trap asymmetries such as uneven delay between trap electrodes will give rise to so called excess micromotion. This excess micromotion is different from the ordinary kind in that it can be eliminated by the right compensation.

#### 2.3.1 Excess micromotion due to static electric fields

Consider a uniform static electric field  $\mathbf{E}_{dc}$  added to equation 2.9. This field would push the ion away from the trap axis, giving a dc offset, and thus increase the amount of micromotion so that a new solution (to first order in  $q_u$ ) to the Mathieu equation would be [122]

$$u(t) \simeq [u_{dc} + u_1 \cos \omega_r t] \left[ 1 + \frac{q_u}{2} \cos \Omega_{rf} t \right], \quad (2.15)$$

where

$$u_{dc} \simeq \frac{Q \mathbf{E}_{dc} \cdot \hat{u}}{m \omega_r^2}. \quad (2.16)$$

In this case the excess micromotion can be eliminated by simply countering the ion position offset with another opposite static potential applied to an appropriate electrode. A simple way to detect micromotion in this case is to lower the rf potential which will in turn lower the secular frequency and increase the dc offset. At low secular frequencies the dc offset will then be clearly seen from the ion position.

Possible causes of static electrical fields in the vicinity of the trap include charging from UV beams, stray potentials applied to electrodes, dielectric material near the trap etc.

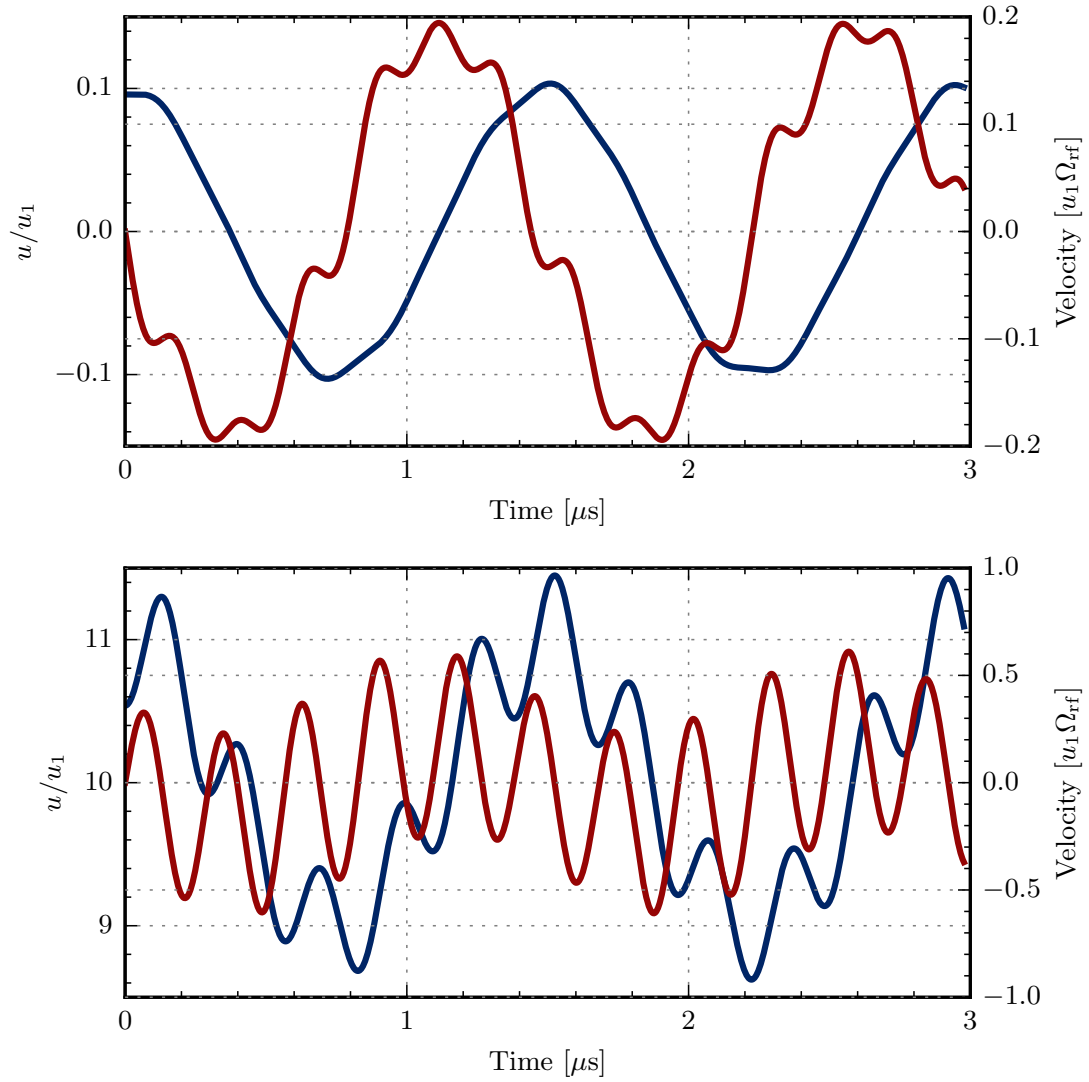


Figure 2.3: **Top:** Position (blue) and velocity (red) of the ion with no excess micromotion for  $a = 0$  and  $q = 0.084$ . **Bottom:** Position (blue) and velocity (red) of the ion with excess micromotion due to an offset  $u_0 = 10u_1$  for  $a = 0$  and  $q = 0.084$ , where  $u_1$  is the amplitude of the secular motion.

### 2.3.2 Excess micromotion due to phase difference

A phase difference between the rf potentials applied to the electrodes will also generate micromotion. A phase difference will occur if e.g. the path length of the trap electrode wires are not equal or if there are differences in the capacitances of the electrodes [122].

The phase difference will give another term in expression 2.11, for the position

$$u'(t) \simeq u(t) - \frac{1}{4}q_u r_0 \alpha \phi_{ac} \sin \Omega_{\text{rf}} t, \quad (2.17)$$

where  $u$  is the ion position without a phase difference,  $\phi_{ac}$ , and  $\alpha$  is a geometric constant of the order of 1 [122]. Note that the effect of the phase difference is a modulation of the ion position, but not an offset. This makes detection harder since the technique of lowering the rf potential will not work in this case. Instead, one can use a detection scheme based on the effect of micromotion on the fluorescence spectrum of an ion, see section 12.2. To compensate for micromotion due to the phase difference between the electrodes the capacitance of the individual electrodes can be adjusted.

## 2.4 Trap depth

In addition to the slope of a particle trap the depth is also of interest. Particles with a temperature  $T$  will have typical kinetic energies of the order of  $k_B T$ . If this energy is larger than the trap depth most particles will escape and be lost. In the case of neutral particles typical trap depths are lower than the typical energy of room temperature particles and cooling is necessary to keep the particles in the trap.

The radial trap depth of a linear Paul trap as discussed in this work is determined roughly by the dimensions and potentials applied to the trap. In the case of a perfectly harmonic trap the depth is given by the pseudopotential at the electrodes

$$\Phi_r(r_0) = \frac{1}{2} M \omega_r^2 r_0^2, \quad (2.18)$$

which for typical trapping parameters is on the order of a few eV or equivalently several thousand kelvin. Thus laser cooling is not strictly necessary for our trap since the trap is at room temperature and the ions created are at  $T \sim 400^\circ\text{C}$  (see section 11.1). This estimate of the trap depth assumes a harmonic trap which is a good approximation for well-designed traps [123].

In the axial direction the trap depth can be estimated simply by the potential difference between the center of the trap and the endcap potentials. This means that the radial and axial depth are about equal.

## 2.5 Ion Coulomb crystals

When more than a single ion is trapped in a Paul trap the dynamics become much more complicated and a whole area of research is dedicated to the structures that form, see [125],[126], and [127] for reviews of the developments in these fields.

The ions will, in addition to the trapping potential, experience the Coulomb repulsion from each other. For the case of two cold ions in a linear Paul trap the mutual repulsion will give new equilibrium positions in the trap where, for identical ions, a symmetric displacement around the trap center will occur. Following [128] we define the ratio

$$\tilde{\alpha} \equiv \frac{\omega_z^2}{\omega_r^2}. \quad (2.19)$$

If we consider the case where the radial confinement is stronger than the axial,  $\alpha < 1$ , the ion displacement will be in the axial direction and be symmetric around the trap center. Adding more ions, a chain will form such that the ions will all lie like on a string along the trap axis. Their equilibrium positions can be trivially, if tediously, calculated and one finds that the harmonic potential makes the ion linear density in the string non-uniform [129]. Since the innermost ions feel the combined force of the confinement of all the other ions, they will be more compressed.

If the number of ions is increased even further there will come a point where the total force pushing on the ions axially will make it more energetically favorable to form a *zig-zag* structure, by pushing ions off the trap axis [128]. The transition from a 1D structure, the string, to a 2D structure, the zig-zag, happens at a specific value of  $\tilde{\alpha}$  which depends on the number of ions,  $N$ ,

$$\tilde{\alpha}_{\text{tr}} = cN^\beta \quad (2.20)$$

where  $c = 0.395$  and  $\beta = -1.73$  are constants which have been found through Molecular Dynamics (MD) simulations [128]. Alternative treatments show qualitative agreement with the power law scaling, but obtain other constants [130]. The dynamics of these situations have been recently investigated with regards to formations of defects, kinks, in the zig-zag structures [131][65].

If the trap has been properly compensated for micromotion the ion string will not experience significantly more micromotion than a single ion. According to theory the axial micromotion in a linear Paul trap should be negligibly small [132]. For ensembles of ions that are not all confined to the trap axis there will be a significant radial micromotion amplitude depending on the distance from the trap center as explained above. This will decrease the effectiveness of laser cooling, see chapter 4.2.

When large numbers of ions are confined in the trap the dynamics are best modeled and understood in terms of plasma theory, where we describe the ion cloud in terms of collective parameters such as its density and temperature, see e.g. [133] for a more detailed treatment. These ensembles of ions will, if cold enough, form ordered structures called ion Coulomb crystals [126]. The zero-temperature density of such an ion Coulomb crystal can be calculated and will be given by

$$\rho_0 = \frac{\epsilon_0 U_{rf}^2}{M r_0^4 \Omega_{rf}^2}, \quad (2.21)$$

where we see that the density solely depends on the amplitude of the rf potential [133]. From this density we can introduce the Wigner-Seitz radius as the radius of a sphere with a volume

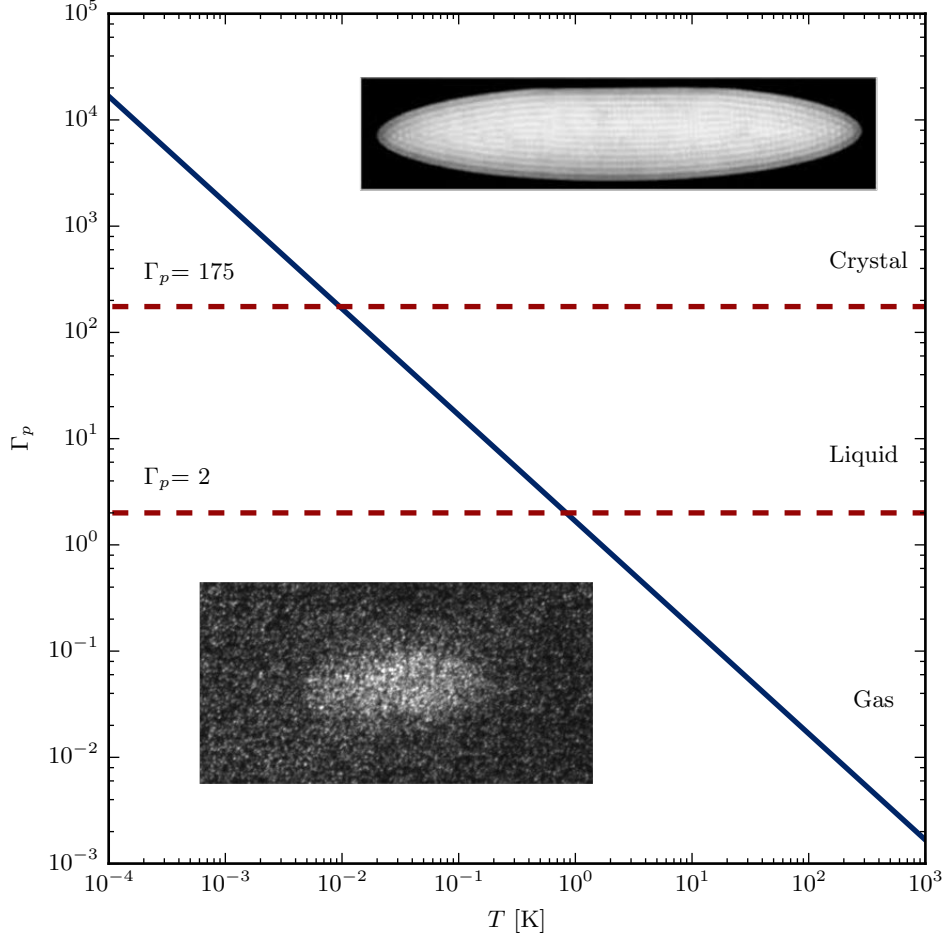


Figure 2.4: Correlation parameter,  $\Gamma_p$  versus the temperature,  $T$  for typical trapping parameters with  $a_{\text{WS}} = 10 \mu\text{m}$  and  $Q = +1e$ . For  $\Gamma_p > 2$  some short range order is expected, while for  $\Gamma_p \gtrsim 175$  long range order and crystallization are expected (for infinite system). Top inset shows a crystal with roughly 6400 ions courtesy of Herskind et al. [77]. Bottom inset shows a cloud of ions, not crystallized, from the trap used in chapter 12.

corresponding to the volume per particle for a zero temperature crystal

$$\frac{4}{3}\pi a_{\text{WS}}^3 = \frac{1}{\rho_0}. \quad (2.22)$$

The shape, size, and density of ion Coulomb crystals are typically well-approximated by the zero temperature charged liquid model even though they are really ordered structures [134]. For a cylindrically symmetric potential this model suggests that the equilibrium shape is a spheroid which we characterize by its aspect ratio, not to be confused with the related  $\tilde{\alpha}$

$$\alpha \equiv \frac{2R}{L} \quad (2.23)$$

where  $R$  is the radius of the crystal and  $L$  is the length. The shape is governed by the Coulomb repulsion and the trap potential and relations can be found in the literature. See e.g. [135] or [133, p. 22ff] for details.

The thermodynamical properties of these charged plasmas is determined by the ratio of the mean energy of the ion-ion interactions

$$E_{\text{Coulomb}} = \frac{Q^2}{4\pi\epsilon_0 a_{\text{WS}}}, \quad (2.24)$$

where  $a_{\text{WS}}$  denotes the Wigner-Seitz radius of the crystallized structure, to the typical energies of the motional degrees of freedom given by

$$E_{\text{kin}} \propto k_B T. \quad (2.25)$$

This motivates the definition of the so-called plasma (or correlation) parameter

$$\Gamma_p = \frac{Q^2}{4\pi\epsilon_0 a_{\text{WS}} k_B T} \propto \frac{E_{\text{Coulomb}}}{E_{\text{kin}}}. \quad (2.26)$$

MD simulations have shown that for finite ion clouds in a Paul trap, correlation effects will begin to manifest as short range order at  $\Gamma_p \gtrsim 2$ . Long range order appears at  $\Gamma_p \sim 100$  as decaying oscillations in the ion density from the edge inwards. As the correlation parameter increases these oscillations manifest as concentric shells [136]. These concentric shells act as the lattice planes of our pseudo-crystal<sup>3</sup> which bend to satisfy the boundary conditions set by the trap. The crystallization thus happens from the outside and works inwards as the correlation parameter increases. This also means that the crystals melt from the inside. Observations of this long range order of small three dimensional ion Coulomb crystals in agreement with MD simulations have been reported [137][138].

For the case of an infinite Coulomb crystal the ions will enter ordered structures with body-centered cubic (bcc) being slightly more energetically favorable than face-centered cubic (fcc) and hexagonal closed packed (hcp) structures [126, sec. 2]. The value of the correlation parameter for which crystallization occurs also changes from  $\Gamma_p = 175$  in the infinite case to  $\Gamma \sim 200$  for  $\sim 10000$  ions and  $\Gamma_p \sim 500$  for  $\sim 100$  ions according to MD simulations [139], see also figure 2.4.

For finite crystals the plasma coupling parameter required for crystallization increases. For typical practical values of  $a_{\text{WS}} \sim 10 \mu\text{m}$  in an rf trap, the crystallization temperature,  $T_{CC}$  for singly-charged ions becomes,

$$T \leq T_{CC} \sim 10 \text{ mK}, \quad (2.27)$$

which is found by assuming an infinite crystal and using eq. 2.26. This compares favorably to the typical expected Doppler cooling temperature in the mK range for the singly charged ions considered in this work, see section 4.2. This means that even for small, finite systems, crystallization should still be attainable by means of Doppler cooling.

---

<sup>3</sup>Ion Coulomb crystals are technically not real crystals as they are not uniform due to the surface effects.

Ion Coulomb crystals have been produced in laboratories around the world since the late eighties [140][141]. They are also expected to be found in white dwarf stars and in the crust of neutron stars where the density allows for crystallization even at several million kelvin [126].

Possible applications of ion Coulomb crystals include quantum memories [142, 143], atomic clocks [144]; for further applications, see e.g. [127] and [126].

## Chapter 3

# Atom-light interactions

In this chapter we focus on the interactions between atoms and light, namely interactions of few-level atoms with near resonant monochromatic light fields which are relevant for this thesis.

First, the density matrix and master equation formalism will be introduced. We will then discuss the quantization of the electromagnetic field and light matter interaction in the dipole approximation. This theory is then applied to a two level atom interacting with an electrical field.

### On notation

A quantum system can be described by quantum states  $|\psi\rangle \in \mathcal{H}$ , where  $\mathcal{H}$  is a Hilbert space corresponding to the system. The direct product of two Hilbert spaces  $\mathcal{H}_1$  and  $\mathcal{H}_2$  is denoted by  $\mathcal{H}_{\text{tot}} = \mathcal{H}_1 \otimes \mathcal{H}_2$ .

In the following we will be using the *Dirac bra-ket notation* [145] where a quantum state in the Schrödinger picture is denoted  $|\psi, t\rangle$  where the  $t$  denotes the time-dependence of the state. In the Schrödinger picture operators are stationary i.e. not a function of time. A state in the Heisenberg picture will be denoted  $|\psi\rangle = |\psi, 0\rangle$ . In the Heisenberg picture states are stationary while the operators are time-dependent. Quantum states in the interaction picture will be denoted  $|\psi, t\rangle_I$ .

### 3.1 Quantum dynamics (intro)

Most texts on quantum mechanics discuss so-called closed quantum systems which are governed by the Schrödinger equation (in the Schrödinger picture [30, p. 82])

$$i\hbar \frac{d|\psi, t\rangle}{dt} = \hat{H}|\psi, t\rangle, \quad (3.1)$$

where  $\hbar$  is the reduced Planck constant,  $|\psi, t\rangle$  is the quantum state of the system and  $H$  is the Hamiltonian.

The Hamiltonian of a quantum system is found by writing an expression for the energy of the system as a function of system operators, i.e. variables of the system corresponding to observable

quantities. Unfortunately any real system will have too many interactions to be modeled exactly, so simpler models and approximations are needed.

Here we will focus on the interaction between atoms and electromagnetic radiation. The first and most situation to consider is that of a closed system which does not interact with its surroundings, such that there is a limited number of variables. Depending on the system the Hamiltonian can take various forms. If stationary solutions to the atomic Hamiltonian have been found<sup>1</sup> we can write the Hamiltonian in terms of these solutions,  $|\psi_k, t\rangle = |\psi\rangle e^{-i\omega_k t}$  and their energies,  $E_k = \hbar\omega_k$ , where  $\omega_k$  is the angular frequency corresponding to the energy of the state,

$$H_A = \sum_k \hbar\omega_k |\psi_k\rangle\langle\psi_k|, \quad (3.2)$$

where the sum runs over all the states found or, in most cases, some subset of these that will be involved in the dynamics. Note that the states in eq. 3.2 are in the Heisenberg picture (i.e. stationary) since they are used to define a time-independent operator.

To include the interaction with the environment we need to extend the Hilbert space, such that we will have a larger Hilbert space,  $\mathcal{H} = \mathcal{H}_{\text{sys}} \otimes \mathcal{H}_{\text{R}}$ , where  $\mathcal{H}_{\text{R}}$  is the Hilbert space of the environment. The Hamiltonian for the total system can then be written as

$$H_{\text{tot}} = H_{\text{sys}} + H_{\text{R}} + V, \quad (3.3)$$

where  $H_{\text{sys}}$  is the system Hamiltonian (equal to  $H_A$  in the example above) acting on the system.  $H_{\text{R}}$  is the environment Hamiltonian, typically corresponding to an infinite number of harmonic oscillators representing the quantized electromagnetic field around the atom.  $V$  is the interaction between the environment and the system. The  $V$  term is the only term acting on both the system and the environment. The dividing line between system and environment and thus ultimately the dividing line between the quantum and classical world is called the Heisenberg cut and it is arbitrary — most often it is dictated by the practicalities of experiments and the tractability of calculations.

In this chapter we will describe two ways of handling the interaction with the environment. Since we are interested in the dynamics of the system we will use the formalism of open quantum system which determines the evolution of the system in the presence of the environment. First, a presentation of the density operator and the corresponding master equation will be given. Second, a description of the Heisenberg picture and an outline of the derivation of the Heisenberg-Langevin equations will be given. Both the master equation and the Heisenberg-Langevin equations describe the same weak interaction with a large environment acting as a reservoir, and either formalism can be used.

## 3.2 Density operator and the master equation

The quantum state describes the state of a quantum system in a given realization. In many cases it is preferable to also consider statistical mixtures, i.e. the uncertainty in the state of the system

<sup>1</sup>See e.g. [146, Ch. 3] for solutions to atomic systems.

not due to quantum mechanics, but rather due to unknown preparation or due to the stochastic nature of collapsing wavefunctions. In these cases the density operator description due to von Neumann is very useful [147, p. 178]. Suppose the quantum state of the system is known to be  $|\psi_k, t\rangle$  with probability  $P_k$ . We define the density operator as [148, p. 22]

$$\rho(t) = \sum_k P_k |\psi_k, t\rangle \langle \psi_k, t|, \quad (3.4)$$

where the  $|\psi_k, t\rangle$  states do not need to be orthogonal. The corresponding density matrix will have elements that correspond to the probabilities and superpositions of the state of the system. The diagonal elements will be the probabilities to find the system in the states corresponding to the chosen basis. The off-diagonal elements are typically called the coherences and describe the degree of superposition of the system in the basis chosen.

For a given density operator it is possible to get the mean value<sup>2</sup> of any operator,  $A$ , from

$$\text{tr}(\rho(t)A) = \text{tr} \sum_k P_k A |\psi_k, t\rangle \langle \psi_k, t| = \sum_k P_k \langle \psi_k, t | A | \psi_k, t \rangle = \langle A \rangle(t). \quad (3.5)$$

To find  $\rho(t)$  we need *von Neumann's equation* for the time derivative of the density operator:

$$\dot{\rho}(t) = -\frac{i}{\hbar} [H, \rho(t)], \quad (3.6)$$

where  $[a, b] = ab - ba$  is the commutator between operators  $a$  and  $b$ . Given some initial conditions the density operator,  $\rho(t)$ , can be found by solving eq. 3.6 [148, Ch. 2, p. 24].

### 3.2.1 Lindblad form

Equation 3.6 describes the unitary evolution of a closed quantum system. For a description of open systems one has to include the effect of the environment, in which case one can get a master equation for the density operator or Heisenberg-Langevin equation for the system's observables. In this thesis we will be working with relatively weak couplings to the environment. Here a weak coupling means that the interaction is small enough or the environment is large enough that the environment is left effectively undisturbed. In this case the effect of the environment interaction on the system can be represented using so-called Lindblad operators,  $L_j$ . These will then represent the various decay channels of the system.

A master equation is said to be in the Lindblad form if it can be written as<sup>3</sup>

$$\frac{d\rho}{dt} = -\frac{i}{\hbar} [H_{\text{sys}}, \rho] + \sum_j [2L_j \rho L_j^\dagger - \{L_j^\dagger L_j, \rho\}] \equiv \mathcal{L}\rho, \quad (3.7)$$

where  $\{a, b\} = ab + ba$  denotes the anti-commutator, and we define  $\mathcal{L}$  which is typically called the Liouvillian<sup>4</sup>. A master equation that can be written in the Lindblad form is guaranteed to be positive semi-definite, which is a requirement for physical results [149][150, p. 121].

<sup>2</sup>For a mixed state this is just the weighted average of the mean values for the operator for the pure states.

<sup>3</sup>See Nielsen and Chuang [30, p. 386] and Gardiner and Zoller [148, p. 147] for definitions, discussion and derivations. Note factor of  $\sqrt{2}$  difference with this definition of the Lindblad form master equation with respect to e.g. Lindblad's original paper [149, eq. (4.3)] and Wiseman [150, p. 119f].

<sup>4</sup>The Liouvillian is the generator of time-evolution for the density operator semi-group.

Equation 3.7 is useful in the case where the decay rates between predetermined system states are known. Consider for example a spontaneous decay from an excited state  $|e\rangle$  to the ground state  $|g\rangle$ . The relevant operator is  $L = \sqrt{\Gamma_{eg}/2}|g\rangle\langle e|$ , where  $\Gamma_{eg}$  is the corresponding decay rate.

### 3.3 Quantized electromagnetic field

Before discussing the interaction between light and matter it is worth reminding ourselves of the quantum treatment of the electromagnetic field, see e.g [151] for an accessible treatment.

Starting from Maxwell's equations without sources, in SI units

$$\nabla \times \mathbf{E} = -\frac{\partial \mathbf{B}}{\partial t} \quad (3.8)$$

$$\nabla \times \mathbf{B} = \mu_0 \epsilon_0 \frac{\partial \mathbf{E}}{\partial t} \quad (3.9)$$

$$\nabla \cdot \mathbf{B} = 0 \quad (3.10)$$

$$\nabla \cdot \mathbf{E} = 0, \quad (3.11)$$

solutions to the electric field,  $\mathbf{E}(\mathbf{r}, t)$  and the magnetic field  $\mathbf{B}(\mathbf{r}, t)$  can be found given the right boundary conditions. Here we consider the case of a one-dimensional cavity with perfectly conducting walls at  $z = 0$  and  $z = L$ . A standing wave solution to Maxwell's equations for the electric and magnetic field in this case can be written as

$$E_x(z, t) = \left(\frac{2\omega^2}{V\epsilon_0}\right)^{1/2} q(t) \sin(kz) \quad (3.12)$$

$$B_y(z, t) = \left(\frac{\mu_0\epsilon_0}{k}\right) \left(\frac{2\omega^2}{V\epsilon_0}\right)^{1/2} \dot{q}(t) \cos(kz), \quad (3.13)$$

where  $\omega$  is the angular frequency of the mode and  $k = \omega/c$  is the wavenumber. Due to the boundary conditions the allowed modes are  $\omega_m = c(m\pi/L)$  for  $m = 1, 2, \dots$ . Here  $q(t)$  has the unit of length and contains the time dependent part; it will act as the canonical position, while  $\dot{q}(t)$  is the corresponding canonical momentum for unit "mass".

The classical field energy of such a single mode field is given by

$$H = \frac{1}{2} \int \left[ \epsilon_0 \mathbf{E}^2(\mathbf{r}, t) + \frac{1}{\mu_0} \mathbf{B}^2(\mathbf{r}, t) \right] d\mathbf{r} \quad (3.14)$$

$$= \frac{1}{2} (p^2 + \omega^2 q^2), \quad (3.15)$$

such that it is apparent that the single mode field is equivalent to a harmonic oscillator with canonical coordinates  $q$  and  $p$ . Second quantization can then be performed by postulating the commutation relation

$$[\hat{q}, \hat{p}] = i\hbar. \quad (3.16)$$

Then the formalism of the quantum harmonic oscillator can be applied, specifically we replace the  $\hat{q}$  and  $\hat{p}$  operators with the creation and annihilation operators  $\hat{a}^\dagger$  and  $\hat{a}$  given by

$$\hat{a}^\dagger = \frac{1}{\sqrt{2\hbar\omega}}(\omega\hat{q} + i\hat{p}) \quad (3.17)$$

$$\hat{a} = \frac{1}{\sqrt{2\hbar\omega}}(\omega\hat{q} - i\hat{p}). \quad (3.18)$$

The Hamiltonian can then be expressed as

$$\hat{H} = \hbar\omega \left( \hat{a}^\dagger \hat{a} + \frac{1}{2} \right), \quad (3.19)$$

and the electric and magnetic field can be expressed as

$$\hat{E}_x(z) = \mathcal{E}_0(\hat{a} + \hat{a}^\dagger) \sin(kz) \quad (3.20)$$

$$\hat{B}_y(z) = -i\mathcal{B}_0(\hat{a} - \hat{a}^\dagger) \cos(kz), \quad (3.21)$$

where the normalization is given by

$$\mathcal{E}_0 = \sqrt{\frac{\hbar\omega}{\epsilon_0 V}}, \quad (3.22)$$

and  $V$  is the effective volume of the cavity found by integrating the spatial structure

The energy eigenstates of the harmonic oscillator are the Fock, or number, states  $|n\rangle$  corresponding to well-defined numbers of photons in the state. The creation and annihilation operators raise and lower the number of photons by one, respectively

$$\hat{a}^\dagger |n\rangle = \sqrt{n+1} |n+1\rangle. \quad (3.23)$$

$$\hat{a} |n\rangle = \sqrt{n} |n-1\rangle. \quad (3.24)$$

Another relevant basis is that of the coherent states, defined such that

$$\hat{a} |\alpha\rangle = \alpha |\alpha\rangle, \quad (3.25)$$

$$\langle \alpha | \hat{a}^\dagger = \langle \alpha | \alpha^*; \quad (3.26)$$

where  $\alpha$  is a complex number [151, p. 43]. The coherent states are also referred to as "quasi-classical states" in the sense that their properties resemble those of classical fields.

The general result for the quantization of the electromagnetic field will be a superposition of many modes. The electric field operator can be given in terms of the annihilation and creation operators,  $\hat{a}_k$  and  $\hat{a}_k^\dagger$ , and the polarization unit vector,  $\hat{e}_k$ , as

$$\hat{\mathbf{E}}(\mathbf{r}, t) = i \sum_{\mathbf{k}, \epsilon} \hat{e}_k \mathcal{E}_k a_k e^{i\mathbf{k}\cdot\mathbf{r}} + \text{H.c.}, \quad (3.27)$$

where H.c denotes the Hermitian conjugate of the preceding terms, and the sum is over all planes waves [151, p. 23]. The sum runs over all valid combinations of wavenumbers,  $\mathbf{k}$ , and polarizations.

In the following we will mostly deal with a single mode of the electric field at a time and the effect of modes not explicitly driven i.e. modes in thermal states, will be treated using the Lindblad formalism.

The normalization constant  $\mathcal{E}_k$ , which we will denote  $\mathcal{E}_0$  when considering single mode fields, has the units of electric field and can be determined by noting that the energy in the number state (for a plane wave) can be given as

$$\langle n | \int \epsilon_0 |\hat{\mathbf{E}}(\mathbf{r}, t)|^2 d^3\mathbf{r} | n \rangle = \hbar\omega(n + 1/2) \quad (3.28)$$

$$\langle n | \epsilon_0 \mathcal{E}_0^2 V (2\hat{n} + 1) | n \rangle = \epsilon_0 \mathcal{E}_0^2 V (2n + 1) = \hbar\omega(n + 1/2) \quad (3.29)$$

$$\mathcal{E}_0 = \sqrt{\frac{\hbar\omega}{2\epsilon_0 V}}, \quad (3.30)$$

where we have defined the effective mode volume as the integral over all space of the spatially dependent part of the wave. The normalization constant  $\mathcal{E}_0$  can also be interpreted as the root-mean-square (r.m.s.) fluctuation of the electric field in the vacuum state or of the coherent states [151, p. 16 and p. 45][68, p. 110]<sup>5</sup>.

The expectation value of the electric field will be zero for any Fock/number state  $|n\rangle$ , but will be non-zero for the coherent states  $|\alpha\rangle$ . For a coherent state (in a single mode) the electric field amplitude will be

$$\langle \alpha | \hat{\mathbf{E}}(\mathbf{r}, t) | \alpha \rangle = 2|\alpha|\mathcal{E}_0 \sin(\omega t - \mathbf{k} \cdot \mathbf{r} - \theta), \quad (3.31)$$

where we have used that a complex number can be written in polar form  $\alpha = |\alpha|e^{i\theta}$ . This means that  $2|\alpha|$  can be interpreted as the amplitude of the electric field in units of  $\mathcal{E}_0$  [151, p. 45].

The intensity of the field defined as

$$I \equiv \frac{1}{2} c \epsilon_0 \langle E^2 \rangle, \quad (3.32)$$

is then given by

$$I = 2c\epsilon_0 \mathcal{E}_0^2 (|\alpha|^2 + 1/4). \quad (3.33)$$

### 3.4 Interactions

To handle the effect of driving the system with lasers we will treat the electric field modes of the lasers separately from the reservoir of modes discussed above. Treating the interaction between the driven light modes and the atom as a perturbation [146, Ch. 4], the interaction energy between a dipole and an electric field to first order is

$$\hat{H}_{\text{int}}(t) = -\hat{\mathbf{d}} \cdot \hat{\mathbf{E}}(t), \quad (3.34)$$

---

<sup>5</sup>The field mode of a standing wave can be formed by adding two plane waves with opposite wavenumbers. By defining a new mode as the superposition of these two modes you can construct a standing wave mode. In the rest of this chapter we will not need to specify whether a running or standing wave is considered, since the difference is absorbed into  $\mathcal{E}_0$ .



Figure 3.1: A two level atom in a laser beam driving the transition between the ground and excited state. The spontaneous decay rate is indicated with by  $\Gamma$ .

where  $\hat{\mathbf{d}} = Q\hat{\mathbf{r}}$  is the dipole operator and  $\hat{\mathbf{E}}(t)$  is the electric field operator for the specific field mode.

We will write the dipole operator,  $\hat{\mathbf{d}}$ , in terms of the stationary states of the atomic Hamiltonian

$$\hat{\mathbf{d}} = \sum_{fi} \mathbf{d}_{fi} |f\rangle \langle i|, \quad (3.35)$$

where  $\mathbf{d}_{fi}$  are the dipole matrix elements for the transition between the  $|i\rangle$  and  $|f\rangle$  states.

Note that this is a vector quantity which makes the interaction polarization dependent. This can be seen here explicitly by decomposing the polarization vector and the dipole operator into their spherical components [146, p. 203f]

$$\hat{\mathbf{e}} \cdot \hat{\mathbf{d}} = q \sum_{q=0,\pm 1} \epsilon_q^* \hat{\mathbf{r}}_q. \quad (3.36)$$

Selection rules for the transition will then apply, see e.g. [146, p. 204].

The interaction Hamiltonian is thus a sum of product operators from the Hilbert spaces of the atom and the laser modes. All interactions with field modes that are not driven, i.e. in the vacuum state (or possibly in some thermal state), will be the source of the spontaneous decay and will be handled using Lindblad operators. In this way the only modes that will be explicitly taken into account in the calculations are the ones close to an atomic resonance and/or driven by a laser. Modes of optical resonators, like e.g. the cavities of this thesis, will be considered separately.

### 3.5 Two level atom example

The two level atom is the simplest non-trivial problem in quantum mechanics. By neglecting far off-resonant interactions many systems can be reduced to effective two level systems. Consider the level scheme shown in figure 3.1. Here a system Hilbert space of dimension  $d = 2$  is coupled to a reservoir of electromagnetic field modes, where one is driven. The corresponding atomic and field

Hamiltonians are,

$$\hat{H}_A = \hbar\omega_g|g\rangle\langle g| + \hbar\omega_e|e\rangle\langle e| \quad (3.37)$$

$$\hat{H}_I = \hbar\omega(\hat{a}^\dagger\hat{a} + 1/2), \quad (3.38)$$

where  $\omega_e$  and  $\omega_g$  are the angular frequencies corresponding to the energies of the states.

We expand the interaction Hamiltonian

$$\hat{H}_{\text{int}}(t) = -\hat{\mathbf{d}} \cdot \hat{\mathbf{E}}(t) = -(\mathbf{d}_{eg}|g\rangle\langle e| + \mathbf{d}_{ge}|e\rangle\langle g|)(\hat{\epsilon}\mathcal{E}_0\hat{a}e^{-i\omega t + i\mathbf{k}\cdot\mathbf{r}} + \text{H.c.}) \quad (3.39)$$

Since we are going to treat the interaction as a small perturbation on the atomic states, it is useful to go to the interaction picture where the dynamics are governed by the interaction Hamiltonian. We thus go into a rotating frame given by  $\hat{U}(t) = \exp(i(\hat{H}_A + \hat{H}_I)t/\hbar)$ , corresponding to rotating the basis states at the rate of the rotation of the atomic eigenstates to cancel their rotation, thereby making the atomic states constant. States and operators in the interaction picture are given by

$$|\psi, t\rangle_I = \hat{U}(t)|\psi, t\rangle_S, \quad (3.40)$$

$$\hat{A}_I(t) = \hat{U}(t)\hat{A}_S\hat{U}^\dagger(t). \quad (3.41)$$

The dynamics of the system are now determined by

$$i\hbar\frac{d|\psi, t\rangle}{dt} = \hat{H}_{\text{int}, I}|\psi, t\rangle. \quad (3.42)$$

The interaction Hamiltonian, in the interaction picture, is

$$\hat{H}_{\text{int}, I}(t) = -\hbar g\hat{U}(t)(|g\rangle\langle e| + |e\rangle\langle g|)(ae^{-i\omega t} + a^\dagger e^{+i\omega t})\hat{U}^\dagger(t) \quad (3.43)$$

$$= -\hbar g(e^{-i\omega_{eg}t}|g\rangle\langle e| + e^{+i\omega_{eg}t}|e\rangle\langle g|)(ae^{-i\omega t} + a^\dagger e^{+i\omega t}) \quad (3.44)$$

$$= -\hbar g(|g\rangle\langle e|ae^{-i(\omega+\omega_{eg})t} \quad (3.45)$$

$$+ |e\rangle\langle g|ae^{-i(\omega-\omega_{eg})t} \quad (3.46)$$

$$+ |g\rangle\langle e|a^\dagger e^{+i(\omega-\omega_{eg})t} \quad (3.47)$$

$$+ |e\rangle\langle g|a^\dagger e^{+i(\omega+\omega_{eg})t}), \quad (3.48)$$

where we have defined  $g = \mathbf{d}_{eg} \cdot \hat{\epsilon}\mathcal{E}_0/\hbar$  and  $\omega_{eg} = \omega_e - \omega_g$ . Here we have made the dipole approximation  $e^{\pm i\mathbf{k}\cdot\mathbf{r}} \simeq 1 \pm i\mathbf{k}\cdot\mathbf{r}$ . This corresponds to a long wavelength approximation and is valid for optical frequencies and typical atomic distances. In later chapters more terms will be included to model optomechanical systems.

Now assume that the drive field frequency is closely tuned to the energy difference between the levels. In this case the detuning

$$\Delta \equiv \omega - \omega_{eg}, \quad (3.49)$$

is much smaller than the other frequencies in the system. Specifically we note that the first and fourth term in the interaction Hamiltonian oscillate at roughly twice the rate of the optical

transition frequencies. This corresponds to the *rate of change* oscillating around zero and therefore the effect averages out over the time scales that characterize the rest of the dynamics. This is equivalent to saying that these terms are very off-resonant.

By dropping these terms (so called Rotating Wave Approximation (RWA) [151, p. 79]) we obtain

$$\hat{H}_{\text{int,I}}(t) = -\hbar g(|e\rangle\langle g|ae^{-i\Delta t} + |g\rangle\langle e|a^\dagger e^{+i\Delta t}). \quad (3.50)$$

We write the equation of motion for the density operator in the interaction picture for this system,

$$\frac{d\rho}{dt} = -\frac{i}{\hbar}[\hat{H}_{\text{int,I}}(t), \rho] + \sum_j [2L_j\rho L_j^\dagger - \{L_j^\dagger L_j, \rho\}], \quad (3.51)$$

where we have inserted  $L_j = \sqrt{\gamma}|g\rangle\langle e|\hat{a}^\dagger$ , with  $\gamma = \Gamma/2$  being the so called dipole decay rate and  $\Gamma$  the spontaneous decay rate of the excited state, while neglecting other sources of decay. We can see this by solving for the derivative of the matrix elements of the density operator. We will assume that the laser is in a coherent state,  $|\alpha\rangle$ . We obtain

$$\begin{aligned} \dot{\rho}_{mn} &= -\frac{i}{\hbar} \left[ H_{\text{int}}, \rho \right]_{mn} + \left[ \Gamma|g\rangle\langle e|\rho|e\rangle\langle g| - \gamma\{|e\rangle\langle e|, \rho\} \right]_{mn} \\ &= ig\langle m| \left( |e\rangle\langle g|ae^{-i\Delta t} + |g\rangle\langle e|a^\dagger e^{+i\Delta t} \right) \rho|n\rangle \\ &\quad - ig\langle m|\rho \left( |e\rangle\langle g|ae^{-i\Delta t} + |g\rangle\langle e|a^\dagger e^{+i\Delta t} \right) |n\rangle \\ &\quad + \Gamma\rho_{ee}\delta_{ng}\delta_{mg} - \gamma(\rho_{en}\delta_{me} + \rho_{me}\delta_{em}) \\ &= ig \left( \delta_{me}\rho_{gn}ae^{-i\Delta t} + \delta_{mg}\rho_{en}a^\dagger e^{+i\Delta t} - \rho_{me}\delta_{gn}ae^{-i\Delta t} - \rho_{mg}\delta_{en}a^\dagger e^{+i\Delta t} \right) \\ &\quad + \Gamma\rho_{ee}\delta_{ng}\delta_{mg} - \gamma(\rho_{en}\delta_{me} + \rho_{me}\delta_{em}). \end{aligned} \quad (3.52)$$

Defining  $\tilde{\rho}_{eg} = \rho_{eg}e^{i\Delta t}$  and  $\Omega \equiv g\alpha$ <sup>6</sup>, the time derivatives of the populations are given by,

$$\dot{\rho}_{gg} = ig(\rho_{eg}\hat{a}^\dagger e^{i\Delta t} - \rho_{ge}\hat{a}e^{-i\Delta t}) + \Gamma\rho_{ee} = i(\Omega^*\tilde{\rho}_{eg} - \Omega\tilde{\rho}_{eg}^*) + \Gamma\rho_{ee} \quad (3.53)$$

$$\dot{\rho}_{ee} = ig(\rho_{ge}\hat{a}e^{-i\Delta t} - \rho_{eg}\hat{a}^\dagger e^{i\Delta t}) - \Gamma\rho_{ee} = -i(\Omega^*\tilde{\rho}_{eg} - \Omega\tilde{\rho}_{eg}^*) - \Gamma\rho_{ee}, \quad (3.54)$$

and the coherences are (in terms of  $\tilde{\rho}_{eg}$ )

$$\dot{\tilde{\rho}}_{eg} = -(\gamma - i\Delta)\tilde{\rho}_{eg} - i\Omega(\rho_{ee} - \rho_{gg}). \quad (3.55)$$

Note that  $\tilde{\rho}_{eg}(t)$  is the complex number representing the mean value of the coherence corresponding to an operator  $\hat{P} = |g\rangle\langle e|$ . These equations are called the Bloch equations.

<sup>6</sup>This is half of the Rabi frequency:  $\Omega_{\text{Rabi}} = 2\Omega$ . Here Rabi frequency is defined such that the time to perform a full Rabi flop ( $2\pi$ -pulse) is  $t_{2\pi} = 2\pi/\Omega_{\text{Rabi}}$  when  $\Delta = 0$ .

### 3.5.1 Steady state

In many cases only the steady state solutions are needed since the relaxation time, determined by the decay rate, is typically very short compared to other changes in the systems.

In steady state we can write

$$\tilde{\rho}_{eg} = \frac{-i\Omega}{\gamma - i\Delta}(\rho_{ee} - \rho_{gg}), \quad (3.56)$$

and insert into the steady state expression for  $\rho_{ee}$ :

$$\rho_{ee} = \frac{-i}{\Gamma}(\Omega^* \tilde{\rho}_{eg} - \Omega \tilde{\rho}_{eg}^*) = -\frac{|\Omega|^2}{\gamma^2 + \Delta^2}(\rho_{ee} - \rho_{gg}). \quad (3.57)$$

We define the saturation parameter

$$s \equiv \frac{2|\Omega|^2}{\gamma^2 + \Delta^2} = s_0 \frac{1}{1 + (\Delta/\gamma)^2}, \quad (3.58)$$

where  $s_0$  is the on-resonance saturation parameter. We can write

$$s_0 \equiv \frac{2|\Omega|^2}{\gamma^2} = \frac{2|\Omega_{\text{Rabi}}|^2}{\Gamma^2} = \frac{I}{I_{\text{sat}}}, \quad (3.59)$$

where we have defined the saturation intensity as

$$I_{\text{sat}} \equiv \frac{I\Gamma^2}{8|\Omega|^2} = \frac{\hbar\Gamma\omega_{eg}^3}{12\pi c^2}. \quad (3.60)$$

and an expression for the spontaneous decay rate [146, Ch. 4.7, eq. (4.167)] In the case of a two level atom the saturation intensity is simply given by eq. 3.60 and the decay rate by

$$\Gamma = \frac{\omega_{eg}^3 |d|^2}{3\pi\epsilon_0 \hbar c^3}. \quad (3.61)$$

For the excited state population we obtain

$$\rho_{ee} = \frac{1}{2} \frac{2|\Omega|^2}{\gamma^2 + \Delta^2} \frac{1}{1 + \frac{2|\Omega|^2}{\gamma^2 + \Delta^2}} = \frac{1}{2} \frac{s}{1 + s}. \quad (3.62)$$

The total spontaneous scattering rate of the atom,  $\Gamma_{\text{FS}}$ , is given by

$$\Gamma_{\text{FS}} = \Gamma\rho_{ee}. \quad (3.63)$$

We can then also write the relevant expression for the coherences

$$\tilde{\rho}_{eg} = \frac{-i\Omega}{\gamma - i\Delta}(2\rho_{ee} - 1) = \frac{-i\Omega}{\gamma - i\Delta} \left( \frac{1}{1 + s} \right). \quad (3.64)$$

These expressions will be relevant for e.g. understanding the Doppler cooling models of section 4.2.

### 3.5.2 Rabi oscillations

If the two level system has no, or only a very small, negligible, spontaneous decay rate the system can be solved. This was first noted by I. Rabi and it is thus called the Rabi model, see e.g. [151, p. 89]. This is one of the simplest systems, but one of the most complicated systems that can be solved analytically. But even here the RWA approximation is needed for simple solutions<sup>7</sup>. To solve the Rabi model we use the time-dependent two-level-atom equations of motion, 3.52, where set  $\Gamma = 0$ . Then after some algebra we obtain solutions such that, assuming the atom to be initially in the ground state,

$$\rho_{ee} = \frac{\Omega_{\text{Rabi}}^2}{\Omega_{\text{gen}}^2} \sin^2(\Omega_{\text{gen}} t/2), \quad (3.65)$$

where we have defined the generalized Rabi frequency

$$\Omega_{\text{gen}} = \sqrt{\Omega_{\text{Rabi}}^2 + \Delta^2}. \quad (3.66)$$

The solutions show the phenomenon of Rabi oscillations, or flops, as the population will oscillate from one state to the other at a rate  $\Omega_{\text{Rabi}}$ . If spontaneous decay cannot be neglected, it is possible to either do quantum trajectory evolution where the spontaneous decay is considered as stochastic events (quantum jumps) which is useful in analyzing single realizations (trajectories) of quantum dynamics as in [35][34][33]. Alternatively, using the Lindblad, or similar, formalism the motion of an average of many trajectories can be modeled which will show damped oscillations [151, p. 244].

## 3.6 Many level systems with many lasers

For handling more complicated system, one writes the Hamiltonians for all parts of the system and for all interactions i.e. Hamiltonian terms which have operators working on at least two subsystems. Using the Lindblad formalism it is possible to find the time derivative of the density operator. The non-unitary evolution is accounted for by including decay terms between levels represented by their effect as an operator and their rate.

In many cases the same laser will drive multiple transitions (e.g. multiple Zeeman substates). In this case the dipole matrix elements in the Rabi frequency are the ones corresponding to the actual transition driven while the squared dipole matrix element of the spontaneous decay rate is the sum of the squared matrix elements of all the decay channels. This can be seen by considering that the laser will have a specific polarization so that it drives transitions with  $q$  being -1, 0, or 1. But the spontaneous decay occurs with all the vacuum modes so the full dipole moment is needed in the expression for  $\Gamma$ . In effect this turns out to be a question of Clebsch-Gordan coefficients [146, p. 203ff].

---

<sup>7</sup>Recently the full system was solved without the RWA [152].

### 3.7 Heisenberg-Langevin equations

Following similar procedure as for finding the master equation, it is possible to derive an expression for the operators in the Heisenberg picture. This equivalent approach is typically useful in the case of larger Hilbert spaces (with e.g. an infinite number of harmonic oscillator states or many atoms).

The unitary evolution in the Heisenberg picture is simply given by Heisenberg's equation of motion

$$\dot{\hat{O}} = \frac{i}{\hbar}[H, \hat{O}]. \quad (3.67)$$

If the Liouvillian of the system is known in the density operator space (as in eq. 3.7) then a corresponding Liouvillian defined on the space of the system operators can be defined<sup>8</sup>. Defining the  $L_j$  Lindblad operators as in eq. 3.7 the derivative of the operator is given by

$$\dot{\hat{O}} = \mathcal{L}(\hat{O}) = \frac{i}{\hbar}[H, \hat{O}] + \sum_j \left( 2L_j^\dagger \hat{O} L_j - \{L_j^\dagger L_j, \hat{O}\} \right). \quad (3.68)$$

We will make use of these Heisenberg-Langevin equations<sup>9</sup> in the following sections since they are easily related to classical parameters.

#### 3.7.1 Two level example as Heisenberg-Langevin equations

As an example to show the equivalence of the master equation and Heisenberg-Langevin equations we will derive the Heisenberg-Langevin equations for the driven two level example from section 3.5. In deriving the Heisenberg-Langevin equations we use that the derivative of any operator of the system is given by eq. 3.68, where  $H$  the same Hamiltonian as before. The Lindblad operators are also those given before, although they are ordered differently in equation 3.68 than in 3.7.

We will define atomic operators for the excited,  $\hat{\Pi}_e = |e\rangle\langle e|$ , and ground state  $\hat{\Pi}_g = |g\rangle\langle g|$ , respectively. The atomic lowering and raising operators,  $\hat{\sigma}^- = |g\rangle\langle e|$  and  $\hat{\sigma}^+ = |e\rangle\langle g|$ , respectively, are also defined. The decay operator for the atom is  $\sqrt{\gamma}\hat{\sigma}^-$ .

The resulting equations for the mean values of these operators are

$$\dot{P} = -(\gamma - i\Delta)P - i\Omega(\Pi_e - \Pi_g) \quad (3.69)$$

$$\dot{\Pi}_e = -\Gamma\Pi_e - i(\Omega^*P - \Omega P^*) \quad (3.70)$$

$$\dot{\Pi}_g = \Gamma\Pi_e + i(\Omega^*P - \Omega P^*), \quad (3.71)$$

where we have defined  $\hat{P} \equiv \hat{\sigma}^- e^{i\omega_l t}$ <sup>10</sup>, by going to a frame rotating at  $\omega_l$ . Equations 3.69, 3.70 and 3.71 are equivalent to the equations for the density operator, eq. 3.52.

<sup>8</sup>This is due to the semi-group theory developed by G. Lindblad which uses that the operators and states are dual. It is then shown that the only positive semi-definite map is the one of the form given in [149].

<sup>9</sup>Also known as quantum Langevin equations in the literature [153, CIV].

<sup>10</sup>This means that the evolution of  $\hat{\rho}_{eg}$  and  $\hat{P}_H(t)$  have the same phase.

## Chapter 4

# Laser cooling

### 4.1 History of laser cooling

Optomechanics, the mechanical influence of light on matter, has been considered since Kepler suggested the radiation pressure from the sun as the explanation for the tails of comets. With Maxwell's equations it was evident that a propagating wave of light would exert a radiation pressure force proportional to its intensity. This was demonstrated experimentally in 1900 by Pyotr Lebedev [154] and in 1901 by Nichols and Hull [155] who were able to deflect a small, light mirror with a beam of light. In 1909 Einstein proved that for Planck's black body relations to hold the photon must carry momentum,  $p = h/\lambda$ , with  $\lambda$  being the wavelength of the photon [156]. The field of laser cooling took off in 1975 with proposals from Wineland and Dehmelt [4] and Hänsch and Schawlow [5] with the first demonstrations reported in 1978 [6][7] with ions, and in the 1980s with neutrals.

In the following sections treatments of Doppler cooling based on Cohen-Tannoudji [157], Wineland [158], and others<sup>1</sup> will be presented. In section 4.4 a new pulsed Doppler cooling scheme is discussed and simulations with a simple model are presented. In section 4.5, extension of these concepts to multilevel atoms, e.g.  $^{40}\text{Ca}^+$ , and practical aspects of laser cooling will be discussed.

---

<sup>1</sup>For other treatments see e.g. [159][160][161][162].

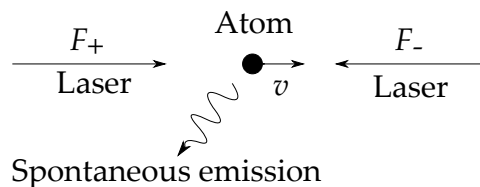


Figure 4.1: Schematic of Doppler cooling by two counter-propagating light fields. The atom is moving towards (away from) the light field on the right (left) with speed,  $v$ , such that the light fields appear to have shorter (longer) wavelengths. This yields a higher (lower) scattering rate, with the net effect of slowing down the atom.

Finally, in 4.6, a short presentation on resolved sideband cooling will be given.

## 4.2 Doppler cooling

An atom in a near-resonant light field will experience a force due to the radiation pressure. A photon of wavelength  $\lambda$  has a momentum of  $\hbar k$  where  $k = \frac{2\pi}{\lambda}$ . Due to momentum conservation each absorption of a photon will add momentum to the atom. The timescales for absorption and re-emission of photons and the time between these are in general much shorter than the timescales for the motion of the atom. For Doppler cooling the number of photons absorbed and re-emitted is very large so we will average the momentum transfer and define the light force from a single light field as

$$F = \hbar k \Gamma \rho_{ee} = \hbar k \Gamma \frac{1}{2} \frac{s}{1+s}, \quad (4.1)$$

where we have used that the scattering rate from the light field will be  $\Gamma \rho_{ee}$ , see eq. 3.63.

In the conceptually simplest Doppler cooling scheme, an atom is placed in two counter-propagating light fields, see figure 4.1. The left (right) light field generates a force,  $F_+$  ( $F_-$ ), pushing towards the right (left). The light fields are arranged and balanced such that the net force on the ion is zero on average. In the following we consider cooling in only one direction.

The Doppler effect changes the detuning between the ion and the light field, such that for a red-detuned light field the ion preferentially absorbs photons when moving towards the light field, thus slowing it down [163].

The Doppler effect, named for Christian Andreas Doppler [164], concerns the perceived change in frequency of a wave depending on the relative speed of the emitter and observer. The perceived frequency,  $\omega_{\text{eff}}$  for an observer approaching (+) or receding from (-) a source emitting at  $\omega_l$  is

$$\omega_{\text{eff}} = \left( \frac{1 \pm v/c}{1 \mp v/c} \right)^{1/2} \omega_l. \quad (4.2)$$

In the non-relativistic limit we can expand the shift around  $v = 0$  to obtain

$$\omega_{\text{eff}} - \omega_l = \pm \frac{v}{c} \omega_l + \frac{1}{2} \frac{v^2}{c^2} \omega_0 + \dots \quad (4.3)$$

$$\approx \pm kv + \frac{1}{2} \frac{v^2}{c^2} \omega_0, \quad (4.4)$$

where we can identify the first and second order Doppler shifts [146, p. 223]. In case of low velocities we can neglect the second order shift, which also will not have a cooling effect.

The Doppler frequency shift due to the motion of the ion will have a magnitude of  $kv_i$  where  $v_i$  is the projection of the motion on the direction of propagation of the light field in question. Depending on the reference frame we can consider either that the atom sees a light field with a higher frequency than in the laboratory frame or that, in the laboratory frame, the atom has a lower resonance frequency.

We are using that the light force depends on the saturation parameter as

$$s = \frac{s_0}{1 + \frac{\Delta_{\text{eff}}^2}{(\Gamma/2)^2}}, \quad (4.5)$$

where we have defined the effective detuning to account for the Doppler shift induced by the atomic motion,  $\Delta_{\text{eff}} \equiv \omega_{\text{eff}} - \omega_0 = \Delta \pm kv$ , and  $\Delta \equiv \omega_l - \omega_0$  is the detuning between the light field and the atomic resonance. Here the plus sign corresponds to the atom moving towards the light field and minus sign corresponds to the atom moving away.

To find the resulting force from the two counter-propagating light fields we first write the forces

$$F_{\pm} = \pm \hbar k \frac{\Gamma}{2} s_0 \frac{1}{1 + s_0 + (\Delta \mp kv)^2 / (\Gamma/2)^2}. \quad (4.6)$$

The resulting total light force is

$$F_{\text{cool}} = F_+ + F_-. \quad (4.7)$$

By expanding  $F_{\pm}$  to first order in  $v$  around  $v = 0$  one obtains

$$\begin{aligned} F_{\pm} &\simeq \pm \hbar k \frac{\Gamma}{2} s_0 \frac{1}{1 + s_0 + (2\Delta/\Gamma)^2} + 4\hbar k^2 s_0 \frac{\Delta/\Gamma}{[1 + s_0 + (2\Delta/\Gamma)^2]^2} v \\ &\equiv \pm F_0 + \frac{\beta}{2} v, \end{aligned} \quad (4.8)$$

where we have defined  $F_0$  (the constant force) and the coefficient of friction  $\beta$ . When adding the two forces the zeroth order terms cancel<sup>2</sup>, so

$$F_{\text{cool}} = F_+ + F_- \simeq \beta v = 4\hbar k^2 s_0 \frac{2\Delta/\Gamma}{[1 + s_0 + (2\Delta/\Gamma)^2]^2} v. \quad (4.9)$$

From this it can be seen that when the light fields are red detuned, i.e.  $\Delta < 0$ ,  $\beta$  will be negative, and  $F_{\text{cool}}$  will act as a friction force.

### 4.2.1 Diffusion due to spontaneous emission

Each time the atom has absorbed a photon it will be in the excited state. It will then spontaneously emit a photon with a rate of  $\Gamma$  and return to the ground state and the process starts over. The photon is spontaneously emitted in a random direction. The spontaneous emission of the photon will also impart a momentum kick to the atom [157]. Since the direction of emission is isotropic and stochastic the average effect of this is zero. But, like for the Brownian motion of particles, this corresponds to a random walk in momentum space.

Since the effect of the spontaneous emission is a random momentum kick, the corresponding force is a random force. Writing a differential equation for this is problematic since each realization would give a different result. This type of dynamics can be investigated using the theory of

---

<sup>2</sup>If the beams are balanced. Otherwise the ions will feel a net force.

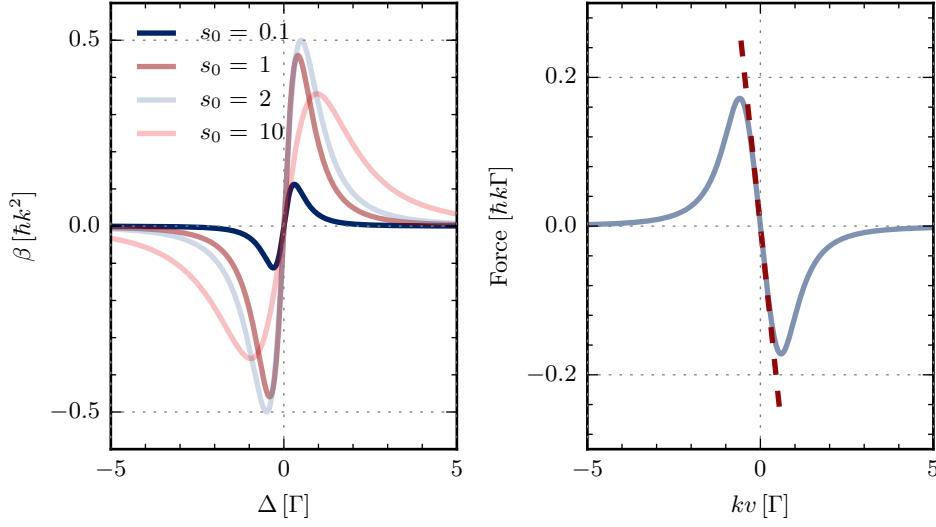


Figure 4.2: On the left the friction coefficient  $\beta$  for various  $s_0$  parameters is shown as a function of  $\Delta$ . On the right the solid line shows the full friction force, for  $s_0 = 1$  and  $\Delta = -\Gamma/2$ , while the dashed line shows the linear approximation with friction coefficient,  $\beta$ .

Stochastic Differential Equations (SDE). The most immediate method is to formulate a Langevin equation and solve for the mean value and variance of the desired coordinates. Alternatively, a Fokker-Planck equation for the probability distribution can be formulated and solved [159].

For our purposes we will first be interested in a differential equation for the momentum. Though each emission imparts a momentum to the atom, the net result will average out over time, so that  $\langle p \rangle = 0$ . The variance of the momentum will increase over time,  $\langle p^2 \rangle > 0$ . To quantify this we can construct a differential equation for the momentum friction and diffusion

$$\left(\frac{dp^2}{dt}\right)_{\text{total}} = \left(\frac{dp^2}{dt}\right)_{\text{cool}} + \left(\frac{dp^2}{dt}\right)_{\text{diff}} \quad (4.10)$$

where

$$\left(\frac{dp^2}{dt}\right)_{\text{cool}} = 2p \left(\frac{p}{dt}\right)_{\text{cool}} = 2pF_{\text{cool}} = 4 \frac{p^2}{2M} F_{\text{cool}} M/p = 4E_{\text{kin}} F_{\text{cool}} M/p \quad (4.11)$$

$$\left(\frac{dp^2}{dt}\right)_{\text{diff}} \equiv 2D, \quad (4.12)$$

where we have introduced the momentum diffusion constant  $D$  in the last line [157, p. 52f]. This equation can be solved numerically, or we can find a steady state solution where

$$\left(\frac{dp^2}{dt}\right)_{\text{total}} = \left(\frac{dp^2}{dt}\right)_{\text{cool}} + \left(\frac{dp^2}{dt}\right)_{\text{diff}} = 0. \quad (4.13)$$

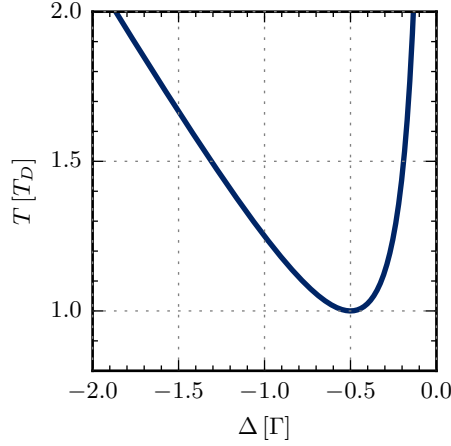


Figure 4.3: The temperature after Doppler cooling as a function of the detuning,  $\Delta$ , in terms of the linewidth of the transition.

inserting the expressions for the cooling and diffusion rates we solve for the kinetic energy

$$-2D = 4E_{\text{kin}}F_{\text{cool}}M/p \quad (4.14)$$

$$E_{\text{kin}} = \frac{-D}{2F_{\text{cool}}M/p} \quad (4.15)$$

To estimate the temperature of the atom after cooling we need to relate the energy to a temperature. In classical thermodynamics the equipartition theorem suggests that any generalized coordinate in an ergodic<sup>3</sup> system which appears squared in the Hamiltonian of the problem will have an average energy associated with it of  $\frac{1}{2}k_B T$ . If we associate this temperature with the kinetic energy the atom we can write

$$k_B T = 2E_{\text{kin}} = -\frac{D}{F_{\text{cool}}M/p}. \quad (4.16)$$

In the limit where  $kv \ll \Gamma, \Delta$  we can then simplify to

$$k_B T = -\frac{D}{\beta v M/p} = -\frac{D}{\beta}, \quad (4.17)$$

where  $\beta$  and  $D$  depend on the exact configuration.

The diffusion constant will in general depend on detuning, saturation and configuration of the light fields. A common setup is to use two counter-propagating light fields of orthogonal polarization. In this case they act like two separate running waves and the diffusion constant from each add to give the total diffusion constant [157, eq. 5.44]

$$D \simeq 2 \left( \hbar^2 k_L^2 \frac{\Gamma}{4} \frac{s}{1+s} + \hbar^2 k_L^2 \frac{s}{(1+s)^3} \{ \dots \} \right) \simeq 2 \hbar^2 k^2 \frac{\Gamma}{2} s = \hbar^2 k^2 \Gamma s \quad (4.18)$$

<sup>3</sup>This simply means that over time all parts of phase space will be visited and is true of most practical systems [165, p. 31].

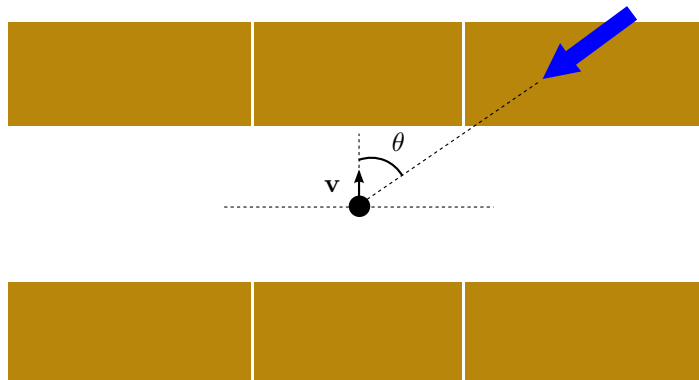


Figure 4.4: Top view of a linear Paul trap. The trap axis is indicated with a dashed line. An ion with velocity,  $\mathbf{v}$ , is indicated. The cooling light field is incident on the atom and the angle between velocity and the light field propagation vector,  $\theta$  is indicated.

where we have assumed a low saturation,  $s_0 \ll 1$  to drop terms of order  $s_0^2$  and higher. In this case the final temperature as a function of  $\Delta$  is given by

$$k_B T = -\frac{D}{\beta} = -\frac{\hbar\Gamma}{2} \frac{[1 + (2\Delta/\Gamma)]^2}{4\Delta/\Gamma}, \quad (4.19)$$

which is plotted in figure 4.3. For optimum cooling in this limit  $\Delta = -\Gamma/2$  and the final temperature is

$$k_B T_D \equiv \frac{\hbar\Gamma}{2}, \quad (4.20)$$

where we have defined  $T_D$  as the Doppler temperature. The Doppler temperature indicates the lower limit of cooling achievable with Doppler cooling. This limit is also called the Doppler limit [158][160][161][162].

The lowest achievable temperature possible with Doppler cooling is thus limited by the width of the transition addressed. For other configurations the ultimate cooling limit will differ, but is generally limited by the width of the transition unless other schemes are employed such as polarization gradient cooling, Sisyphus cooling or sideband cooling [159, Ch. 8].

### 4.3 Doppler cooling in a Paul trap

In section 4.2 we described Doppler laser cooling of a free atom by two counter-propagating light fields. In our experiments we will be cooling ions trapped in linear Paul traps. In this case the potential of the trap will influence the cooling in several ways.

Firstly, the trapping potential makes the ions oscillate such that the ion velocity changes sign at the rate of the secular frequency. This means that only a single light field is needed to dampen the motion of the ion along the propagation direction of the light field. For an asymmetric trap the eigenmodes of oscillation will be non-degenerate and any motion will be a superposition of

these modes. If the light field has a projection on each of these modes then a single light field will be able to cool all three directions. In the case of a symmetric trap the ion motion could be in a plane perpendicular to the light field wave-vector which would not be cooled. With only a single light field the cooling force will not balance out; the trap and cooling force will balance each other at a new equilibrium which we can estimate by

$$\Delta u = \frac{\hbar k \Gamma}{m \omega_r^2} \frac{s}{1+s}, \quad (4.21)$$

where  $\omega_r$  is the secular frequency in the direction of the wave-vector. By inserting typical numbers the effect can be estimated to be in the range from  $\mu\text{m}$  to tens of  $\mu\text{m}$ .

Secondly, the rf potential of the linear Paul trap will induce micromotion in the ion position and velocity. This modulates the Doppler shift between light field and ion if the micromotion is in the direction of propagation of the light field, see figure 4.4.

One way to avoid this effect is to cool along the trap axis. In this case the light field will be orthogonal to the micromotion oscillations and no modulation will occur. Another way is to ensure that the ions are all on the rf nodal line of the trap.

If however the cooling light field does have a projection on an axis with micromotion the micromotion will influence the scattering rate and thus the cooling rate. In the following sections we will attempt a simple model to quantify and alleviate this problem by using a pulsed cooling scheme.

Berkeland et al. [122] give estimates of the size of typical micromotion. The main point is that for a suitably optimized trap, micromotion can be minimized. Any micromotion apart from this minimum amount is called excess micromotion. The excess micromotion is typically not considered in treatments of the effect of micromotion since it is typically possible to eliminate it. For this reason many treatments (like the one given above) assumes that the Doppler shift of the ion is small compared to the detuning and linewidth, thus prompting the Taylor expansion to first order in  $v$  [166]. For significant ion motion this approximation breaks down as is indicated in figure 4.2.

A single ion will experience micromotion to varying degrees depending on the  $q_u$  parameters of the trapping potential, the potential phase delay, and dc position offsets from the rf null line [122]; see also section 2.3. We model the micromotion, as follows [122, eq. 21, 22]<sup>4</sup>

$$\mathbf{k} \cdot \mathbf{v}_{\text{mm}} = \mathbf{k} \cdot \dot{\mathbf{u}}' = \beta_{\text{mm}} \Omega_{\text{rf}} \cos(\Omega_{\text{rf}} t), \quad (4.22)$$

where  $u'$  denotes the components of the position determined by the micromotion and

$$\beta_{\text{mm}} = \frac{1}{2} k_u q_u u_{\text{dc}}, \quad (4.23)$$

where we have assumed that any phase delay between electrodes has already been eliminated. Here  $k_u = 2\pi/\lambda \cos\theta$ ,  $u_{\text{dc}}$  is the average radial position of the ion in question with respect to the rf-nodal line, and  $q_u$  is the  $q$  parameter in the direction investigated.

<sup>4</sup>Note that there is a typo in the paper by Berkeland et al. in eq. 21. The equation should read:  $\mathbf{k} \cdot \mathbf{u}'(t) = \beta_{\text{mm}} \cos(\Omega_{\text{rf}} t + \delta)$ .

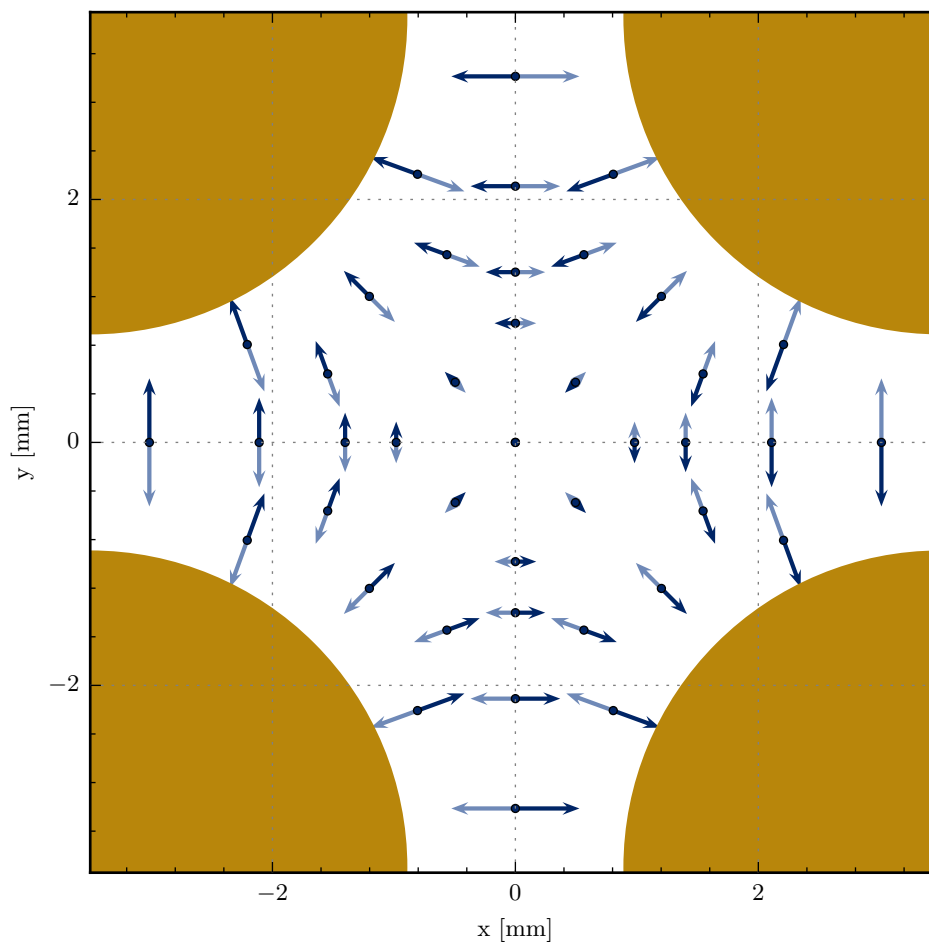


Figure 4.5: The geometry of the micromotion in the trap. At the center the magnitude of the micromotion is zero while it increases with distance from the center. The arrows indicate the direction and magnitude of the micromotion, where the dark blue arrows indicate the motion at one time and the light blue indicates the micromotion at a time  $\pi/\Omega_{\text{rf}}$  later. Moving from the center towards an electrode will increase the radial micromotion. Moving along the  $x$  and  $y$  directions will induce micromotion perpendicular to the displacement from the center.

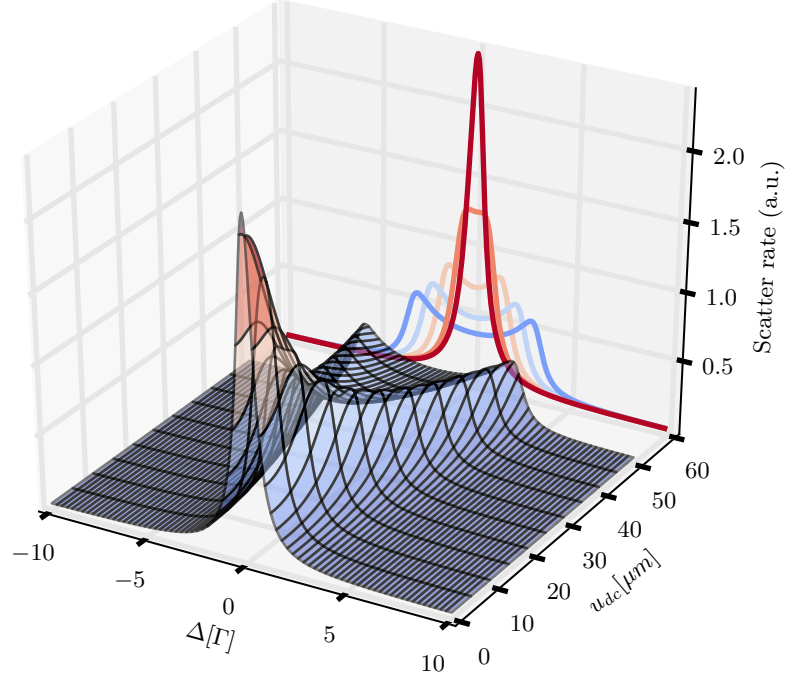


Figure 4.6: Line shape as a function  $u_{dc}$ . In this plot  $q_u = 0.084$ ,  $s_0 = 0.1$ ,  $\Omega_{rf} = 2\pi \cdot 3.6$  MHz and  $\Gamma = 2\pi \cdot 23$  MHz (corresponding to the  $S_{1/2}-P_{1/2}$  transition of  $^{40}\text{Ca}^+$ ).

In the case of only a few ions, it will be possible to confine them all on a single 1D structure along the trap axis. Cooling along the trap axis will then eliminate the micromotion induced Doppler shift, but no cooling will happen on the radial motion. For a single ion this will mean no radial cooling at all, while for strings of ions the coupling of the ions will sympathetically cool the radial motion to some extent. Unfortunately this cooling will not be very efficient.

For larger ensembles of ions most of the ions will experience significant micromotion. To estimate this micromotion we can use the result from the Berkeland paper, eq. 4.22 and insert a dc offset corresponding to a typical crystal width to estimate the amplitude of the micromotion and thus the Doppler shift. The micromotion will shift the resonance faster than the ion will react and we can thus average over a period of the micromotion to obtain the effective linewidth for a given micromotion amplitude. Figure 4.6 shows the line shape as a function of increasing radial offset position,  $u_{dc}$ .

It is clear that the Doppler shift in these cases can be much larger than the linewidth,  $\Gamma$ , of the transition probed. In this case both heating and cooling can occur when the Doppler shift changes the sign of the effective detuning. In this case net heating will occur since the ion will spend more time at the turning points of the velocity. Thus it will be heating effectively in one

extrema and cooled ineffectively at the other extrema. Alternatively one can increase the detuning to ensure that only cooling occurs, but this will decrease the cooling rate faster than the heating rate due to diffusion since this is independent to first order on the detuning while the cooling is very dependent on the slope of  $\beta$  which changes with detuning.

This means that cooling from a direction which sees the micromotion of the ions will not be as efficient as the expressions 4.10 indicated.

### Modeling Doppler cooling with micromotion

In this section we will first describe a simple model of the effect of micromotion on Doppler cooling. We will present simulations and some intuitive pictures for the effects observed. Then we will describe a pulsed cooling scheme and present simulated results for the expected minimum temperature and cooling rate in this simple model.

This model will use the steady state two level results from section 3.5. For this to be valid, the relaxation to the steady state values of the system will need to be faster than the other time scales of the system. Every time a photon is emitted from the atom, the dynamics are reset, so the relevant timescale is the scattering rate

$$\frac{\Gamma}{2} \frac{s}{1+s} \approx \frac{\Gamma}{2} s \quad (4.24)$$

in the low saturation regime  $s \ll 1$ . Thus, we require that  $\omega_r \ll \Omega_{\text{rf}} \ll \frac{\Gamma}{2} s$ . This assumption is not quite fulfilled for relevant physical systems. Consider  $^{40}\text{Ca}^+$  with the decay rate  $\Gamma = 2\pi \cdot 23.7 \text{ MHz}$  and  $s = 0.05$  which gives a scattering rate  $\sim 2\pi \cdot 1 \text{ MHz}$ , which is smaller than typical rf-frequencies used. In this model we keep the assumption. The effect of this approximation can be estimated by numerically solving the Bloch equations with a time-varying detuning. Such an investigation is planned.

Under this assumption we solve for the dynamics of the internal degrees of freedom for a set of velocities, and light field parameters in steady state. The steady state solution is then used to set up differential equations for the ion momentum.

In the previous derivation of the rate equations and Doppler cooling limit we made a Taylor expansion to first order in the velocity of the ion,  $v$ , since we were interested in the low velocity limit. In the case of large amplitude micromotion this approximation will not hold since the Doppler shift will be larger than the detuning  $\Delta$ . In this case the full expression in eq. 4.6 is needed.

The micromotion and the secular motion are at two different time scales given respectively by  $\Omega_{\text{rf}}$  and

$$\omega_r = \sqrt{q^2/2 + a\Omega_{\text{rf}}} \sim q\Omega_{\text{rf}}, \quad (4.25)$$

where typically  $q \ll 1$  and  $a \simeq 0$ . So the total velocity of the ion can be divided into

$$v = v_{\text{sec}} + v_{\text{mm}}, \quad (4.26)$$

and the Doppler shift from each velocity term can be handled separately.

The Doppler shift from the micromotion will oscillate at the angular frequency  $\Omega_{\text{rf}}$  and thus modulate the effective detuning of the light force. If, per the previous assumption, the steady state expressions can be used, then the effect of the micromotion amplitude is to effectively broaden the resonance peak. Figure 4.6 shows this broadening which in the case of very large micromotion will actually split the resonance into two peaks. This can be understood as the ion spending more time at the extrema of the motion.

A first (naive) estimate for the final temperature of the atom, still assuming low saturation, is

$$k_B T = -\frac{\hbar\Gamma_{\text{eff}}}{2} \frac{[1 + (2\Delta/\Gamma_{\text{eff}})]^2}{4\Delta/\Gamma_{\text{eff}}}, \quad (4.27)$$

which has a minimum at  $\Delta = -\Gamma_{\text{eff}}/2$ . Here  $\Gamma_{\text{eff}}$  is the effective linewidth obtained from the time averaged spectrum of the atomic transition in the presence of micromotion (or other broadening effects). The effective linewidth is only well defined as long as the peak has not split into two parts, and when it still looks somewhat Lorentzian. So far the effect of micromotion is just line-broadening perturbation.

To model this system numerically it is in principle necessary to perform Molecular Dynamics (MD) simulations where the dynamical equation for the velocity of the ion is solved in the presence of stochastic diffusion forces and the effect of the micromotion, and the results are averaged over many realizations [167]. This type of simulation is often very resource intensive and a simpler scheme is used here.

We will numerically simulate equation 4.10 for the variance of the momentum,  $p^2$ . Instead of using the linear approximation of  $F_{\text{cool}}$  in  $v$ , we will use the full expressions of equations 4.6 and 4.7 namely

$$F_{\text{cool}} = F_+ + F_-, \quad (4.28)$$

where

$$F_{\pm} = \pm \hbar k \frac{\Gamma}{2} s_0 \frac{1}{1 + s_0 + (\Delta \mp kv)^2 / (\Gamma/2)^2}. \quad (4.29)$$

Here we will separate the velocity in two parts

$$v = v_{\text{sec}} + v_{\text{mm}} \quad (4.30)$$

corresponding to the secular motion and micromotion, respectively. The secular motion is treated as before such that we associate the momentum with the secular motion

$$p^2 = M^2 v_{\text{sec}}^2. \quad (4.31)$$

The micromotion, which is a driven motion, is assumed to be given by eq. 4.22. Here we assume that the phase relation between the secular motion and the micromotion is quickly averaged out due to the different order of magnitude of the oscillation frequencies.

Thus the cooling force will be a function of both the secular velocity and time. Here it should be noted that since the differential equation is in terms of  $p^2$  the sign of the velocity of the secular motion is not known. This means that information about whether the two velocity components add or subtract is lost. This is assumed to be inconsequential due to the fast oscillation of the micromotion velocity which is much faster than the secular motion,  $\omega_r \ll \Omega_{\text{rf}}$ .

For time scale relevant for the secular motion, the micromotion will have passed through many periods and the effect of having the wrong sign of the velocity will have averaged out, see e.g. figure 2.3, where the position and velocity of an ion with and without a radial offset are plotted.

Since the cooling force is not linear in the velocity for large detunings, it is not clear that the ion should be in a state with a well defined energy after the cooling [159, p. 65]. Here we will not claim that this is the case; instead we will associate a mean energy  $E = \frac{p^2}{2M}$  with the motion. While it is clear that the ion is not in thermal equilibrium, we will still refer in the following to its "temperature" as given by

$$T = \frac{2E}{Mk}. \quad (4.32)$$

Figure 4.7 shows a numerical solution of this differential equation, where we compare the temperature for no micromotion (offset of 0  $\mu\text{m}$ ) with the temperature in the presence of micromotion (offset up to 50  $\mu\text{m}$ ). The overall cooling dynamics is similar, but the modulation makes the temperature higher. Note that for large offsets the interaction becomes weak enough that almost no cooling or heating occurs.

#### 4.4 Pulsed cooling

The model investigated above hints at the problems with Doppler cooling in the presence of significant micromotion. As discussed in section 2.3 and 2.5, excess micromotion for single or strings of ions can be effectively eliminated, but for 3D structures like large ion Coulomb crystals, the ions not at the nodal line will necessarily feel an excess micromotion corresponding to their position; see e.g. figure 4.5 [168][169].

Typically, large ion Coulomb crystals are cooled along the rf free axis, i.e. along the trap axis. Motion in the radial directions is then sympathetically cooled. This works reasonably well, and in this way large ion Coulomb crystal have been made in rf traps. This other degrees of freedom are not cooled very efficiently though and for initial cooling or after having gotten warm for whatever reason, the cool-down time can be significant. In these cases it would be advantageous to cool the radial degrees of freedom directly, even at lower cooling rates. For the trap discussed in chapter 10, another complication arises since the rf free axis is not optically accessible in a flexible way. This is due to two cavity mirrors HR coated for the wavelength of the cooling light. In previous designs, see Herskind [133]), the mirrors were transmissive at the cooling wavelength so cooling along the axis was still possible. In the new design the mirrors are highly reflective and light can only be injected at the resonance frequency of the cavity. Cooling along this axis is possible, but

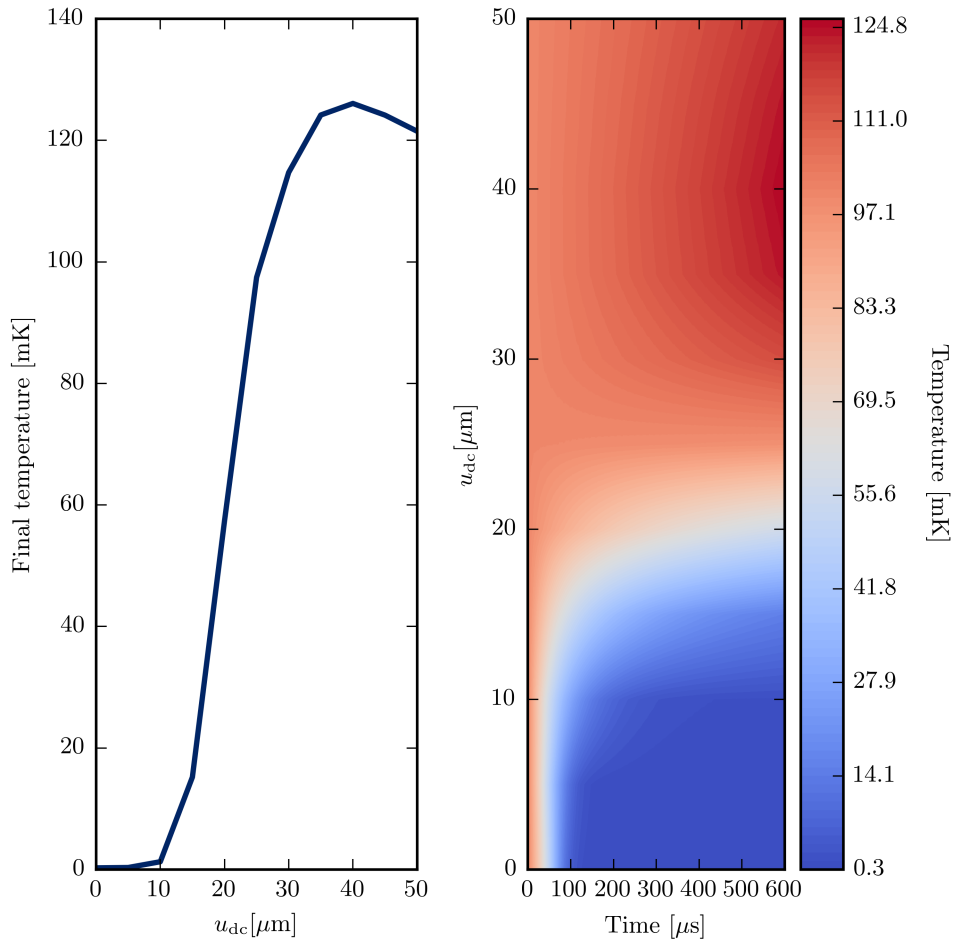


Figure 4.7: Cooling dynamics for  $s_0 = 0.05$ ,  $\delta = -\Gamma/2$  and an initial temperature of 100 mK. The temperature is shown as a function of the cooling time and  $u_{dc}$ . For low or no micromotion the system is cooled to the steady state quickly. For moderate micromotion the cooling is slower and the steady state temperature is higher. For  $u_{dc} \gtrsim 30 \mu\text{m}$  heating is observed. For even higher  $u_{dc}$  even the heating effect is slowing down due to the extreme broadening of the transition.

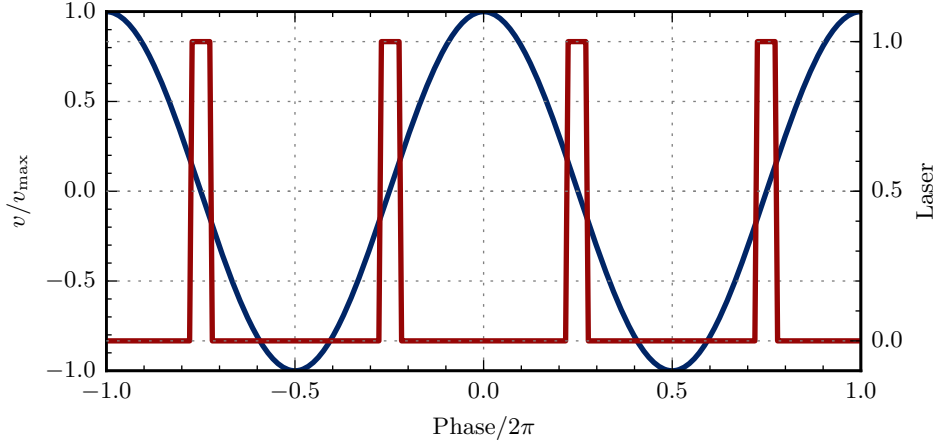


Figure 4.8: The normalized ion velocity due to micromotion as function of the phase (blue). The red line indicates the duty cycle of the cooling light field.

not practical while performing other experiments. Thus an alternative scheme to ensure efficient cooling of large crystals along radial directions is required.

Michael Drewsen has proposed to use a pulsed Doppler cooling scheme where the cooling light field is turned on and off in synchronization with the rf drive of the Paul trap. If the light field is only incident on the ions when they are at rest ( $v_{\text{mm}} \simeq 0$ ), there will effectively not be any Doppler shift due to the micromotion, and potentially efficient laser cooling could be achieved.

This requires that the light field can be switched on and off on a fast enough timescale and that no other dynamics results from the pulsing of the cooling. Previous calculations have shown that pulsed cooling in the low saturation regime on the relevant timescales will not lead to any significant new dynamics [170].

Assume that the pulsing is done as a square-signal turned on for a fraction of the period of the rf oscillation denoted by  $d$ .<sup>5</sup> Then we can write the on-resonance parameter  $s_0(t) = s_0 f(\Omega_r f t, \phi_0)$  where

$$f(\phi, \phi_0) = \begin{cases} 1 & \text{for } \phi_0 - \pi d \leq \phi \pmod{2\pi} \leq \phi_0 + \pi d \\ 0 & \text{otherwise,} \end{cases} \quad (4.33)$$

where  $\phi_0$  is the phase with respect to the rf drive. For  $\phi_0 = 0$  the light field is on while the rf voltage attains its maximum value and the velocity is minimal. For  $\phi_0 = \pi/2$  the velocity is maximal when the light field is on, see figure 4.8.

The model given above has been investigated numerically. The effective line shape has been plotted as a function of the duty cycle,  $d$ , in figure 4.9. This plot was generated in a manner similar to figure 4.6 by averaging over a period of the micromotion with the light field for a fraction of

<sup>5</sup>Usually called duty cycle in signal theory. In reality there will be a rise/fall time, see section 12.4.

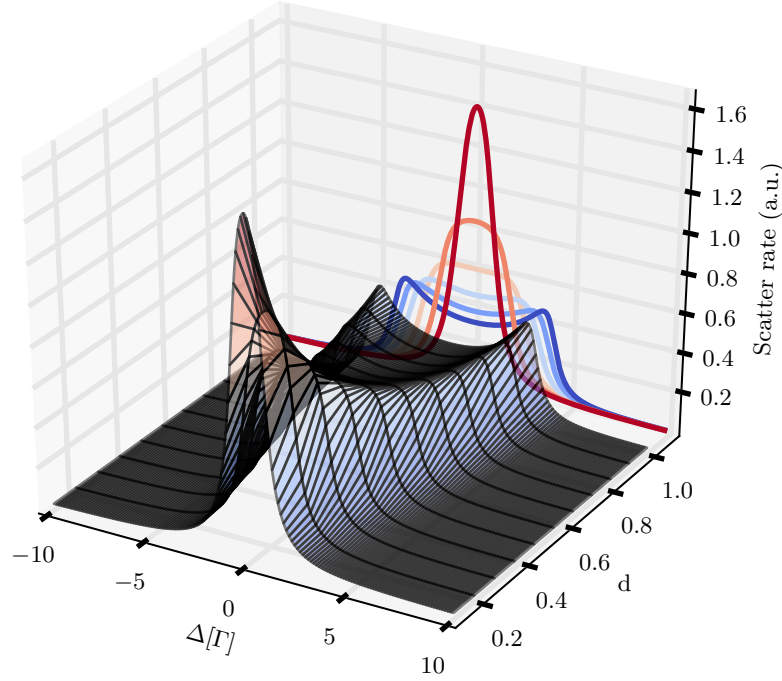


Figure 4.9: The line shape as a function of duty cycle,  $d$ , with  $u_{dc} = 50 \mu\text{m}$  and otherwise the same parameters as in figure 4.6. The scattering rate plotted has been rescaled by  $1/d$  for clarity.

the time,  $d$ . The scattering rate plotted has been rescaled by  $1/d$  for clarity. This shows that we can regain the original line shape by lowering the duty cycle as expected. The line shape has been scaled up by a factor of  $1/d$  to be easily visible. Comparing the pulsed scheme to the cw scheme we note a potential problem in that, for very short pulses, we would require an increase in the saturation, which would lead to power broadening. Alternatively, a lower cooling rate could be used. This has practical disadvantages, but should in principle lead to lower final temperatures.

This is only true, if other heating rates can be neglected. Other heating rates include the coupling of the large energy of the micromotion to the secular motion due to finite temperature. This was investigated in [171]. They found that this coupling is very small for low temperature, but scales quadratically with temperature. This is in agreement with experiments [172], where the heating rate was investigated by turning of the laser cooling for extended periods of time ( $\sim 90$  s) without significant heating or melting of the crystal. Background gas collisions can also heat up the ions. In practice, the pulsed cooling scheme is then a trade-off between the final temperature achieved and the cooling rate.

The previous cooling dynamics simulations were then repeated for the offset  $u_{dc} = 50 \mu\text{m}$  and a variable duty cycle. The results are shown in figure 4.10. The effect of a low duty cycle is clearly

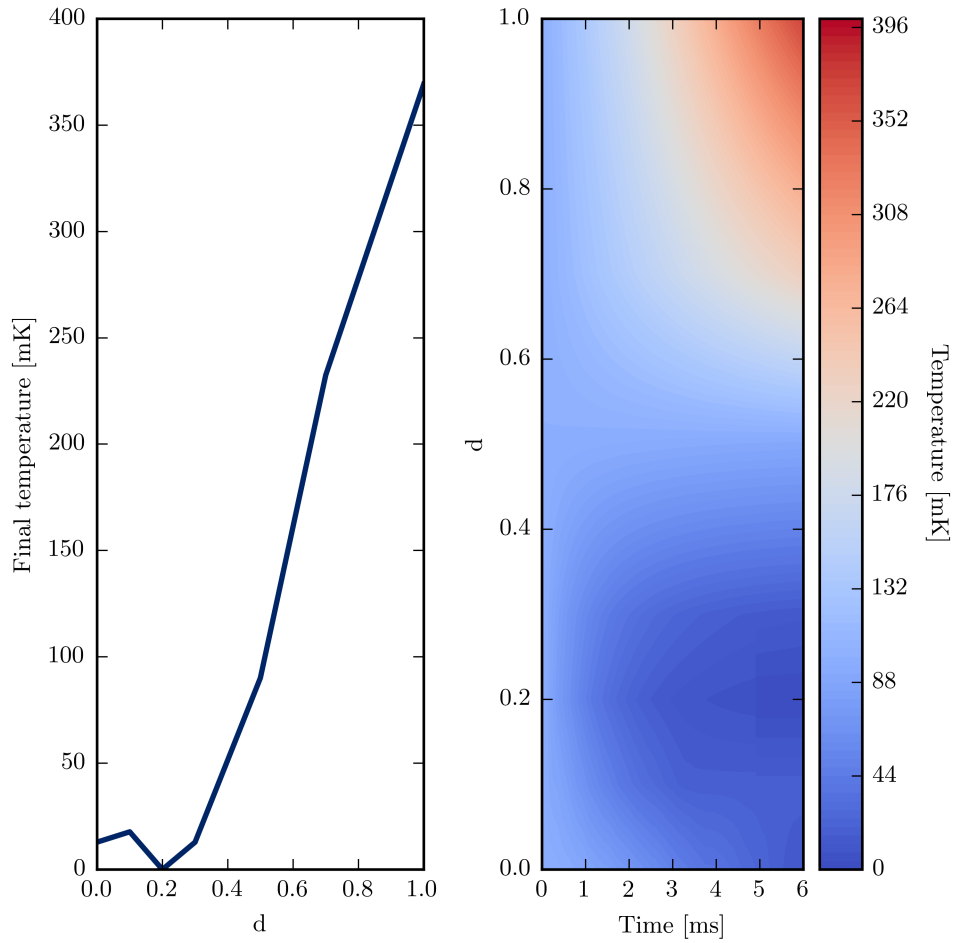


Figure 4.10: The cooling dynamics as a function of the duty cycle for  $u_{dc} = 50 \mu\text{m}$ . The peak around  $d \sim 0$  is due to the low cooling rate, since steady state was not reached within the simulation time. Other parameters are as before.

a lower final temperature. Note that it also means a slower cooling, so much slower that at 6 ms the steady state was not achieved for the lowest duty cycles.. For initial cooling it might be preferable to use a larger detuning. One can envision scanning the detuning while the atom cools down to effectively increase the capture range and still have the benefit of a lower final temperature. There is a large parameter space that can be investigated e.g. detuning, power, and duty cycle and these could in principle be time-dependent. It would also be interesting to perform full Molecular Dynamics (MD) simulations to confirm our simple model.

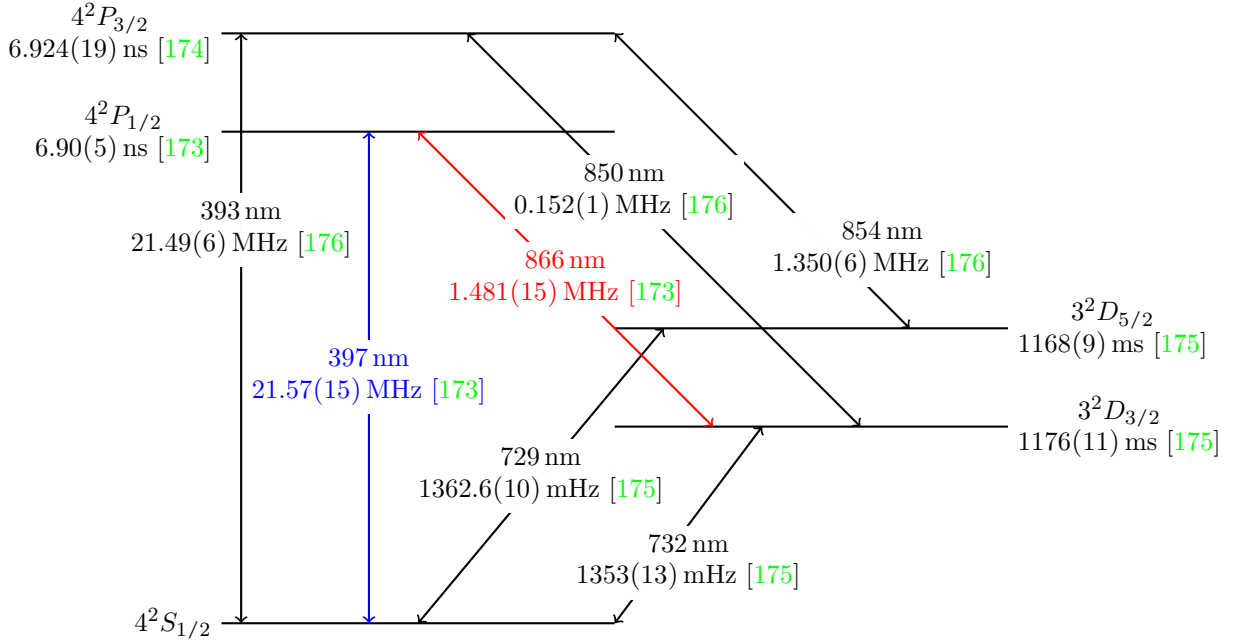


Figure 4.11: Level structure of  $^{40}\text{Ca}^+$ . See also appendix A for details.

## 4.5 Laser cooling of multi level atoms

Figure 4.11 shows the relevant level structure of the calcium-40 ion. The  $4^2S_{1/2}$  to  $4^2P_{1/2}$  transition at 397 nm is used for Doppler cooling because of its fast decay. This is important since the lifetime of the excited state determines the maximum number possible of scattered photons and, thus, the cooling rate. Alternatively, the 393 nm transition to  $4^2P_{3/2}$  could have been used, but this has more decay channels.

There is a branching ratio of  $(6.42 \pm 0.07)\%$  to go to the  $3^2D_{3/2}$  state from the  $4^2P_{1/2}$  state and this state has a lifetime of  $(1176 \pm 11)$  ms so it will only take a small number of absorbed photons on average to put the ion in this state in which it will stay on average for 1176 ms effectively stopping the Doppler cooling. To avoid this, a light field at 866 nm (called the repumper) is added. This will drive the ion from the  $3^2D_{3/2}$  to  $4^2P_{1/2}$  state, thus making it effectively reenter the Doppler cooling cycle. The relative detunings of the cooling beam and the repumper need to be carefully adjusted to avoid accumulation into dark states (e.g.  $3^2D_{3/2}$ ) [177]. By applying a bias magnetic field and driving the ion with light polarized perpendicular to the magnetic field (i.e. driving  $\sigma_+$  and  $\sigma_-$  transitions) we can avoid these dark states [177][146, p. 203].

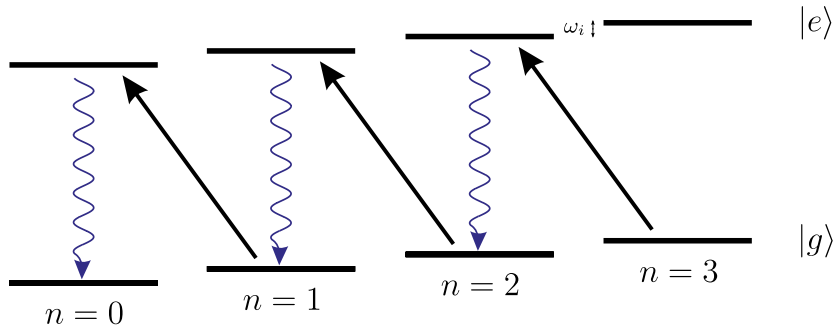


Figure 4.12: The sideband cooling scheme. The ion is driven into the excited state on the red sideband thus decreasing the motional quantum number by one. The ion will then decay preferentially via a carrier transition (sideband decays not shown). Schematic courtesy of G. Poulsen.

## 4.6 Sideband cooling

To reduce the temperature below the Doppler cooling limit alternative techniques exist, including cavity cooling (discussed in section 8) and sideband cooling [163].

Sideband cooling is an efficient cooling technique to reach the motional ground state after initial Doppler cooling. The requirement is a transition that allows resolving of the mechanical sidebands i.e.  $\Gamma < \omega_i$  where  $\omega_i$  are the secular frequencies of the corresponding trap axes,  $i = x, y, z$ . Since secular frequencies are usually of the order of  $\sim 2\pi \cdot 0.1\text{--}1$  MHz the dipole transitions of the typically trapped ions cannot be used. Instead the quadrupole-allowed  $S$ – $D$  transitions of the ions can be used since these can have lifetimes of the order of seconds. Sideband cooling can reach the quantum regime of the motion, so the harmonic motion of the ions needs to be quantized. Considering only one dimension this will be a simple quantum harmonic oscillator, where we can define creation and annihilation operators in a way very analog to the electromagnetic fields considered in section 3.3 and chapter 5.

The principle of sideband cooling, as illustrated in figure 4.12, is to drive the narrow transition on the so-called red sideband such that the atomic detuning is

$$\Delta = \omega_l - \omega_0 = -\omega_i, \quad (4.34)$$

where  $\omega_l$  is the light field angular frequency,  $\omega_0$  is the atomic transition angular frequency and  $\omega_i$  is one of the secular frequencies of the ion motion. By driving the transition coherently a Rabi  $\pi$ -pulse will bring the ion to the  $D_{5/2}$  state with one less quantum, phonon, in the ion motion. When the ion decays to the ground state it will primarily happen on the carrier transition. In this way population will accumulate in the motional ground state. Since the lifetime of the excited state is long an additional light field is typically used to excite the ion further to a quickly decaying state. This can be done in a pulsed or continuous scheme. For each cycle one phonon will be removed, i.e. the motional state will go from  $|n\rangle$  to  $|n-1\rangle$  except if the ion was already in the motional ground state, which is a dark state for this dynamic.

We introduce the Lamb-Dicke parameter which relates the wavelength of the light field,  $\lambda$ , to the zero-point motion of the ion,  $z_0$ , i.e. the r.m.s. fluctuations of the position in the ground state, as

$$\eta_{LD} = kz_0 = \frac{2\pi}{\lambda} \sqrt{\frac{\hbar}{2M\omega_z}}, \quad (4.35)$$

where we have singled out the  $z$ -axis. The position operator along the  $z$ -axis can then be written

$$\hat{z} = z_0(\hat{a} + \hat{a}^\dagger), \quad (4.36)$$

where  $\hat{a}^\dagger$  and  $\hat{a}$  are the creation and annihilation operators for the motion along the  $z$ -axis. The Lamb-Dicke regime is then defined as

$$\eta_{LD}^2(2n+1) \ll 1, \quad (4.37)$$

where  $n$  is the mean occupation number of the harmonic oscillator of the ion motion. In the Lamb-Dicke regime the terms involving  $\eta_{LD} = kz_0$  are small so Taylor expansions to low orders are suitable [43][178]. In this case we can expand the Hamiltonian to first order in  $\eta_{LD}$  from which Rabi frequencies for Rabi oscillations corresponding to the carrier is  $\Omega_{\text{Rabi}}$ , and for the red and blue sidebands

$$\Omega_{n,n-1} = \Omega_{\text{Rabi}}\sqrt{n}\eta_{LD} \quad \text{and} \quad (4.38)$$

$$\Omega_{n,n+1} = \Omega_{\text{Rabi}}\sqrt{n+1}\eta_{LD}, \quad (4.39)$$

respectively, where in each case the transition is driven resonantly.

The interaction Hamiltonian, in the interaction picture, for the sideband cooling scheme can be written

$$\hat{H}_{\text{int}}^{\text{LD}} = \hbar \frac{\Omega_{\text{Rabi}}}{2} \left[ \hat{\sigma}_+ e^{i\omega_i t} + \hat{\sigma}_- e^{-i\omega_i t} + i\eta_{LD}(\hat{\sigma}_+ \hat{a} + \hat{\sigma}_- \hat{a}^\dagger) + i\eta_{LD}(\hat{\sigma}_+ \hat{a}^\dagger e^{i2\omega_i t} + \hat{\sigma}_- \hat{a} e^{-i2\omega_i t}) \right], \quad (4.40)$$

where we have assumed that the light field is tuned to the the red motional sideband  $\Delta = -\omega_i$ ,  $\Omega_{\text{Rabi}}$  is the Rabi-frequency of the system and we have performed the RWA. The Rabi frequency will depend on the type of transition driven, see [163, p. 291] for details.

The dynamics of this system could be found by simulating using a master equation by adding the Lindblad operators corresponding to the decays. This is not necessary however since every cooling cycle involves a spontaneous decay and the dynamics can be solved efficiently using rate equations.

The cooling rate for an ion in the  $|n\rangle$  state, in analogy to the Doppler cooling case, will be given by

$$R_n = \tilde{\Gamma} P_e(n) = \tilde{\Gamma} \frac{(\eta_{LD}\sqrt{n}\Omega_{\text{Rabi}})^2}{2(\eta_{LD}\sqrt{n}\Omega_{\text{Rabi}})^2 + \tilde{\Gamma}^2}. \quad (4.41)$$

where  $\tilde{\Gamma}$  is the decay rate from the excited state (including e.g. the effect of another light field driving to another fast-decaying state). This rate goes to zero for  $n \rightarrow 0$ . The final temperature is the steady state population reached from competition between the cooling rate and heating due to off-resonant excitation of the carrier and blue sideband. When  $\omega_i \gg \tilde{\Gamma}$  the final mean occupation number is

$$\bar{n} \approx \left( \frac{\tilde{\Gamma}}{2\omega_i} \right)^2. \quad (4.42)$$

We can also express this in terms of the temperature of the motion

$$k_B T = \hbar \omega_i (\bar{n} + 1/2). \quad (4.43)$$

Thus the final temperature depends primarily on the ratio of the decay rate to the secular frequency. It is also clear from this that in this case the fundamental limit becomes from the secular frequencies itself, since this sets the level of the zero-point motion.

The sideband cooling light field can also be used as a temperature gauge since the strengths of the sidebands are temperature dependent. The strengths of these sidebands can be measured by driving them and then measuring the degree of shelving, that is, the population in the excited state. The temperature of the ion can then be determined from the expression

$$n = \frac{R}{1 - R}, \quad (4.44)$$

where

$$R \equiv \frac{|\Omega_{\text{Rabi}} \sqrt{\bar{n}}|^2}{|\Omega_{\text{Rabi}} \sqrt{\bar{n} + 1}|^2} = \frac{\bar{n}}{\bar{n} + 1}, \quad (4.45)$$

where a proper derivation needs to take into account that the ions are likely in thermal states after cooling. For details see [178, p. 78], [163]. A more complicated scheme, where fits to the Rabi oscillations on the sidebands are used to measure temperatures above the Doppler limit is discussed in [179, p. 103]. This method of determining the final temperature of the ions will be used in section 9.2, as a comparison with a cavity-based temperature measurement method.

## Chapter 5

# Cavity theory

In this chapter we will present the theory of optical resonators, specifically linear Fabry-Perot cavities. First the spatial structure of the modes of a cavity will be discussed, followed by a derivation of the spectrum and dynamics of an empty cavity field. Then in section 5.3 we will derive Heisenberg-Langevin equations for the interaction between two-level atoms and cavity fields.

### 5.1 Modes of a cavity

Consider two spherical mirrors with radius of curvature  $R$  separated by a distance  $L$ , as in figure 5.1. By using highly reflective mirrors, large electromagnetic fields can build up inside the cavity and strong coupling between ions and intracavity fields can be realized. This type of optical resonator is called a linear Fabry-Perot cavity or interferometer.

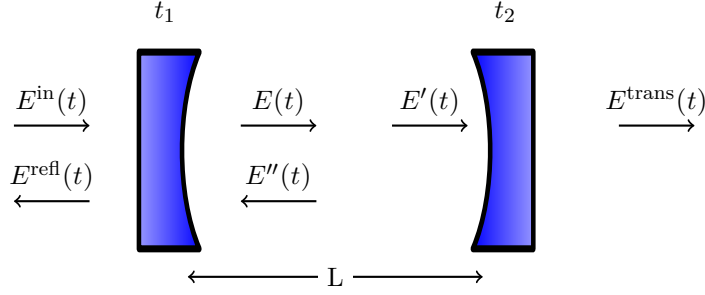
The mirrors set boundary conditions for the fields between them. Using these boundaries and Maxwell's equations, or more specifically the paraxial approximation to the wave equation, we can derive the conditions for a standing wave in the cavity [180][181].

The modes can be considered in the paraxial approximation since the cavities that we will consider use small mirrors at relatively large distances so they subtend a small angle. In this case we can follow the procedure in [180, p. 505] to find the spatial modes and resonance conditions. The resonance conditions are governed by the accumulated phase while going through one round trip of the cavity.

The slow varying part of the electric field will be

$$\begin{aligned} \mathcal{E}_{mn}(x, y, z) = & \frac{w_0}{w(z)} H_m\left(\sqrt{2}\frac{x}{w(z)}\right) H_n\left(\sqrt{2}\frac{y}{w(z)}\right) \\ & \times \exp i[kz - (m + n + 1) \tan^{-1}(z/z_0)] \\ & \times \exp[ik(x^2 + y^2)/(2R(z))(z)] \\ & \times \exp -(x^2 + y^2)/w^2(z), \end{aligned} \quad (5.1)$$

where  $H_m$  and  $H_n$  refer to the  $m^{\text{th}}$  and  $n^{\text{th}}$  Hermite polynomial, respectively,  $w_0$  and  $w(z)$  are the

Figure 5.1: Typical cavity setup.  $L$  denotes the distance between the mirrors.

waist and spot-size of the beam. The spotsize is given by

$$w(z) = w_0 \sqrt{1 + z^2/z_R^2}, \quad (5.2)$$

where the Rayleigh range has been defined as

$$z_R = \frac{\pi w_0^2}{\lambda}. \quad (5.3)$$

The phase of these modes is given by

$$\phi(z) = kz - (m + n + 1) \tan^{-1}(z/z_0), \quad (5.4)$$

and for a resonance it is required that the phase delay of a round trip in the cavity should be a multiple of  $2\pi$ . The resonance frequencies of these transverse modes are then

$$\nu_{qmn} = \frac{c}{2L} \left( q + \frac{1}{\pi} (m + n + 1) \cos^{-1} \sqrt{g^2} \right), \quad (5.5)$$

where  $q, m, n$  are positive integers or zero and  $g = 1 - L/R$ . These modes are called Transverse ElectroMagnetic (TEM) $_{mn}$  modes. The fundamental TEM $_{00}$  mode has a transverse Gaussian intensity distribution and is the most commonly used mode in the experiments of this thesis.

The waist of the cavity mode can be determined by [181, eq. 48]

$$w_0^2 = \frac{\lambda}{2\pi} \sqrt{L(2R - L)}. \quad (5.6)$$

A cavity with two identical spherical mirrors and  $R = L$  is called confocal. In an ideal confocal cavity the modes with  $m + n$  odd are degenerate and the modes with  $m + n$  even are degenerate. For a nearly confocal cavity the degeneracy will lift although modes with equal  $m + n$  will still be degenerate unless birefringence is present. If the modes are resolved they can be treated independently [180, p. 505].

Using the cavity mode solutions, eq. 5.1, and the quantization of the standing wave, eq. 3.20, we can express the electric field operator as

$$\hat{\mathbf{E}}(\mathbf{r}, t) = \mathcal{E}_0 [\varepsilon_{mn}(x, y, z) + \varepsilon_{mn}^*(x, y, z)] (\hat{a} + \hat{a}^\dagger). \quad (5.7)$$

## 5.2 Empty cavity spectrum and dynamics

In this section the spectrum around one of the resonances of an empty cavity will be calculated. A dynamical equation for the cavity field amplitude, which will also be necessary to treat the interaction with atoms will be derived.

Mirrors 1 and 2 have amplitude transmission coefficients  $t_1$  and  $t_2$ , respectively. The corresponding intensity transmission coefficients are  $T_i = t_i^2$ ,  $i = 1, 2$ . To account for scattering and absorption losses due to a reflection we define  $\alpha$  is the coefficient corresponding to the fraction of the light amplitude *not* "lost" in a round-trip: The total intra-cavity loss coefficient per round trip (due to absorption on the mirrors, scattering, etc.) is denoted by  $\mathcal{L}$  and is related to  $\alpha$  as  $\alpha = \sqrt{1 - \mathcal{L}/2}$ . From energy conservation we have  $T_i + R_i + \mathcal{L}/2 = 1$  for each of the mirrors.

A light field with frequency  $\omega_l$ , close to a cavity resonance  $\omega_c$ , is injected into the cavity through mirror 1, see figure 5.1, with an electric field denoted  $E^{\text{in}}(t)$  while the field leaking out at mirror 1 and 2 are called  $E_1^{\text{refl}}(t)$  and  $E_2^{\text{trans}}(t)$  respectively. The intra-cavity field after the first mirror is given by

$$E(t) = t_1 E^{\text{in}}(t) + \alpha E''(t) r_1 e^{i\pi}, \quad (5.8)$$

where  $e^{i\pi}$  is the phase shift from one reflection off mirror 1 and  $E''(t)$  is the field going the other way right before reflection.

The returning field inside the cavity,  $E''(t)$ , is given by

$$E''(t) = \alpha r_2 E(t - \tau) e^{i(\phi + \pi)}, \quad (5.9)$$

where  $E(t - \tau)$  is the intra-cavity field after the first mirror at an earlier time  $t - \tau$  where  $\tau = \frac{2L}{c}$  is the round trip time of the cavity. In equation 5.9 the phase is delayed by  $e^{i(\pi + \phi)}$  from the reflection on mirror 2 and the round trip delay,  $\phi = \tau\omega_l$  where  $\omega_l$  is the angular frequency of the light field.

Combining these equations we get an expression for the intra-cavity field in terms of the drive field and the retarded intra-cavity field at  $t - \tau$ ,

$$E(t) = t_1 E^{\text{in}}(t) + \alpha^2 r_1 r_2 E(t - \tau) e^{i\phi}. \quad (5.10)$$

By taking the Fourier transform of this equation we obtain the frequency spectrum of the cavity field (here  $\tilde{E}$  denotes Fourier transform of an electric field),

$$\tilde{E}(\omega) = \frac{t_1 \tilde{E}^{\text{in}}(\omega)}{1 - \alpha^2 r_1 r_2 e^{i(\phi - \tau\omega)}}. \quad (5.11)$$

The transmitted light amplitude is then simply the intra-cavity field amplitude multiplied by the field transmission coefficient,  $t_2$

$$\tilde{E}^{\text{trans}}(\omega) = t_2 \tilde{E}(\omega). \quad (5.12)$$

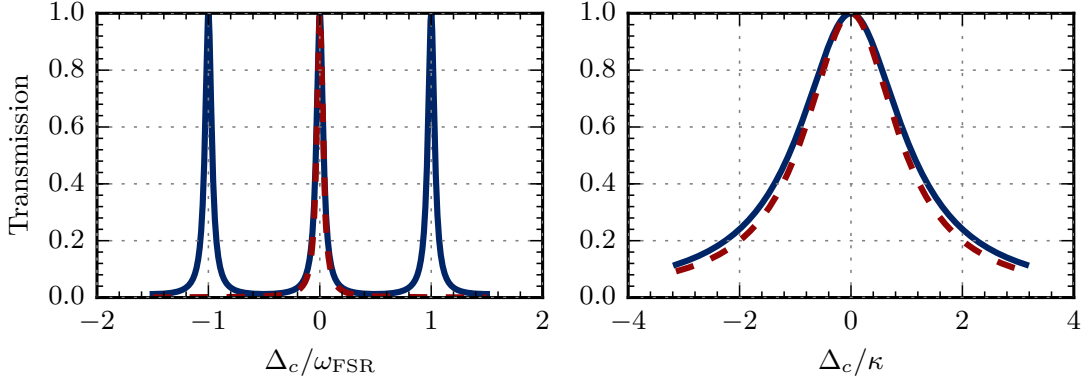


Figure 5.2: The transmission spectrum of a lossless cavity with finesse  $\sim 15$ , showing a full FSR on the left and showing details of one resonance on the right. The blue line shows the Airy function (eq. 5.13), while the dashed red line is the Lorentzian approximation (eq. 5.16).

The transmission of the cavity for a monochromatic drive,  $\tilde{E}^{\text{in}}(\omega) = E_0 \frac{1}{2} [\delta(\omega_l - \omega) + \delta(-\omega_l - \omega)]$ , will be

$$T(\omega) \equiv \frac{|\tilde{E}_2^{\text{out}}(\omega)|^2}{|E_0|^2} = \frac{(t_2 t_1)^2}{1 + \alpha^4 r_1^2 r_2^2 + 2\alpha^2 r_1 r_2 \cos(\phi - \tau\omega)}, \quad (5.13)$$

which, in interferometry, is called the Airy function<sup>1</sup>.

The peaks of the Airy function are separated by the Free Spectral Range (FSR) which is given by the periodicity of the transmission function eq. 5.13,  $\Delta\phi = \tau\Delta\omega_l = 2\pi$  such that

$$\omega_{\text{FSR}} = 2\pi f_{\text{FSR}} = 2\pi \frac{c}{2L}. \quad (5.14)$$

We define the cavity detuning  $\Delta_c \equiv \omega_l - \omega_c$  with  $q$  a positive integer such that  $\omega_c = 2\pi q \frac{c}{2L}$  is the nearest cavity resonance. In figure 5.2 the transmission spectrum of a lossless cavity showing two adjacent resonances is plotted on the left.

Consider the limit  $\mathcal{L}, T_1, T_2 \ll 1$ . We introduce the field decay rates  $\kappa_i = \frac{1-r_i}{\tau} \simeq \frac{T_i}{2\tau}$  and  $\kappa_{\mathcal{L}} = \frac{\mathcal{L}}{2\tau}$ . Expanding and keeping only first order terms

$$\alpha^2 r_1 r_2 = (1 - \kappa_{\mathcal{L}}\tau)(1 - \kappa_1\tau)(1 - \kappa_2\tau) \approx 1 - \kappa_{\mathcal{L}}\tau - \kappa_1\tau - \kappa_2\tau = 1 - \kappa\tau, \quad (5.15)$$

where we have defined the total cavity decay rate  $\kappa = \kappa_{\mathcal{L}} + \kappa_1 + \kappa_2$ . By substituting the cavity detuning in the expression for the cavity field, eq. 5.10, it can be simplified by expanding to first order around  $\Delta_c = 0$  to obtain the well known Lorentzian intensity transmission spectrum,

$$T(\Delta_c) = \frac{T_2 T_1 / \tau^2}{\kappa^2 + \Delta_c^2} = \frac{4\kappa_1 \kappa_2}{\kappa^2 + \Delta_c^2}. \quad (5.16)$$

<sup>1</sup>Not to be confused with the special Airy functions Ai and Bi.

The Lorentzian approximation to the Airy function is very good near the resonance and for high finesse; it is plotted on the right in figure 5.2.

The finesse of a cavity is the ratio of the FSR and the Full Width Half Maximum (FWHM) linewidth

$$\mathcal{F} \equiv \frac{\text{FSR}}{\text{FWHM}} = \frac{\omega_{\text{FSR}}}{2\kappa} = \frac{2\pi}{T_1 + T_2 + \mathcal{L}}, \quad (5.17)$$

which is a measure of the resolution of the cavity. We can express the

Another typical measure of resonators is the quality factor

$$Q \equiv \frac{\omega_c}{2\kappa} = \omega_c \frac{\mathcal{F}}{\omega_{\text{FSR}}} = \mathcal{F}q, \quad (5.18)$$

where  $q$  is the mode number in the the cavity, which for many optical cavities is of the order of  $10 \times 10^4$ . Thus optical cavities are very high quality resonators which explains why they are used to e.g. stabilize laser systems to high precision.

A differential equation can be obtained by noting that for high finesse cavities the round trip time,  $\tau$ , is very short compared to other time scales of the system (i.e.  $\kappa \ll \omega_{\text{FSR}}$ ) so the field does not change appreciably during one round trip time and eq. 5.10 can be rewritten as

$$\dot{E}(t) \approx \frac{E(t) - E(t - \tau)}{\tau} = -(\kappa_{\mathcal{L}} + \kappa_1 + \kappa_2 + i\Delta_c)E(t - \tau) + \sqrt{\frac{2\kappa_1}{\tau}}E^{\text{in}}(t) \quad (5.19)$$

$$= -(\kappa + i\Delta_c)E(t) + \sqrt{\frac{2\kappa_1}{\tau}}E^{\text{in}}(t). \quad (5.20)$$

From the dynamics we readily obtain the cavity field decay time,  $1/\kappa$ , which is the inverse of the half-linewidth in frequency space. The differential equation is well suited for investigating effects of vibrations, noise and interactions with ions, even in non-steady state situations.

The decay of the mode of a cavity is an exponential decay with a rate of  $\kappa$  for the field and  $2\kappa$  for the intensity or energy. The average lifetime of a photon in an optical cavity is thus  $1/(2\kappa)$ . Comparing to the round trip time  $\tau$  we see that the average number of round trips for a photon is

$$\frac{1/2\kappa}{\tau} = \frac{c/2L}{2\kappa} = \frac{\mathcal{F}}{2\pi}, \quad (5.21)$$

which yields another interpretation of the finesse. Since the average photon will take this number of round trips instead of just one the number of photons will increase by this factor called the build-up factor.

The intra-cavity intensity can be determined from the input intensity, or from the output power, if one knows the finesse and transmission coefficients. The intracavity intensity (on resonance) at the center of the cavity will be given, in terms of the input power,

$$I_0 = 4T_1 \frac{\mathcal{F}^2}{\pi^2} \frac{2P_{\text{in}}}{\pi w_0^2} = \frac{8}{\pi} \frac{T_1}{T_1 + T_2 + \mathcal{L}} \frac{\mathcal{F}}{\pi} \frac{2P_{\text{in}}}{\pi w_0^2}, \quad (5.22)$$

and the spatial structure is given by (assuming the fundamental TEM mode)

$$I(\mathbf{r}) = I_0 \cos^2(kz) \frac{w_0}{w(z)} \exp \left[ -(x^2 + y^2)/w^2(z) \right]. \quad (5.23)$$

The transmitted power can be expressed in terms of  $I_0$  as

$$P_{\text{trans}} = \frac{I_0}{4} T_2 \frac{\pi \omega_0^2}{2}. \quad (5.24)$$

### 5.3 Atom-cavity interaction

In chapter 3 we showed that an optical cavity can be shown to obey equations like a harmonic oscillator. Quantum mechanically we can go even further with this analogy since the cavity mode will be a quantum harmonic oscillator with the quanta being the photons in the cavity.

In this section we will derive Heisenberg-Langevin equations for the derivatives of the system operators in the Heisenberg picture. These will be governed by Liouvillian superoperators derived from decay operators and Hamiltonians.

In the derivation of the equations it is useful to note that for high-finesse cavities the unitary and non-unitary evolution is separable and can be added together at the end. Additionally the dynamics due to separate decay operators and terms in the Hamiltonian can be treated separately and added at the end. This is due to the linearity of the Liouvillian.

Consider a two level atom (Hilbert space  $\mathcal{H}_{\text{atom}}$ ) coupled to a high-finesse optical cavity (Hilbert space  $\mathcal{H}_{\text{cav}}$ ), where the cavity is driven by a monochromatic light field; see figure 5.3. The total Hilbert space is  $\mathcal{H}_{\text{atom}} \otimes \mathcal{H}_{\text{cav}}$  and the total Hamiltonian is

$$H_{\text{tot}} = H_A + H_{\text{cav}} + H_l + H_i, \quad (5.25)$$

where  $H_A$  is the atomic Hamiltonian,  $H_{\text{cav}}$  is the cavity Hamiltonian defined in section 3.3,  $H_l$  is the Hamiltonian for the interaction between the cavity and the external light field, and  $H_i$  is the interaction Hamiltonian between the cavity field and the atom. Note that this system models an atom in a cavity where the cavity (not the atom) is being driven by a laser. This differs from the previous example where the atom was driven directly by an outside field and the atom was assumed to not perturb the field.

We will define atomic operators for the excited,  $\hat{\Pi}_e = |e\rangle\langle e|$ , and ground state  $\hat{\Pi}_g = |g\rangle\langle g|$ , respectively. The atomic lowering and raising operators,  $\hat{\sigma}^- = |g\rangle\langle e|$  and  $\hat{\sigma}^+ = |e\rangle\langle g|$ , respectively, are also defined. The decay operators for this system are  $\sqrt{\kappa}\hat{a}$  and  $\sqrt{\gamma}\hat{\sigma}^-$  for the cavity and atom decay respectively.

$$H_A = \hbar(\omega_g|g\rangle\langle g| + \omega_e|e\rangle\langle e|) = \hbar(\omega_g\hat{\Pi}_g + \omega_e\hat{\Pi}_e) \quad (5.26)$$

$$H_{\text{cav}} = \hbar\omega_c(\hat{a}^\dagger\hat{a} + 1/2) \quad (5.27)$$

$$H_l = -\hbar f_0(\hat{a}^\dagger e^{-i\omega_l t} + \hat{a} e^{i\omega_l t}) \quad (5.28)$$

$$H_i = -\hbar g(\hat{a}^\dagger\hat{\sigma}^- + a\hat{\sigma}^+), \quad (5.29)$$

where all Hamiltonians have been written in the Schrödinger picture. We assume that  $\omega_l \sim \omega_c \sim \omega_{eg} = \omega_e - \omega_g$  (the angular frequency of the laser, the cavity and the atomic transition respectively) such that we can perform the RWA by eliminating energy-non-conserving terms.

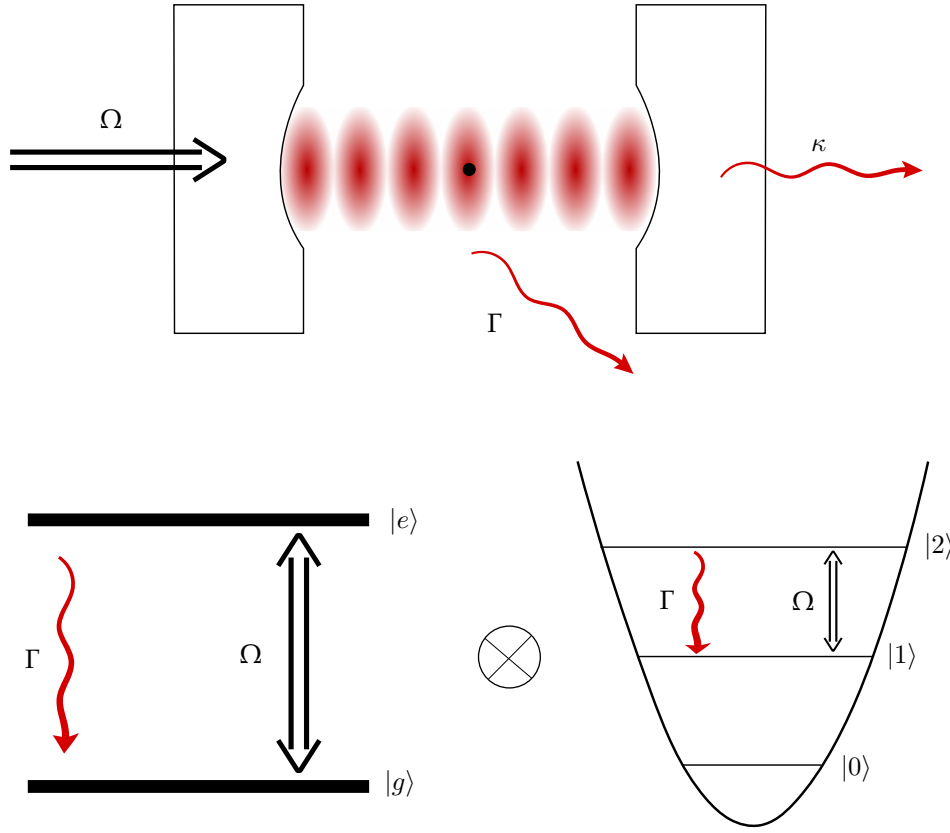


Figure 5.3:

For each of the terms of the Hamiltonian we can write a Liouvillian which is then the generator of time evolution for the operators. The spontaneous terms give the expected decay rates. The unitary part of the evolution is just the Heisenberg equation of motion. In deriving the equation of motion the following commutators are useful,

$$[\hat{\sigma}^{\pm}, \hat{\Pi}_e] = \mp \hat{\sigma}^{\pm} \quad (5.30)$$

$$[\hat{\sigma}^{\pm}, \hat{\Pi}_g] = \pm \hat{\sigma}^{\pm} \quad (5.31)$$

$$[\hat{a}^{\dagger}, \hat{a}] = 1 \quad (5.32)$$

$$[\hat{a}^{\dagger} \hat{a}, \hat{a}] = -\hat{a} \quad (5.33)$$

$$[\hat{\sigma}^+, \hat{\sigma}^-] = \hat{\Pi}_e - \hat{\Pi}_g. \quad (5.34)$$

We define the atomic and cavity detunings<sup>2</sup>

$$\Delta = \omega_l - \omega_{eg} \quad (5.35)$$

$$\Delta_c = \omega_l - \omega_c. \quad (5.36)$$

<sup>2</sup> Note that the detunings have been defined such that the detuning is negative for a red-detuned laser.

Using the commutators (and the fact that operators on separate subsystem automatically commute) and the decay operators we can derive the Heisenberg-Langevin equations for the system. In the following we will only be concerned with the expectation values of the operators so we take the expectation value of the Heisenberg-Langevin equations to obtain<sup>3</sup>

$$\dot{\Pi}_e = -\Gamma\Pi_e - ig(a^\dagger\sigma^- - a\sigma^+) \quad (5.37)$$

$$\dot{\Pi}_g = +\Gamma\Pi_g + ig(a^\dagger\sigma^- - a\sigma^+) \quad (5.38)$$

$$\dot{\sigma}^- = -(\gamma + i\omega_{eg})\sigma^- - iga(\Pi_e - \Pi_g) \quad (5.39)$$

$$\dot{a} = i(-\omega_c a + ga\sigma^- + f_0 e^{-i\omega_l t}) - \kappa a, \quad (5.40)$$

where  $\kappa$  is the cavity field decay rate calculated in section 5.2 and  $\Gamma$  and  $\gamma = \Gamma/2$  are the spontaneous and dipole decay rates respectively.

It is preferable to eliminate the explicit time dependence by going to a frame rotating at the laser frequency so we define

$$\tilde{a} \equiv ae^{i\omega_l t}, \quad P \equiv \sigma^- e^{i\omega_l t}, \quad (5.41)$$

$$(5.42)$$

which gives

$$\dot{\tilde{a}} = -(\kappa - i\Delta_c)\tilde{a} + i(gP + f_0) \quad (5.43)$$

$$\dot{P} = -(\gamma - i\Delta)P - ig\tilde{a}(\Pi_e - \Pi_g) \quad (5.44)$$

$$\dot{\Pi}_e = -\Gamma\Pi_e - ig(\tilde{a}^\dagger P - \tilde{a}P^\dagger) \quad (5.45)$$

$$\dot{\Pi}_g = +\Gamma\Pi_g + ig(\tilde{a}^\dagger P - \tilde{a}P^\dagger). \quad (5.46)$$

These are the Heisenberg-Langevin equations for the mean values of the system operators and are equivalent to a corresponding master equation. They are simply a set of three coupled differential equations that can be solved numerically or investigated analytically to determine the time evolution of the system.

### 5.3.1 Many atoms interacting with a cavity mode

So far, the analysis has been concerned with single atoms. In the single excited limit one can extend this to many atoms if they do not interact with the internal degrees of freedom of each other, a good approximation for trapped ions since they are always well separated due to the Coulomb repulsion. If the laser and cavity acts uniformly with all atoms the extension can be expressed simply by the replacement of the lowering, raising, and population operators by sums of the operators for single-atoms. Detailed treatments can be found in [133, p. 7] and [182, p. 26ff] where also the effect of non-uniform coupling to the cavity is discussed. The result is that an effective number of atoms,  $N$ , will interact with the cavity and the coupling strength  $g$  is replaced with a collective coupling strength  $g\sqrt{N}$ .

<sup>3</sup>For the full treatment including noise terms, additional terms in the Hamiltonian are needed and the driving light field should be treated quantum mechanically.

### 5.3.2 Steady state and Cooperativity

We solve the Heisenberg-Langevin equations in steady state. We assume a low excitation regime, such that  $\langle \Pi_e - \Pi_g \rangle \approx -N$ , where  $N$  is the effective atom number as defined before. We obtain

$$\tilde{a} = \frac{if_0}{\kappa' - i\Delta'_c}, \quad (5.47)$$

where we have defined a effective cavity field decay rate and detuning

$$\kappa' = \kappa + g^2 N \frac{\gamma}{\gamma^2 + \Delta^2} = \kappa + C \frac{\gamma^2}{\gamma^2 + \Delta^2} 2\kappa, \quad (5.48)$$

$$\Delta'_c = \Delta_c - g^2 N \frac{\Delta}{\gamma^2 + \Delta^2} = \Delta_c - C \frac{\Delta\gamma}{\gamma^2 + \Delta^2} 2\kappa. \quad (5.49)$$

Here the cooperativity  $C$  has been defined as

$$C \equiv \frac{g^2 N}{2\gamma\kappa}, \quad (5.50)$$

as in [69][77]. Other sources<sup>4</sup> use another definition of the cooperativity of  $\eta_C = 2C$ .

The cooperativity is an important parameter in CQED experiments and can be understood as the ratio between light scattered into cavity and light scattered into free space (up to the factor of two in the definition). This seems plausible from the definition since it involves the rate of coherent coupling in the numerator and the decay rates in the denominator. Consider a two level atom driven directly by a coherent field, e.g. the two level example of section 3.7.1, in the presence of an cavity (not driven). The corresponding Heisenberg-Langevin equations are easily obtained by combining the result of the previous section with eq. 5.43 and taking  $f_0 = 0$ . The result is

$$\dot{\tilde{a}} = -(\kappa - i\Delta_c)\tilde{a} + igP \quad (5.51)$$

$$\dot{P} = -(\gamma - i\Delta)P - i\Omega(\Pi_e - \Pi_g) \quad (5.52)$$

$$\dot{\Pi}_e = -\Gamma\Pi_e - i(\Omega^*P - \Omega P^*) \quad (5.53)$$

$$\dot{\Pi}_g = \Gamma\Pi_e + i(\Omega^*P - \Omega P^*). \quad (5.54)$$

The cavity scattering rate is the rate at which photons are entering the cavity which in steady state is equal to the rate at which photons decay from the cavity,

$$\Gamma_{\text{cav}} = 2\kappa|\tilde{a}|^2, \quad (5.55)$$

where  $\kappa$  is the field decay rate of the cavity and  $\langle a \rangle$  is the steady state value of the cavity field operator expectation value. The steady state the driven atom has coherences

$$P = \frac{-i\Omega}{\gamma - i\Delta} \frac{1}{1 + s}, \quad (5.56)$$

---

<sup>4</sup>See e.g. [102],[183] and [179].

which leads to

$$\tilde{a} = \frac{igP}{\kappa - i\Delta_c} = \frac{g}{\kappa - i\Delta_c} \frac{\Omega}{\gamma - i\Delta} \frac{1}{1+s}. \quad (5.57)$$

Inserting the steady state values we obtain

$$\Gamma_{\text{cav}} = 2\kappa \frac{g^2}{\kappa^2 + \Delta_c^2} \frac{s}{(1+s)^2}. \quad (5.58)$$

The ratio of cavity scattered and free space scattered photons zero cavity detuning is

$$\frac{\Gamma_{\text{cav}}}{\Gamma_{FS}} = \frac{g^2}{\kappa\gamma} \frac{1}{1+s} = 2C \frac{1}{1+s}, \quad (5.59)$$

where we have used eq. 3.63 for the free space scattering rate. At low saturation this ratio becomes twice the cooperativity,  $2C = \eta_C = g^2/(\kappa\gamma)$ .

For another interpretation of the cooperativity it is useful to rewrite it in terms of cavity parameters which shows that it can be considered as a purely geometric quantity. First, we rewrite the coupling strength

$$g^2 = \frac{d^2 \mathcal{E}_0^2}{\hbar^2} = \frac{3\pi c \Gamma}{V k^2}, \quad (5.60)$$

so that we can rewrite

$$C = \frac{g^2 N}{2\gamma\kappa} = \frac{N 3\pi c}{\kappa V k^2} = N \frac{12\mathcal{F}}{\pi w_0^2 k^2}, \quad (5.61)$$

where we have used eq. 3.61,  $\mathcal{E}_0^2 = \hbar\omega_0/(\epsilon_0 V)$  with  $V = L\pi w_0^2/2$ , and  $\mathcal{F} = \frac{\pi c}{2L\kappa}$ . If we identify  $\pi w_0^2/2 = \sigma_{\text{cav}}$  and  $\sigma_{\text{atom}} = 3\lambda^2/(2\pi) = \frac{6\pi}{k^2}$  then we can write

$$C = N \frac{\mathcal{F}}{\pi} \frac{\sigma_{\text{atom}}}{\sigma_{\text{cav}}}, \quad (5.62)$$

where the interpretation becomes clear.  $C$  can be interpreted as the product of the (effective) number of atoms times the average number of round trips of a photon in the cavity<sup>5</sup> times the ratio of the atomic and cavity cross sections, which gives the single-pass absorption probability per atom of a photon [183].

We note that in this case it is clear that the geometry of the cavity is the primary determiner of the cooperativity while the atom merely scales the interaction with the cavity according to the wavelength of the light. Note that this result is valid only for a two level atom with one spontaneous decay channel. In real applications there will be multiple decay channels and the cooperativity will be lowered as a result. This results in the cooperativity being scaled by the relevant Clebsch-Gordan coefficient squared.

---

<sup>5</sup>The average number of rounds trip in the cavity is actually  $\mathcal{F}/2\pi$ , but the photon "passes" the atom twice in a round trip.

## Chapter 6

# Optical dipole potentials

Another application of the interaction between atoms and light is that of optical trapping which will be relevant in chapter 13 when we discuss trapped ions in optical potentials. First considered by Askar'yan (1962) and later Letokhov (1968) the subject experienced a great breakthrough when Chu et al (1986) constructed the first optical trap for neutral atoms. See [104] for an introduction to dipole traps and their applications.

In section 6.1 a simple classical model of optical potentials will be presented. In section 6.2 optical potentials are derived for a two level atom and the result is compared to the classical model.

### 6.1 Classical model

We will start by presenting a simple classical model of a bound electron in a classical electric field, as is done in [104]. The radiation pressure force introduced in section 4.2 neglected the effect of the gradient of the intensity. We again start from the dipole interaction Hamiltonian

$$H = -\mathbf{d}\mathbf{E}, \quad (6.1)$$

which holds classically as well as quantum mechanically. To calculate the classical interaction energy of the electric field with the induced dipole of the atom we will need to assume a relation between the dipole moment and the electric field. The simplest model is that of a linear relation for the electric dipole

$$\mathbf{d} = \alpha\mathbf{E}. \quad (6.2)$$

Here we have assumed no permanent dipole (relevant for atoms, while molecules can have non-zero permanent dipole moments). The dipole here is induced by the electric field, and it is determined by the complex polarizability of the atom,  $\alpha$ . The interaction energy of an induced dipole is given by

$$U_{\text{dip}} = -\frac{1}{2}\langle\mathbf{d}\mathbf{E}\rangle, \quad (6.3)$$

where the average is over one period of the oscillation of the electric field and the factor of two comes from the fact that the dipole moment is induced<sup>1</sup>.

Consider an electric field given by

$$\mathbf{E}(\mathbf{r}, t) = \hat{\epsilon}E(\mathbf{r})e^{-i\omega t} + \text{c.c.} \quad (6.6)$$

Performing the time average while assuming that  $\mathbf{d} = \alpha\mathbf{E}$

$$U_{\text{dip}} = -\frac{1}{2}\langle\mathbf{d}\mathbf{E}\rangle = -\frac{1}{2\epsilon_0 c}\Re(\alpha)I, \quad (6.7)$$

where we have used that  $I = 2\epsilon_0 c|E(\mathbf{r})|^2$ . The real part of  $\alpha$  corresponds to the part of the dipole moment which is in phase with the electric field and thus represent the dispersive part of the interaction. The atom will experience a dipole force equal to the gradient of this dipole potential

$$\mathbf{F}_{\text{dip}}(\mathbf{r}) = -\nabla U_{\text{dip}}(\mathbf{r}) = \frac{1}{2\epsilon_0 c}\Re(\alpha)\nabla I(\mathbf{r}). \quad (6.8)$$

In addition the atom will absorb and re-emit light from the light field. The absorbed power is given by

$$P_{\text{abs}} = \langle\mathbf{p}\mathbf{E}\rangle = \frac{\omega}{\epsilon_0 c}\Im(\alpha)I(\mathbf{r}), \quad (6.9)$$

where  $\Im(\alpha)$  is the imaginary part of the polarizability and corresponds to the out-of-phase part of the dipole moment. A quantity of interest is the spontaneous scattering rate

$$\Gamma_{\text{sc}}(\mathbf{r}) = \frac{P_{\text{abs}}}{\hbar\omega} = \frac{1}{\hbar\epsilon_0 c}\Im(\alpha)I(\mathbf{r}). \quad (6.10)$$

A simple classical model of the polarizability is that due to Lorentz. Here, an electron of charge  $-e$ , and mass  $m_e$  is bound elastically with spring constant  $k$  to an infinite mass nucleus. The polarizability can then be found by solving the equation of motion

$$\ddot{x} + \Gamma_\omega\dot{x} + \omega_0^2x = -eE(t)/m_e, \quad (6.11)$$

<sup>1</sup> This is in contrast to the Hamiltonian given before which does not suggest a factor of 1/2. To see why there seems to be no factor of two quantum mechanically it is helpful to have a specific model of the polarizability in mind. Consider a classical oscillator where an electron is bound harmonically to the nucleus. The classical and quantum mechanical Hamiltonians are both

$$H = \frac{1}{2}kx^2 - qEx, \quad (6.4)$$

where  $k$  is the spring constant and  $E$  is the electric field which is pointing in the positive x-direction. The Hamiltonian equations of motion can be solved and the equilibrium position  $x_0 = Eq/k$  will give the dipole moment  $d = qx_0$ . Inserting this expression into the Hamiltonian to find the energy from the two terms yields

$$H = \frac{1}{2}kx_0^2 - qEx_0 = \frac{1}{2}dE - dE = -\frac{1}{2}dE, \quad (6.5)$$

where the first terms is the energy required to induce the dipole and the second term is the interaction energy of the electric field and the dipole. Both are proportional to the electric field amplitude (a consequence of the harmonic nature of the model) and partially cancel, yielding the net effect given in eq. 6.3.

where

$$\Gamma_\omega = \frac{e^2 \omega^2}{6\pi\epsilon_0 m_e c^3}, \quad (6.12)$$

is the classical damping rate given by the Larmor formula, and  $\omega_0 = \sqrt{k/m}$ . The equation of motion can be solved to find

$$\alpha = \frac{e^2}{m_e} \frac{1}{\omega_0^2 - \omega^2 - i\omega\Gamma_\omega} = 6\pi\epsilon_0 c^3 \frac{\Gamma/\omega_0^2}{\omega_0^2 - \omega^2 - i(\omega^3/\omega_0^2)\Gamma}, \quad (6.13)$$

where we have defined the on-resonance damping rate  $\Gamma \equiv \Gamma_{\omega_0} = (\omega_0/\omega)^2 \Gamma_\omega$ .

By the correspondence principle we expect the classical model to hold in the classical limit. In fact the expression given here is, for low saturation, a very close approximation to the actual atomic polarizability. To make the model exact for low saturation ( $s \ll 1$ ) we make the replacement of the decay rate with the spontaneous decay rate of the atom

$$\Gamma = \frac{\omega_0^3}{3\pi\epsilon_0 \hbar c^3} |e|\mathbf{d}|g\rangle|^2. \quad (6.14)$$

Actually the Larmor formula, eq. 6.12, gives a good estimate in the case of alkali atoms, or alka-like ions, e.g. singly ionized calcium where  $\Gamma_{\omega_0} = 2\pi \cdot 22.45$  MHz and the measured value is  $\Gamma = 2\pi \cdot (23.05 \pm 0.15)$  MHz which suggests that the dynamics of the atoms can be understood classically to a large extent [104].

The simple model however does not take into account the saturation of transitions. We will show later that the effect of taking saturation as well as multilevel structure etc. into account will only lead to a numerical correction while the shape of the potentials will be unaltered.

Inserting 6.13 and 6.2 into 6.3, we obtain the dipole trap potential and scattering rate

$$U_{\text{dip}}(\mathbf{r}) = -\frac{3\pi c^2}{2\omega_0^3} \left( \frac{\Gamma}{\omega_0 - \omega} + \frac{\Gamma}{\omega_0 + \omega} \right) I(\mathbf{r}), \quad (6.15)$$

$$\Gamma_{\text{sc}}(\mathbf{r}) = \frac{3\pi c^2}{2\hbar\omega_0^3} \left( \frac{\omega}{\omega_0} \right)^3 \left( \frac{\Gamma}{\omega_0 - \omega} + \frac{\Gamma}{\omega_0 + \omega} \right)^2 I(\mathbf{r}). \quad (6.16)$$

This is the full relevant expression, at low saturation and large detuning  $\Delta \gg \Gamma$ .

In the case where  $\omega_0 + \omega \gg \Delta \gg \Gamma$  we can again perform the rotating wave approximation (RWA) by noting that the last terms contain the sum of the resonance and the drive frequency. We obtain the more common, simpler expressions (we also assume  $\omega_0 \approx \omega$ )

$$U_{\text{dip}}(\mathbf{r}) = \frac{3\pi c^2}{2\omega_0^3} \left( \frac{\Gamma}{\Delta} \right) I(\mathbf{r}), \quad (6.17)$$

$$\Gamma_{\text{sc}}(\mathbf{r}) = \frac{3\pi c^2}{2\hbar\omega_0^3} \left( \frac{\Gamma}{\Delta} \right)^2 I(\mathbf{r}). \quad (6.18)$$

From these two simple equations, the major dynamics of optical dipole trapping can be understood. We note that for a red-detuned laser,  $\Delta < 0$ , the trapping potential is negative i.e. the maxima

of the field intensity attracts the atom while for blue detuning,  $\Delta > 0$ , the atoms will be pushed towards low intensity regions.

In most experiments it is desirable to have a deep potential. This can be achieved by increasing the intensity of the field or by decreasing the detuning. But at low detuning the scattering will increase. Looking at the ratio

$$\hbar\Gamma_{\text{sc}} = \frac{\Gamma}{\Delta}U_{\text{dip}}, \quad (6.19)$$

it is clear that if a deep trap and low scattering rate is desired the detuning needs to be large.

In our case we will be interested in the case of optical fields in linear Fabry-Perot cavities where the intensity can be quite high. In addition to a factor of four due to the standing wave nature of the cavity light, one benefits from the finesse of the cavity.

The shape of the potential will be given by the intensity profile. For the fundamental TEM<sub>00</sub> mode near the center of the cavity we can expand to second-order

$$U_{\text{dip}} = -U_0 \cos^2(kz) \left[ 1 - 2\left(\frac{r}{w_0}\right)^2 - \left(\frac{z}{z_R}\right)^2 \right], \quad (6.20)$$

where  $U_0$  is given by equation 6.15 for  $I(\mathbf{r} = 0) = I_0$  as given by equation 5.22 [181][104]. The confinement in the radial direction is determined by the waist of the cavity while the axial confinement is determined by the wavelength of the light. The axial envelope is determined by the Rayleigh length  $z_R = \frac{\pi w_0^2}{\lambda}$ . Typically  $\lambda \ll w_0 \ll z_R$  for the field of a linear Fabry-Perot cavity. Thus the confinement will be tighter in the axial direction than in the radial. The trap depth is simply given as the potential difference between maximum and minimum of the intensity.

## 6.2 Quantum mechanical approach

To confirm the classical approach we will sketch out a quantum mechanical derivation. If we consider the  $H_{\text{int}}$  as a small perturbation on the atomic energy levels we can use regular second order perturbation theory to calculate the energy shifts due to the interaction. The energy shift of the ground state of the atom will be

$$\Delta E = \sum_{j \neq g} \frac{|\langle j | H_{\text{dip}} | g \rangle|^2}{E_g^0 - E_j^0}, \quad (6.21)$$

where  $E_j^0$  is the zero-order energy of level  $i$  [184, p. 256]. In solving this it can be useful to use the dressed state approach due to Dalibard and Cohen-Tannoudji [157]. Here the state of the system is considered to be the state of the atom and electromagnetic field together so that the relevant states are i) atom in ground state with  $n$  photons in field and ii) atom in an excited state,  $j$ , with  $n - 1$  photons in the field. The corresponding energies are

$$E_g^0 = \hbar\omega(n + 1/2), \quad (6.22)$$

and

$$E_j^0 = \hbar\omega(n - 1 + 1/2) + \hbar\omega_0 = \hbar\omega(n + 1/2) - \hbar\Delta_{ij}, \quad (6.23)$$

so that the difference becomes  $\mathcal{E}_i - \mathcal{E}_j = \hbar\Delta_{ij}$ .

For a simple two level system using eq. 6.14 and the dipole interaction Hamiltonian we get

$$\Delta E = \frac{|\langle e|H_{\text{dip}}|g\rangle|^2}{\hbar\Delta_{eg}} = \pm \frac{3\pi c^2}{2\omega_0^3} \frac{\Gamma}{\Delta} I, \quad (6.24)$$

which is in agreement with eq. 6.17. We can make the general assumption that we are in the ground state since we have assumed low saturation.

As discussed earlier the detailed interaction with multilevel atoms adds the complexity of polarization dependence. But in the case of being far detuned these expression simplify to a sum of contributions like equation 6.24.

## Part II

# Ion cavity experiments at MIT

## Chapter 7

# MIT experimental setup

In this part we will present the experiments performed while visiting the group of Isaac Chuang at Massachusetts Institute of Technology (MIT). This chapter consists of a brief introduction to the experimental setup that was originally constructed by David Leibbrandt for cavity cooling experiments. We will discuss the setup and some of the techniques used such as Doppler and sideband cooling. Further details can be found in [179, Ch. 5].

The experiments performed in this part are all done with strontium-88 ions. The level structure, transition wavelengths, and decay rates are shown in figure 7.2.

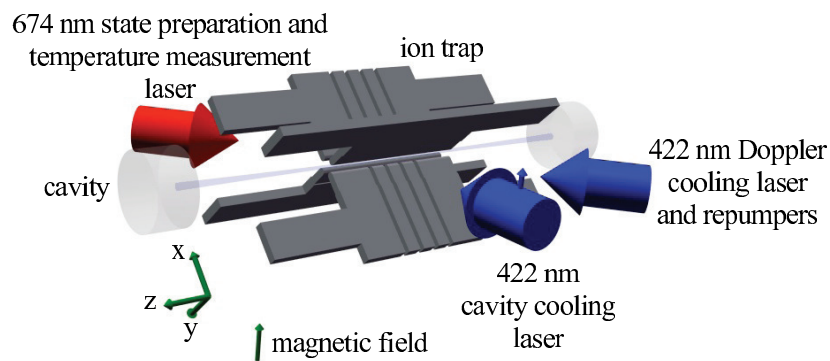


Figure 7.1: Schematic of the cavity cooling trap setup, here the direction of the magnetic field is vertical ( $\hat{x} - \hat{y}$ ). Schematic courtesy of [179].

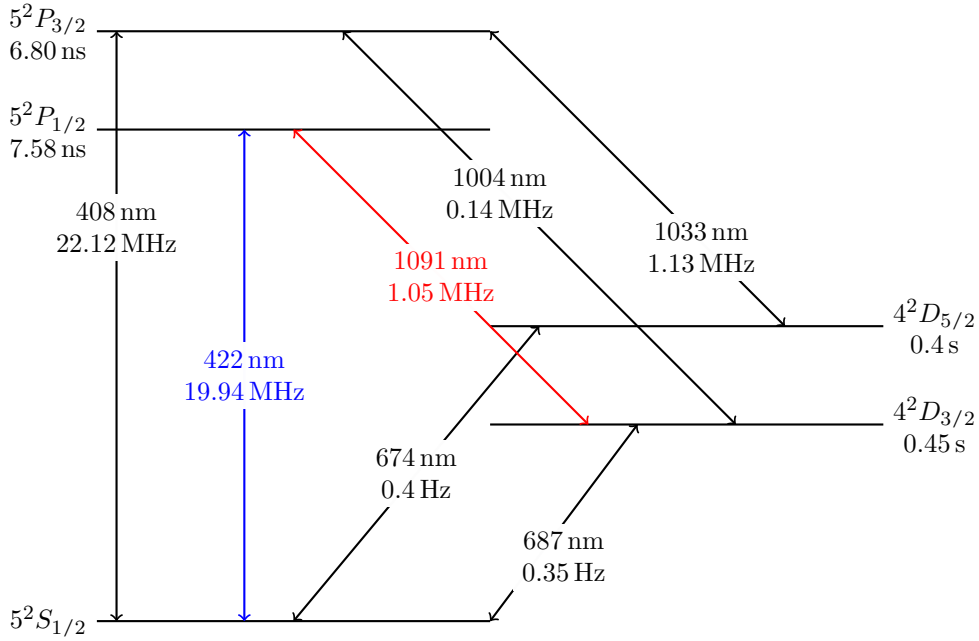


Figure 7.2: The level structure of the  $^{88}\text{Sr}^+$  ion with decay rates. All values are from [185] and references therein.

## 7.1 The trap

The ion trap is a knife-edge type trap and was fabricated by the research group of S. Urabe at Osaka University [179, p. 86], and is similar to the trap characterized in [186]. The choice of a four rod trap instead of e.g. a surface-electrode trap is due to the shielding from stray fields that the electrodes give in the four rod configuration.

In figure 7.1 a schematic of the trap is shown. The distance from the trap axis to the electrodes is  $r_0 = 0.6$  mm. In contrast to the generic theory presented in chapter 2, only two diagonally opposite electrodes have an applied rf potential. The other two electrodes are segmented and only dc potentials are applied to these. The segments are 5, 2, 2, 2, and 5 mm, respectively and are there to enable compensation of stray electric fields. A compensation electrode is placed 3 mm below the trap axis between the knife-edges (not shown in figure). This, in combination with the dc electrodes makes it possible to compensate stray electric fields in all directions. The two rf electrodes are driven at  $\sim 390$  V with a frequency of  $2\pi \times 14.33$  MHz using a helical resonator. The end dc electrodes are biased at 150 V. The secular frequencies are  $(\omega_z, \omega_y, \omega_x) = 2\pi \times (0.87, 1.2, 1.45)$  MHz.

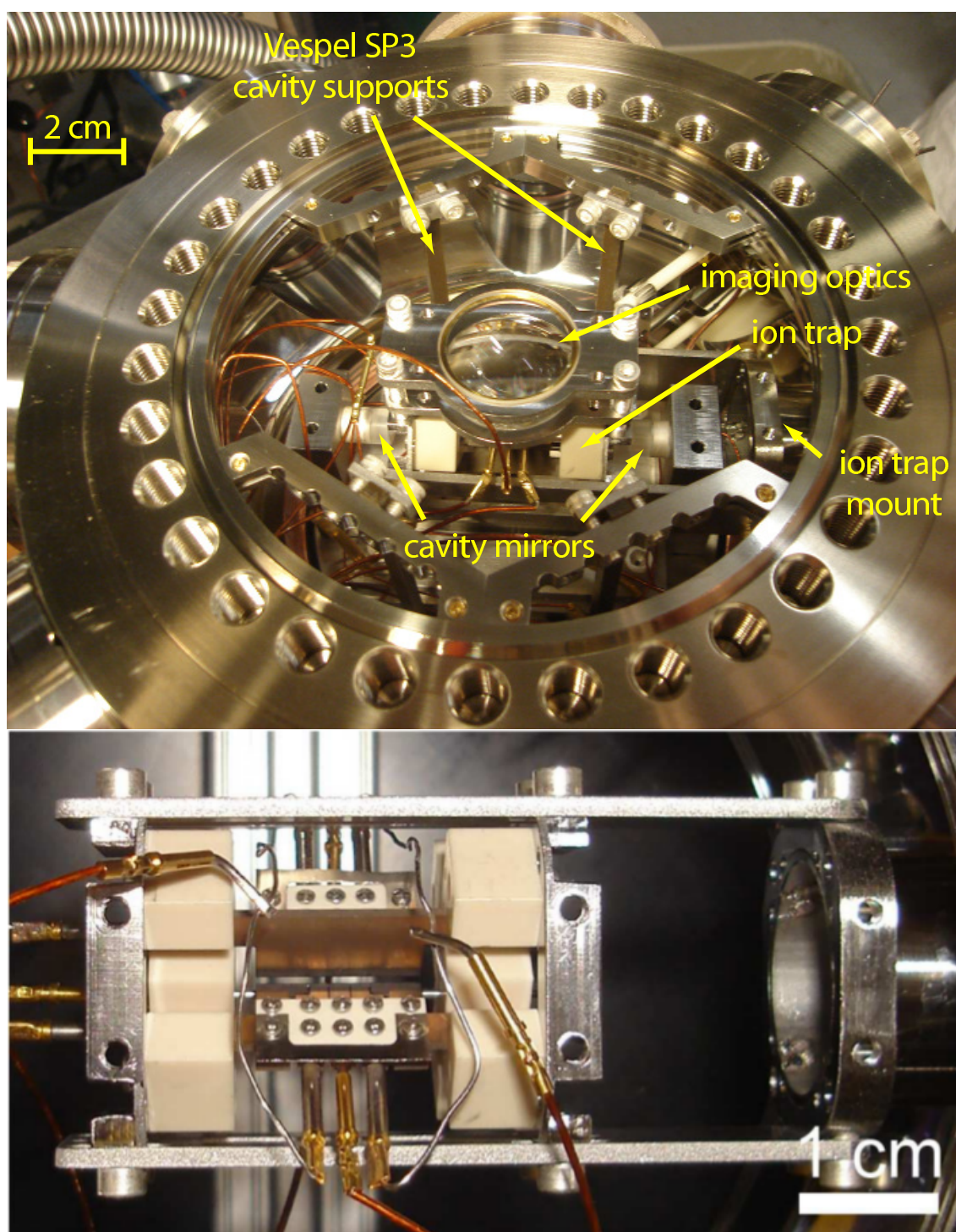


Figure 7.3: Top: Picture of trap and cavity installed in the vacuum chamber. Bottom: Trap mount, before cavity was installed. Photos courtesy of [179].

## 7.2 Imaging system

The imaging is done along the  $\hat{x} - \hat{y}$  axis in figure 7.1. The first two lenses of the imaging system are placed inside the vacuum chamber for improved light collection efficiency, see figure 7.3. After the vacuum window there is an additional lens and a bandpass filter for 427 nm photons<sup>1</sup>. A 75/25 beam-splitter is placed in the imaging system to direct 25% of the light to a CCD camera<sup>2</sup>. The remaining light is incident on a Photo Multiplier Tube (PMT)<sup>3</sup> which is used for most of the data analysis. The total detection efficiency with the PMT has been calibrated to  $(0.43 \pm 0.04) \%$ .

## 7.3 B-fields

The experiment has coils for generating a magnetic field. There are coils for generating a vertical B-field as well as coils in the two horizontal directions to cancel the Earth's magnetic field. In addition, water cooled coils oriented to generate a B-field along the cavity axis have been installed. Using this setup, a field of  $\sim 5$  G can be generated in the  $\hat{x} - \hat{y}$  (vertical) direction or in the  $\hat{z}$  (axial) direction.

## 7.4 Lasers

### 7.4.1 Ionization lasers

An atomic beam is generated by resistive heating of a strontium sample. The natural abundance of the desired  $^{88}\text{Sr}^+$  isotope is 83%. Ionization is accomplished using a two photon photo-ionization scheme [187][188][179, p. 59]. The first ionization laser excites the neutral strontium from the  $5s^2\ ^1S_0$ -state to the  $5s5p\ ^1P_1$ -state using a Toptica TA-SHG110 diode laser frequency doubled to 461 nm. A second ionization laser at 405 nm is a free running diode laser which couples to the auto-ionizing state  $5p^2\ ^1D_2$ . Since this transition is very broad the laser is not actively stabilized.

### 7.4.2 Monolasers

The remaining lasers are all based on the same monolithic system developed by [189]. They are External Cavity Diode Lasers (ECDL) [190] in a Littrow configuration with a built-in filter cavity. The cavity filters the mode of the laser and is used for tuning the laser. The whole laser is placed in a temperature stabilized, aluminum box in vacuum (except for the 422 nm laser). The linewidth achieved with these lasers is less than 30 kHz [189, p. 75].

Below, the various lasers and their uses are listed, along with typical power levels at the experiment.

- Light from the 422 nm laser is used for Doppler and cavity cooling as well as for stabilizing the cavity length. The power available from the laser is  $P = 72\ \mu\text{W}$  which is divided between

---

<sup>1</sup>Bandpass filter has 98% transmission at 422 nm.

<sup>2</sup>Princeton Instruments PhotonMax512.

<sup>3</sup>Hamamatsu H7360-02.

the Doppler cooling and cavity cooling beams. For the Doppler cooling beam the radius waist is 90  $\mu\text{m}$ . Polarization is aligned to drive  $\pi$ -transitions for the given B-field configuration, i.e. vertical for a vertical B-field and horizontal for the axial configuration.

- Light from the 1092 nm laser is used for repumping from the  $D_{3/2}$  to the  $P_{1/2}$  state.  $P = 52 \mu\text{W}$ . Radius waist is 0.29 mm and polarization is set for  $\sigma$ -transitions to avoid dark states [177].
- Light from the 1033 nm laser is used for repumping from the  $D_{5/2}$  to the  $P_{3/2}$  state when doing qubit manipulations like sideband cooling.  $P = 45 \mu\text{W}$ . Radius waist is 0.29 mm and polarization is set to address  $\sigma$ -transitions.
- The 674 nm laser is additionally stabilized to an Ultra Low Expansion (ULE) high finesse cavity so that the final linewidth is 100 Hz [189, p. 78]. The laser is used for qubit manipulations on the narrow  $S_{1/2}$  to  $D_{5/2}$  transition.  $P = 730 \mu\text{W}$ . The polarization is chosen to be perpendicular to the B-field. Using this, Rabi frequencies of  $\Omega_{\text{Rabi}} \approx 2\pi \cdot 150 \text{ kHz}$  can be achieved.

The laser beams for Doppler cooling, repumping and ionization are all combined into one beam and injected at  $45^\circ$  to the trap axis thus ensuring Doppler cooling in all three directions. The sideband cooling laser beam is injected along the same axis, but in the opposite direction.

All the lasers can be tuned on a slow timescale by changing the filter cavity length. The light frequencies are then measured by a wavemeter<sup>4</sup> accurate to within a few MHz.

The laser are all frequency shifted by Acousto Optic Modulators (AOM). A Field Programmable Gate Array (FPGA) based pulse programmer/sequencer is used to generate short light pulses by switching the frequency and amplitude of the drive signals for the AOMs [189].

## 7.5 Doppler cooling optimization

All experiments performed include an initial Doppler cooling step. Doppler cooling was discussed for two-level atoms in section 4.2 and for multilevel atoms in section 4.5 using calcium as an example. Here, we cool  $^{88}\text{Sr}^+$  on the  $S_{1/2}$  to  $P_{1/2}$  transition at 422 nm, see level structure in figure B.1. Additionally, part of the scattered Doppler cooling light is collected by the imaging system for imaging and state detection.

The procedure of optimizing Doppler cooling uses scans of the 422 nm laser frequency across the resonance in the fluorescence spectrum of the  $S_{1/2}$  to  $P_{1/2}$  transition, see figure 7.4, which shows one half of the Lorentzian resonance peak, see section 3.5.1. Data such as this is used to diagnose and optimize most parameters relevant for Doppler cooling by examining its width and overlap with Gaussian and Lorentzian distributions.

The 422 nm laser is tuned using the wavemeter to within 10 MHz of the  $S_{1/2}$  to  $P_{1/2}$  transition. After loading an ion into the trap an  $S_{1/2}$  to  $P_{1/2}$  scan is performed and assuming that a nice

---

<sup>4</sup>HighFinesse WS/7, calibrated daily to the ULE cavity of the 674 nm laser.

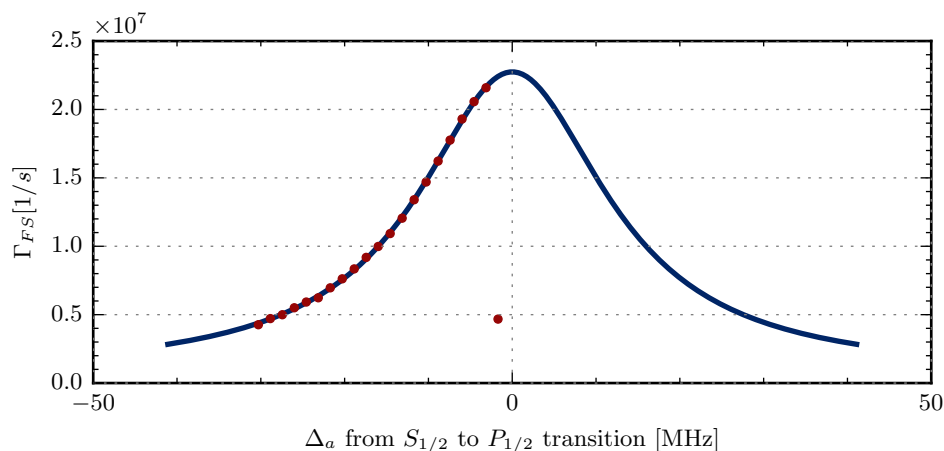


Figure 7.4: Scattering rate as a function of detuning from the  $S_{1/2}$  to  $P_{1/2}$  transition (red data points). Only the red part of the scan is shown since on the blue side Doppler heating will quickly heat up the ion enough that it stops scattering. This can be seen at the data point closest to the resonance. The blue line is a result of a Lorentzian fit to all but the last data point yielding a FWHM of 27.4 MHz.

Lorentzian scan is achieved, optimization of the number of counts on resonance is done by adjusting alignment, power and detuning of both the 422 nm and the 1092 nm lasers. Typical temperatures achieved with Doppler cooling after optimization are  $\sim 0.6$  mK.

## 7.6 Sideband cooling

In the following sections sideband cooling and temperature measurements based on the qubit transition will be used. Figure 7.5 shows the measured shelving rate while scanning the 674 nm laser frequency across the resonance of the  $S_{1/2}$  to  $D_{5/2}$  transition. The scan shows the transitions between Zeeman substates  $m_{-1/2}$  and  $m_{-5/2}$ . The scan is obtained by sending a fixed length pulse of light at 674 nm to drive the  $S_{1/2}$  to  $D_{5/2}$  transition after Doppler cooling. Since this transition is long-lived, the spontaneous decay can be neglected and the ion performs undamped Rabi oscillations between the  $S_{1/2}$  and  $D_{5/2}$  states, as described in section 3.5.2. The detection scheme is based on the shelving technique first used to observe quantum jumps of ions in 1986. Here it is used as a background free method of detecting the state of the ion. By illuminating the ion with 422 nm light, the transition between  $S_{1/2}$  and  $P_{1/2}$  will be driven. If the ion is in a superposition of the  $S_{1/2}$  and  $D_{5/2}$  state, this "observation" collapses the superposition into one of these states. If the ion collapses to the ground state it will fluoresce due to the 422 nm light and the scattered light is collected. If however the ion collapses to the excited  $D_{5/2}$  state, it will not be affected by the 422 nm light and no fluorescence will be observed. In this way many photons can scatter from the ion and thus the discrimination between "bright" and "dark" states of the ion is very good. The probability of type I and type II errors are below  $1 \times 10^{-3}$  for individual realizations

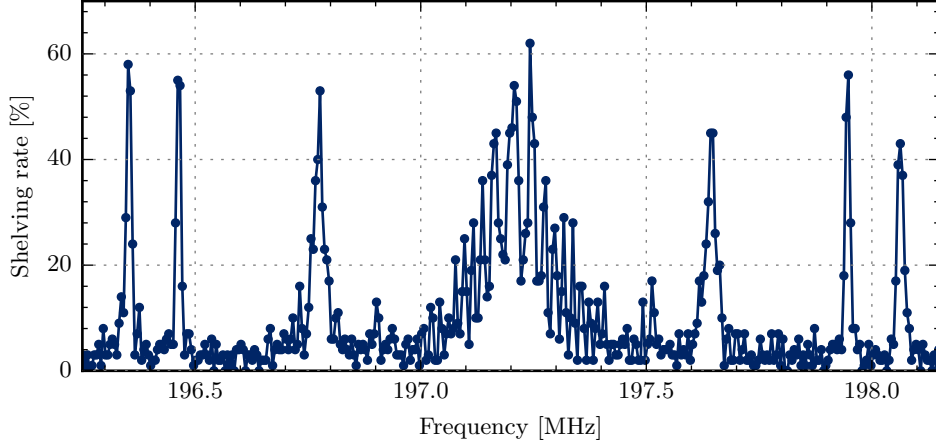


Figure 7.5: Shelving rate as a function of the frequency offset from the ULE cavity used to stabilize the laser 674 nm laser. In the figure the transition from  $S_{1/2}, m = -1/2$  to  $D_{5/2}, m = -5/2$  is seen as well as sidebands from the ion motion. The structure of the main peak is due to Rabi oscillations during the pulse time of 60  $\mu\text{s}$ .

so the state detection is limited by the statistical noise due to the limited number of realizations [191, p. 142ff]. In our experiments the shelving rate was measured using 100 repetitions. The uncertainty in determining the state can be derived from a binomial distribution; the result is

$$\sigma(P(D)) = \sqrt{100 \cdot P(D)(1 - P(D))}, \quad (7.1)$$

where  $P(D)$  is the probability to be in the dark state and  $\sigma(P(D))$  its uncertainty. This number represents the uncertainty for a given true value of  $P(D)$ ; to obtain the uncertainty for a measurement, this has to be inverted. The uncertainty depends on the populations and is not symmetric at the extrema, but for roughly equal superpositions it is about 5%.

The choice of polarization and angle of incidence determines the relative strengths of the transitions between the magnetic substates as detailed in [178, p. 32].

The motional sidebands corresponding to the secular frequencies of the trap are also visible. This is how the trap secular frequencies are determined. By tuning to the carrier of this transition and varying the pulse length so-called Rabi oscillations can be observed, see also section 3.5.2. By doing this over longer periods of time an estimate for the coherence time can be obtained. Such a scan is shown in figure 7.6. Note that Rabi oscillations are also observable in figure 7.5 since the pulse time is longer than the  $\pi$ -time i.e. the time corresponding to maximal excitation to the  $D_{5/2}$ -state. In the Lamb Dicke regime the relative strengths of the sidebands are given by equation 4.38. Rabi oscillations at the sideband frequency will have a lower Rabi frequency than at the carrier frequency due to the lower coupling strength, but will give information about the temperature of the ion, see section 4.6. For low temperatures a direct comparison between the shelving rate at the red and blue sideband frequencies suffices to measure temperature. For

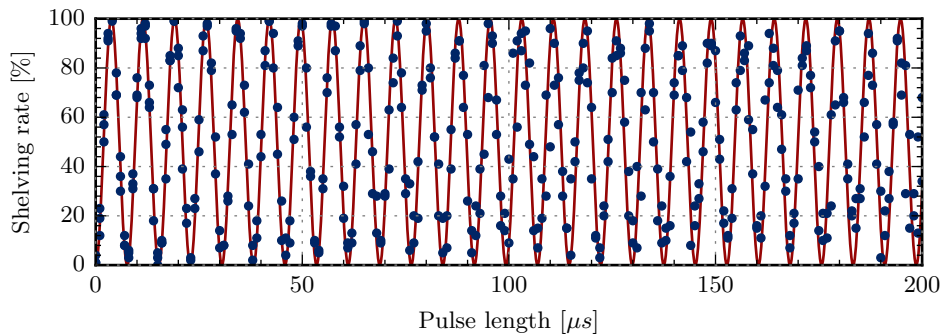


Figure 7.6: Shelving rate as a function of pulse length on the carrier of the  $S_{1/2}$  to  $D_{5/2}$  transition. Many exchanges of excitations are observed corresponding to a coherence time longer than 200  $\mu\text{s}$ .

higher temperatures the contrast disappears and longer and slower schemes must be used where longer Rabi oscillation scans are done on the sidebands. The scans are then fitted to obtain the temperature. See [179, p. 103] for details.

A pulsed, three dimensional, sideband cooling scheme is implemented. By adjusting the number of sideband cooling loops performed, the final temperature can be chosen. Details on the implementation can be found in [189] and [179].

## 7.7 Cavity design and characterization

The cavity was designed to be near-confocal. This means that the cavity length,  $L = 5$  cm, is almost equal to the radius of curvature of the mirrors

$$L = R + 250 \mu\text{m}, \quad (7.2)$$

which according to equation 5.6 gives a waist of  $w_0 = 58 \mu\text{m}$  for a wavelength of  $\lambda = 422$  nm. It also gives a splitting of 9.4 GHz between the  $\text{TEM}_{00}$  and  $\text{TEM}_{11}$  modes. This frequency interval ensures that the transverse modes do not broaden the cavity linewidth. The mirror transmissions were measured to be  $T_1 = T_2 = 38$  ppm and the losses per mirror  $\mathcal{L}/2 = 53$  ppm. For more details and assembly, see [179, p. 90].

Using ringdown spectroscopy the cavity finesse was initially measured to  $\mathcal{F} = 34\,500 \pm 500$ , but this has since declined, most likely due to contamination from the strontium oven during the commissioning phase of the trap. It is also possible that decay is related to oxygen depletion from the  $\text{Ta}_2\text{O}_5$  outer layer of the dielectric coating of the mirrors<sup>5</sup>. More recent measurements of the linewidth indicate a value of  $\mathcal{F} = 24\,000 \pm 1000$ . No birefringence has been observed. The bare linewidth is broadened due to the finite laser linewidth, such that measuring the linewidth by looking at the resonance peak always gives a lower finesse than using e.g. ringdown spectroscopy.

<sup>5</sup>Coating performed by Advanced Thin Films, Boulder (Colorado).

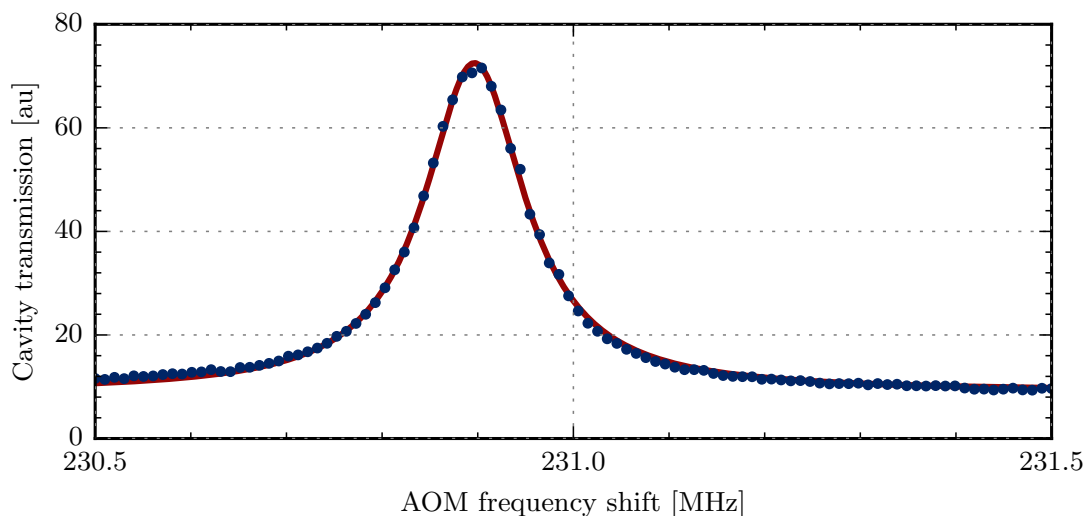


Figure 7.7: Cavity transmission as a function of the frequency of the input light (blue). The result of a Lorentzian fit shown (red) yielding a FWHM linewidth of  $(127.7 \pm 0.9)$  kHz.

See figure 7.7 for an example of a cavity transmission spectrum. Here light was injected into the cavity and detected with the cavity transmission PMT.

The light injected into the cavity will leak out equally through both mirrors. On the far side of the cavity fiber coupled PMT is placed to efficiently detect the cavity light. The detection efficiency of this setup has been calculated to  $(0.97 \pm 0.19)$  % [179, p. 98].

## 7.8 Cavity stabilization

### 7.8.1 Locking scheme

The cavity length is stabilized using light from the Doppler cooling laser. This locking employs the Pound-Drever-Hall scheme which is suitable for locking to a cavity resonance without introducing power dependence in the locking performance [192].

The real locking scheme is fairly complicated. Here a simplified scheme is explained; for full details see [102]. Two pairs of sidebands are generated by driving an EOM at  $(9.1750 \pm 0.0060)$  GHz. This light is injected into the cavity and the reflected light is detected by an APD from which an error signal can be generated. This error signal is used to adjust the frequency shift applied by the EOM to keep the light resonant with the cavity.

The cavity mirrors are mounted on piezoelectric transducers (PZT). One mirror is mounted on a long, slow PZT (low pass at 10 Hz), which has a long range, while the other mirror is mounted to a small, fast PZT. The fast PZT is used for scanning the cavity length (and in section 7.8.2 for scanning the interferometer). The lock of the electronics of the laser to the cavity resonance

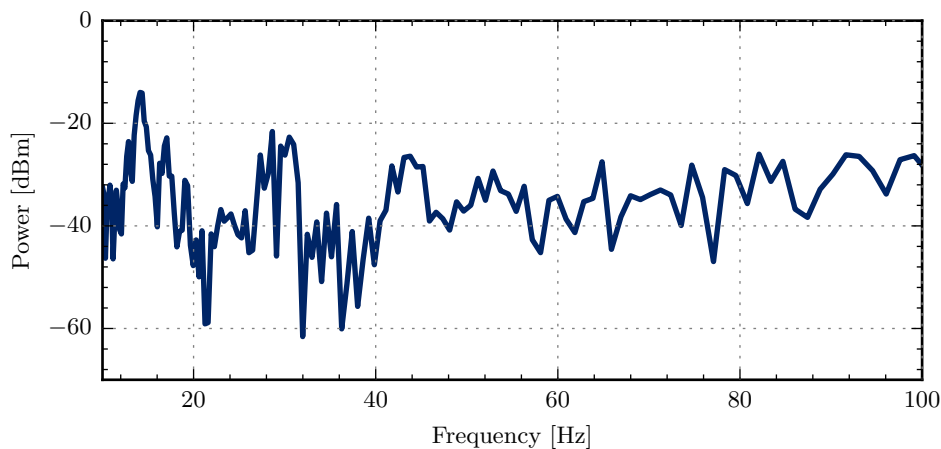


Figure 7.8: The interferometer signal showing the resonance at 15 Hz.

does not have an integrator part. The integrator signal is instead sent to one of the PZTs which corrects for the slow drift of the cavity resonance relative to the laser frequency.

Using the Doppler cooling beam to lock the cavity is potentially a problem since the ion can then interact with the lock beam. This is avoided in several ways. Firstly, the lock beam is coupled in the  $\text{TEM}_{11}$  mode of the cavity which has a node at the trap center where the ion is located. The cavity is locked to sidebands at 9 GHz generated by an Electro-Optical Modulator (EOM). This moves the lock beam frequency far away from the atomic resonance. Lastly, during the most sensitive measurements, the lock beam is switched off for the duration of data collection [179].

### 7.8.2 Cavity and trap mount

It is important that the ion trap and the cavity are aligned with each other such that the trap axis is at the center of the cavity mode. This is achieved by mounting the trap on an adjustable arm with micrometer screws outside of the vacuum chamber. The cavity mount is constructed with thin Vespel rods connecting it to the vacuum chamber and a heavy base to limit the coupling to the vacuum chamber and thus the surrounding environment. The Vespel rods are visible in figure 7.1. By having the trap mount mechanically low pass filtered the noise coupled through the vacuum chamber was diminished to a degree that the cavity could be locked[179].

The motivation for the low pass filter was a strong tuning fork resonance, see figure 7.9, at  $(4.4 \pm 0.1)$  kHz. The addition of the low pass filter made it possible to stabilize the cavity length, although it remains extremely sensitive to acoustic noise.

Since the cavity and trap are not mounted directly together, any relative motion of one will change the relative position between the cavity field and the ion. The unfortunate side effect of mechanically low passing the cavity mount is that the cavity becomes sensitive to low frequency

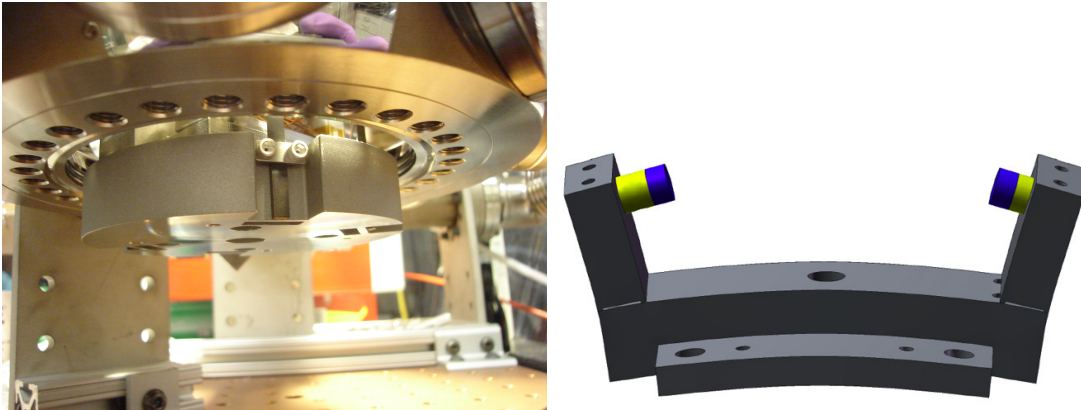


Figure 7.9: **Left:** View from below of Big Ben, the 1.65 kg mass attached to thin Vespel rods is visible in the center. **Right:** Simulation of the mechanical resonance of the cavity mount at  $(4.4 \pm 0.1)$  kHz which motivated the Big Ben construction.

oscillations. Simulations predict a low pass cut off frequency of 50 Hz. These oscillations change the relative position between trap and cavity and will completely average out the coupling of the ion with the standing wave field. This construction was nicknamed Big Ben since the end result was a construction looking and functioning like a bell, see figure 7.9.

The effect of Big Ben went undiscovered for several months. A contributing factor to not discovering the cause of the poor resolution of the standing wave scans was that it only occurred intermittently. It seemed to be as changing as the weather, which actually turned out to be the case, since it was discovered that the main driver of the motion of Big Ben was the Air Conditioning of the laboratory. The AC had a large, slowly turning fan spinning at 15 Hz. Whenever the laboratory was heating up the AC would spin more and the experiments would fail.

The effects were not completely understood until an interferometer setup was constructed and used to measure the movement of the cavity coupling mirrors. By analyzing this interferometer signal it was clear that both the camera fan and the AC were constantly exciting vibrations in Big Ben that were exceeding the range of the interferometer (roughly 200 nm) and this would yield a low visibility for the ion-cavity coupling.

A temporary solution for this was to turn off any vibration generating equipment for the duration of the experiment. It was also considered that by measuring the interferometer signal and feeding back to the PZTs of the cavity it would be possible to cancel out this motion. This was tried briefly and seemed to stabilize the motion, but in the end it was decided that the simpler solution was to turn off the noisy equipment during experiments.

## Chapter 8

# Cavity interactions: Theory

In this chapter we will derive expressions for the scattering rate for a single, trapped ion into the cavity, both when the ion is illuminated with light close to resonance with the  $S_{1/2}$  to  $P_{1/2}$  transition frequency either by means of a free-propagating beam perpendicular to the cavity (side drive) or injected into the cavity (axial drive). We will then describe a simple model of cavity cooling and derive corresponding rate equations.

### 8.1 Scattering rates

We will focus on assumptions and approximations relevant for the experimental setup:

**Assumption 1** *The ion can be modeled as a two-level system trapped by in harmonic potential. The multilevel structure can be effectively handled by changing constants and defining an effective cooperativity.*

This assumption should be valid when the system is in the low saturation regime.

**Assumption 2** *We are in the Lamb-Dicke regime (see section 4.6). The Lamb-Dicke parameter is*

$$\eta_{LD} = kz_0 = \frac{2\pi}{\lambda} \sqrt{\frac{\hbar}{2M\omega_z}} = 0.12, \quad (8.1)$$

*for the  $S_{1/2}$  to  $P_{1/2}$  ( $\lambda = 422$  nm) transition of the ion and  $\omega_z = 2\pi \cdot 870$  kHz. The Lamb-Dicke criterion is in principle  $\eta_{LD}^2(2n+1) \ll 1$ . Here,  $\eta_{LD}^2(2n+1) = 0.33$ , which means that the system is not completely in the Lamb-Dicke regime.*

**Assumption 3** *The driving field detuning is large as compared to the size of the magnetic splitting and the secular motional frequencies.*

As in section 4.6, we will consider the motion of the ion to be a quantum harmonic oscillator and we single out the motion along the cavity axis,  $\hat{z}$ . Let  $n$  be the average occupation number

(i.e. number of phonons) in the axial mode of the harmonic potential of the ion/trap system.  $\Gamma_{\text{FS}}$  is the scattering rate on the  $S_{1/2}$  to  $P_{1/2}$  transition and  $\hbar\omega_z$  is the phonon energy. We define the recoil energy as

$$E_{\text{rec}} \equiv \frac{\hbar^2 k^2}{2M} = \hbar\omega_z \eta_{\text{LD}}, \quad (8.2)$$

where  $k$  is the photon wavenumber  $k = \frac{2\pi}{\lambda}$  and  $M$  is the mass of the ion.  $\Gamma_+$  and  $\Gamma_-$  will be the rates of scattering processes that coherently increases or decreases the phonon number by one, respectively.

### 8.1.1 Coherent scattering

We have already calculated the cavity scattering rate in section 5.3.2. We now define the scattering rate into the cavity when the ion is at the anti-node and the cavity is on resonance ( $\Delta_c = 0$ ) by

$$\Gamma_{\text{cav},0} = \frac{g^2}{2\kappa} \frac{s}{(1+s)^2} = \eta_C \gamma \frac{s}{(1+s)^2}. \quad (8.3)$$

Isolating the relative strengths of the sidebands and the carrier and the effect of the cavity detuning we can write the rates of coherent increase or decrease in motional quantum number as

$$\Gamma_{\pm} = \Gamma_{\text{cav},0} \frac{\kappa^2}{\kappa^2 + (\Delta_c \pm \omega_z)^2} S_{n\pm 1,n}, \quad (8.4)$$

where we have used the fact that we are in the resolved sideband regime where the coupling to the sidebands separate, and  $S_{n\pm 1,n}$  are the relative coupling strengths compared to the carrier transition at the anti-node.

### Axial drive

For an axial drive the relative coupling strengths can be expressed as

$$S_{n\pm 1,n} = \left| \sum_m \langle n \pm 1 | \cos(k\hat{z} + \phi) | m \rangle \langle m | \cos(k\hat{z} + \phi) | n \rangle \right|^2, \quad (8.5)$$

where  $\phi$  is the relative phase with respect to the anti-node of the standing wave field. To derive selection rules and strengths we note that

$$\hat{z} = \sqrt{\frac{\hbar}{2M\omega_z}} (\hat{a}^\dagger + \hat{a}) = z_0 (\hat{a}^\dagger + \hat{a}), \quad (8.6)$$

is the position operator with  $\hat{a}$  and  $\hat{a}^\dagger$  being the lowering and raising operators respectively and  $z_0$  is the zero-point motion amplitude of the ion. In writing equation 8.4, we have used assumption 3 to make the relative strengths independent of atomic detuning.

Equation 8.5 can be simplified by noting that the sum over  $|m\rangle\langle m|$  is the identity. We thus have

$$S_{n\pm 1,n} = \left| \langle n \pm 1 | \cos^2(k\hat{z} + \phi) | n \rangle \right|^2. \quad (8.7)$$

By assumption 2, we are in the Lamb-Dicke regime meaning that  $\eta_{LD} \ll 1$ . For typical values  $z_0 \sim \sqrt{\frac{\hbar}{2M\omega_z}} \sim 10$  nm, which is indeed small compared to  $\lambda = 422$  nm.

Using trigonometric identities and orthogonality of the Fock states we can show that

$$\begin{aligned} S_{n\pm 1,n} &= \left| \langle n \pm 1 | \cos^2(k\hat{z} + \phi) | n \rangle \right|^2 \\ &\simeq \left| \langle n \pm 1 | -2k\hat{z} \cos(\phi) \sin(\phi) | n \rangle \right|^2, \end{aligned} \quad (8.8)$$

where we have neglected terms of higher order in  $\eta_{LD}$ .

$$\begin{aligned} S_{n\pm 1,n} &= \left| \langle n \pm 1 | -2k\hat{z} \cos(\phi) \sin(\phi) | n \rangle \right|^2 \\ &= \frac{4k^2 \hbar \cos^2 \phi \sin^2(\phi)}{2m\omega_z} \left| \langle n \pm 1 | \hat{a} + \hat{a}^\dagger | n \rangle \right|^2 \\ &= 4 \cos^2 \phi \sin^2(\phi) \eta_{LD}^2 \begin{cases} n+1 \\ n. \end{cases} \end{aligned} \quad (8.9)$$

### Side drive

Equivalent results for the case of a drive at  $90^\circ$  to the cavity axis (side drive) can be calculated from

$$S_{n\pm 1,n} = \left| \sum_m \langle n \pm 1 | \exp[i\mathbf{k}_{\text{side}} \cdot \hat{\mathbf{r}}] | m \rangle \langle m | \cos(k\hat{z} + \phi) | n \rangle \right|^2, \quad (8.10)$$

where the  $\exp[i\mathbf{k}_{\text{side}} \cdot \hat{\mathbf{r}}]$  factor now accounts for the running wave  $90^\circ$  field. The result is

$$S_{n\pm 1,n} = \eta_{LD}^2 \sin^2(\phi) \begin{cases} n+1 \\ n. \end{cases} \quad (8.11)$$

### 8.1.2 Incoherent scattering

For each scattered photon into free space the energy of the ion will change. Since we are only interested in the axial temperature it is enough to look at the axial component of the imparted momentum from the photon.

In the case of driving the cavity from the side (at  $90^\circ$  to the cavity axis) there is no Doppler cooling term and only recoil needs to be considered. For an axial drive there will also be a Doppler cooling term, see below. The energy increase from emitting a photon is

$$\begin{aligned} \Delta E = E_{\text{after}} - E_{\text{before}} &= \frac{(\vec{p} + \hbar\Delta\vec{k})^2}{2M} - \frac{p^2}{2M} \\ &= \frac{p^2}{2M} - \frac{p^2}{2M} + \frac{2\hbar\vec{p}\Delta\vec{k}}{2M} + \frac{(\hbar\Delta\vec{k})^2}{2M} \\ &= \frac{2\hbar\vec{p}\Delta\vec{k}}{2M} + \frac{(\hbar\Delta\vec{k})^2}{2M}, \end{aligned} \quad (8.12)$$

where  $\vec{p}$  is the initial momentum of the ion and  $\Delta\vec{k}$  is the change in momentum due to the emission of the photon. The first term will average out, since for spontaneous emission the emission angle is symmetric in  $\hat{z}$ . While there would be a net force on the ion for a running wave this force is canceled by the counter-propagating wave in the case of the cavity drive.

To get the average of the last term of eq. 8.12 we need to integrate over the radiation distribution of the particular transition which the ion is emitting on. Since we do not care about the radial temperatures we only look at the axial direction.

We are interested in the weighted average of  $(\Delta\vec{k})_z$  i.e. the momentum change from an average scattering event along the cavity axis,

$$k^2 A = \int f(\theta) (\Delta\vec{k} \cdot \hat{z})^2 d\Omega, \quad (8.13)$$

where the  $f(\theta)$  is the normalized radiation pattern of the relevant transition.

The branching ratios are  $b_\pi = 1/3$  for  $\pi$ -transitions and  $b_\sigma = 2/3$  for  $\sigma$ -transitions. To obtain the rate of increasing the motional quantum number due to the incoherent scattering we use the average effect of a scattering and multiply by the free space scattering rate  $\Gamma_{\text{FS}}$

$$\Gamma_{\text{incoh}} = 2\Gamma_{\text{FS}} \frac{(\Delta E)_{\text{avg}}}{\hbar\omega_z} = \Gamma_{\text{FS}} \eta_{\text{LD}}^2 A. \quad (8.14)$$

The relevant (normalized) radiation patterns for  $\pi$  and  $\sigma^\pm$  transitions are:

$$f_{\text{sc}}^0 = \frac{3}{8\pi} \sin^2 \theta, \quad (8.15)$$

$$f_{\text{sc}}^\pm = \frac{3}{16\pi} (1 + \cos^2 \theta). \quad (8.16)$$

$A$  will in general be dependent on the various ways the atom can decay back to the  $S_{1/2}$  state after having been excited to the  $P_{1/2}$  state.

The branching ratios for spontaneous emission from  $P_{1/2}$  level are denoted  $b_S$  and  $b_D$  for transitions to the  $S_{1/2}$  and  $D_{3/2}$  states, respectively, such that  $\Gamma_{P \rightarrow S} = \Gamma_{\text{FS}} b_S$  and  $\Gamma_{P \rightarrow D} = \Gamma_{\text{FS}} b_D$ .  $A_{SPS}, A_{SPD}, A_{DPS}, A_{DPS}$  denote the correction factors to the recoil energy from the various emission events where e.g.  $A_{SPS}$  means a transition from the  $S$  state to the  $P$  state and back to the  $S$  state. All  $A$ 's involving the  $D$ -state will be considered a small correction to the major  $A_{SPS}$  due to the small branching ratio  $b_D = 0.08$ .

$$A = b_S A_{SPS} + b_D (A_{SPD} + b_S A_{DPS} + b_D (A_{DPS} + \dots)) \quad (8.17)$$

$$= b_S + b_D (A_{SPD} + A_{DPS}) + \frac{b_D^2}{1 - b_D} A_{DPS}. \quad (8.18)$$

**Assumption 4** We will in the following assume  $b_D = 0$ , which corresponds to neglecting all transitions to the  $D_{3/2}$  state.  $b_D = 0.08$  so this is well justified.

Let us consider 3 particular situations:

**case 1) Axial drive and B-field along z-axis:**

In this case the ion is driven on a  $\sigma^\pm$ -transition and the effective cooperativity compared to a two level system will be  $\eta = (2/3)\eta_C$  due to the branching ratios. The factor  $A$  is then

$$A_{SPS} = \frac{2}{3} \int f^\pm(\theta)(1 - \cos \theta)^2 d\Omega + \frac{1}{3} \int f^0(\theta)(1 - \cos \theta)^2 d\Omega \quad (8.19)$$

$$= \frac{2}{3} 2\pi \int f^\pm(\theta)(1 - \cos \theta)^2 \sin \theta d\theta + \frac{1}{3} 2\pi \int f^0(\theta)(1 - \cos \theta)^2 \sin \theta d\theta = \frac{4}{3}. \quad (8.20)$$

**case 2) Side drive and B-field along z-axis:**

In this case the ion is driven on a  $\sigma^\pm$ -transition and the effective cooperativity compared to a two level system will be  $\eta = (2/3)\eta_C$ . The factor  $A$  is then

$$A_{SPS} = \frac{2}{3} \int f^\pm(\theta)(\cos \theta)^2 d\Omega + \frac{1}{3} \int f^0(\theta)(\cos \theta)^2 d\Omega \quad (8.21)$$

$$= \frac{2}{3} 2\pi \int f^\pm(\theta)(\cos \theta)^2 \sin \theta d\theta + \frac{1}{3} 2\pi \int f^0(\theta)(\cos \theta)^2 \sin \theta d\theta = \frac{1}{3}. \quad (8.22)$$

**case 3) Side drive and B-field vertical:**

In this case the ion is driven by a  $\pi$ -transition and the effective cooperativity compared to a two level system will be  $\eta = (1/3)\eta_C$ , again due the Clebsch-Gordan coefficients. Here the factor of  $A$  is the same as for case 2)

$$A_{SPS} = 1/3. \quad (8.23)$$

This is the configuration that was used in [102].

**Doppler cooling term**

It is also possible to have Doppler cooling if the light is injected along the axis. In this case a regular Doppler cooling term will appear in eq. 8.27. This term will be

$$\frac{dE_z^{\text{Doppler}}}{dt} = \frac{d \langle p^2 \rangle}{dt} \frac{1}{2M} = \langle 2p\dot{p} \rangle \frac{1}{2M} = \langle pF \rangle \frac{1}{M} = \langle p\beta v \rangle \frac{1}{M} = \langle p^2 \rangle \frac{\beta}{M^2}, \quad (8.24)$$

where we have used the usual Doppler cooling expression for cooling in a standing wave,  $F = \beta v$ , where

$$\beta = 4\hbar k^2 \frac{s}{(1+s)^2} \frac{\gamma \Delta_a}{\gamma^2 + \Delta_a^2} \sin^2(\phi). \quad (8.25)$$

This expression for the Doppler cooling term is justified by [166] and [193, p. 246]. In terms of motional quanta the Doppler cooling rate can be written as

$$\begin{aligned} \Gamma_{\text{Doppler}} &= \frac{\langle p^2 \rangle}{\hbar \omega_z M^2} 4\hbar k^2 \frac{s}{(1+s)^2} \frac{\gamma \Delta_a}{\gamma^2 + \Delta_a^2} \sin^2(\phi) \\ &= \frac{8(n+1/2)}{\hbar} E_{\text{rec}} \frac{s}{(1+s)^2} \frac{\gamma \Delta_a}{\gamma^2 + \Delta_a^2} \sin^2(\phi), \end{aligned} \quad (8.26)$$

where we have used  $\frac{2\langle p^2 \rangle}{2M} = \hbar\omega_z(n + \frac{1}{2})$  and divided by the phonon energy,  $\hbar\omega_z$ . Note that  $\Gamma_{\text{Doppler}}$  is negative for  $\Delta_a < 0$ .

## 8.2 Cavity cooling

After having derived the rates for coherent and incoherent scattering for axial and side drive, as well as the Doppler cooling term for the axial drive, we are now ready to discuss cavity cooling.

Consider that the atom is in some initial (thermal) state characterized by a mean motional quantum number  $n$ . The dynamics of the motion along the  $z$ -axis can now be modeled by a rate equation [98]. Given the assumptions of the previous sections, we can write the derivative of  $n$  as

$$\dot{n} = \Gamma_+ - \Gamma_- + 2A\eta_{\text{LD}}^2\Gamma_{\text{FS}} + \Gamma_{\text{Doppler}}, \quad (8.27)$$

where the first two terms corresponds to increasing and decreasing the phonon number coherently and the last two terms correspond to recoil heating from emitting incoherently into the vacuum modes and a possible Doppler cooling term if the drive beam is along the cavity axis.  $A$  is the previously defined geometrical factor which depends on the transition and, thus, on the atomic dipole radiation pattern.

We define  $N^{\text{Doppler}}$  and  $N^+$  such that

$$N^{\text{Doppler}} = \frac{8}{\hbar} E_{\text{rec}} \frac{\gamma\Delta_a}{\gamma^2 + \Delta_a^2} \sin^2(\phi) \quad (8.28)$$

$$N^+ = 2\eta_{\text{LD}}^2 A\gamma, \quad (8.29)$$

and

$$R^\pm = \eta_C \gamma \frac{\kappa^2}{\kappa^2 + (\Delta_c \pm \omega_z)^2} 4 \cos^2 \phi \sin^2 \phi \eta_{\text{LD}}^2. \quad (8.30)$$

We can now rewrite eq. 8.27 as

$$\dot{n} = \frac{s}{(s+1)^2} \left[ (s+1)N^+ + R^+ - N^{\text{Doppler}}/2 - (N^{\text{Doppler}} + R^- - R^+)n \right]. \quad (8.31)$$

## Chapter 9

# Cavity interactions: Experiments

In this chapter experiments based on the previously discussed cavity interactions will be presented. We will present results of probing the spatial structure of ion-cavity coupling and measurements of the cooperativity. The sideband structure in the cavity spectrum will be discussed. The results are compared to the theory of section 8.1. Two techniques for measuring the temperature of the ion using the cavity interaction will then be presented. Finally, results on sub-Doppler resolved sideband cavity cooling will be presented.

### 9.1 Ion-cavity coupling characterization

In the following sections the atomic detuning will be  $\Delta = -\Gamma/2$  in all cases and the saturation parameter (except in the case of the cooperativity measurements) will be fixed at  $s_0 = 0.07$ . In the cases of side drive the B-field and polarization were vertical so that  $\pi$  transition were driven.

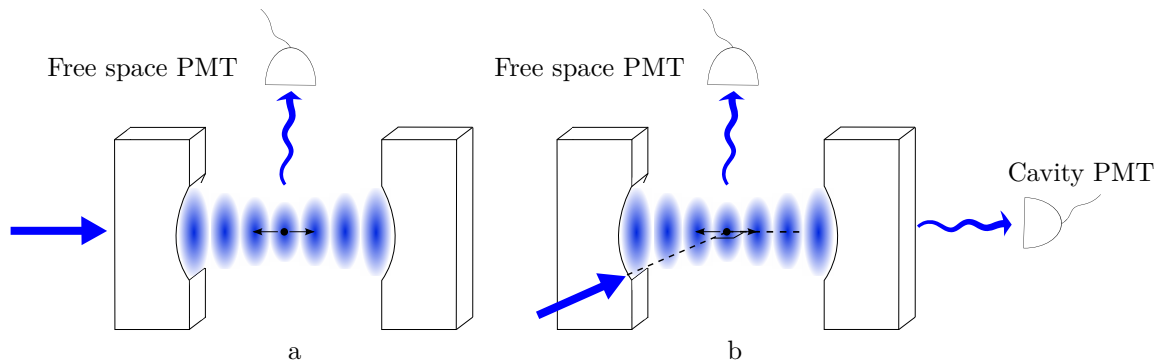


Figure 9.1: **a)** Axial drive: Here, light is injected into the cavity through the left mirror. Scattered light can then be detected using the free space PMT of the imaging system. **b)** Side drive: Here, light is driving the ion at  $90^\circ$  to the cavity axis and scattered light can be detected using the free space PMT, or in the case of light scattered into the cavity, using the cavity PMT which detects light decaying through the right mirror.

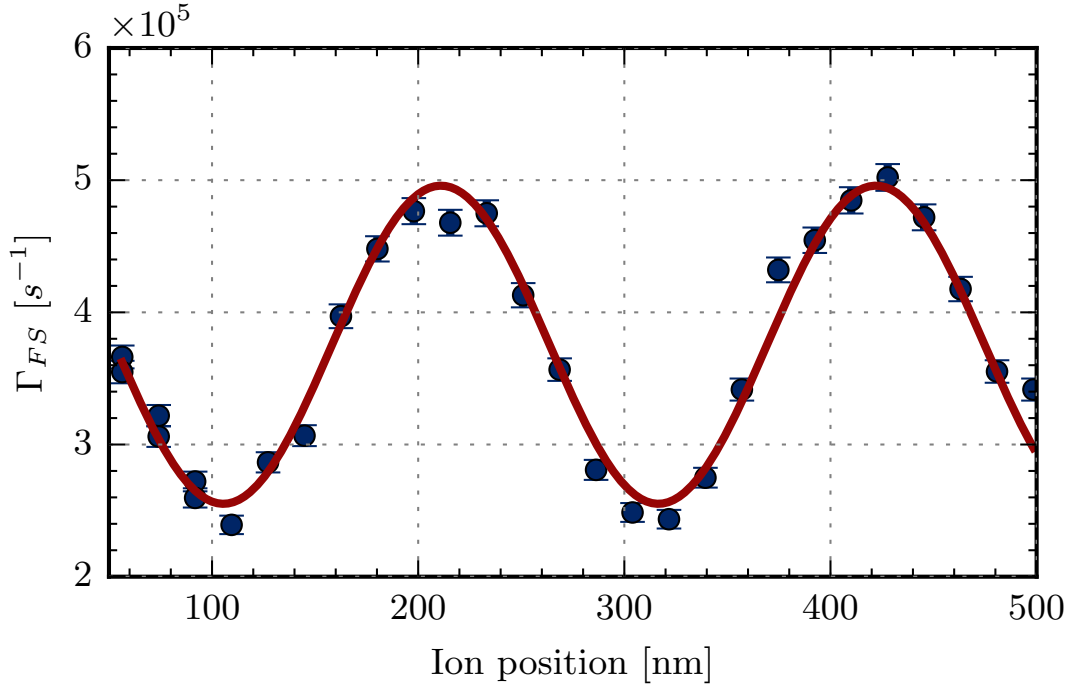


Figure 9.2: Scattered photons from the cavity mode into free space as a function of the longitudinal ion position. The ion position is controlled by adjusting the voltage of one of the DC electrodes. The experimental sequence consists of Doppler cooling for 5 ms and then collecting photons scattered into free space for 50  $\mu$ s (while the cavity lock beam is disabled). This is repeated 400 times for a total collection time of 20 ms. Geometry is as in figure 9.1a).

For the axial drive, the B-field was aligned with the propagation of the drive beam, such that  $\sigma$  transitions were driven. When discussing scattering rates detected the numbers are corrected for the detection efficiency for both the cavity and free space PMT.

### 9.1.1 Ion-cavity coupling

The ion cavity coupling is strongly dependent on the ion position through the dependence of  $g$  on the spatial structure of the electric field. In the Lamb-Dicke regime one expects that the fluorescence emitted by the ion has a sinusoidal pattern when displacing it along the cavity axis and resonantly driving with near resonant light. In figure 9.2 this behavior is shown with an axial drive. Here a laser beam is injected into the cavity through mirror 1 and the photons scattered by the ion into free space are detected. The opposite measurement is also possible where light is directed at  $90^\circ$  to the cavity (side drive) and photons are scattered into the cavity and detected.

### 9.1.2 Ion position lock

The longitudinal position of the ion needs to be determined and fixed with respect to the cavity mode. The standing wave data shown in the previous section indicates how this can be accomplished. By translating the ion to different longitudinal positions, measuring the scattering rate and fitting the results, it is possible to obtain the position of the ion with respect to the standing wave. By feeding back the position to a locking circuit the endcap voltages (on one end of the trap) can be adjusted to position the ion with precision  $\lesssim 10$  nm in the standing wave. This can correct for drift of the ion position on slow times scales due to e.g. heating from the oven or charging in the chamber. The precision is estimated from the uncertainty in the phase of the fit shown in figure 9.2. The temperature (and ultimately the zero-point motion amplitude) thus sets the limit for the precision of the ion position, along with the technical problems discussed in section 7.8.2.

The successful operation of this position lock was one of the main challenges of much of this work since many parameters of the experiment, e.g.  $g$ , depend on the ion position. The *Big Ben* structure of the cavity mount discussed in section 7.8.2 made this ion position lock very unreliable since it depended on only having drift slower than the time it takes for the lock to run, typically 15 seconds. Thus, any vibrations decreased its effectiveness. It was observed that if the amplitude of vibration of the cavity mount was more than  $\sim 200$  nm the standing wave pattern would be completely averaged out on the timescale of detection ( $\sim$  seconds). For the data presented in this and the following chapter, the interferometer of section 7.8.2 was used to monitor the vibrations of the cavity mirrors. Data for which significant vibrations were observed were discarded.

### 9.1.3 Cooperativity measurements

The cooperativity of the cavity can be estimated by sending in light resonant with the cavity at  $90^\circ$  to the cavity axis and collecting photons scattered into the cavity and into free space. If the ion was a two-level system, and if the collection efficiencies in both cases are properly calibrated this should match the theory of section 5.3.2, specifically equation 5.59. These measurements were performed for a vertical B-field with a vertically polarized 422 nm light field with a radius waist of  $\sim 12$   $\mu$ m. The ion is held at the anti-node of the cavity field by the ion position lock.

The two-level model predicts the shape of the curve, but since there are effectively at least 3 levels a three level model is required. A three level solution shows that by substituting  $s \rightarrow 3s$  in the two-level model this will still give reasonable results for low  $s$ . This substitution has been made in figure 9.3 where the red line shows the expected free space scattering rate as a function of saturation parameter,  $s$ , and the red data points show good agreement with this. For  $s > 1.5$  a more refined analysis is required. For the remaining experiments all data has been obtained for  $s < 1$  for which the theory fits well. The blue line shows the expected scattering rate into the cavity for a cooperativity of  $\eta_{\text{eff}} = 0.011$ . The laser used for these cooperativity measurements was not the same used for the measurement presented in [179]. The new laser is also of the same Monolaser design, but lases at 844 nm and is then frequency doubled to 422 nm. A larger linewidth of this laser can probably explain (at least partly) the measurement of a lower cooperativity than

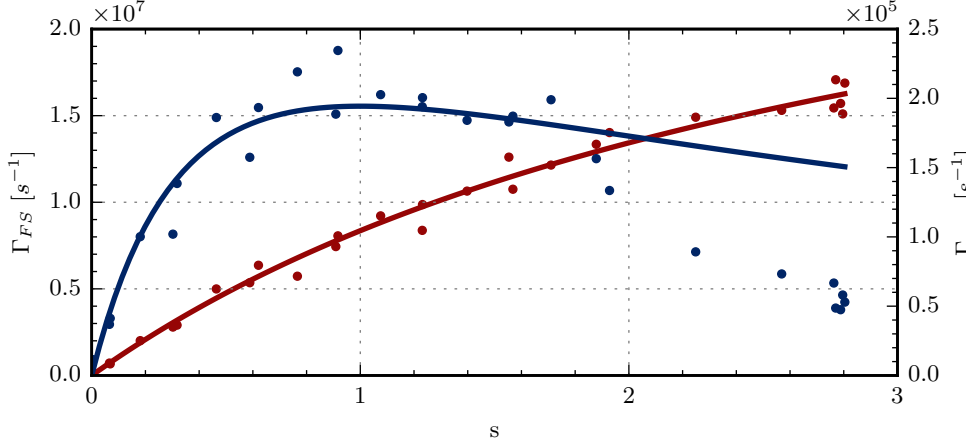


Figure 9.3: Red (Blue) line and points are theory and data respectively for scattering rate into free space (into cavity). The blue line corresponds to an effective cooperativity of  $\eta_{\text{eff}} = 0.011$ . The experimental sequence consists of Doppler cooling for 2 ms and then collecting photons scattered into cavity for 50  $\mu\text{s}$  (while the cavity lock beam is disabled). This is repeated  $4 \times 10^4$  times for a total collection time of 2 s. The geometry is as in figure 9.1b).

expected. The new laser is known to be broader than the earlier laser, but the linewidth has not been measured directly.

### Discussion of the cooperativity measurements

The ideal two-level cooperativity can be calculated from equation 5.61. For the parameters of the MIT experiment this becomes  $\eta_C = 0.26$ . In practice, several factors decrease this value so that the cooperativity effectively equals

$$\eta_{C,\text{eff}} = \eta_{CG} \eta_r \eta_P \eta_l \eta_T \eta_C, \quad (9.1)$$

where  $\eta_{CG} = 1/3$  is due to the Clebsch-Gordan coefficient of the  $\pi$ -transition ( $\eta_{CG} = 2/3$  for  $\sigma$ -transitions),  $\eta_r = 0.93$  accounts for inefficient repumping from the  $D_{3/2}$  state. A transverse positioning error of about 10  $\mu\text{m}$  gives a further reduction of cooperativity,  $\eta_P$ , between 1 and 0.89. The laser linewidth is expected to decrease cooperativity by  $\eta_l = 0.82$  for a 20 kHz laser (obtained via a stochastic phase noise added in master equation simulation) which corresponds to the expected linewidth of the Monolaser systems used to obtain the data of [102]. The non-zero Doppler temperature will also decrease the effective cooperativity by about  $\eta_T = (1 - \eta_{LD}^2(n + 1/2))^2 \sim 0.7$ . Combining these factors we obtain a theoretical estimate of the cooperativity  $\eta_{C,\text{eff}} = 0.04$ . See [179, p. 98] for further details. The measured cooperativity is thus lower than expected. One contributing factor to this is the linewidth of the laser used which is larger than the one previously used. Otherwise, the collection efficiencies could be incorrectly calibrated.

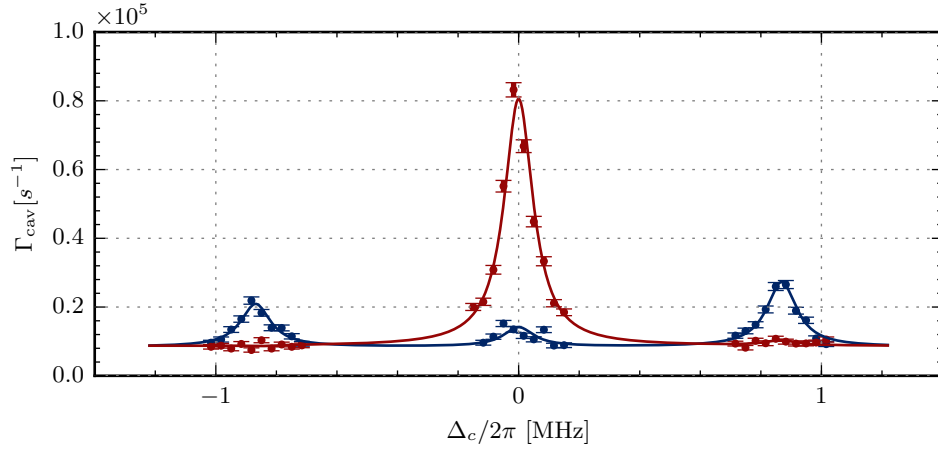


Figure 9.4: Photons scattered into the cavity by the ion illuminated by a side driving field (as in figure 9.1 right). Red points and red line are data and the results of a fit to eq. 8.4 for the ion locked to an antinode of the cavity field while blue points and line are for the ion locked to a node of the cavity field. The experimental sequence consists of Doppler cooling for 2 ms and then 50  $\mu$ s of collecting photons scattered into cavity (while the cavity lock beam is disabled). This is repeated  $4 \times 10^4$  times for a total collection time of 2 s.

#### 9.1.4 Cavity sideband scan

Because the ion-cavity system is in the resolved sideband regime it is possible to observe the motional sidebands in the cavity spectrum. With a vertical B-field and a vertically polarized laser beam at  $90^\circ$  to the cavity axis light is scattered into the cavity and detected, as shown in figure 9.1b). The motional sidebands appear in the cavity spectrum when scanning the laser frequency. Such a scan is showed in figure 9.6, where the red points correspond to the ion positioned at the anti-node of the cavity standing wave field and the blue points correspond to the ion being positioned at a node of the field. This clearly shows the selection rules for  $90^\circ$  drive given in equation 8.11.

## 9.2 Cavity Thermometry

### 9.2.1 Principle

Optically measuring the temperature associated with the motion of a single atom or molecule constitutes one of the most fundamental examples of thermometry, but is typically challenging due to low signal to noise ratios in the scattering measurements. In this respect trapped ions are an excellent system: they are single quantum systems which can be confined for interrogation over extended periods of time [163] and measurements of the motional degree of freedom of ions cooled to sub-millikelvin temperature can be realized [9][46]. However, such experiments generally rely on

complex laser systems specific to the atomic ion under investigation and typically require a narrow transition and a closed optical cycle. This precludes temperature measurements of molecules because they typically lack one or more of these features. The production and characterization of cold molecules is an active area of research and control [127][194].

Recently, there has been a growing interest in alternatives to these temperature measurement methods, including schemes based on high-resolution imaging of single ions [195, 196], capable of temperature measurements in the range of  $\sim 1 - 1000$  mK, as well as a method based on an interferometric signal derived from a single mirror demonstrating a range of 200  $\mu$ K to 4 mK [197].

Here we will present thermometry methods based on the cavity interactions derived in chapter 8. These methods depends neither on a narrow transition nor a closed optical cycle, but requires instead a strong enough coupling to a narrow linewidth optical resonator [92]. The independence of the scheme with respect to the atomic level structure makes it a viable method for systems without closed level structures, e.g., molecules.

The results of this section will be presented in a paper currently in preparation [198].

Equations 8.11 and 8.3 give the rates for scattering into the resonator mode in the case of a side driving field. Combining these we get

$$\Gamma_c = \Gamma_0 \cos^2(\phi) \cdot [1 - \eta_{LD,z}^2(n_z + 1/2)]^2 \quad (9.2)$$

$$\Gamma_r = \Gamma_0 \sin^2(\phi) \cdot \eta_{LD,z}^2 n_z \quad (9.3)$$

$$\Gamma_b = \Gamma_0 \sin^2(\phi) \cdot \eta_{LD,z}^2 (n_z + 1), \quad (9.4)$$

where c, r and b denote that the field is resonant with carrier, red sideband and blue sideband, respectively. Eq. 9.2, 9.3 and 9.4 represent the carrier, red sideband and blue sideband scattering rates [96].

The *Carrier Strength Method* utilizes the temperature dependence present in Eq. 9.2. We adjust the laser to the carrier frequency of the resonator and position the ion at the anti-node. The scattering rate is then given by eq. 9.2 where the second factor accounts for the carrier depletion due to the finite temperature of the ion. The applicability of this theory is limited by the breakdown of the Lamb-Dicke regime at high  $n_z$ , but this can be remediated by including more terms in the expansion leading to a more complicated expression. Another limitation is at the point where the atomic wavepacket width is on the order of the wavelength of the cavity light. The lower limit is dictated by the signal to noise ratio when  $n_z$  is small since we need to detect a small change in a large scattering rate. For low  $n_z$  the *Cavity Sideband Method* is more appropriate.

The *Cavity Sideband Method* uses the relative strengths of the sidebands. From Eq. 9.3 and 9.4, it is immediately obvious that the relative strengths of the sidebands hold information about the mean phonon number,  $n_z$  in the axial mode, as in the free space method [9, 46]. Scanning the resonator detuning,  $\Delta_c$ , relative to the drive laser for a fixed ion position,  $\phi$ , while collecting the scattered light from the ion into the resonator, will thus produce a spectrum from which the

temperature can be deduced via

$$n_z = \frac{\Gamma_r}{\Gamma_b - \Gamma_r}. \quad (9.5)$$

An advantage of this method is that all three motional modes can be measured with a single resonator and a single laser beam, when the motional modes are well separated.

The precision of the *Cavity Sideband Method* is fundamentally limited by the cavity linewidth, which determines the rate of off-resonant excitations. In a manner similar to standard sideband cooling, the fundamental limit for the precision of this method is set by  $n_z \sim (\kappa/\omega_z)^2$ , where  $\kappa$  is the cavity decay rate [2]. However, in this work, the primary limitation was due to dark counts of the detector.

The upper limit for effective temperature measurements with this method is again set by the signal to noise ratio when comparing  $\Gamma_r$  and  $\Gamma_b$ , which for  $n_z > 5$  are almost equal.

The ion is driven by a laser beam at 422 nm along the  $(\hat{x} + \hat{y})/\sqrt{2}$  direction, perpendicular to the resonator axis,  $\hat{z}$ .

In general the temperature of the radial motion will change when changing axial temperature thus changing the effective cooperativity. By assuming an equal temperature of all the motional modes and associating the mean phonon number,  $n_z$ , with a temperature,  $T_z$  via  $k_B T_z = \hbar\omega_z(n_z + \frac{1}{2})$ , where  $k_B$  is the Boltzmann constant we derive an expression for the mean quantum number in the radial mode as a function of  $n_z$ .

### 9.2.2 Experimental sequence

Here we outline the experimental sequence which is common to both measurement methods. Primarily, ion temperature preparation and verification, and ion-cavity coupling parameters. Firstly, the initial temperature state of the ion is prepared as follows. The ion is Doppler cooled to a temperature of about  $n_z = 11$  (0.5 mK), and further cooled to near the motional ground state via sideband cooling on the narrow  $5^2S_{1/2} \leftrightarrow 4^2D_{5/2}$  transition of the ion, driven by a free space propagating field from a narrow-linewidth laser ( $\sim 100$  Hz [189, p. 78]). The final temperature can then be tuned through the duration of this sideband cooling process or, alternatively through the power and detuning in the Doppler cooling process (while entirely skipping the sideband cooling). In this way, we can prepare the ion at any temperature within a range of  $n_z \simeq 0$  (0.02 mK) to  $n_z = 25$  (1 mK). This preparation is then verified using the well-established free space sideband spectroscopy technique, see section 4.6. We use this technique to validate the two methods implemented in this work.

The cavity thermometry probe is then applied to the prepared ions. The saturation parameter for our drive beam is  $s_0 = 0.07$ , where the saturation intensity is  $I_{\text{sat}} = 36 \text{ mW/cm}^2$  and the excited  $5^2P_{1/2}$  state has a linewidth,  $\Gamma = 2\pi \cdot 21.6 \text{ MHz}$ . Further details are given in the respective sections for the two methods.

Next, we outline requirements for our methods to be applicable and discuss our specific limitations in meeting these requirements. Three key requirements for this thermometry scheme exist:

1) The system needs to be in the resolved sideband regime. 2) The relative ion-cavity position needs to be kept stable to within a fraction of the cavity mode wavelength. 3) The ratio of photons scattered into the resonator compared to scattered into free space (i.e. cooperativity) has to be high or the system has to be stable for extended periods of time to collect enough statistics.

Requirement 1: Our setup is in the resolved sideband regime due to the narrow cavity linewidth of  $2\kappa = 2\pi \times 0.128$  MHz, and high secular frequencies,  $(\omega_x, \omega_y, \omega_z) = 2\pi \times (1.20, 1.45, 0.87)$  MHz.

Requirement 2: To keep the ion-cavity relative position constant requires mechanical stability and is needed because any transverse or longitudinal misalignment of the ion position with respect to the cavity mode will decrease the interaction and increase the measurement time. The transverse alignment is performed by monitoring the scattering into the cavity while moving the cavity with respect to the ion trap using translation stages. This alignment is accomplished to a precision of  $\sim 10$   $\mu\text{m}$  at the center of the cavity waist of 58  $\mu\text{m}$ . To ensure an interaction of, e.g., at least 90% of the theoretical maximum it is also necessary to control the ion position along the cavity axis with good precision (within 5% of the 422 nm wavelength). This requirement is satisfied by using the ion position lock discussed in section 9.1.2.

Requirement 3 is only partly fulfilled in our setup due to the relatively low effective cooperativity. This means that collecting statistics is a very slow process both due to the lower rate of photons scattered into the cavity and the need for resetting the experiment periodically to recool and prepare the ions.

### 9.2.3 Carrier strength method

We assume the resonator to be tuned to the carrier frequency and ion positioned at the anti-node with a certain width. The scattering rate is

$$\Gamma_{\text{cav}} = \Gamma_{\text{cav},0} [1 - \eta_{\text{LD},z}^2 (n_z + 1/2)]^2, \quad (9.6)$$

where  $\Gamma_{\text{cav},0}$  is the on resonance cavity scattering rate at the anti-node defined in eq. 8.3, and the second factor accounts for the carrier depletion due to finite temperature of the ion [178, p. 16].

Figure 9.5 shows the cavity scatter rate as a function of the mean quantum number,  $n_{\text{free space}}$ , as determined using the free space sideband thermometry technique on the  $5^2S_{1/2} \leftrightarrow 4^2D_{5/2}$  transition. Here we detected for a total of 2 s per data point in the standing wave scan (the inset shows an example). There are then 13 data points per  $\Gamma_{\text{PP}}$  point in the main figure. There is a clear tendency which serves as a calibration of the measurement technique. In our case the highest measured temperature of  $\sim 30$  quanta was limited by the temperature preparation. The temperature was adjusted by varying the power of the 422 nm light. Further range could have been achieved by changing the detuning. The lower temperature limit in this case is the Doppler limit since cooling with sideband cooling would be exceedingly slow due the low cooperativity and thus large number of scattered photons needed for statistics.

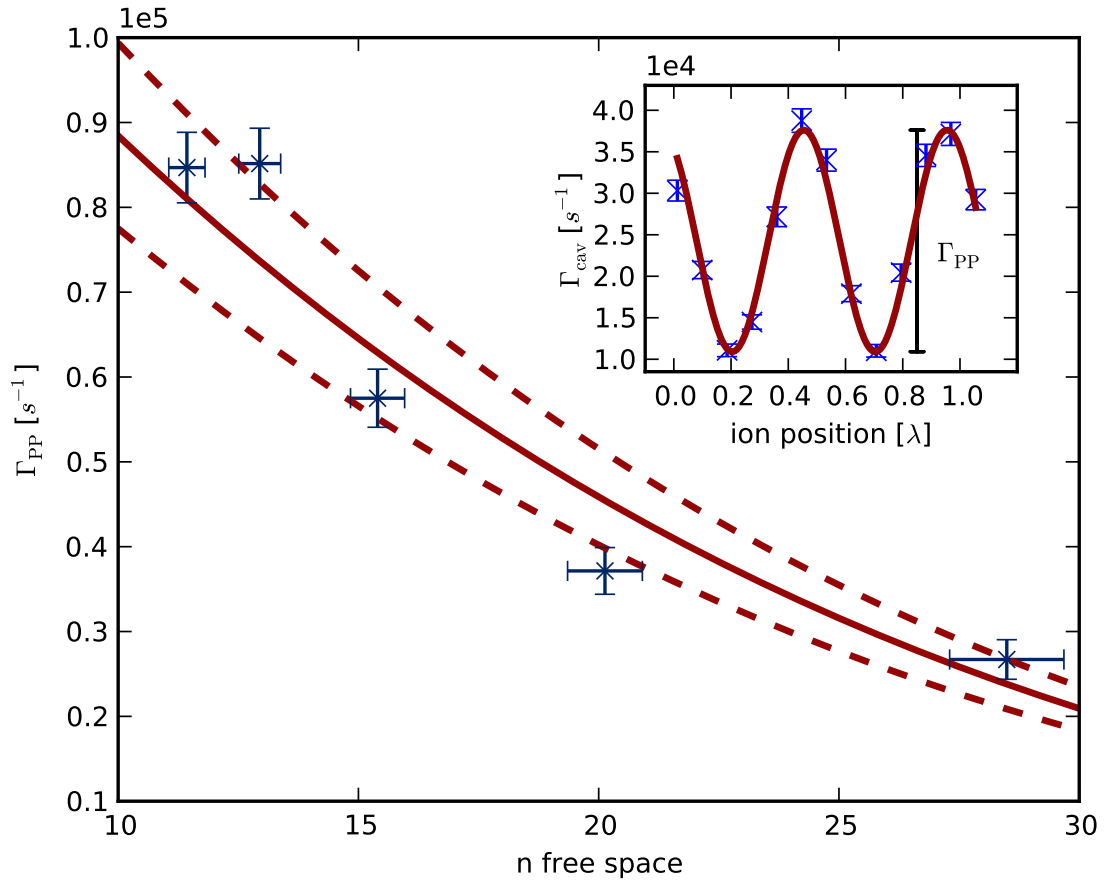


Figure 9.5: The peak to peak variation of the scattering rate,  $\Gamma_{PP}$ , in a scan of the standing wave, as shown with a fit in the inset, plotted as a function of mean quantum number,  $n_{\text{free space}}$ . The red solid line is a fit to eq. 9.2 with the dashed lines denoting 95% confidence intervals of the proportionality constant,  $\Gamma_0 = 3.3(2) \cdot 10^4 \text{ s}^{-1}$ . The experimental sequence consists of Doppler cooling for 2 ms and then  $50 \mu\text{s}$  of collecting photons scattered into cavity (while the cavity lock beam is disabled). This is repeated  $4 \times 10^4$  times for a total collection time 2 s per data point in the inset. The geometry corresponds to figure 9.1b.

### 9.2.4 Cavity Sideband Method

Here, as in the *Carrier Strength Method*, we focus on the  $z$ -axis of motion. To obtain maximal signal on the sidebands, we position the ion at the node ( $\phi = \pi/2$ ) using the ion position lock. By measuring the strength of the blue and red sidebands, the temperature can be inferred via Eq. 9.5. Figure 9.6 summarizes the results obtained with this method. The temperature measured with the resonator is recorded as the ordinate, while the temperature measured via the  $5^2S_{1/2} \leftrightarrow 4^2D_{5/2}$  transition,  $n_{\text{free space}}$ , is recorded as the abscissa. The inset shows an example of a sideband spectrum.

We note the deviation between cavity and free space measurements at high  $n_z$ . We attribute this to our interrogation time being 500  $\mu\text{s}$ , which induces a bias, due to a sideband and temperature dependent heating, increasing the blue sideband strength disproportionately as compared to the red sideband. This can in principle be calibrated out (or the interrogation time can be shortened) in order to allow for a larger temperature measurement range. For low temperatures this heating effect is less than the uncertainty of the measurements and we have thus not corrected for it [102].

As in the case of the free space analogue, the accuracy of this measurement scheme is best at low  $n_z$ , due to the difficulty in discerning the difference of the sideband strengths at larger  $n_z$ , which limits the range of the method. In the free space case the range can be extended by measuring the Rabi frequencies of the sidebands. By positioning the ion at  $\phi = \pi/4$  a comparison of the sideband and carrier strengths offers an alternative that in principle works at higher temperatures, but leads to higher sensitivity to the ion position due to changes in the relative strengths of sidebands and carrier. The errorbars in the inset represent the shot noise. The errorbars in the main figure are the errorbars from fitting sideband scans, one of which is shown as the inset.

### 9.2.5 Discussion

The usefulness of the *Carrier Strength method* is limited by the need for a careful calibration which is technically difficult due to mechanical and thermal stability of the trap and cavity mount. This calibration can be done independently by measuring collection efficiencies, light intensities and the effective cooperativity or by using another temperature measurement scheme as in our case [163].

The upper limit corresponds to a wavepacket size comparable to the wavelength of the cavity mode in which case further heating will not decrease the coupling any further. This results in a theoretical range of 20  $\mu\text{K}$  to 2 mK in our specific system. The fundamental limit is  $\delta n_z = (\kappa/\omega_z)^2 = 0.02$  or  $T = 20 \mu\text{K}$  which is in fact the lowest measured temperature. To further improve the sensitivity would require a higher finesse cavity (or a more strongly confined ion). Another limit is the background counts of the PMT which in our case also limits the sensitivity at 20  $\mu\text{K}$ . This could be improved upon by increasing cooperativity and collection efficiency. This would also decrease the time required to perform the measurement.

Beyond single ion thermometry, the *Cavity Sideband Method* offers the possibility of studying the thermodynamics of larger ensembles of ions such as strings. With a tightly focused driving laser one could probe only a small fraction of the ions at a time (ideally a single ion assuming

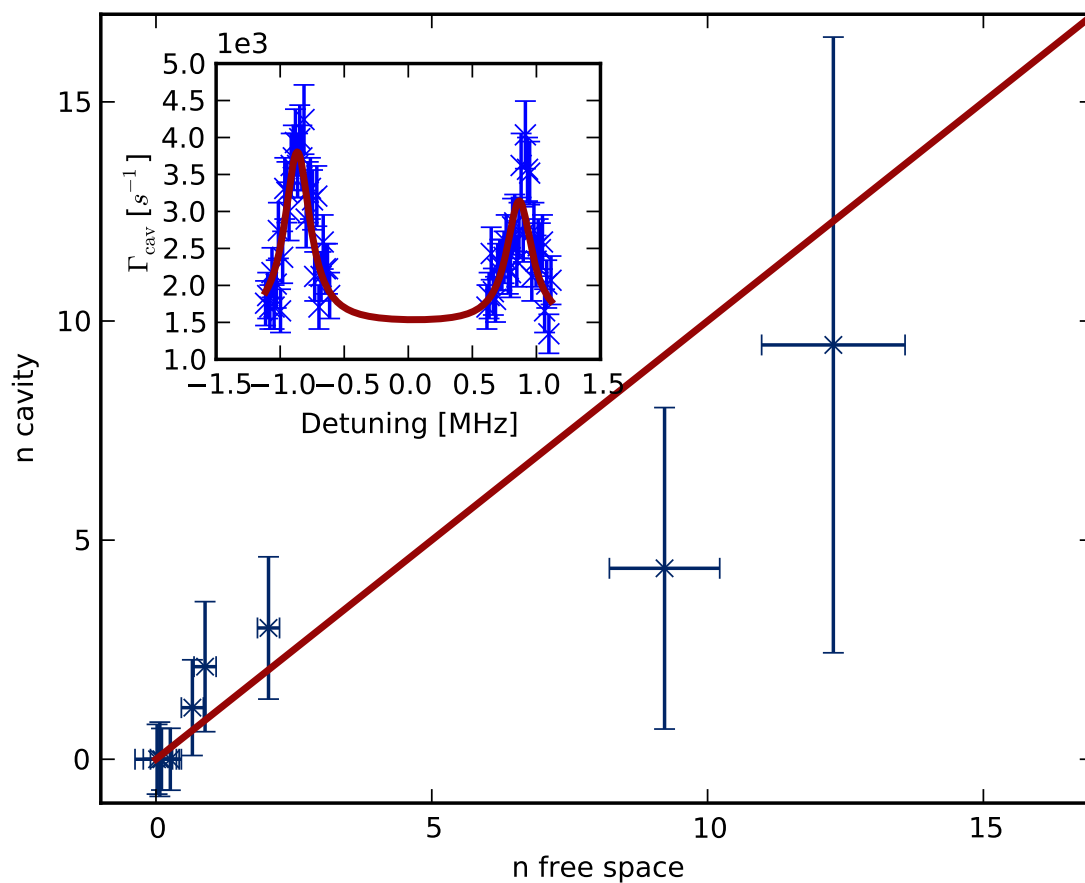


Figure 9.6: Temperature as measured by cavity sideband spectrum plotted against free space method. The red line denotes the theoretical  $n_{\text{free space}} = n_{\text{cavity}}$ . The inset shows a typical sideband scan. The experimental sequence consists of sideband cooling to the desired temperature and then  $500 \mu\text{s}$  of collecting photons scattered into cavity (while the cavity lock beam is disabled). This is repeated  $2 \times 10^3$  times for a total collection time 1 s per data point in the inset. Geometry is as in figure 9.1b.

the cooperativity was low enough that scattering is not influenced by the other ions) and open for studies of the local temperature fluctuations [199].

Here we have shown two methods for measuring the temperature of the motional state of an ion in an optical resonator in the range  $20 \mu\text{K}$  to  $1 \text{mK}$ . The main advantage of the methods is that the need for a stable narrowband laser at a specific wavelength is replaced by a narrow linewidth cavity which can be coupled to various transitions and species, hence more generally applicable in principle. Instead one needs stability with respect to the optical resonator.

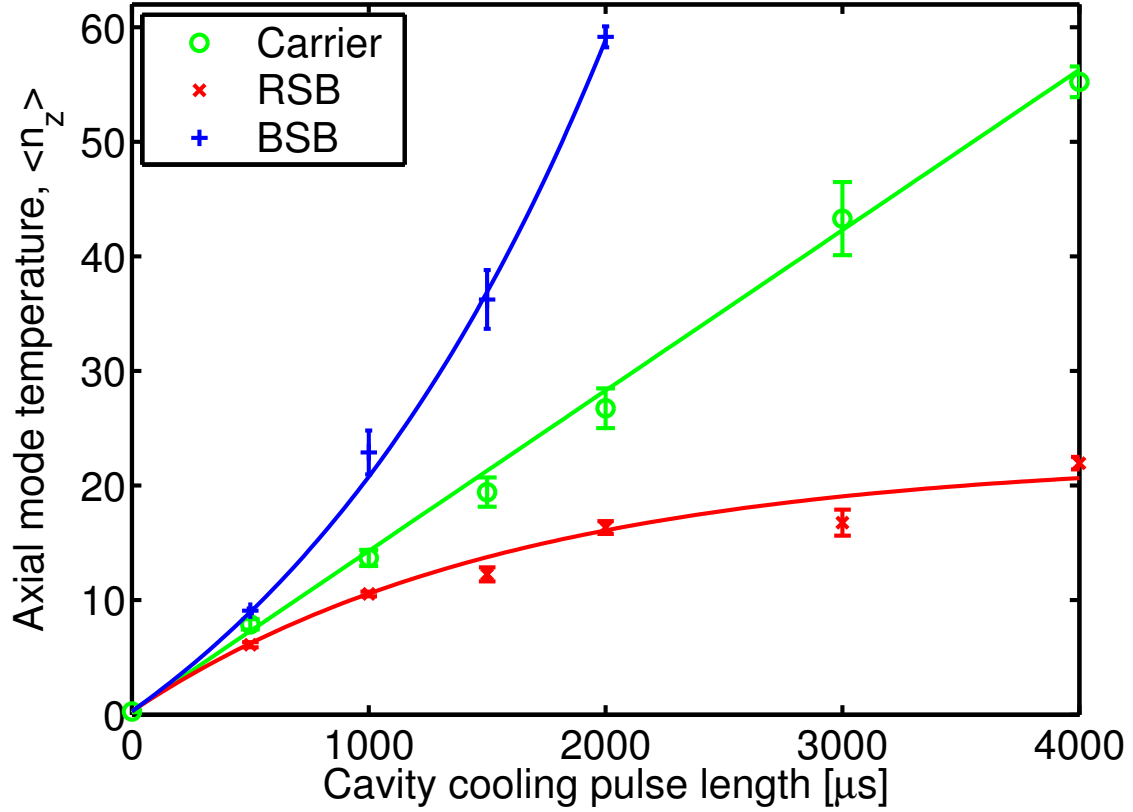


Figure 9.7: Results from the old setup using vertical B-field and coupling and side drive. Figure from [102]. Geometry as in figure 9.1b.

### 9.3 Cavity cooling

Leibrandt et al. demonstrated the effect of the cavity interaction on the motional state of a single trapped ion [102], but the interaction was not strong enough to achieve cooling, instead only reduced (or increased) heating was observed. In [179] cooling from a high temperature of  $n \sim 50$  was shown. The configuration used for these results was a vertical B-field and a drive from the side at  $90^\circ$  to the cavity axis.

The theory of cavity cooling was presented in chapter 8. The results of [102] of diminished cooling correspond to an  $A = 1/3$  value and an effective cooperativity  $\eta_{\text{eff}} = \eta_C/3$  due to Clebsch-Gordan coefficients of driving  $\pi$ -transitions. The results obtained in this situation are shown in figure 9.7. Here the ion was prepared in the motional ground state by sideband cooling and a cavity cooling pulse was applied either at the blue sideband, the red sideband or the carrier. Afterwards temperature was measured using sideband Rabi oscillations on the  $S_{1/2}$  to  $D_{5/2}$  transition as discussed in [179].

### 9.3.1 New configuration

It was realized however that, by changing the magnetic field configuration and injecting light directly into the cavity, that cooling could be improved and cooling below the Doppler limit would be possible. This section will describe this change and the results. The new axial cooling configuration improves on the old configuration in two respects. First, the shift to an axial drive with an axial B-field means that the ion is driven on  $\sigma$ -transitions which have stronger dipole coupling and thus the effective cooperativity is increased by a factor of two:  $\eta_{\text{eff}} = \eta_C 2/3$ . Secondly, a Doppler cooling term appears since we are driving the atom along the direction along which we are cooling. In the earlier setup there was only a Doppler recoil term, whereas now the Doppler cooling assists the cavity cooling. Here, as before,  $s_0 = 0.07$  and  $\Delta = -\Gamma/2$ .

### 9.3.2 Steady state

**Assumption 5** *Assuming steady state  $\dot{n} = 0$  and laser resonant with red sideband (cooling).*

Solving eq. 8.31 for the steady state  $n$

$$n = \frac{(s+1)N^+ + R^+ - N^{\text{Doppler}}/2}{N^{\text{Doppler}} + R^- - R^+}. \quad (9.7)$$

Inserting numbers into this expression;  $A = 4/3$  for axial drive and B-field,  $\phi = \pi/4$  for ion position in the middle between node and anti-node, atomic detuning  $\Delta_a = -\gamma$ ,  $\omega_z = 2\pi \cdot 870$  kHz and  $\kappa = 2\pi \cdot 63$  kHz. The cavity detuning is  $\Delta_c = -\omega_z$ . The cooperativity is estimated at  $\eta_{\text{eff}} = 0.12$  due to increased Clebsch-Gordan coefficients and insensitivity to radial temperature compared to [179]. The expected rates are then

$$N_+ = 2\pi \cdot 0.4 \text{ MHz} \quad (9.8)$$

$$N^{\text{Doppler}} = -2\pi \cdot 0.025 \text{ MHz} \quad (9.9)$$

$$R^+ = 2\pi \cdot 2 \times 10^{-5} \text{ MHz} \quad (9.10)$$

$$R_- = 2\pi \cdot 0.02 \text{ MHz}. \quad (9.11)$$

These numbers give a lower limit for the steady state temperature for  $s \rightarrow 0$  at  $n_z \sim 9$ . The cooling rate for Doppler cooling is actually of the same order as the rate for cavity cooling. For our experimental parameters the sub-Doppler steady state values are thus dependent on the Doppler cooling contribution. At present the rates given above are not completely understood and further work is needed.

### 9.3.3 Results

With the new configuration cooling below the Doppler temperature is possible. In figure 9.8 the cavity cooling dynamics from a higher than Doppler limit starting point are shown. The ion is Doppler cooled to  $n_z = 15$  (higher than the Doppler limit of 11 due to finite  $s$ ). Cavity cooling pulses

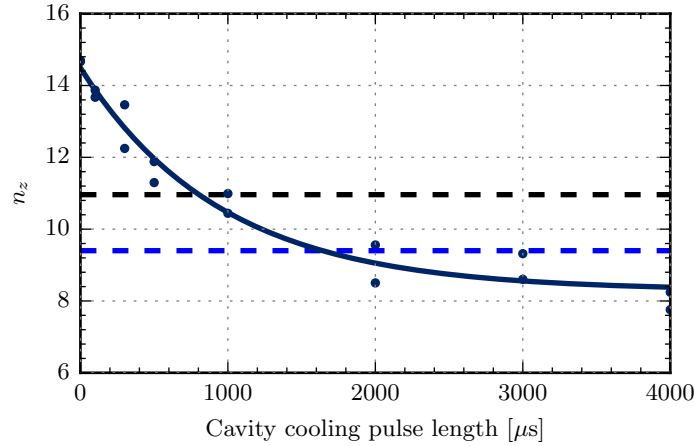


Figure 9.8: Axial mode temperature as a function of cavity cooling pulse length from an above Doppler limit starting point,  $n_z = 15$  reaching below the Doppler limit ( $n_z = 11$ ), marked by black dashed line. The steady state temperature is about  $n_z = 8$ , while the expected steady state temperature is  $n_z = 9$  (blue dashed line).

of varying lengths were applied using the axial beam driving  $\sigma$ -transitions. The temperature was measured using the quadrupole transition from  $S_{1/2}$  to  $D_{5/2}$  as detailed in section 4.6 and [179, p. 103]. The Doppler temperature is marked with the black dashed line and the temperature is clearly seen to go below this. This is one of the first sub-Doppler cavity cooling results. The expected steady state value is marked in blue. That the ion temperature does not reach this level is likely due to imperfect Doppler cooling or the non-zero saturation parameter. Additionally, problems with the ion position lock would also tend to deteriorate the cooling. Finally, the cooperativity in the axial direction has not been directly measured, but only inferred from the measurement of the cooperativity using a side drive (see section 9.1.3), so it could be lower than expected. The heating rate in the trap has been measured to be around 10 quanta per second which is much slower than the other cooling rates in the setup, so it is not expected to play a major role on the time scale of the measurements.

In ref. [103] they present sub-Doppler cavity cooling beyond the Lamb-Dicke regime of single  $^{138}\text{Ba}^+$  ions. They show cooling below the Doppler limit to about half the Doppler temperature. Their effective cooperativity is  $C = 0.446(21)$ , which is larger than ours.

## 9.4 Conclusion

In the experiments presented in this chapter we have shown good control of the coupling in the ion-cavity system. The experimental setup developed by in [179] has been developed further and new applications have been shown. Further work could be performed to improve various technical aspects of the setup such as stabilization of the vibrations of the system and cavity lock. The

thermometry results along with the resolved sideband cavity cooling results add to the possibilities offered by ion based cavity QED. These techniques all have the appeal that they can be applied to a range of system such as molecules, as pointed out in [\[92\]](#).

## Part III

# Ion cavity experiments in Aarhus

## Chapter 10

# Design and construction of the Blue Cavity trap

In this part, we will be concerned with the design, construction, and initial commissioning of a new cavity trap experiment in the Ion Trap Group of Michael Drewsen at Aarhus University. This linear rf trap incorporates an optical cavity on its longitudinal axis, whose mirrors are coated to be highly reflective at the wavelengths of the  $S_{1/2}-P_{1/2}$  (397 nm) and  $S_{1/2}-P_{3/2}$  (393 nm) transitions of calcium ions. It is similar in design to an existing cavity trap in the group, in which cavity mirrors are highly reflective at the wavelengths corresponding to the  $D-P$  transitions of the calcium ion (850, 854, 866 nm). We will refer to these traps as the Blue and Red Cavity trap, respectively.

In this chapter, the design and construction of the Blue Cavity trap will be discussed, and its assembly and the cavity alignment will be presented.

In chapter 12, the surrounding experimental setup, including imaging system, magnetic field coils, ovens, and vacuum system, will be discussed. The loading, trapping, and laser cooling of ions in the new trap will also be covered, and there will be a short discussion on the progress so far and an outline of the optimization and characterization to come.

In chapter 13, we will consider the general possibilities offered by this new cavity trap for performing cavity optomechanics experiments, simulating many body physics models or improving the control of ion Coulomb crystals.

### 10.1 Blue cavity trap design considerations

The new setup is a linear 4 rod Paul trap, which incorporates a "blue" cavity, designed to operate on the ground to excited states  $S_{1/2}-P_{1/2}$  (397 nm) and  $S_{1/2}-P_{3/2}$  (393 nm) transitions of  $^{40}\text{Ca}^+$ . This is in contrast with the existing Red Cavity trap, which has a cavity resonant with the metastable to excited state transitions  $D_{3/2}-P_{1/2}$  (866 nm),  $D_{3/2}-P_{3/2}$  (850 nm), and  $D_{5/2}-P_{3/2}$  (854 nm). See appendix A for the level structure of calcium.

The design of the new Blue Cavity trap is based on previous designs used in the group. The fundamental design is based on the original Linear Paul trap configuration by Prestage et al.

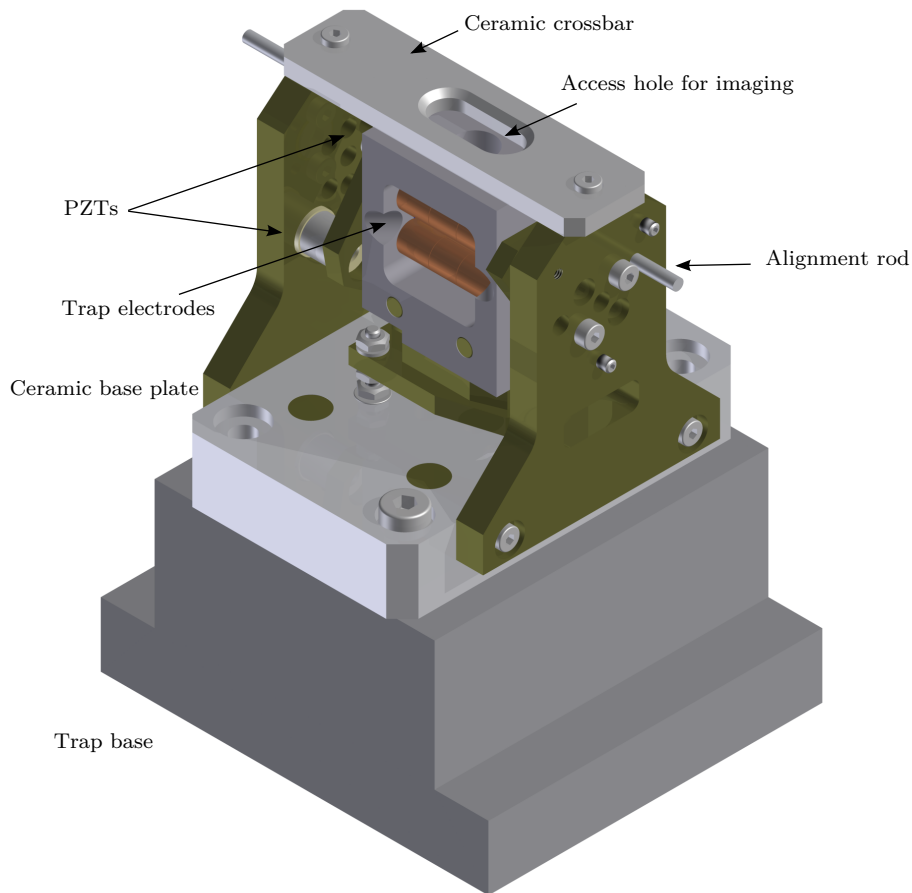


Figure 10.1: Angled view of the Blue Cavity trap. For scale the middle electrode length is 5 mm. See table 10.1 for dimensions. Grey parts are ceramic, while titanium parts are green.

[39]. Iterations of this design in our group was performed over several years, which lead to the development of a large trap with shorter middle electrodes for optimized trapping characteristics. The development of cavity traps in Aarhus was started during the PhD of Anders Mortensen [143], who designed the first trap in the years 2002–2005. This version never trapped ions, but was modified and improved by Aurelien Dantan and Peter Herskind from 2005 and on [133]. With this cavity trap collective strong coupling [77], Cavity Electromagnetically Induced Transparency (EIT) [78], and optical pinning of ions [107][200] was demonstrated recently. It is this successful design that is the basis for the Blue Cavity trap described in this thesis.

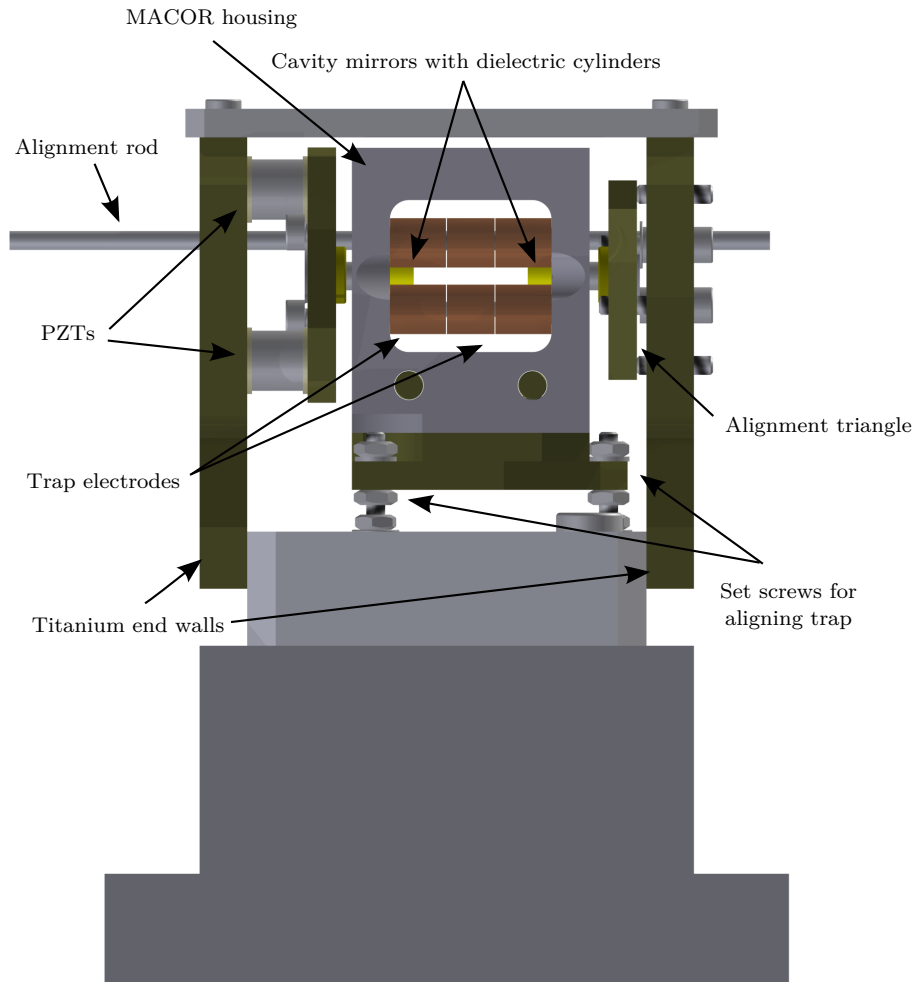


Figure 10.2: Side view of the Blue Cavity trap. Green parts are titanium, light gray is ceramics. The alignment rod is only present for the first rough alignment. The yellow parts are the hollow dielectric cylinders around the cavity mirrors. The cavity mirrors are flush with the cylinders and are thus not visible.

Table 10.1: Table of trap parameters. The mirror radius given is for the whole substrate – the curved part is only half of this. The  $a$  and  $q$  parameters are calculated for the most abundant calcium and barium isotopes. Typical voltages for  $U_{\text{end}}$  and  $U_{\text{rf}}$  are 1 V–15 V and 150 V–400 V, respectively.

Mirror substrate radius	$r_m = 1.5$ mm
Cavity length	$L = 12.8$ mm
Electrode inscribed radius	$r_0 = 2.35$ mm
Electrode radius	$r_e = 2.6$ mm
Center-electrode length	$2z_0 = 5.00$ mm
End-electrode length	$2z_{\text{ec}} = 5.90$ mm
Axial geometrical constant <sup>a</sup>	$\eta = 0.342$
rf-frequency	$\Omega_{\text{rf}} = 2\pi \times 3.6$ MHz
a-parameter( $^{40}\text{Ca}^+$ )	$a = -1.02 \times 10^{-3} U_{\text{end}}/\text{V}$
q-parameter( $^{40}\text{Ca}^+$ )	$q = 1.68 \times 10^{-3} U_{\text{rf}}/\text{V}$
a-parameter( $^{138}\text{Ba}^+$ )	$a = -0.294 \times 10^{-3} U_{\text{end}}/\text{V}$
q-parameter( $^{138}\text{Ba}^+$ )	$q = 0.487 \times 10^{-3} U_{\text{rf}}/\text{V}$

<sup>a</sup> See thesis of Anders Mortensen for calculation [143, p. 94].

## 10.2 Trap geometry

The trap is a four rod trap with each rod segmented into three electrodes, see figure 10.1, 10.2, and table 10.1. The rods have a radius set by the electrode radius,  $r_e$ , and the diagonal distance between them is  $2r_0$ , where  $r_0$  is the radius of the inscribed circle of the electrode rods. For a perfectly harmonic trap the electrodes should be hyperbolically shaped, but a good approximation with cylindrical rods is obtained by choosing the ratio of  $r_e$  and  $r_0$  to eliminate the first order above the quadrupole, i.e. the 12-pole term. The result is that the ratio has to be  $r_e/r_0 = 1.1468$  [123]. For the Red and Blue cavity traps this ratio is  $r_e/r_0 = 2.6 \text{ mm}/2.35 \text{ mm} = 1.1064$ . The slight anharmonicity caused by this mismatch can be estimated [123], but has so far not had noticeable consequences in experiments, since very large (up to  $1 \times 10^5$ ) and highly symmetric Coulomb crystals have been trapped in it [201]. Table 10.1 lists the relevant geometrical parameters.

The size of the trap was chosen to allow for trapping and cooling of a large number of ions and for having good optical access. It represents a trade-off between the advantages and disadvantages of a larger trap. A large trap typically allows for low heating rates [202], large trap-depth, good optical access, and large trapping area, which enables trapping of the order of  $10^5$  ions in this case. A disadvantage of a large trap is that it imposes a long distance between the dielectric cavity mirrors if one keeps them out of the trapping region to avoid perturbing the field lines. The consequence of moving the mirrors farther from each other is that the cavity mode volume increases and the interaction strength  $g$  decreases.

The effect on the harmonicity of trap due to the length of the center electrode was investigated using simulations, and an electrode length of  $2z_0 = 5$  mm was chosen [143, p. 98]. The potential difference between the center of the trap and the end cap is about  $0.8U_{\text{end}} \sim 2$  V for typical trap

parameters. This means that the trap depth is of this order as well [143, p. 94ff]. The effect of the presence of the mirror substrates near the trapping region was also investigated, and it was found that by filling the volume between the mirror substrates and the trap with a cylinder of the same material, fused silica, the uniformity of the dielectric constant would minimize the disturbance due to the mirrors [143, p. 94f].

## 10.3 Mechanical design and assembly

### 10.3.1 Design

The mechanical design of the base and mount for trap and cavity also parallels the previous Red Cavity trap design. The base of the trap is clamped to a base plate inside the vacuum chamber, see section 11.3.1. The base and most of the mount is made from titanium. Titanium is a good choice for vacuum purposes since it is machinable, strong and UHV compatible. For the purposes of ion trapping the primary advantage is that it is non-magnetic. This is crucial for some experiments, since a ferromagnetic material would disturb the magnetic field around the ions.

A plate of a low expansion ceramic material<sup>1</sup> is mounted on the trap base. Two end walls are mounted on the ceramic on either side, see figure 10.2. These end walls hold the cavity mirrors, and are secured to the ceramic at the bottom and to another ceramic cross-bar at the top. The ceramic was chosen due to its low thermal expansion coefficient, which limits the change in the cavity length due to changes in temperature.

The trap is mounted in a monolithic MACOR<sup>2</sup> housing which insulates the trap electrodes from the rest of the trap mount. The MACOR housing has holes drilled for the electrode guide rods. These rods are made from ZERODUR<sup>3</sup> and are  $1.6^{+0.00}_{-0.01}$  mm wide.

The MACOR housing is mounted to the ceramic base using three set screws. Before fastening the MACOR housing, and thus the trap, it is free to move on the order of 1 mm, and the height and angle of the trap can thus be adjusted. Steel alignment rods were constructed to align the trap with the end walls, which hold the cavity mirrors. The rods were inserted through both end walls and MACOR housing to define the height, position, and angle of the trap.

The whole trap was machined in the mechanical workshop on a Computerized Numerical Control (CNC) machine. The precision of the CNC machine is 5  $\mu$ m over 200 mm.

### 10.3.2 Vibration isolation

Due to its high finesse, the cavity is very sensitive to vibrations. For example for a finesse of  $10^4$  at a wavelength of 397 nm, the cavity is sensitive to vibrations of the order of  $397 \text{ nm}/10000 \sim 40 \text{ pm}$ .

To limit the amount of vibration transmitted through the optical table and vacuum chamber to the cavity mount, a few design changes have been made from the Red Cavity trap. Some effort

<sup>1</sup>MC-LD from MarkeTech International Inc.

<sup>2</sup>MACOR is a UHV compatible, machinable ceramic produced by Corning.

<sup>3</sup>An ultra low expansion glass manufactured by Schott.

was spent on the design of the trap base to limit the amount of vibrations transmitted through to the trap and cavity.

In other experiments with similar sensitivities to vibrations, layered structures of damping materials have been investigated [203][204]. It was found that a sandwich structure of alternating hard and soft materials would dampen vibrations. Similar solutions were thus considered for the Blue Cavity trap. The requirements of such a system for our purposes is that it will retain its damping characteristics after a bake-out (temperature at 150 °C for several days) and is UHV compatible. In addition, it should be mechanically stable with respect to movement of the whole experiment<sup>4</sup>, and over time when e.g. ovens are heating up the base plate of the chamber. Several UHV compatible rubbers were considered including Vespel, Kalrez, and Viton, which are all known to be UHV compatible after sufficient bake out. In the end the passive vibration damping system was discarded since it would be difficult to confirm the effect under realistic experimental parameters and due to time constraint. Without the passive damping system the trap will be more mechanically stable, as the passive damping would have needed to be based on gravity to keep the experiment in place.

To alleviate the problem of vibrations, the design of the end walls and mirror mounts were changed. In the Red Cavity trap, three Piezoelectric Transducers (PZT) were used to move one of the mirrors back and forth to change the cavity length. In the Blue Cavity trap this design has been replaced with two PZTs, and the plate connecting the PZTs, which holds the mirrors, has been made much lighter. If we consider the end wall as a cantilever with an added mass at the end (the PZTs and plate), then it is obviously better to make the mass lighter to obtain a higher resonance frequency of the system. The reason for using two PZTs in the new design is to ensure redundancy in case one of the PZTs breaks during experiments, since replacing it would mean redoing a larger part of the construction and assembly of the whole experiment. The PZTs are visible on figure 10.2 on the left as the two dark gray cylinders.

### 10.3.3 Assembly

The mirrors are mounted on cross beams, see figure 10.2. The cross beams are mounted to PZTs<sup>5</sup> for translation, which in turn are mounted to the end wall of the mount. The PZTs are isolated from the mounts by small ceramic MACOR spacers. The metal pieces, PZTs and MACOR, are all glued together using an electrically isolating UHV compatible glue<sup>6</sup>.

The PZT wires are glued with an electrically conductive glue<sup>7</sup>. The diameter of the wire is 1 mm with a Kapton coating<sup>8</sup>. The wires are glued to the PZTs since UHV compatible soldering requires higher temperature and can be technically more difficult. The disadvantage of gluing is

<sup>4</sup>All of the experiments of the Ion Trap Group were recently relocated. This involved lifting the optical tables with a crane and transporting them on a truck.

<sup>5</sup>Ferroperm Piezoceramics A/S, pz27, Tubes with OD=6.35 mm, ID=5.2 mm, L=6.35 mm with capacitance  $C = (2.6 \pm 0.1)$  nF.

<sup>6</sup>EPO-TEK H74F.

<sup>7</sup>EPO-TEK H21D.

<sup>8</sup>Kapton is an electrically isolating, UHV compatible polyimide tape developed by DuPont. The thickness of the wire made it less flexible, and one PZT wire broke, and was replaced with a 0.5 mm uninsulated wire.

the need for curing at 150 °C for 5 min–50 min. Additionally, the strength of the conductive glue is lower than the epoxy glue<sup>9</sup>. This is combined with the problem of the silver electrode coating of the PZT surface peeling off when the wires are stressed. This makes gluing and installing the PZTs and wires a very delicate job.

The mirror substrates are then mounted in their respective titanium plate on the end walls. The mirror substrates are cylindrical with a diameter of 3 mm and length 100 mm. The substrates are fastened using a clamping washer. This is only tightened enough for the mirrors to not slide freely. By tightening too much it is possible to get strain-induced birefringence, although this has not been observed with this cavity.

The other end wall has no PZTs. Instead, a combination of pushing and pulling screws allow for the angling of a titanium plate which holds the other mirror. Thus the mirror at the PZT end is not tiltable, while this mirror is adjustable for alignment purposes.

The cavity was aligned by first sending in light through the cavity mount without mirrors. The farthest mirror (PZT end) was then inserted and the reflected beam was overlapped with the incoming beam using the in-coupling mirrors of the beam. The other mirror (at the end with the alignment triangle) was then inserted and was aligned to obtain a good coupling of the light to the TEM<sub>00</sub> mode.

### 10.3.4 Alignment of cavity and trap

Before mounting the trap electrodes, it was necessary to perform a very precise alignment of the trap and cavity with respect to each other. The waist of the cavity is 37 μm, so it is necessary to align the trap such that the trap center is within this range of the cavity mode. The rough alignment was done with alignment rods (visible in figures 10.2 and 10.1), although this does not allow for a precise measure of the alignment.

For the fine alignment, two small alignment tools were developed, see figure 10.3. A small aluminum piece was machined with high precision ( $\sim 5 \mu\text{m}$ ). Steel rods were inserted into the holes in the MACOR mount intended for the electrode rods. The alignment tool was then placed on the rods, and the center of the trap was indicated with a set of crossing triangular grooves of roughly 75 μm width. The grooves were made with a custom built tool of High Speed Steel (HSS). At the intersection of these grooves, a hole was drilled through the piece, and platinum wires with diameter 25 μm were glued to the bottom of the grooves.

The alignment tool has been inspected in a Scanning Electron Microscope (SEM) to check its precision, see figure 10.3. First, the machining itself was inspected, which was correct to within the tolerance of 5 μm. Next, the grooves with the glued platinum wire were inspected. The offset was less than 8 μm.

The tool was used for aligning the trap with respect to the cavity. The alignment tool hung from the eventual position of the ZERODUR rods. Since the ZERODUR rods are fragile and we did not want to break them, we had some steel rods machined with the same diameter. With the

---

<sup>9</sup>EPO-TEK H74F.

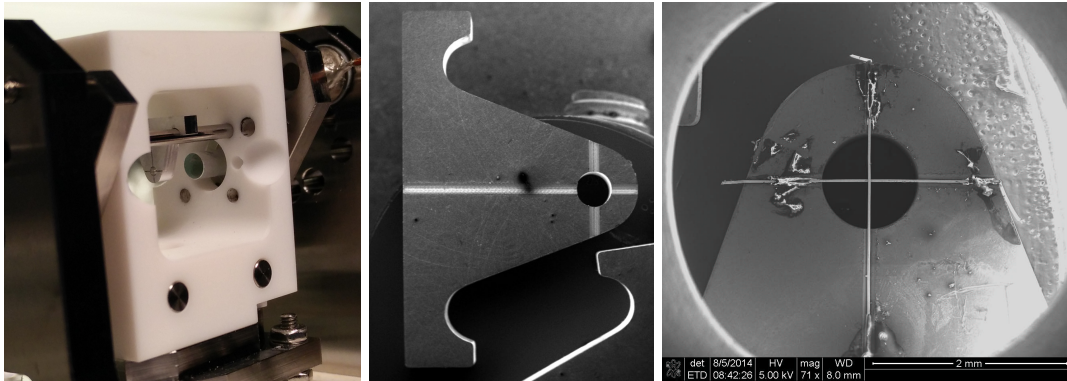


Figure 10.3: Left: Photo of alignment tool mounted in the MACOR housing on steel rods. Middle: Close-up of alignment tool taken with a Scanning Electron Microscope (SEM) before the platinum wires were glued. Right: Alignment tool with platinum wires.

steel rods inserted and the alignment tool hanging to indicate the center of the trap with the wire cross, it was possible to fine-tune the alignment.

Since 794 nm light was already mode-matched to the cavity, this light could be used for the alignment. Using a camera, the 794 nm light on the cross was detected, and by moving the trap vertically and horizontally the cross could be placed at the center of the cavity mode. An alternative alignment tool was constructed without a central hole and wires. This had the advantage that the smooth surface scattered light more uniformly than the round platinum wires.

By iteratively moving each end of the trap, measuring the displacement of the alignment tool from the cavity mode, and confirming that the light was still coupled into the cavity, it was possible to obtain a good overlap. A rough estimate of the alignment precision is  $\lesssim 100 \mu\text{m}$ . The main uncertainty is the determination of the position of the cavity mode on the mirrors (figure 10.8). The alignment tool itself was machined and assembled to high precision, but determining the position of the beam on the wire cross and moving the MACOR housing was difficult and ended up limiting the accuracy of the method.

### 10.3.5 Mounting trap electrodes

After ensuring the cavity-trap alignment, the trap electrodes were mounted on the ZERODUR rods. The electrodes are gold coated copper cylinders. The gold coating serves to passivate the surface with a high conductivity material. The electrodes are cylindrical and each have an M2-threaded through-hole perpendicular to the their symmetry axis. Using titanium screws and washers, the electrode wires where mounted to the electrodes by wrapping them around the stem of the screw in a loop. Mounting the electrodes was done by inserting the ZERODUR rod into the MACOR mount. The tolerances are very tight in this case due to geometric constrains, and the need for a mechanically stable trap. An electrode with a pre-mounted wire is then placed on the ZERODUR rod. A circular piece of Kapton foil, thickness 0.1 mm, is then slid onto the ZERODUR rod after

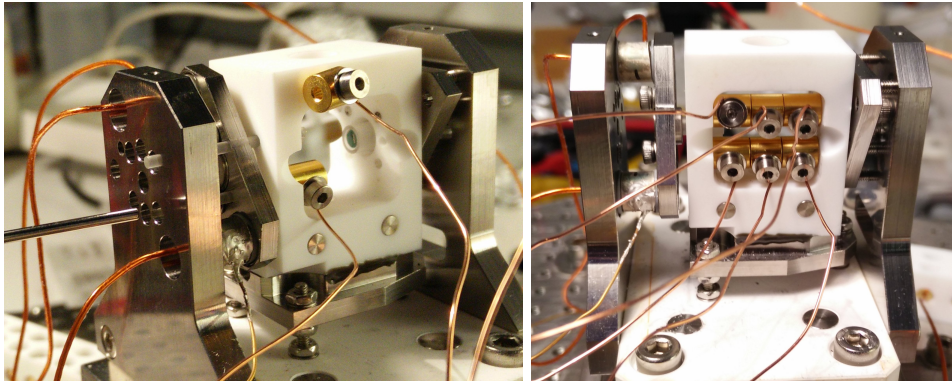


Figure 10.4: Left: Assembly of trap. ZERODUR rods have been partly inserted and one electrode has been mounted with another ready. Right: All electrodes on one side have been mounted.

the electrode. The Kapton foil is cut to have a slightly smaller radius than the electrode to not disturb the electrical fields generated by the electrodes. The next electrode is placed, followed by another piece of Kapton foil. The last electrode is mounted and the ZERODUR rod is pushed all the way into the MACOR piece. At this point it is not possible to remove the rod again without taking the mount apart and realigning both cavity and trap, since it is held in place by static friction and there is no way to push it out.

The electrode wires are made of 0.5 mm uninsulated copper. The wires are bent such that all laser beams can propagate freely and such that the wires do not touch each other and the chamber lid, which is only a few mm from the top of the trap. The electrode wires are gathered in ceramic terminals<sup>10</sup>, which are clamped to the vacuum chamber baseplate for stability. The stiffness of the electrode wires keeps the electrodes from rotating on the ZERODUR rods. From the ceramic terminals the wires are 1 mm Kapton insulated wires to avoid short circuits in case a wire shifts during bake or later. The wires are guided to a vacuum feedthrough (along with the wires for the PZTs of the cavity).

#### 10.4 Trap voltages supplies

The trap drive consists of an rf function-generator<sup>11</sup> which outputs a sine wave with an amplitude less than 100 mV. This is amplified<sup>12</sup> and sent to a resonant circuit that mixes the DC voltages with the rf.

The resonant circuit was designed by Erik Søndergaard from the local electronics department. A more detailed analysis of the schematic and workings of this circuit is presented in [133, p. 68]. A simplified version of the rf part of the circuit is shown in figure 10.5.

<sup>10</sup>Cu terminals are used for terminating the wire and continuing with a heavier gauge.

<sup>11</sup>Agilent 33210A.

<sup>12</sup>Electronic Navigation Industries, model 325LA rf Power Amplifier, 50 dB, 250 kHz–150 MHz, 25 W.

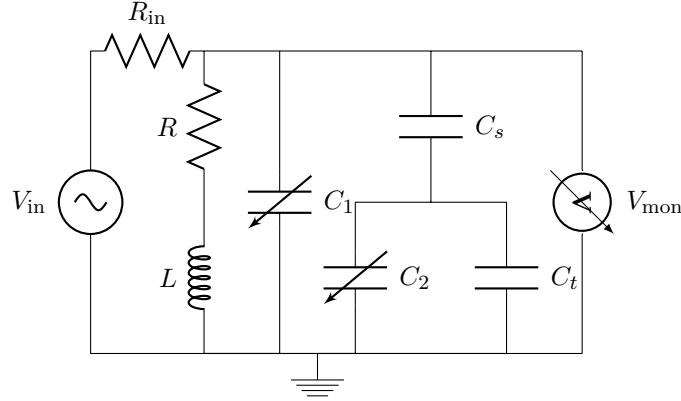


Figure 10.5: This simplified version of the mixer circuit shows that the circuit can be understood as a parallel RLC circuit.  $V_{\text{in}}$  is the input voltage,  $V_{\text{mon}}$  is the monitor voltage,  $L$  is the coil inductance, and  $C_t$  is the capacitance of the trap.

The resonant circuit can be modeled as an RLC-circuit, where the majority of the capacitance  $C$  is due to the trap electrodes and wires connecting them to the mixer. The inductance  $L$  is provided by a coil in the mixer, which also serves as the input for the rf by the mutual inductance with another coil. The resonance of such an RLC circuit is given by

$$\omega_0 = \frac{1}{\sqrt{LC}}. \quad (10.1)$$

Resonators are typically characterized by the quality factor  $Q$ , which is the ratio of the resonance frequency,  $\omega_0$ , to the Full Width Half Maximum (FWHM) of the resonance. The FWHM is defined as the difference between the two half-power frequencies,  $\Delta\omega = \omega_2 - \omega_1$ , on either side of the resonance. The quality factor for an RLC circuit can be expressed as

$$Q \equiv \frac{\omega_0}{\Delta\omega} = \frac{1}{R} \sqrt{\frac{L}{C}}, \quad (10.2)$$

where  $R$  is the effective resistance of the circuit. The resistance of the circuit is due to the resistance of the wires used and it should be minimized. From these equations it is clear that to obtain a high  $Q$  parameter, and thus a large gain from the circuit, it is necessary to keep the capacitance as low as possible while increasing the inductance. A high inductance will however lower the resonance frequency, which is undesirable since the rf frequency,  $\Omega_{\text{rf}}$ , determines the secular frequency for a given  $q$ -parameter, and for optimum driving of the trap  $\Omega_{\text{rf}} \approx \omega_0$ .

The electrode capacitances have been measured with and without feedthrough wires. The capacitance of the electrodes is mainly determined by their size and relative placement. Lower capacitance could be achieved by making the electrodes smaller, but this has other unwanted side-effects, since the whole trap would have to be made smaller in this case.

Figure 10.6 shows the resonance of the trap as the drive frequency is scanned. The ordinates are the monitor (1:100) output of the resonant circuit. The mixer has two monitors, which are

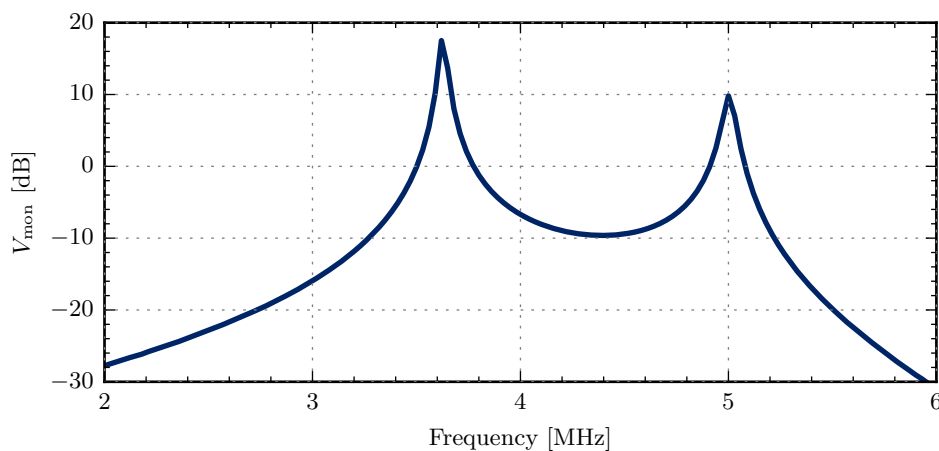


Figure 10.6: The resonance as measured on the mixer monitor output. The resonances are characteristic for coupled RLC circuits.

coupled  $180^\circ$  out of phase. Only one is shown here. The resonance is split into two peaks. The phase difference between the monitor signals at the first peak is  $180^\circ$ , while they are in phase at the second resonance. The reason for the split resonance is that the circuit is split into two RLC circuits with very similar resonance conditions and a coupling between them<sup>13</sup>.

## 10.5 794/397 nm laser system

In this section we introduce the laser systems used for injecting 794 nm and 397 nm light into the cavity. In this work we will primarily be using a commercial Tapered Amplifier diode laser system<sup>14</sup> with a custom-built doubling cavity to generate 397 nm light. This laser system is described in much more detail in [205, Ch. 7]. In our case the fundamental 794 nm light will also be used in the experiments, both for locking our experimental cavity and for generating a far off-resonant dipole trap, see section 6.

The master diode of the TA pro system generates about 50 mW of light at 794 nm. This light is split between several lines. One path is directed at a commercial wave-meter<sup>15</sup> and the frequency of the light is measured. Another part is directed to a double pass AOM setup, which can be used to lock the laser to a reference cavity<sup>16</sup>.

The remaining part of the light ( $\lesssim 40$  mW) is injected into the tapered amplifier. The tapered amplifier can deliver up to 1 W of light. This light is sent through two optical isolators to limit the effect of back-reflections and is then split between to lines.

<sup>13</sup>This is analogous to two coupled harmonic oscillators.

<sup>14</sup>Toptica TA pro 794.

<sup>15</sup>HighFinesse Ångstrom WS-U. See section 11.2.3.

<sup>16</sup>These reference cavities are described in [206].

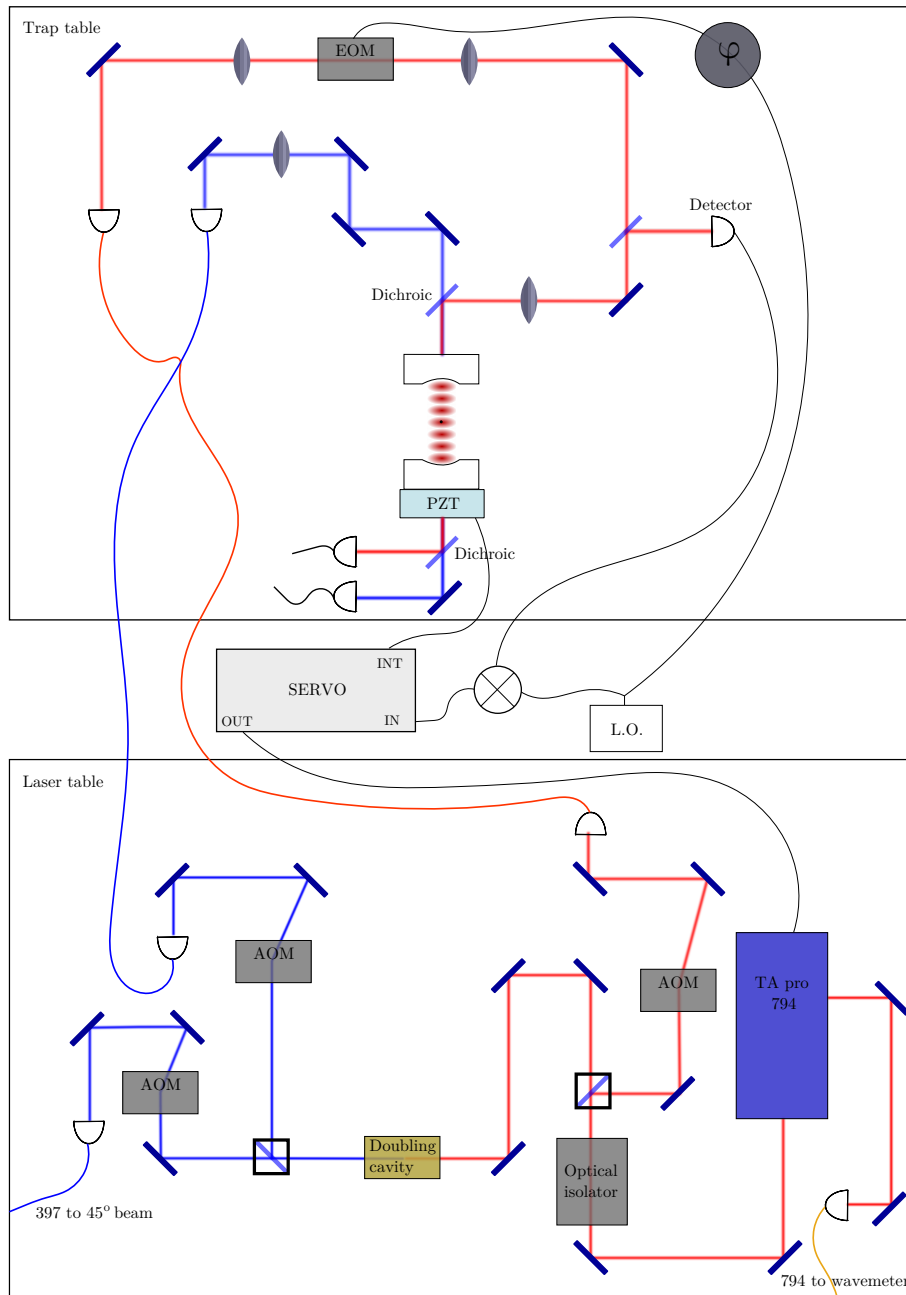


Figure 10.7: Laser systems used for cavity injection and locking circuit. 794 nm (red) light is generated by the TA pro laser and sent to the doubling cavity for generation of 397 nm (blue) light. The 397 nm light is divided between two lines. The light is frequency shifted by single pass AOM setups and fiber coupled to the trap table. The light is injected into the cavity and the transmitted light is detected. The 794 nm light is also frequency shifted by a single pass AOM setup and fiber coupled. This light is then phase-modulated by an EOM and injected into the cavity and the transmitted light is detected. The reflected light is detected, and the detection signal is mixed with the Local Oscillator (LO) of the EOM. The resulting error signal is sent to the servo amplifier. The output of the servo amplifier modulates the TA pro laser current. The integrated signal output from the servo amplifier is used to stabilize the cavity length by applying High Voltage to the cavity PZT.

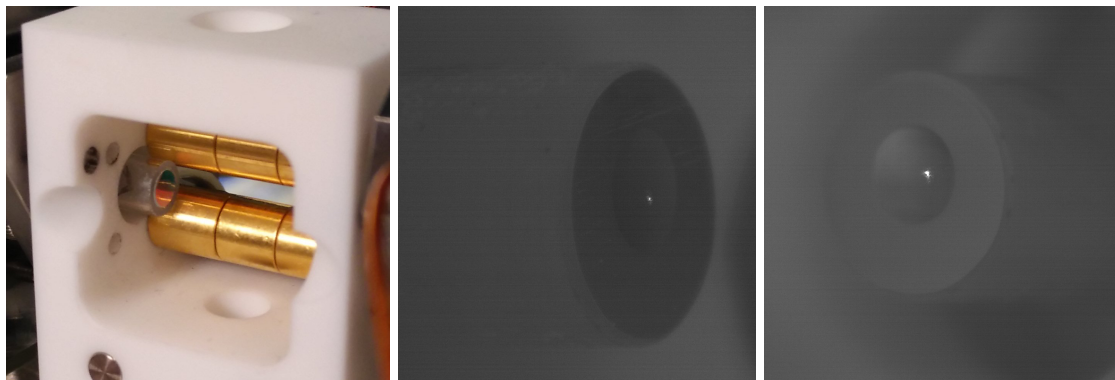


Figure 10.8: Left: Mirror substrate with quartz cap mounted. Half of the trap electrodes have been mounted. Middle/Right: Mirror substrates. In the center the curved part of the mirror is visible, the bright spot is the 794 nm laser light when its frequency is scanned across the cavity resonance.

One part is sent through a single pass AOM setup and then sent through a fiber to the experiment. The AOM setup is optimized for fast switching on and off, since it is used to do ringdown spectroscopy of the experimental cavity (see section 10.6.4).

The other part is sent to a doubling cavity system, which generates the 397 nm light needed for the experiment. The doubling cavity is in a bow-tie configuration, uses a PPKTP<sup>17</sup> crystal, and is stabilized via a Hänsch-Couillaud locking scheme [207]. Up to 60 mW of 397 nm light can be generated, although for stable generation over hours we typically operate at a 40 mW output level. For details on the doubling system see [205, Ch. 7].

The 397 nm light is also split into several paths and frequency shifted using AOMs. One beamline is coupled into a fiber after being blue-shifted by 270 MHz by a fast AOM<sup>18</sup>. An alternative beamline is blue-shifted by only 80 MHz<sup>19</sup>, fiber coupled, and sent to the experiment where it is delivered to the chamber at 45° to the trap axis.

The last beamline goes to a fiber-coupled pigtail AOM with a fixed frequency of 180 MHz. This AOM is described in more detail in section 12.4.1.

## 10.6 The cavity

### 10.6.1 Cavity mirrors

The integrated optical resonator of the Blue Cavity trap is a symmetric linear Fabry-Perot cavity; these cavities were discussed in section 5.2. The mirror substrates are shown in figure 10.8. The substrates are UV Fused silica with a refractive index of  $n = 1.454$  and a length of 10 mm. The mirror diameter is 3 mm, and the cavity facing surface is flat with a curved part in the center with

<sup>17</sup>Periodically poled potassium titanyl phosphate (PPKTP) is an optically nonlinear crystal often used for frequency doubling.

<sup>18</sup>Brimrose TEF-270-100, 270 MHz.

<sup>19</sup>Intra-Action corp AOM.

a diameter of 1.5 mm. The radius of curvature of the curved part of the mirrors is  $R = 25$  mm. The cavity length has been measured using a Vernier caliper to be  $L = (12.45 \pm 0.10)$  mm. This corresponds to cavity waists for the 397 nm and 794 nm light of, using eq. 5.6,  $w_{397} = 37 \mu\text{m}$  and  $w_{794} = 52 \mu\text{m}$ , respectively.

Both the flat and curved part of the cavity facing surfaces have been High Reflection (HR) coated. The outwards facing surfaces have been Anti-Reflection (AR) coated. Both coatings work at 390 nm–400 nm and 780 nm–800 nm. The wavelengths correspond to the  $S$  to  $P$  transitions in singly ionized calcium, see appendix A, as well as the double wavelength of these. This has several benefits. The Doppler cooling light at 397 nm is generated by doubling the 794 nm light from a Tapered Amplifier diode laser (see section 10.5), which means that by making the 794 nm light resonant with the cavity resonance, the 397 nm light can be simultaneously ensured. In theory this should be guaranteed, but due to the frequency shifting effects of the AOMs and the difference in effective length of the cavity, some work is required for this, see section 10.6.2. Using the 794 nm for locking the laser to the cavity has the advantage that the 794 nm light is far off-resonant with respect to all relevant transitions in calcium (and barium for that matter). It will thus not drive transitions in the ions and can be left on during experiments. Another benefit is the possibility of using the cavity enhancement for the 794 nm light to achieve a deep, far off-resonant optical lattice with a spatial period intrinsically matched to the wavelength of the interaction light. Optical potentials are discussed in sections 6 and 13.3.

The intensity transmission coefficients for 397 nm and 794 nm are  $T_{397} = 100$  ppm and  $T_{794} = 220$  ppm, respectively, according to the specifications and measurements from the company that performed the coating<sup>20</sup> as well as measurements performed in-house. This suggests theoretical, i.e. no-loss, finesses of

$$\mathcal{F}_{397} = \frac{2\pi}{2T_{397}} = 31400 \quad (10.3)$$

$$\mathcal{F}_{794} = \frac{2\pi}{2T_{794}} = 14300, \quad (10.4)$$

where we have used equation 5.17.

### 10.6.2 Simultaneous resonance

For injection of light into the cavity two beam lines have been set up, as shown in figure 10.7. The first is 794 nm light, which is shaped, and sent through an Electro-Optic Modulator (EOM) for locking purposes. The light is then matched to the cavity mode. The amount of input light available here can be very large ( $\gtrsim 100$  mW as required for future experiments with optical lattices. For locking purposes only a few  $\mu\text{W}$  are necessary.

The 397 nm beam is likewise shaped and matched to the cavity mode, and combined with the 794 nm beam before being injected into the cavity. For the 397 nm beam it is *essential* to be well matched to the cavity, and to use very low power to avoid that scattered light from the cavity

<sup>20</sup>Advanced Thin Films, Boulder (Colorado).

damages the image intensifier used to collect the fluorescence from the ions (see section 11.3.3), since this is very sensitive at this wavelength.

After the cavity, the light is split using a dichroic mirror, and each wavelength is detected separately using a commercial photodiode with a trans-impedance amplifier<sup>21</sup> (397 nm) and a commercial diode<sup>22</sup> (794 nm).

For a cavity of length of  $L$ , we have shown in chapter 5 that the resonance condition for the TEM<sub>00</sub> mode is

$$\omega_l = 2\pi q \frac{c}{2L} \quad \text{or} \quad \lambda = \frac{2L}{q}, \quad q \in \mathbb{N}. \quad (10.5)$$

Resonance between the cavity and a laser beam can then be ensured by changing either the length of the cavity (using the PZTs) or by changing the wavelength of the laser.

Since the 397 nm light is exactly doubled from the 794 nm light, they should in principle have simultaneous resonances, i.e. for any resonance wavelength of the 794 nm light,  $\lambda_{794} = 2L/q_{794}$ , we should have

$$\lambda_{397} = 2L/q_{397} = \frac{2L}{2q_{794}} = \frac{\lambda_{794}}{2}. \quad (10.6)$$

Unfortunately, the effective length of the cavity is different for the two wavelengths due to the optical coating. Thus, for e.g. the 794 nm light resonant with the cavity, the 397 nm light will need to be frequency shifted by about 2 GHz, or one could shift the 794 nm light by about 1 GHz, or a combination. In practice, the simultaneous resonance has been achieved by shifting the 794 nm light by  $-793$  MHz and the 397 nm light by  $+270$  MHz.

The difference in effective cavity length can be understood from the way the dielectric coating stack is constructed. The mirror substrates are UV-grade fused silica<sup>23</sup> upon which 52 alternating layers of SiO<sub>2</sub> and Ta<sub>2</sub>O<sub>5</sub> are deposited. The outermost layer is Ta<sub>2</sub>O<sub>5</sub>. The layer thicknesses vary such that for a beam coming from the air/vacuum side, the first 24 layers are reflective for 397 nm light while transmitting 794 nm. The next 28 layers are reflective for 794 nm light. The extra optical path length for the 794 nm light is then four times the optical path length of the first 24 layers, since the light has to traverse it twice per mirror. To estimate the effect of this requires detailed knowledge of the refractive indices of the dielectrics as a function of wavelength and layer thickness. By estimating the refractive indices from the bulk values and scaling with values obtained from the company that performed the optical coatings<sup>24</sup> we get an expected offset between the two resonances of 970 MHz for the 794 nm light. Our measurements indicate that the offset is closer to 928 MHz. This discrepancy can easily be explained from the uncertainty associated with determining the refractive indices. Here, we have scaled the refractive indices to obtain a reflectivity matching the measurements of the coatings at 794 nm<sup>25</sup>.

<sup>21</sup>Thorlabs PDA8A/M.

<sup>22</sup>Thorlabs Det10a/m.

<sup>23</sup>Fused silica or fused quartz is typically used where high transmission at UV wavelengths are required due to its high purity and thus low absorption.

<sup>24</sup>Advanced Thin Films, Boulder, Colorado.

<sup>25</sup>M. Gutierrez, private communication.

### 10.6.3 Locking the cavity/laser

For most experiments involving the cavity it is important to control the relative detuning between the laser and cavity frequencies,  $\Delta_c = \omega_l - \omega_c$ . This is typically done by locking the laser and cavity together. In practice, this means that either the laser frequency is controlled using a feedback loop to stay resonant with the cavity, or vice versa.

The scheme employed for stabilizing the laser frequency and cavity length is the Pound-Drever-Hall (PDH) technique; see [192] for a good introduction. Here, we will give a short presentation. The light from the laser is phase modulated using an Electro-Optic Modulator<sup>26</sup> (EOM). This phase modulation will generate sidebands, in the cavity transmission spectrum. The phase-modulated light is injected into the cavity, and the reflected light is sent to a detector. The detector signal is mixed with the same local oscillator that is driving the EOM. The output of the mixer will be the so-called error signal that is proportional to the laser-cavity detuning.

The error signal is then sent to a servo-controller which amplifies the signal according to a predefined transfer function. The servo output is used to control either the cavity length or the frequency of the laser.

There are advantages and disadvantages in both schemes. The cavity length can be tuned by several free spectral ranges (FSR) by changing the voltage applied to the piezoelectric transducers (PZT), which hold one of the mirrors. In this way the cavity can also be kept resonant with the laser. There is however some limitation to how fast the cavity length can be changed. The PZTs can in principle be operated at ultrasound frequencies, but due to the relatively large mass of the mirrors and mounts, the mechanical resonances will be lower than this. The PZTs can be damaged by driving them at their resonance frequency, and the phase delay increases around a resonance such that the feedback can be detrimental. Due to the mechanical resonance frequencies of the piezoelectric elements, we decided that a more sophisticated locking scheme was required.

By controlling the laser frequency instead of the cavity resonance frequency, a much larger bandwidth of the servo can be achieved. The laser frequency can be controlled in several ways, the simplest being to control the laser current. Other possibilities include frequency shifting with an Acousto-Optic Modulator (AOM) or an EOM. EOMs are cost-prohibitive and AOMs do not have the required tuning range and efficiency. Therefore, it was decided to use the current modulation.

Using the PDH technique while modulating the laser diode current, it was possible to lock the laser to the cavity with a bandwidth of up to 100 kHz. We are using the 794 nm beam for locking, since this will not disturb the atoms. In practice, it is not desirable to move the frequency of the laser very far since the laser is also used for Doppler cooling, and therefore it needs to be tuned close to the atomic resonance of the  $^{40}\text{Ca}^+$  ion. Consequently, a more complicated locking scheme was developed, where the laser is locked to the cavity on fast timescales, and the cavity is locked to the laser on slow timescales. This is done by feeding the integrated part of the servo output back to the cavity PZTs on a timescale  $\sim 10$  Hz. In this way, the DC part of the current feedback will be zero. The quality of the locking can be estimated from the ratio of the standard deviation,

<sup>26</sup>This is a Pockels cell, i.e. a crystal that has a voltage dependent phase delay.

$\sigma_P$ , to the mean,  $P$ , of the cavity transmission signal, which has been measured to be  $\frac{\sigma_P}{P} \lesssim 2\%$ . The limiting factor seems to be electronic resonances of either the laser current supply or the servo box. We believe we can improve on this by employing custom filters in the servo-loop.

Finally, the laser can be tuned by the voltage applied to PZTs of the ECDL master diode of the TA pro laser, see section 10.5. The PZTs can be controlled by a feedback loop from the wavemeter (sec. 11.2.3) so that the laser can be accurately tuned to the atomic resonance.

From the laser, up to about 1 W of power is available, but taking into account the frequency shifting and fiber coupling, we have achieved locking the 794 nm light to the cavity with a maximum of 165 mW of input power, or  $\sim 500$  W in the cavity.

#### 10.6.4 Measuring the finesse and linewidth

The mirrors were coated by AT Films, and their transmission has been measured to be  $T = 100$  ppm at 397 nm and  $T = 200$  ppm at 794 nm. Losses around 100 ppm at 397 nm and 10-20 ppm at 794 nm are expected when the mirrors are clean.

The finesse is a critical characteristic of a cavity, as described in section 5.2. There are several ways to measure the finesse. The simplest is to scan the cavity length (or laser frequency) and look at the transmission of the cavity. By comparing the width of the spectrum around a resonance with the FSR one gets the finesse directly. Unfortunately, the response of a PZT is typically not very linear when scanning over large ranges, which makes the measurement imprecise. Scanning the laser is a possibility, but using an AOM is not possible, since the FSR is  $(12.04 \pm 0.10)$  GHz, which is more than the range of an AOM. Additionally, the linewidth of the laser can also contribute to the measured linewidth of the cavity.

By measuring the cavity length precisely using a Vernier caliper ( $L = (12.45 \pm 0.10)$  mm), and thus the FSR, it is possible to obtain a better estimate of the finesse from a measurement of the linewidth. Using an EOM, to generate sidebands in the cavity spectrum will generate a scale, since the EOM modulation frequency is well-known. This scheme avoids the problem of the non-linearity of the PZT, since it can be assumed linear for short ranges. Figure 10.9 show a cavity spectrum with applied sidebands. Using this method, a finesse of  $(1.4 \pm 0.2) \times 10^4$  for 794 nm light has been measured, and  $(1.1 \pm 0.3) \times 10^4$  for 397 nm.

Alternatively, the finesse can also be measured using so-called ringdown spectroscopy [208]. Ringdown spectroscopy is performed by injecting light into the cavity, and then switching off the input light quickly. By measuring and fitting the cavity transmission decay (see figure 10.9), it is possible to determine the energy decay rate,  $2\kappa$ . See section 5.2 for details on the dynamics of the cavity. This measurement has the advantage of having fewer systematic error sources. It does, however, require a fast shuttering mechanism for the light. Here, single-pass AOM setups are used, with decay times  $\tau = 12$  ns for 397 nm and 40 ns for 794 nm, respectively.

Once the cavity is installed in a vacuum chamber and has been baked-out, the finesse is measured again. This is done to determine whether the bake-out and vacuum has had any detrimental effects on the mirrors. It has been noted that mirrors coated for high reflectance in the blue parts

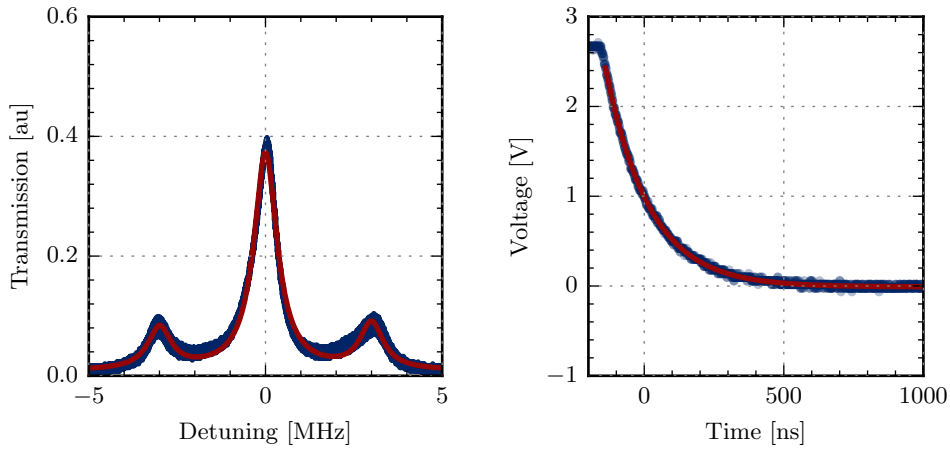


Figure 10.9: **Left:** Cavity spectrum at 794 nm with sidebands at 3 MHz. The result of a fit of this trace corresponds to  $\kappa = 2\pi \cdot 400$  kHz and finesse  $\mathcal{F}_{794} = (1.4 \pm 0.2) \times 10^4$ . **Right:** An example of ringdown a measurement of the cavity finesse at 794 nm. In this case fitting to an exponential gives a decay time of  $\tau = (156.0 \pm 0.3)$  ns, which corresponds to a finesse of  $\mathcal{F}_{794} = 11\,800 \pm 100$ .

of the spectrum are likely to deteriorate over time [209]. This is hypothesized to be caused by surface oxygen depletion in the outermost layer of tantalum oxide  $\text{Ta}_2\text{O}_5$  of some optical coatings. The optical coating of the mirrors used in Blue Cavity trap is a dielectric stack of layers alternating between silicon oxide  $\text{SiO}_2$  and  $\text{Ta}_2\text{O}_5$ , with the air/vacuum facing layer being  $\text{Ta}_2\text{O}_5$ . This is unfortunate, since a layer of  $\text{SiO}_2$  would not have shown the same depletion. In [209] it is discussed how even a layer of a few nm is enough to passivate the surface of the optical coating and prevent oxygen depletion over time. For existing setups it is also discussed how the loss can be reversed by exposing the mirrors to atmospheric pressure oxygen. Simultaneous illumination with near UV light will increase the rate of recovery.

The finesse measured using ringdown spectroscopy after the first and second bake-outs<sup>27</sup> were somewhat lower than measurements performed prior to bake-out. There are several possible reasons why this could happen. As discussed above, oxygen depletion of the outer-most layer of  $\text{Ta}_2\text{O}_5$  could lead to increased losses. This effect is usually only significant over longer periods of time, but increased temperature typically increases the oxygen depletion rate [209]. Another possibility is that the mirrors were contaminated during the re-opening of the chamber, but this was tested for by regularly measuring the finesse while baking. The biggest drop in finesse happened close to when the sublimation pump, ion pump, and ion gauge were degassed, so it is possible that contaminants from these were released into the chamber and contaminated the mirror surface. However, this also seems unlikely, since the mean free path is rather large, so that contaminants will not scatter before hitting a surface. One would therefore expect that contaminants would

<sup>27</sup>Two bake-outs were performed due to a short-circuit, which necessitated a re-opening of the chamber.

adsorb to other surfaces in the chamber before reaching the mirrors. While the mirrors were exposed to air for months, there did not seem to be any appreciable increase in losses. Previously, the increased losses happened at times when other work was performed around the mirrors, thus indicating e.g. dust as the cause.

Results from the post bake-out ringdown measurements suggest that the present finesses are  $\mathcal{F}_{397} = 7200$  for 397 nm light, and  $\mathcal{F}_{794} = 12000$  for 794 nm light.

## Chapter 11

# Experimental setup for the Blue Cavity trap

In this chapter the experimental setup for the Blue Cavity trap described in the previous section will be outlined.

Figure 11.1 shows the layout of the vacuum chamber. Shown here is the baseplate of the vacuum chamber with equipment mounted. Not shown are the ion gauges, sublimation pump, and ion pump as well as various valves. In the figure laser beams are labeled and shown as colored lines. In the following the other parts will be described.

### 11.1 Ionization

#### 11.1.1 Two-photon ionization scheme

Several schemes exist for ionizing calcium. In the past, electron bombardment of neutral atomic beams was extensively used, but today the technique of resonance enhanced two-photon ionization has become popular. For calcium, this was first demonstrated using the 272 nm based scheme described below [210]. Alternative schemes have been demonstrated [211], see figure 11.2b), where, light fields at 390 nm and 423 nm are needed instead.

The common advantages of these schemes is the resonance enhancement of optically driving a dipole transition. Since the isotope shifts of the transitions are of the order of GHz<sup>1</sup> [212], it is possible to selectively ionize only a specific isotope. For this to hold generally, the Doppler shift has to be minimized by using the crossed laser/atom beam technique, so that the Doppler shift only affects directions orthogonal to the ionization laser. Using this technique, large pure ion Coulomb crystals have been produced [211][212].

We drive the  $4s^{21}S_0$ - $4s5p^1P_1$  transition of calcium, see figure 11.2a). After being excited to the  $^1P_1$  state, the atoms can either decay to the  $4s3d^1D_2$  state, or absorb another 272 nm photon

---

<sup>1</sup>See appendix A for these shifts.

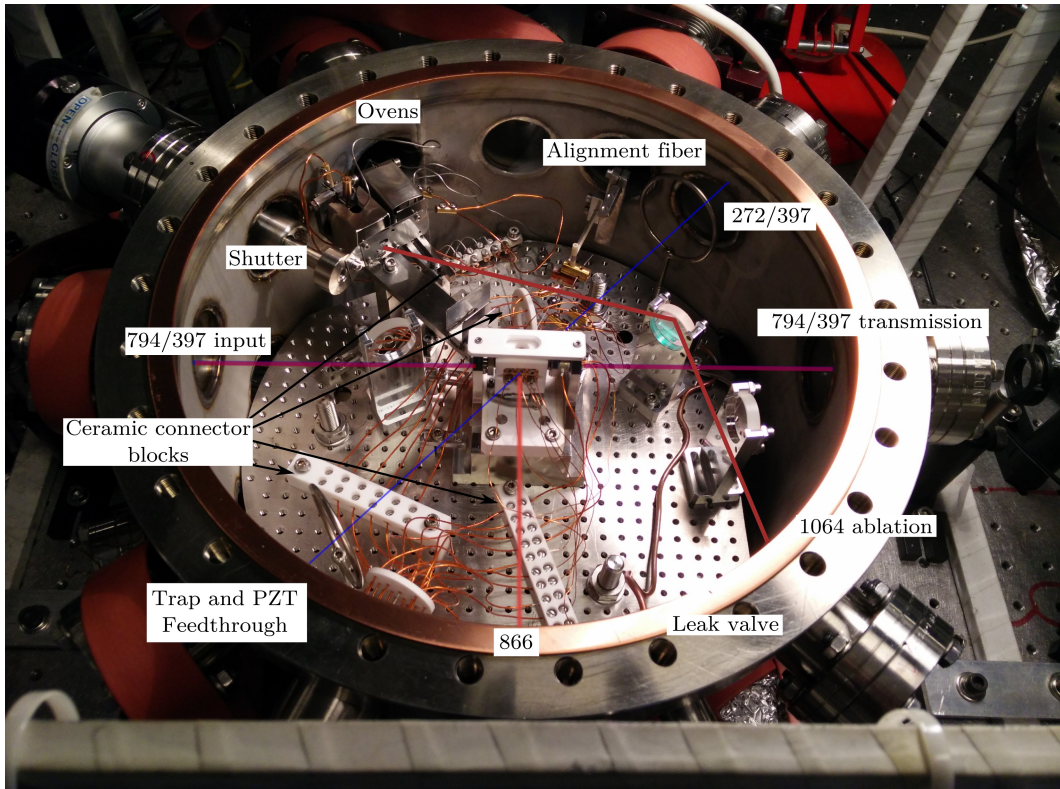


Figure 11.1: Sideview of the vacuum chamber. Laser beams are indicated by colored lines. The inner diameter of the chamber is 20 cm.

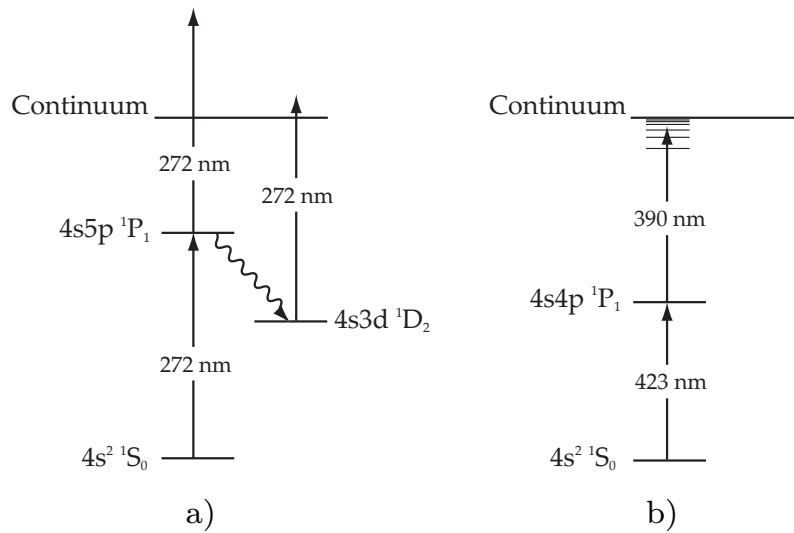


Figure 11.2: a) Two photon ionization scheme for calcium used in this work. The lifetime of the  $4s5p \ ^1P_1$  state is 17 ns–60 ns and the lifetime of  $4s3d \ ^1D_2$  is 18 ms. b) Alternative ionization scheme for calcium.

which is energetic enough to excite to a continuum state. The 272 nm is also energetic enough to ionize the atom from the  $4s3d^1D_2$  state.

Due to the high energy per photon of the 272 nm, charging of dielectrics in the chamber is a risk. This means that the 272 nm laser beam should be carefully steered so that it never hits any part of the trap or the trap surroundings. The 397 nm beam co-propagating with the 272 nm beam is used as a guide. By aligning this first (so that it hits the alignment fiber) and then using a flip-mirror to align the 272 nm beam with this, the 272 nm beam never hits anything inside the chamber. If the beam were to hit parts of the trap, charging could occur, which means that electrons are stripped from the materials, leading to stray potentials. This would influence the equilibrium position of trapped ions, thus making it harder, perhaps impossible, to trap ions, until this charge has diffused.

The diffusion of the charge can take from minutes to hours, and even if trapping is successful, drift will still be an issue since the charge will gradually shift the ion positions.

### 11.1.2 Oven

Two ovens have been placed in the chamber along with two ablation targets. The ovens are of identical design, but the content in one is calcium while the other is loaded with barium<sup>2</sup>.

The oven design is simple. A crucible has been machined from carbon and loaded with the atomic element of choice. A tungsten wire is wound around the crucible and connected with copper wires<sup>3</sup> to a vacuum feedthrough and a current supply.

When a current is supplied the tungsten wire will heat the crucible, and at a point below the melting temperature the vapor pressure of the calcium or barium will be high enough that an atomic beam will emanate from a small hole in the crucible<sup>4</sup>. The atomic beam will spread out from the hole so a steel housing is placed such that the atomic beam is directed at skimmers, see figure 11.3.

As mentioned above, there are two ovens which share a single set of skimmers. The skimmers are a set of three steel plates with small slits cut into them to skim the beam and make a very narrow beam. The narrowness of the beam is essential to avoid depositing the atoms on the electrodes or, in our case even more critically, the cavity mirrors.

The ovens and skimmers were aligned using a light bulb<sup>5</sup> which was inserted into the back of the crucibles before loading them. The light from the bulb will spread out like the atomic beam and the light was aligned through the trap, using a small camera and a piece of paper placed at the trap center. The piece of paper is inserted through the top of the trap and is placed with less than 1 mm accuracy in the middle of the hole used for imaging. A camera is then used to image the

---

<sup>2</sup>Calcium and barium purchased from Sigma-Aldrich. Barium was bought as: "Barium beads, 0.5 mm–2.0 mm" and "Barium, rods ~ 2 cm diameter, 99+% metals ba". Calcium was bought as: "Calcium, granules, Ca. 6 Mesh, 99%" and "Calcium, drehsphaene, 99%."

<sup>3</sup>Copper wires going to the feedthrough are  $\varnothing 1$  mm.

<sup>4</sup>The vapor pressure of calcium is  $P = 3.44 \times 10^{-5}$  mbar at 700 K = 427 °C [213] and the melting point is 842 °C.

<sup>5</sup>Incandescent light bulb from a Maglite flashlight.

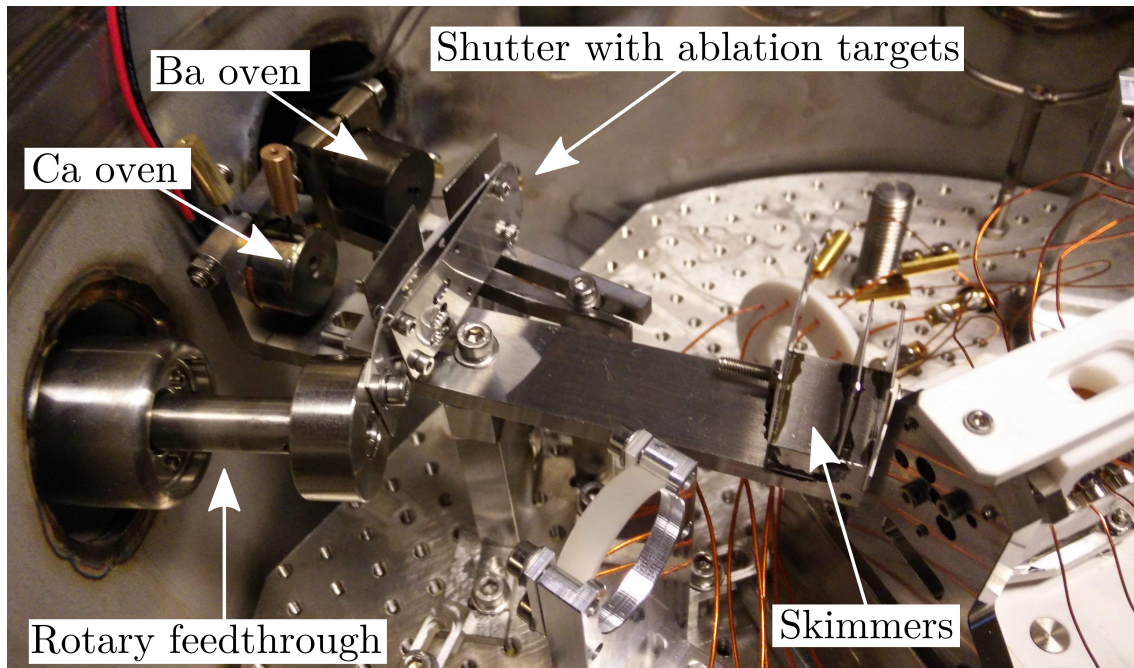


Figure 11.3: The ovens are shown here without their housing. The top oven is loaded with barium, the lower oven is loaded with calcium. The shutter is in front of the ovens. Two ablation targets are placed in the shutter at the corresponding positions of the ovens so that atoms from the ovens and ablation targets can use the same skimmers. The skimmers are visible as three steel plates on the right in the picture.

light from the oven onto the paper. By using image analysis software<sup>6</sup> to determine the distances to the electrodes, the ovens and skimmers were aligned within a few hundred micrometers of the trap center. For a more detailed discussion of the characteristics of an effusive oven beam as used here see [143, p. 46].

Due to the size of the ovens the warming and cooling takes several tens of minutes. In addition, the heat from the oven will heat the surrounding metal parts of the chamber base plate. This will ultimately influence e.g. the cavity length and it is thus not desirable to change the oven temperature while performing experiments. Instead, the ovens are kept on while doing experiments and an oven shutter has been placed in front of the ovens to physically block the atomic beam, see figure 11.3 and 11.4. The shutter can be manipulated by a rotary feedthrough.

To monitor the temperature of the ovens, thermocouples have been inserted into holes in the crucible. This ensures a measurement as close as possible to the atoms themselves. A third thermocouple is monitoring the temperature of the chamber base plate roughly 10 cm from the ovens.

Specially machined corner pieces were pushed against the base of the oven mounts and clamped to the base plates. These serve as a reproducible corners so that the ovens could be removed and

<sup>6</sup>Imagej, <http://imagej.nih.gov/ij/>.

replaced at the same position. This means that the alignment is only done once.

The ovens were removed and put in an argon atmosphere, where they were loaded with barium and calcium. The argon atmosphere is necessary since calcium oxidizes quickly and barium will react with both oxygen and nitrogen within a few minutes in atmospheric air. This also makes it a challenge to install the ovens in the vacuum chamber since the whole chamber cannot be kept in a perfect argon atmosphere while the main chamber lid is removed.

### 11.1.3 272 nm laser light for ionization of calcium

As discussed in section 11.1.1, laser light at 272 nm is required for the photo-ionization scheme for calcium used in this work. Unfortunately, lasers at UV wavelengths are nontrivial to construct, as there are no simple laser diodes available. Instead, most systems rely on one or more doubling stages. The system used in this work consists of a fiber laser (1088 nm), frequency doubled twice to generate 272 nm light [214].

The pump light is generated by an ytterbium-doped distributed-feedback fiber laser<sup>7</sup> at 1088 nm, which typically delivers 1 W through a fiber. This light is sent to a doubling cavity with a LiNbO<sub>3</sub> crystal and is frequency doubled to 544 nm<sup>8</sup>. The power output of this cavity is in the range of 300 mW to 800 mW [214]. Some portion of this light is directed at a single-mode fiber and coupled to the wavemeter (see section 11.2.3).

The remaining 544 nm light is directed at a second doubling cavity which generates 272 nm light with an efficiency of originally 14 % [214]<sup>9</sup>. After passing through a pinhole of 30  $\mu\text{m}$ , approximately 8 mW of 272 nm light is available for experiments.

Light at 272 nm is not efficiently transported in commonly available commercial fibers<sup>10</sup>. Instead, a beam distribution setup with motorized flip-mounted mirrors<sup>11</sup> is used to send 272 nm light to the various experiments of the lab. The efficiency of this beam path going to our experiment is about 68 %. The beam is expanded to about 2 mm at the trap table.

It is combined with the 397 nm beam at 45° to the trap axis and sent through the trap. About 1 mW–5 mW is available for ionization with a beam radius at the center of the trap of  $w = 150 \mu\text{m}$ .

The frequency reading of the wavemeter is used in a feedback loop to control a PZT in the fiber laser to lock the output wavelength. Using this PZT the 544 nm light can be tuned (tuning range is  $\sim 1\text{GHz}$ ), or locked such that the doubled light at 272 nm is within a few MHz of the resonance of the  $4s^2\ ^1S_0$  to  $4s5p\ ^1P_1$  of the neutral calcium atom.

### 11.1.4 Ablation setup

Using the method of [218] it is possible to photo-ionize atoms ablated from targets. Ablation targets have been embedded between two steel plates of the shutter with holes milled for laser access, see

<sup>7</sup>Koheras Boostik.

<sup>8</sup>This cavity is locked using the Pound-Drever-Hall (PDH) technique [215].

<sup>9</sup>The conversion efficiency has declined since installation of this system and is currently less than 5 %.

<sup>10</sup>There is ongoing efforts to improve this situation [216][217].

<sup>11</sup>Thorlabs MFF101/M.

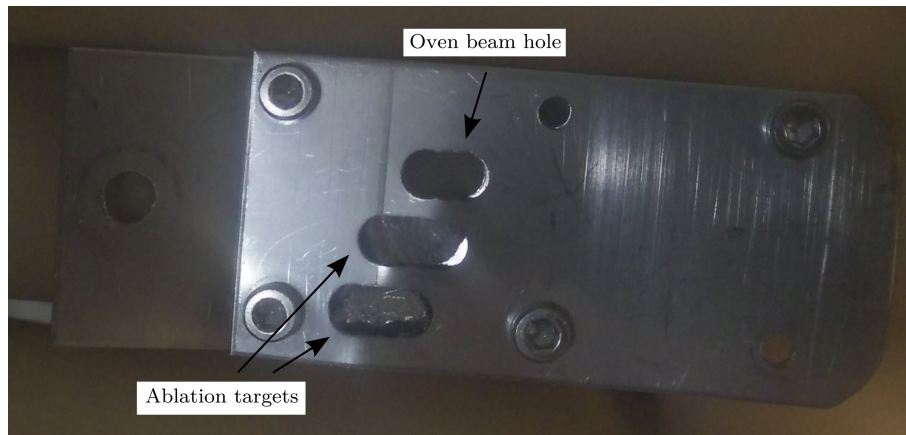


Figure 11.4: The oven shutter with ablation targets.

figure 11.4. The ablation targets are larger pieces of barium and calcium with dimensions  $\sim 1\text{--}4$  mm. By adjusting the shutter it is possible to open either the barium oven, the calcium oven, or to expose either the calcium or barium ablation target. A 1064 nm beamline has been setup to enable ablation of either target. Mirrors mounted on PZTs can be used to raster scan the beam position across the ablation targets.

A Q-switched laser with a repetition rate of 25 kHz is directed at the ablation targets. In [218] they achieve loading rates as high as 125 ions per second using a fluence of  $240 \text{ mJ cm}^{-2}$ . Ablation loading has not yet been attempted with the Blue Cavity trap.

## 11.2 Lasers and beam lines

Figure 11.1 shows the layout inside the chamber. For scale the white, ceramic crossbar on the trap is 56 mm long. Laser beams are indicated by colored lines. 397 nm and 794 nm lines are injected into the cavity and the transmitted and reflected light can be detected, as discussed in section 10.5. 866 nm light for repumping is incident perpendicular to the trap axis. Intra-chamber mirrors can be used to direct repumper or Doppler cooling light at an angle close to the trap axis. This light is then reflected on the flat part of the cavity mirrors, see figure 11.5. The edge of the cavity mirrors are not curved, but are polished to reflect the cooling beams which then cross the cavity axis at a small angle ( $12^\circ$ ), bouncing it twice in the cavity, see figure 10.8.

### 11.2.1 397 nm beam at 45 degrees

As shown in figure 11.1 we send in 397 nm light for Doppler cooling at an angle of  $45^\circ$  with the trap axis. Cooling the ions with this beams will be sensitive to micromotion. The advantage of this beam is that it has components on all normal modes of the trap. In addition the beam is shaped into an elliptical Gaussian beam with the wide side being horizontal. This enables cooling

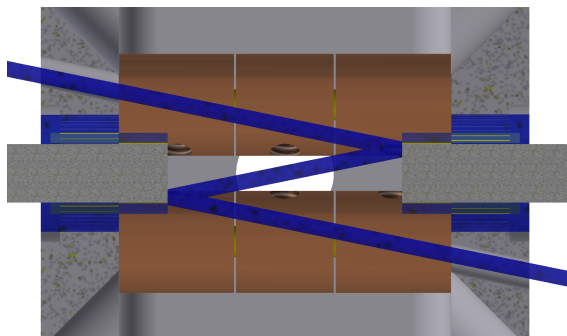


Figure 11.5: Bouncing beams principle. It is possible to inject light (blue line) through holes in the MACOR housing close to the trap axis ( $11.5^\circ$ ). This light can then bounce off the flat part of the cavity mirrors and exit on the opposite side.

of wide crystals and is less sensitive to the precise alignment of the beam. The beam width is adjustable using dovetail rails, typically the radius waists have been  $(w_H, w_V) = (560 \mu\text{m}, 220 \mu\text{m})$  for horizontal (H) and vertical (V) respectively. The polarization of this beam is horizontal (i.e. perpendicular to the B-field). As shown in figure 11.1 this beam is combined with the ionization beam at 272 nm and aligned through the trap. The power available for this beam is up to several mW. The saturation intensity for the  $S_{1/2}$  to  $P_{1/2}$  transition is  $I_{\text{sat}} = (45.07 \pm 0.31) \text{ mW cm}^{-2}$ . The intensity at the beam center is  $I_0 = \frac{2P}{\pi w_x w_y} \sim 500 \text{ mW cm}^{-2}$  or  $s \sim 8$  when driving  $\sigma$  transitions<sup>12</sup>.

Great care has to be taken in this alignment since the lifetime of the image intensifier<sup>13</sup> is very dependent on the total amount of light absorbed over time. The disadvantage of this beam is that it scatters relatively more light onto the image intensifier which will wear it down over time. It will also make the signal to noise ratio of the fluorescence detection worse, thus making it harder to detect the trapped ions.

### 11.2.2 IR diode lasers

For wavelengths between 810 nm and 880 nm laser diodes are easily available. This covers the  $D$  to  $P$  transitions in calcium at 850, 854, and 866 nm. For driving these transitions a number of External Cavity Diode Laser (ECDL) systems were available.

For the experiments reported here an ECDL at 866 nm in a single mode (linewidth 100 to 200 kHz) is used. The laser frequency is stabilized by locking to a commercial wavemeter (see section 11.2.3). A typical maximum of 10 mW shared between two experiments is available. Some

<sup>12</sup>To take into account the Zeeman magnetic substructure of the transition it is enough to replace the saturation intensity  $I_{\text{sat}}$  by  $I_{\text{sat}}/C_{CG}^2$ , where  $C_{CG}$  are the Clebsch-Gordan coefficients of the transition.  $C_{CG}$  is  $\sqrt{1/3}$  for  $\pi$ -transitions and  $\sqrt{2/3}$  for  $\sigma$ -transitions between the  $S_{1/2}$  and  $P_{1/2}$  states.

<sup>13</sup>See section 11.3.3.

of the light from this laser goes through a single pass AOM setup before being fiber coupled and sent to the trap table.

At the experiment this light is used to repump population from the  $D_{3/2}$  state. The beam typically has 2 mW power available (and can be tuned in power and frequency). Its polarization is horizontal, which, combined with a vertical B-field, is used to destabilize dark states [177]. The beam is sent in perpendicular to the trap axis and has a radius waist of  $w = 700 \mu\text{m}$  at the trap center.

### 11.2.3 Wavemeter

For precise measurements of the wavelength/frequency of generated laser light, a HighFinesse Wavemeter<sup>14</sup> is available. This wavemeter can measure laser wavelengths from 350-1100 nm, thus covering most of the required range for our experiments. In the case of 272 nm, the measurements are actually performed before the last doubling step on the 544 nm light. The precision of the wavemeter on short time scales is roughly 1 MHz and on longer time scales the wavemeter can be calibrated with a temperature stabilized He-Ne laser<sup>15</sup>.

In addition to measuring the frequency of multiple lasers simultaneously the wavemeter is also used as a laser control. A Proportional-Integral-Derivative (PID) controller card enables feedback to tuning inputs on the lasers, so that the lasers can be stabilized within a few MHz of the desired frequencies.

### 11.2.4 Alignment fiber

Locating the center of the trap can be practically difficult. To do this in a reproducible manner, an alignment fiber has been constructed. A piece of fiber was cleanly cleaved from a spool of fiber. The fiber is coated with a thin supporting rubber coating. This was removed by soaking the fiber piece in sulfuric acid on a hot plate until the coating came off. The pieces were rinsed in water, ethanol, and finally isopropanol.

The fiber pieces were inspected with a microscope and those with the cleanest possible cleaves were picked. The width of the fiber was confirmed to be  $125 \mu\text{m}$ . The fiber was then glued onto a linear feed-through which can move many centimeters into and out of the trap and for which sideways alignment is possible.

The fiber and mount was installed in the chamber and the fiber was slowly inserted between the electrodes. A camera placed above the chamber was aligned with the center of the electrodes. The fiber tip was then adjusted until it was at the center of the trap as confirmed by the camera. A camera from the side ( $90^\circ$  to cavity axis) was used to confirm the height of the fiber.

The alignment fiber can thus be used for focusing the imaging system and for aligning laser beams through the trap center.

---

<sup>14</sup>HighFinesse Ångstrom WS-U.

<sup>15</sup>Also available for frequency reference is a frequency comb and a ULE cavity [219, Ch. 9].

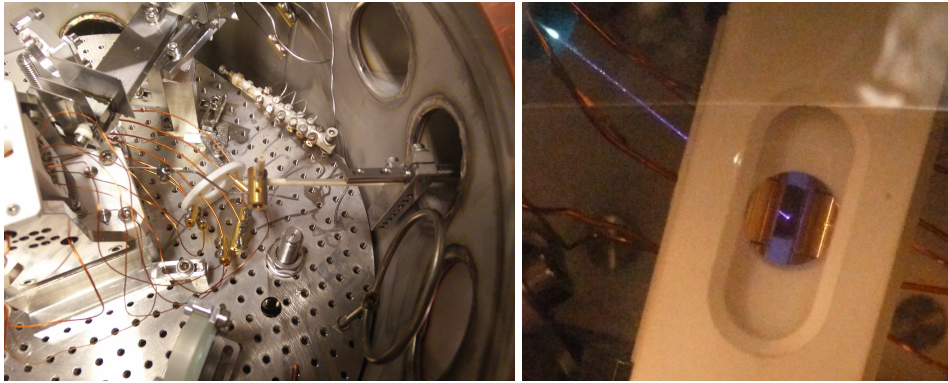


Figure 11.6: The alignment fiber: On the left the fiber mount is in the center and the fiber is (barely) visible near the trap. On the right the alignment fiber is inserted into the trap area and is being illuminated by the 397 nm laser.

### 11.3 Bakeout, magnetic field and imaging

#### 11.3.1 Vacuum system and UHV bake

The main cause of ion loss in a linear Paul trap is collision with background gases [160, Sec. 4.1.9]. Therefore very high vacuum is required for the stable working of the trap. Pressures below  $10 \times 10^{-9}$  mbar are usually called Ultra High Vacuum (UHV). The requirement of UHV restricts the available materials that can be used inside the vacuum chamber. Many materials will have vapor pressures higher than the target UHV pressure. These materials will keep outgassing if placed in UHV and will thus limit the final pressures possible. Even an ordinary fingerprint will contain greases and oils from the skin that can out-gas significantly and can spoil a good vacuum; therefore all handling of UHV parts is done wearing latex gloves. Materials used for the construction of the trap and otherwise in the chamber have to be chosen carefully; vacuum chambers are typically constructed from specially treated stainless steel. The Blue Cavity trap is machined from titanium, copper and various ceramics that are all vacuum compatible. The glue used also has low outgassing rates, while solder is typically avoided due to residual flux. Kapton is used for insulating wires.

All components are washed after machining to remove oils and grease. They are then sonicated<sup>16</sup> for 10 minutes in ethanol followed by sonication in isopropanol<sup>17</sup> for 10 minutes.

After installing the trap, ovens, and all the other equipment in the vacuum chamber the lid is put on and sealed. A valve on the side of the chamber is then opened and a pumping station is connected. The pumping station has a roughing pump that will pump down from atmospheric pressure. Once the pressure is low enough, a turbomolecular pump will start. In less than an hour

<sup>16</sup>Sonication is a cleaning method that involves soaking a part in a solvent while exposing it to ultra sound. The ultra sound will exert large forces on contaminants, thus cleaning the part.

<sup>17</sup>Also 2-propanol or isopropyl alcohol.

the pressure can go from atmospheric pressure ( $1 \times 10^3$  mbar) to  $\sim 1 \times 10^{-7}$  mBar.

Once the pressure has stabilized at  $\sim 1 \times 10^{-7}$  mBar a bake-out is performed. Since all parts have been cleaned as described above, most parts should not have any significant contaminants. The exception is water vapor from the air that adsorbs on the surface of all the parts. This water vapor will slowly evaporate, but the rate is very low so the pressure will stay high. The pressure will be a steady state given by the pump capacity and the total outgassing rate of all the parts in the chamber.

By heating up all the surfaces of the chamber the outgassing can be dramatically increased such that the remaining water vapor can be pumped out in a few days. The higher the temperature, the faster the evaporation and the better the final pressure achieved, but many components of the chamber and trap cannot handle high temperatures. In our case the main limiting factor is the vacuum viewports, the windows through which laser beams are directed. The viewports are rated for  $150^\circ\text{C}$  so this is the temperature of the bake-out.

The whole chamber is wrapped in heatbands (flexible resistive heating elements) and thermocouples are added in many places around the chamber to monitor the temperature. The heatbands are controlled by a bang-bang control circuit, so that the chamber can be slowly and uniformly heated to  $150^\circ\text{C}$  in about a day. While baking, the pressure will first increase due to increased evaporation, but as the evaporation decays so will the pressure. After baking for a few days the pressure will stabilize again and the temperature will be lowered.

The chamber also contains a titanium sublimation pump which consists of a titanium filament which is heated by sending a large current through it. Titanium will evaporate and coat the inside of the sublimation pump. Titanium is very reactive and residual gases will react with the thin film of deposited titanium. By firing the sublimation pump many reactive gases can be pumped effectively.

Finally an ion pump is used. The working principle of the ion pump is the same as a Penning gauge or trap. A filament discharges electrons that interact with residual gases, thus ionizing them. The ions are accelerated into a titanium surface. When the ion pump is turned on, the pressure will decrease further. At this point the chamber valve is closed and the turbomolecular pump and roughing pump are disconnected. Otherwise the ion pump would simply be pumping against the turbomolecular pump.

The chamber is equipped with an ion gauge. This measures the pressure by ionizing the residual gas and measuring the current of ions hitting an anode. The ion gauge has a calibration between the pressure and current. This calibration depends on the type of residual gas, and it is important to note that at UHV the pressure in the chamber will not be uniform since the mean free path of particles will be longer than typical distances in the chamber. Thus the pressure will be lowest near the ion pump.

The final pressure reading of the ion gauge after bake-out is  $4.8 \times 10^{-10}$  mBar.

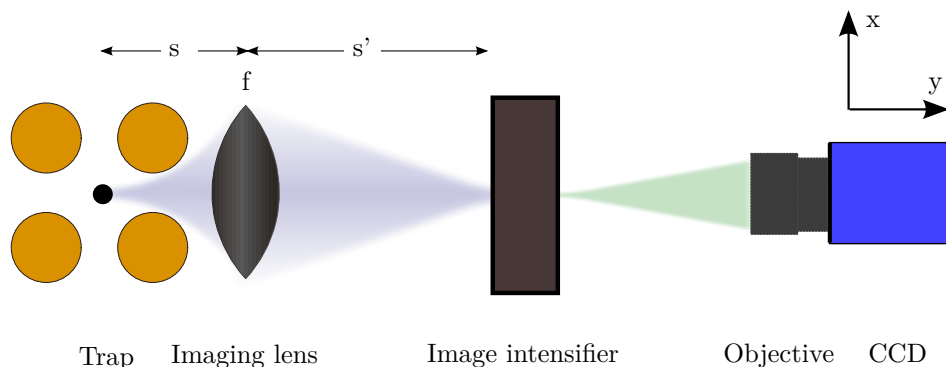


Figure 11.7: The imaging system. Light is collected by the imaging lens and is focused onto the image intensifier which can be gated quickly. The light emitted from the image intensifier is collected by an objective and focused on the CCD.

### 11.3.2 Magnetic field coils

For the purposes of efficient laser cooling it is important to destabilize so-called dark states [177]. Dark states occur when population is trapped in states of the system that do not participate in the cooling cycle. By applying a static magnetic field in the  $y$ -direction (vertical) the degeneracy of the magnetic sub-states is lifted and a quantization axis is chosen. By driving  $\sigma^\pm$  transitions the magnetic substates are mixed and no dark states will appear.

To produce a suitable magnetic field a coil was constructed. 71 turns of insulated copper wire was wound around a  $\varnothing 153$  mm cylinder<sup>18</sup> in four layers (18+18+18+17=71). After each layer of wires a layer of epoxy glue was applied. This ensures a solid structure that fits on the top of the chamber lid, but is easily removable. The epoxy glue is heat resistant up to 65 °C, so the coil should be removed before any bake-out.

The B-field can be adjusted from 0 to 12 Gauss by adjusting the current from 0 to 2 A.

### 11.3.3 Imaging

A significant advantage of working with laser cooled, trapped ions is the possibility of detection and imaging. The laser cooling process involves the spontaneous emission of millions of photons per second. These are emitted almost isotropically. A camera placed to capture these photons will be able to image the ions.

The imaging system employed in this setup consists of an imaging lens<sup>19</sup> which focuses the light from the ions onto an imaging intensifier<sup>20</sup>. The light from the image intensifier is then focused onto a Charged Coupled Device (CCD) camera<sup>21</sup> using a commercial objective<sup>22</sup>; see figure 11.7.

<sup>18</sup>The top chamber viewport, used for imaging, is 6 inches (152.4 mm) in diameter.

<sup>19</sup>Sill Optics S6ASS2241, S/N 81617, f-number  $N = 1.6$ ,  $f = 70$  mm.

<sup>20</sup>Proxitronic BV 2581 BY-V 5N #4512, "Felicia".

<sup>21</sup>PCO Sensicam, pixel size  $6.45 \mu\text{m} \times 6.45 \mu\text{m}$ , bit depth: 12 bit, resolution  $1376 \times 1040$ .

<sup>22</sup>Nikon AF micro Nikkor 60 mm 1:2.8 D.

Gating time	5 ns
Limiting resolution	32 lp/mm
Gain at 480 nm	$1.5 \times 10^6$ W/W

Table 11.1: Specifications for the image intensifier from Proxitronic.

The magnification from the ion to the image intensifier is given by  $m = -s'/s$ , where

$$\frac{1}{s} + \frac{1}{s'} = \frac{1}{f}. \quad (11.1)$$

The imaging lens is roughly 70 mm from the trap center and the image intensifier is approximately 700 mm from the imaging lens. This corresponds to a magnification of  $m = 10$ . A 10X image is formed on the image intensifier. The objective focuses the light emitted from the image intensifier onto the CCD with a magnification of  $m = 0.5$ . This means that the total magnification of the imaging system is  $m = 5$  or  $5\times$ .

The Red Cavity trap has an almost identical imaging setup, with a measured total detection efficiency of  $1.66 \times 10^{-4}$  at 397 nm. For details on the imaging system, see [205, Ch. 9].

### Image intensifier

The image intensifier is used to amplify the light from the ions and/or to achieve very fast gating. It is used to detect the 397 nm light from the  $^2S_{1/2} \rightarrow ^2P_{1/2}$  transition of the  $^{40}\text{Ca}^+$  ion.

The image intensifier consists of a photocathode, a double Micro Channel Plate (MCP), and a luminescent screen. Incident light hits the photocathode causing electrons to be released. The electrons are accelerated and amplified through the MCPs. The accelerated electrons hit the luminescent screen which emits light. The image intensifier has a spatial resolution such that an image will form on the luminescent screen. The resolution of the image intensifier is 32 lines/mm or about  $30 \mu\text{m}$  per line. At a magnification of 10X this means that we should be able to resolve features larger than  $3 \mu\text{m}$ . This also means the the imaging intensifier is the limiting factor of the resolution of the imaging system. The CCD has a better resolution as is easily confirmed since the noise of the CCD has smaller structure than the noise of the image intensifier.

By switching the acceleration voltage quickly with a homemade HV supply (switching time  $\sim 10$  ns) the image intensifier can be gated for short timescales making it possible to e.g. collect light only in certain phases of the ion micromotion.

## Chapter 12

### First ions

The first trapping of ions in the new trap and preliminary optimizations will be discussed. We will then discuss a technique for moving the rf nodal line and the preparations for the pulsed cooling experiments proposed in section 4.4.

#### 12.1 Trapping parameters and cooling

The system is initially set up for loading large amounts of calcium ions. This is done to increase the amount of fluorescence and thus improve the chance of detecting the ions, even if the imaging system, oven, trap or cooling is not optimized. Many of these parameters are difficult to inspect directly, so initial trapping is more difficult than subsequent experiments.

An advantage of commissioning a new trap in an existing ion trap lab infrastructure is that laser wavelengths can be reliably tuned before loading the first ions, because a working trap can be used as the calibration. In this way the lasers for ionization, Doppler cooling, and repumping were all tuned to the relevant frequencies, see appendix A. For initial cooling, where parameters are not optimized and where the ions created are warm, it is desirable to have a larger, e.g.  $\Delta = 2\pi \cdot 100$  MHz, detuning from the  $S_{1/2}$  to  $P_{1/2}$  transition since the linewidth will be considerably

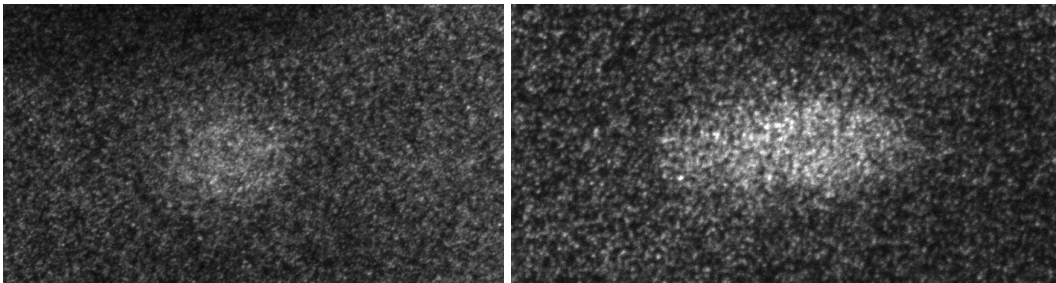


Figure 12.1: **Left:** The first ion cloud trapped. **Right:** After optimization of Doppler cooling, imaging was improved.

Doppler broadened.

The repumper laser does not need to be precisely tuned since a lot of power is available and the cooling dynamics are not as dependent on it as the Doppler cooling laser [177].

The trapping potential was chosen to have a very *open* trap, that is, a trap with low secular frequencies. This was done to have low micromotion amplitude and in an attempt to minimize the energy of the initially created ions. Initially  $q = 0.05$  and  $a = -0.002$  (see table 10.1). All other dc voltages that we can control are initially set to zero, on the assumption that the trap by itself is well balanced.

For an oven current of  $I = 8.4$  A, the calcium oven stabilizes at  $450^\circ\text{C}$ . At this current the pressure in the vacuum chamber goes up to about  $P = 5 \times 10^{-9}$  mbar.

The procedure for loading ions is in general the following:

- Turn on the oven and wait for it to reach between  $350^\circ\text{C}$ – $430^\circ\text{C}$ .
- Check alignment of all laser beams going through the trap. Especially the ionization beam needs to be well aligned at all times, since it could potentially charge up the trap surface, thus making trapping very difficult.
- Open up the oven shutter and send in the ionization beam.
- Wait for ions to appear on the screen.

Figure 12.1 left shows a picture of the first ions ever trapped in our trap<sup>1</sup>. In this image ions are barely discernible above the background noise from the scattering of the Doppler cooling light on the trap and windows. In the picture on the right imaging parameters were optimized and detuning was decreased thus increasing the scattering rate. Since micromotion is presumably not well minimized, these ions are not crystallizing, and thus the Doppler shift is still considerable which decreases the effectiveness of the laser cooling.

An iterative procedure of optimization of cooling, imaging, loading, etc. is then required to be able to load reliably and to crystallize larger clouds.

The first trapping was observed with the Doppler cooling beam pointed at  $45^\circ$  to the trap/cavity axis. With the  $45^\circ$  beam, micromotion is difficult to avoid, especially initially when the trap is not optimized. For this reason the  $397$  nm beam that is coupled into the cavity was subsequently used, since it does not drive radial micromotion. Unfortunately, the cavity beam and the trap center are not well overlapped, which limits the efficiency of cooling due to micromotion. Attempts to move the trap center and balance the trap will be discussed below. For now the coldest ions have been observed in strings of 5-10 ions; see figure 12.2. An attempt at crystallizing a cloud of ions can be seen in figure 12.3. Here both the  $45^\circ$  and cavity beam were employed. The size of the cavity beam can be seen from the part of the cloud brighter than the rest.

---

<sup>1</sup>First ions were trapped on 2015-04-07.

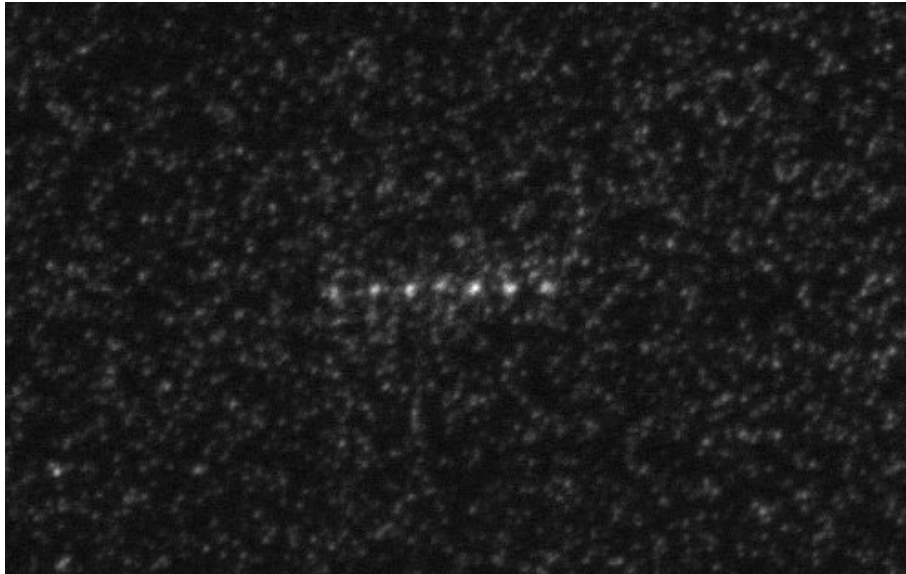


Figure 12.2: A string of 7 ions cooled by the cavity beam. Distance between ions is  $\sim 25 \mu\text{m}$ .

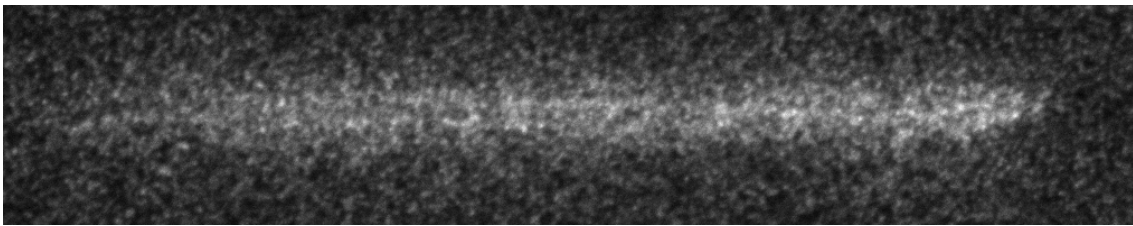


Figure 12.3: Ion cloud cooled by  $45^\circ$  and cavity beam. The ions at the center are much brighter than at the edges since they are being cooled by the cavity beam.

## 12.2 Micromotion minimization and balancing

### 12.2.1 Moving the rf null line

Since the cavity and trap electrodes are geometrically fixed after the trap has been installed in the vacuum chamber, and we require high precision alignment, it will be necessary to be able to fine adjust the trap center with respect to the cavity after trapping ions for the first time. Techniques for doing this have been used in previous work [133, Ch. 8][220] and will only be summarized here. The Red Cavity trap used in these references is of an almost identical design to the one employed in this work.

The main idea of the technique is to imbalance the trap electrode loads such that the amplitudes on some sets of electrodes are larger than on the others, see figure 12.4c). In this way the rf null line will be moved. This can be done by changing the effective capacitance of the electrodes and

should not affect the amount of micromotion experienced by the trapped ions [220].

The simpler alternative would be to change the dc electrode potentials thereby translating the ions, see figure 12.4b), but unfortunately this will not move the rf null of the trap, and the amount of micromotion experienced would increase — so-called *excess micromotion*. See section 2.3 and [122].

In the following, the center of the trap is to be understood as the point at which the rf potential is zero. This means that it is the point where the potentials applied from the four sets of electrodes cancel. At this point the ions will not experience any excess micromotion.

We recall that the motion of the ions will have the following form (equation 2.15)

$$u(t) = (u_{dc} + u_0 \cos(\omega_u t)) \left[ 1 - \frac{q_u}{2} \cos(\Omega_{\text{rf}} t) \right]. \quad (12.1)$$

Assume for simplicity that  $u_{dc} = 0$ . We will in the simple case only consider two sets of electrodes, A and B, which are applied potentials 180° out of phase, with rf amplitudes given by

$$U_{\text{rf}}^B = \delta U_{\text{rf}}^A, \quad (12.2)$$

where  $\delta < 1$  is an attenuation parameter that controls the relative imbalance between the electrodes. The potential from the two electrodes will be given by

$$\phi(\tilde{x}) \propto \frac{U_{\text{rf}}^B}{\tilde{x} + r_0} - \frac{U_{\text{rf}}^A}{\tilde{x} - r_0} = \frac{U_{\text{rf}}^A + U_{\text{rf}}^B}{r_0} - \frac{U_{\text{rf}}^A - U_{\text{rf}}^B}{r_0} \frac{\tilde{x}}{r_0} + \frac{U_{\text{rf}}^A + U_{\text{rf}}^B}{r_0} \frac{\tilde{x}^2}{r_0^2} + \mathcal{O}\left(\frac{\tilde{x}^3}{r_0^3}\right), \quad (12.3)$$

where we have made a Taylor expansion to second order in  $\tilde{x}/r_0$  since we will consider only relatively short excursions from the geometrical center of the trap. We solve for the minimum,  $x_0$ , of this approximate potential

$$x_0 = \frac{U_{\text{rf}}^A - U_{\text{rf}}^B}{U_{\text{rf}}^A + U_{\text{rf}}^B} \frac{r_0}{2} = \frac{1 - \delta}{1 + \delta} \frac{r_0}{2} \approx \frac{1 - \delta}{4} r_0, \quad (12.4)$$

where we expanded to first order in  $\delta$  around 1. We have thus translated the rf null.

This simple analysis suggests that by imbalancing the rf-potentials, it will be possible to move the rf-null. To accomplish this it is necessary to change the electronic circuit driving the trap. The principle (outlined in [220]) is to add either capacitance in series or parallel to the driving circuit of specific electrodes. If a capacitance is added in parallel by e.g. extending the length of the cables, the ions can be displaced, but the effective capacitance of the circuit is increased leading to lower rf resonance, as discussed in section 10.4. If, instead, capacitance is added in series, the effective capacitance is not increased very much while the ions can still be displaced. Thus serial capacitance is the preferred method of displacing the ions.

### 12.3 Detecting rf null displacement

By loading an ion cloud or crystal it is possible to measure the displacement directly. The optimal strategy is to use an ion Coulomb crystal with two different species and determine the optimum from the the asymmetries of this, see figure 12.5 for an example and [220] for details.

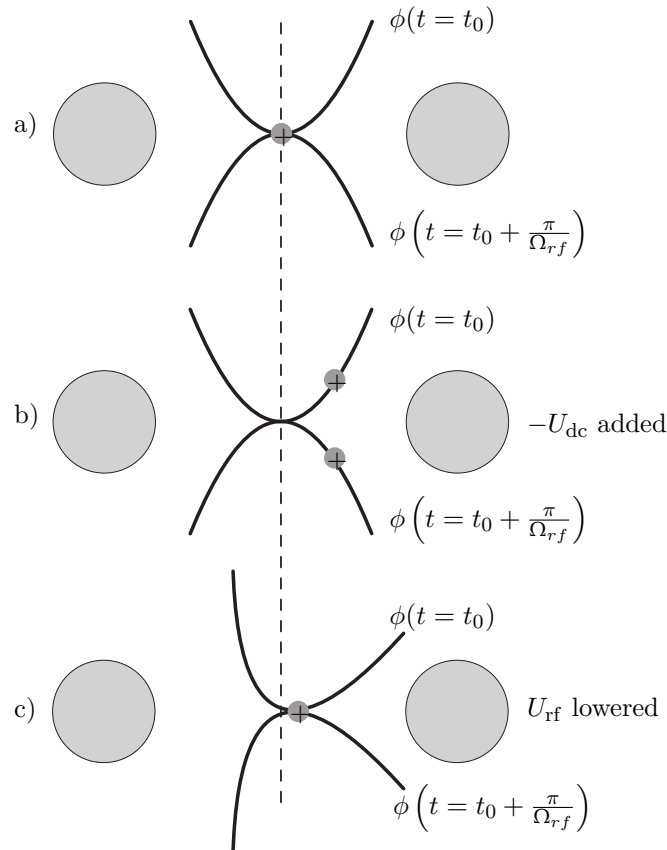


Figure 12.4: The principle of moving the rf nodal line. **a)** For a symmetric trap the ions will be located at the nodal line. **b)** If the ions are displaced by e.g. dc potentials they will experience excess micromotion. **c)** If the rf potential on the right electrode is lowered relative to the potential on the left the rf nodal line will move to the right, but without experiencing excess micromotion. The potential is plotted at two times separated by half a period of the rf motion.

However, currently we do not have well crystallized, large numbers of ions in the trap which makes it more difficult to optimize. An alternative simpler strategy is to load a cloud of ions and try to optimize the centering using this. By lowering the radial rf potential the ions will move towards the minimum defined by the dc potentials. By adjusting the dc potentials such that the ions are not displaced when going from high rf potential to low rf potential the center of the trap can be found, at least in the direction perpendicular to the axis of the imaging system. To improve the alignment in the direction parallel with the imaging system axis an additional camera could be placed next to a viewport at  $90^\circ$ .

### 12.3.1 Current status

So far the adjustments of the rf null line have been minor. The optimal strategy for improving the trapping requires loading of bi-crystals.

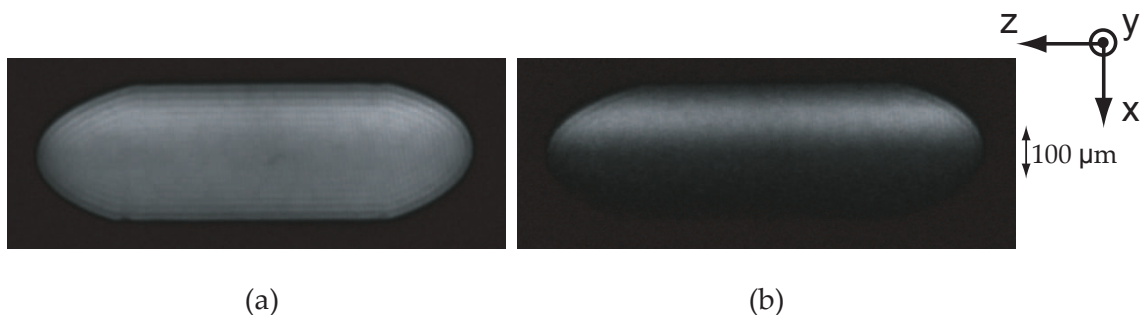


Figure 12.5: Illustration of the proposed scheme for determining cavity-trap offset. Here a bicrystal of  $^{40}\text{Ca}^+$  and  $^{44}\text{Ca}^+$  ions is trapped. (a) 866 nm repumper sent in along  $x$ -axis (b) 866 nm repumper injected into cavity mode. The fluorescing part of the crystal indicates the cavity mode. From the asymmetry of the crystal the cavity-trap offset can be determined, here  $\simeq 90 \mu\text{m}$ . Picture is from the Red Cavity trap, courtesy of Peter Herskind [133, p. 106][220].

Bi-crystals are ion Coulomb crystals consisting of two different elements, e.g. Ca and Ba, or two different isotopes of the same element e.g.  $^{40}\text{Ca}^+$  and  $^{44}\text{Ca}^+$ . By inspection of eq. 2.14 for the secular frequencies, we see that heavier ions are less confined than lighter ions; this means that the heavier (e.g. Ba or  $^{44}\text{Ca}^+$ ) will equilibrate at the edge of the crystal. This can be used to detect the position of the ion crystal relative to the cavity mode by driving the ions with the cavity and seeing which part of the crystal lights up. A similar measurement for the Red Cavity trap is shown in figure 12.5. There the 866 nm repumper was coupled to the optical cavity and only ions within the cavity mode were effectively repumped.

By adjusting dc electrodes and capacitances as described above while monitoring the shape of the bright ions compared to the full crystal it is possible to align the crystal correctly in the cavity mode [220].

The prerequisites for this method is the ability to trap large clouds (or crystals) and cool them well. For this it will be advantageous to use the  $45^\circ$  Doppler cooling beam since this can be much larger and can be adjusted for overlap with the crystal.

## 12.4 Pulsed cooling preparations

In chapter 4.4 we discussed the theory of a pulsed Doppler cooling scheme for avoiding the micro-motion always present for ion Coulomb crystals. In the section the practical considerations of such a system will be presented and preliminary characterization of the equipment will be discussed.

The pulsed cooling scheme depends on short reproducible pulses. A fast AOM and a driver have been acquired. Their specifications promise pulse rise and fall times of 9 ns. The light from this AOM will be directed through the trap at  $45^\circ$  to the trap axis, so that it can cool all modes of the ion motion. From the simulations it is expected that the cooling rate will be slower than continuous cooling due to the low duty cycle. Increasing the cooling rate is not straightforward

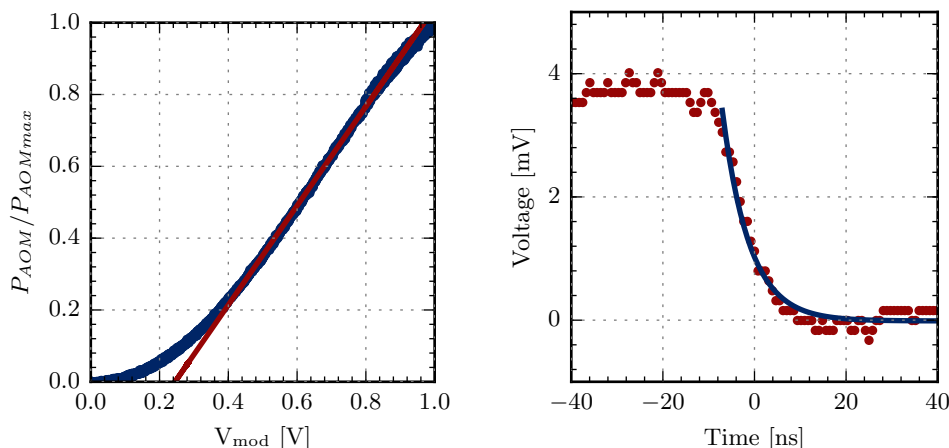


Figure 12.6: **Left:** Relative power out of pigtail AOM as a function of the input voltage (blue). The red line indicates a fit to the linear part of the data and the fitted expression is  $y = ax + b$  with  $a = (1.3815 \pm 0.0007) \text{ V}^{-1}$  and  $b = -0.3386 \pm 0.0004$ . **Right:** The decay of the pigtail AOM. The blue light is the result of fitting an exponential decay. This measurement was repeated 100 times and the resulting time is  $t_R = (13.7 \pm 1.6) \text{ ns}$ .

since cooling efficiency is lowered when saturation is increased; so just increasing the power while the laser is on is not sufficient.

For detection of the efficiency of the cooling scheme, we will use the imaging system. At first any detection of an effect will be sufficient, so by varying the phase between the rf cycle and the pulses we should be able to see both heating and cooling by the effective resolution of the ions on the camera. The heating and cooling should be large enough that the spreading of the ions due to heating will lead to smearing on the imaging system.

By gating the CCD chip in phase with the rf drive, it should also be possible to investigate to which extent the pulses are correctly placed in time. Another possibility is to look at the linewidth of the  $S_{1/2}$  to  $P_{1/2}$  (with the pulsed beam) such that the line is only broadened by the secular motion, not the micromotion. The width of this line should then contain information on the temperature of the ions.

### 12.4.1 Pigtail AOM

A fiber coupled AOM<sup>2</sup> has been acquired for the pulsed cooling experiments. The input and output of the AOM are connectorized polarization maintaining fibers<sup>3</sup>, hence the name pigtail AOM. The specifications for the pigtail AOM suggest a fast rise/fall time of 9 ns. The driver<sup>4</sup> is similarly fast

<sup>2</sup>AA Opto-Electronic MQ180-B9-Fio-PM-J3V-A-023.

<sup>3</sup>PM 400.

<sup>4</sup>AA Opto-Electronic MOD180-B2-34.

and both have been characterized in the following<sup>5</sup>.

The driver can be controlled by an input voltage between 0 V and 1 V, see figure 12.6. The driver itself has a bandwidth of 440 MHz and an output capacity of 2.5 W. The AOM and driver are fixed frequency, meaning that they operate at the same fixed frequency of 180 MHz. This also means that the frequency of the light is shifted by 180 MHz. The efficiency of the AOM depends, of course, on the input voltage as shown in figure 12.6, while the overall efficiency depends on the fiber coupling efficiency. A maximum of 27 % of the input light has been measured at the output, but since this include effects due to a poor mode-matching, the actual efficiency of the AOM is likely close to 40 % and in agreement with the specifications that promise less than 5 dB loss [221].

In the following rise and fall times denote the 90 %-10 % time of e.g. exponential decays. If an exponential decay is given by

$$P(t) = P(0) \exp(-t/\tau), \quad (12.5)$$

where  $P(t)$  is the power at time  $t$  and  $\tau$  is the decay time, then the fall time is given by  $t_r \simeq 2.197\tau$ .

The rise and fall times of the AOM has been investigated, see figure 12.6. A fall time of  $t_R = (13.7 \pm 1.6)$  ns was measured. This should be compared to an estimate based on the addition of rise times from all the components of the system. The pulse generator<sup>6</sup> has a minimum rise/fall time of 5 ns. The signal of the pulse generator is sent to the driver with a rise time of 5 ns. The AOM has a specified rise time of 9 ns and the detector<sup>7</sup> used has a rise time of 1 ns. Finally the oscilloscope has a bandwidth of 100 MHz and thus a rise time of 3.5 ns<sup>8</sup>. The total rise time of the system is then [222]

$$t_r = \sqrt{\sum_i t_i^2} = 12 \text{ ns}, \quad (12.6)$$

where  $t_i$  is the rise time of the  $i$ th step in the system. This is in agreement with the measured results. Due to the way rise times add in equation 12.6, the slowest component dominates the measurement and thus there is only a little benefit to improving the rise time of the pulse generator. The oscilloscope itself adds to the rise time in the measurement, but since the bandwidth is known, the effect of this can be subtracted. Alternatively, the measurement could be repeated with a faster oscilloscope.

In figure 12.7, examples of pulses are shown. The shortest possible pulse with the current setup is shown as the dark blue graph with a FWHM of 12.5 ns. The light blue indicates a pulse of a larger width (24.6 ns). Note the differences in peak power between the two: this is due to the shortness of the pulse, since the power of the AOM does not have sufficient time to reach the optimum before the pulse is over.

<sup>5</sup>Characterization done by Hans Harhoff Andersen and Martin Sand Nielsen. Details of the characterization can be found in the thesis of MSN [221].

<sup>6</sup>Agilent 81101A 50MHz Pulse Generator.

<sup>7</sup>Thorlabs DET10A/M.

<sup>8</sup>The bandwidth of a simple first order circuit is given by  $\omega_{\text{BW}} = 2\pi f_{\text{BW}} = 1/\tau$ .

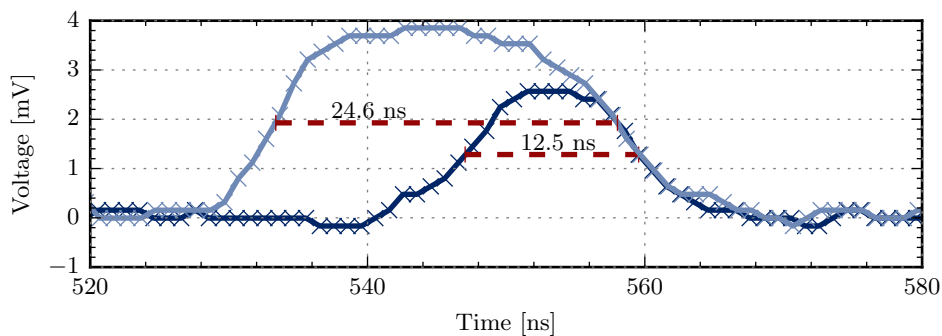


Figure 12.7: Attainable pulse widths of the pigtail AOM. Note that the shorter pulse has a lower peak power. This is due to the shortness of the pulse where the AOM does not fully turn on before being turned off again. The pulse widths were controlled by the pulse generator and were programmed to 25 ns and 10 ns.

## 12.5 Conclusion and future aspects of the Blue Cavity Trap

Ions have been trapped in the new Blue Cavity trap. We have shown that we can reliably load ions and that we can cool small strings and clouds of ions. In the near future we will be working to improve trapping and crystallization of larger clouds, and investigate the presence of excess micromotion. For this, improvements in the cooling are required, potentially using the pulsed cooling scheme. Moreover, the fine alignment between trap and cavity should be performed.

Preparations have been made for pulsed cooling. We have shown that pulses as short as 12.5 ns can be generated. This results in a duty cycle of  $d = 12.5 \text{ ns} / 280 \text{ ns} = 0.045$ , which means that pulses corresponding to the lowest duty cycles of the simulations performed in section 4.4 can be generated. The intensity achievable with the currently available power and waist of the  $45^\circ$  Doppler cooling beam is  $I_0 \simeq 1000 \text{ mW/cm}^2$ . This corresponds to  $s_0 = 14$ , but the cooling rate will be diminished by a factor of  $d$  to give an effective on-resonance saturation parameter of the pulsed light of  $s_0 d = 1.4$ , which is still sufficient to adequately saturate the transition. Here we have assumed a beam with radius waists of  $(w_H, w_V) = (560 \mu\text{m}, 220 \mu\text{m})$  for horizontal (H) and vertical (V) respectively.

## Chapter 13

# Optomechanics with ensembles of ions

### 13.1 Comparison with other setups

The Blue Cavity trap has similarities and differences with both the MIT setup, discussed in chapter 7, and the Red Cavity trap described here [133][77]. The MIT trap and the Blue Cavity trap are very similar in purpose. Both are linear Paul traps with an integrated high finesse cavity coated for the  $S_{1/2}$  to  $P_{1/2}$  transition of their respective ions. A difference from the MIT setup is the larger size of the trap, designed to operate with large ion crystals ( $> 10^4$  ions). Working with ensembles of ions rather than single ions offers interesting possibilities. First, the increase in the coupling strength resulting from the collective interaction between the cavity field and the ions in the crystal allows for operating in the collective strong coupling regime of CQED, as demonstrated with the Red Cavity trap [107]. Second, the cavity interaction allows for enhanced optomechanical forces exerted on the ions, which can be exploited for the observation of cavity optomechanics phenomena with cold atomic ensembles [223] and for investigations of structural [224] and thermodynamical [225] properties of cold solid-like objects such as ion Coulomb crystals.

The Blue Cavity trap and the Red Cavity trap are alike in many respects. The main difference is the choice of optical coating. The Red Cavity trap is coated in the IR range encompassing the  $D$  to  $P$  state transitions of calcium. The Red Cavity trap is designed for interactions where the "ground" states are metastable excited states (lifetime  $\sim 1$  s). This was used in experiments performed with strong coupling and cavity electromagnetically induced transparency (EIT), in which the ions can be considered two or three level systems, such as [77][78]. Obtaining highly reflective cavity mirrors in the blue-UV wavelength region is more challenging than in the near-IR. However, a "blue" cavity offers the advantage of working with transitions with stronger dipole coupling and removes some of the complexities associated with operating on a metastable-excited state transition with an unfavorable branching ratio in which decay from the excited to the ground state is the most probable.

The new setup has similar length, but a stronger transition and higher finesse ( $\sim 7 \cdot 10^3$ ) compared to the Red Cavity trap ( $\sim 3 \times 10^3$ ) [77]. The total decay rate of the  $^{40}\text{Ca}^+$   $P_{1/2}$  state is  $\Gamma = 2\pi \cdot (23.07 \pm 0.17)$  MHz and the field decay rate (at 397 nm) is  $\kappa \approx 2\pi \cdot 800$  kHz. The coupling

strength is  $g \approx 2\pi \cdot 0.83$  MHz where a  $\sigma$  transition has been assumed. The single ion cooperativity is  $C_0 = 0.036$ . Thus unit collective cooperativity for  $N \leq 30$  atoms should be achievable. One should then be able to operate deeper in the strong coupling regime than with the existing setup [77].

Stronger coupling also allows for stronger optical forces on ions, which can be exploited for localization and dynamics in fine-structure potentials, as demonstrated in [107] and for the simulation of solid-state models such as the Frenkel-Kontorova model [110]. See sections 13.3 and 13.4.1 respectively.

The new setup could also be used for cavity cooling. In that sense the MIT experiments can be seen as a precursor of this project. Cavity cooling of collective modes [225] and other cavity optomechanical phenomena could be investigated with large ion Coulomb crystals.

## 13.2 Structural properties of ion Coulomb crystals

Many of the planned experiments will revolve around the detailed control of structures of ions confined in the trap. The toolbox includes the use of bi-crystals for shaping and determining structure. It has previously been shown that the loading of ion species with different charge-to-mass ratios,  $q/m$ , will lead to bi-crystals i.e. crystals of separate regions consisting almost exclusively of one or the other species [134][138].

In [134] it was shown and explained how the confinement of one ion species inside another species would yield two separate structures in a trap. The inner structure has been compared to the expected structure of an infinitely long, cylindrically symmetric single component crystal [226]. The experimental results conform to the model which predicts strings, shells, and strings with shells depending on the linear ion density [134]. Those experiments were performed with  $^{40}\text{Ca}^+$  and  $^{24}\text{Mg}^+$  ions. Later experiments with bicrystals of  $^{40}\text{Ca}^+$  and  $^{44}\text{Ca}^+$  showed the effect of an RF-induced anisotropy of the interaction between the ions [138]. In this case the structure of the inner species could not be predicted by simple pseudo-potential simulations. Full MD simulations could however show the structure change of the two species crystal (of similar charge-to-mass-ratio). The new structure was determined to be either a face-centered tetragonal (fct) lattice or an fcc or bcc structure [138]. The uncertainty is due to the small difference between the potential energies of these systems as has also been observed in single-component crystals [137].

In the new trap it will be possible to load both barium and calcium. Simulations of the dynamics of Ion Coulomb crystals using the pseudo-potential approximation have shown that equidistant strings like in [134] can be created by loading a larger number of barium ions along with e.g. 16 to 26  $^{40}\text{Ca}^+$  ions. In this case the structure would resemble the structures in [134]. An example of such a bicrystal is shown in figure 13.1. Preliminary results show mean ion spacings of e.g.  $8.9 \mu\text{m}$  with a spread of  $0.1 \mu\text{m}$ . This should be compared to the spacing of a string without surrounding barium of  $12.7 \mu\text{m}$  with a spread of  $2.1 \mu\text{m}$ . These simulations are ongoing work, and are being performed by master student Mai Aalund Olsen.

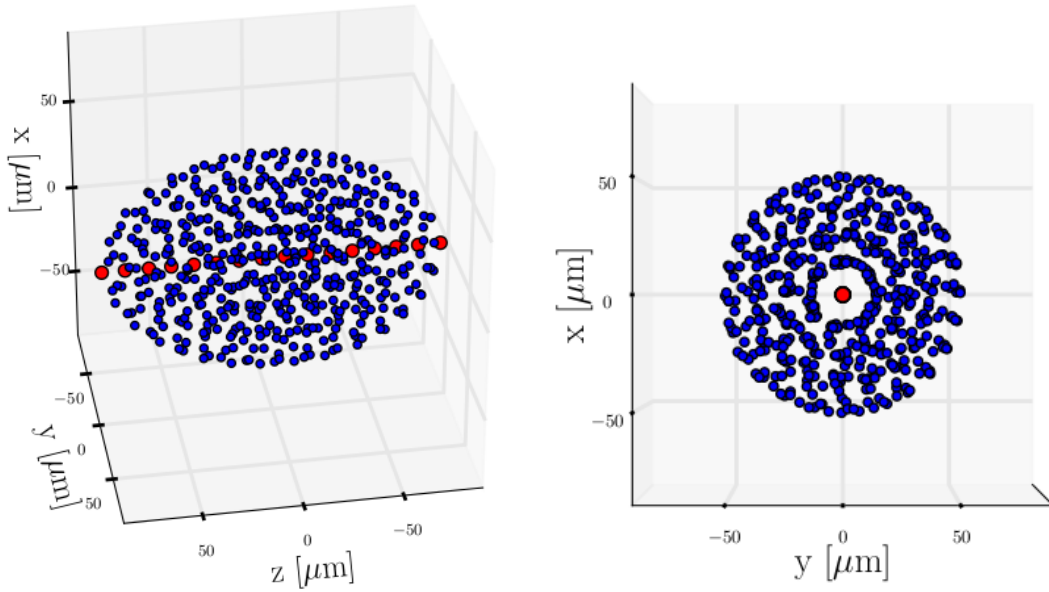


Figure 13.1: 500  $^{138}\text{Ba}^+$  ions (blue) trapped with 16  $^{40}\text{Ca}^+$  ions with  $U_{\text{rf}} = 200\text{ V}$  and  $U_{\text{end}} = 15\text{ V}$ , where the Blue Cavity trap has been assumed; see parameters in table 10.1. Simulations performed by Mai Aalund Olsen.

Equidistant strings of ions have a number of useful applications including the potential of matching the distance to the period of an intracavity standing wave field, thus ensuring that all of the ions have the same coupling to said lattice. This could be useful for increasing the collective coupling strength,  $g\sqrt{N}$  in CQED experiments.

While the control of the structure of ion Coulomb crystals can be manipulated by loading multi-species crystals and use this effect to improve the collective coupling strength in the experiments, it is also possible to work in the opposite direction. By exploiting the strong light forces, structural properties of ion crystals could be controlled and stabilized as predicted in [224]. This could enable further studies of the structural properties of ion Coulomb crystals in rf traps.

### 13.3 Optical potentials in the Blue Cavity trap

In section 6 we discussed the theory of optical potentials. Optical potentials have been employed as an important tool in neutral atom physics for several decades [104], but have only recently been explored in relation to charged particles [107][108][227].

In this section we will discuss the generation of an optical potential in the Blue Cavity trap experiment. The wavelength of the light used for the dipole trap will be 794 nm for which a tapered amplifier laser is available. This is the same laser that feeds the doubling cavity for the 397 nm light used for Doppler cooling of  $^{40}\text{Ca}^+$  (see section 10.5).

An optical potential from a standing wave in a cavity has slightly different characteristics

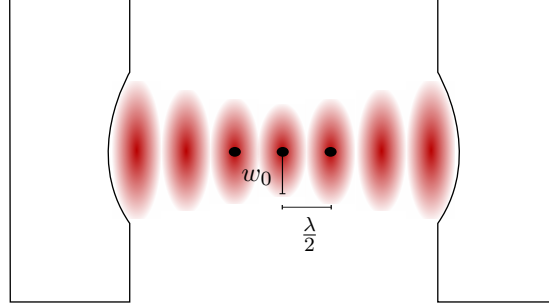


Figure 13.2: Schematic of the dipole trap; not to scale. The red field indicates the intensity of the trapping field while the black circles indicating ion positions. The period of the potential,  $\lambda/2$ , is indicated as well as the waist,  $w_0$ , of the mode.

compared to that of a running wave discussed in section 6. The primary differences are a dramatic increase in intensity and a large gradient associated with the standing wave along the cavity axis.

The dipole potential is given by eq. 6.15 and the intra cavity intensity distribution by eqs. 5.23 and 5.22. The dipole potential seen by an ion at the center of the cavity will be expanding to second order

$$U_{\text{dip}}(\mathbf{r}) \simeq -U_0 \cos^2(kz) \left[ 1 - 2 \left( \frac{r}{w_0} \right)^2 - \left( \frac{z}{z_R} \right)^2 \right] \simeq -U_0 (1 - (kz)^2) \left[ 1 - 2 \left( \frac{r}{w_0} \right)^2 - \left( \frac{z}{z_R} \right)^2 \right]. \quad (13.1)$$

To a good approximation the longitudinal restoring force is approximately harmonic with a frequency

$$\omega_{\text{tr}} = k \sqrt{\frac{2U_0}{m}}. \quad (13.2)$$

for small amplitudes around the potential minima.

$U_0 = U(0)$  is the potential minimum corresponding to the intensity  $I_0$ .

Due to the high finesse of the cavity the field strength can be very large. The total amplification of the dipole trap becomes, for e.g. the 794 nm light,

$$4T_1 \frac{\mathcal{F}^2}{\pi^2} \sim 13000, \quad (13.3)$$

compared to a dipole trap generated by a single Gaussian beam of the same power and size. The large longitudinal gradient has the added advantage of confining the ions in very small micro potentials suitable for various purposes as discussed below.

In our case, since we will be using light at 794 nm, to pin atoms with a transition at 397 nm the rotating wave approximation breaks down and the full expression, eq. 6.15, is used. The large detuning  $\Delta = \omega_0$  also means that the magnetic sub-levels are unimportant [104]. In fact, the light is detuned enough that the splitting between the  $P_{1/2}$  and  $P_{3/2}$  states become unimportant and they can be considered as one state with one decay rate.

Table 13.1: Expected performance of dipole trap in the setup.  $\lambda$  is the wavelength of the lattice light, transition denotes the addressed transition,  $P_{\text{in}}$  is the input power before the cavity,  $U_{\text{dip}}$  is the expected trap depth,  $\Gamma_{\text{sc}}$  is the spontaneous scattering rate,  $\Delta$  is the detuning, and  $\omega_{\text{tr}}$  is the longitudinal dipole trap frequency.

$\lambda$	Transition	$P_{\text{in}}$ [mW]	$U_{\text{dip}}$ [mK]	$\Gamma_{\text{sc}}$ [ $\text{s}^{-1}$ ]	$\Delta$ [THz]	$\omega_{\text{tr}}/2\pi$ [MHz]
794	$S$ - $P^{\text{a}}$	180	4.0	5	-377.611	1.6
405	$S_{1/2}$ - $P_{1/2}$	$\sim 10$	6.7	$1.0 \times 10^3$	15 THz	4.1
405	$S_{1/2}$ - $P_{1/2}$	$\sim 40$	14	$1.4 \times 10^3$	15 THz	6.0
397	$S_{1/2}$ - $P_{1/2}$	0.6	12	$1.1 \times 10^5$	0.2 THz	5.7

<sup>a</sup> Due to the large detuning, the  $P$ -states can here be considered as one state.

The  $D_{3/2}$  transition is not as far detuned, but the transition to  $S_{1/2}$  is dipole forbidden so that no appreciable shift will occur. The  $P$  states do have a significant decay rate to the  $D_{3/2}$  state. This will give rise to a shift of the transition. This shift can be large ( $\sim$  GHz) for relevant experimental parameters.

To estimate the intra-cavity intensity one needs to know the coupling efficiency, transmission coefficients, and finesse rather accurately. However, if the power after the cavity can be measured and the transmission coefficient is known, one can estimate the intra cavity power from this. This is a more direct measure if the transmission coefficient is well known.

Using the current record for power injected into the cavity at 794 nm of about  $\sim 180$  mW, we can estimate the trap depth and scattering rate. Results are tabulated in 13.1.

These optical potentials can be used for optical pinning experiments [107][200] and potentially for controlling the crystal structure of ion Coulomb crystals [224].

### 13.3.1 Heating in dipole traps

In addition to the heating generally experienced in ion traps [202], ions trapped in an optical potential will be heated from a couple of other sources. Most obviously, absorption and spontaneous emission events will lead to heating as in Doppler cooling. In the cases that we will be investigating this will however be a negligible effect due to a very large detuning, see 13.1.

Another source of heating/loss is background gas collision, which for neutral atoms, is roughly  $1 \text{ s}^{-1}$  at a pressure of  $P = 3 \times 10^{-9}$  mbar which is comparable to pressures in our experiment [104].

Technical heating, defined as heating due to intensity fluctuations and pointing instabilities, may also contribute significantly. The mechanism here is easily understood: By changing shape of the trapping field the ions will find their motion to be parametrically driven. If fluctuations happen at frequencies close to twice the frequency of oscillation this motion will be excited. If the position of the trap moves, i.e. pointing instability, at the frequency of oscillation the motion will be resonantly driven [104][228]. Thus the technical heating rate is caused by noise at  $\omega_{\text{tr}}$  and  $2\omega_{\text{tr}}$ .

The heating rate due to intensity fluctuations can be derived from first order perturbation

theory as

$$\langle \dot{E} \rangle = \Gamma_{\text{heat}} \langle E \rangle, \quad (13.4)$$

where

$$\Gamma_{\text{heat}} \equiv \frac{\pi}{2} \omega_{\text{tr}}^2 S_{\text{int}}(2\omega_{\text{tr}}), \quad (13.5)$$

and  $S_{\text{int}}$  is the one-sided power spectrum of the fractional intensity noise of the light in the cavity [228]. The noise that will induce heating is only that around twice the trapping frequency (as expected) which will be in the MHz range. The relevant noise at these frequencies will not be acoustical, but rather electronic in origin. A measurement of the noise spectrum of the driving laser should provide an estimate. Even better would be to perform the measurement on the locked cavity and measure the noise spectrum of this, since it will include any intensity modulation due to EOM and cavity, see section 10.6.3 for details.

Savard et al also discuss pointing instability heating, i.e. heating due to the micro-potentials shaking. We do not expect this to be a concern since the micro-potential centers are given by the positions of nodes which are determined by the mirror positions, and these 1) only move at acoustic frequencies (lower than about 50 kHz) and 2) do not move much more than a few cavity linewidths (less than 1 nm).

### 13.3.2 Possibilities for optical pinning

By carefully choosing the  $q$  numbers of the 794 nm and 397 nm light we can adjust the relative positions of the minima and maxima of the standing waves. By choosing  $q_{397} = 2q_{794}$ , the minima and maxima of the 794 nm intensity will coincide with minima of the 397 nm field, see figure 13.3 bottom. By choosing  $q_{397} = 2q_{794} + 1$ , the minima and maxima of the 794 nm intensity will still coincide with the minima of the the 397 nm at the ends of the cavity near the mirrors which determine the boundary conditions. However, as we move along the cavity axis, the maxima and minima shift linearly such that at the center of the cavity the maxima and minima of the 794 nm light intensity are coincident with the maxima of the 397 nm. This is because the *extra* half-wavelength of the 397 nm field is evenly distributed along the length of the cavity and at the center the shift is one-half thus switching minima for maxima; see figure 13.3 top. This actually holds for  $q_{397} = 2q_{794} + \delta q$  for any odd  $\delta q$  near the center. For high  $\delta q$  the overlaps between the intensities diminish faster as the the distance to the center of the cavity increases.

In the Blue Cavity trap optical pinning experiments like those presented in [107][200] could be performed. The use of 794 nm light means that detuning will be very large and excitation of the ion and thus spontaneous emission will be highly suppressed. For  $q_{397} = 2q_{794} + 1$  the dipole trap would pin the ion in the maxima of the intensity of the 397 nm field. This would ensure maximal coupling strength,  $g$ , in experiments based on the collective coupling strength.

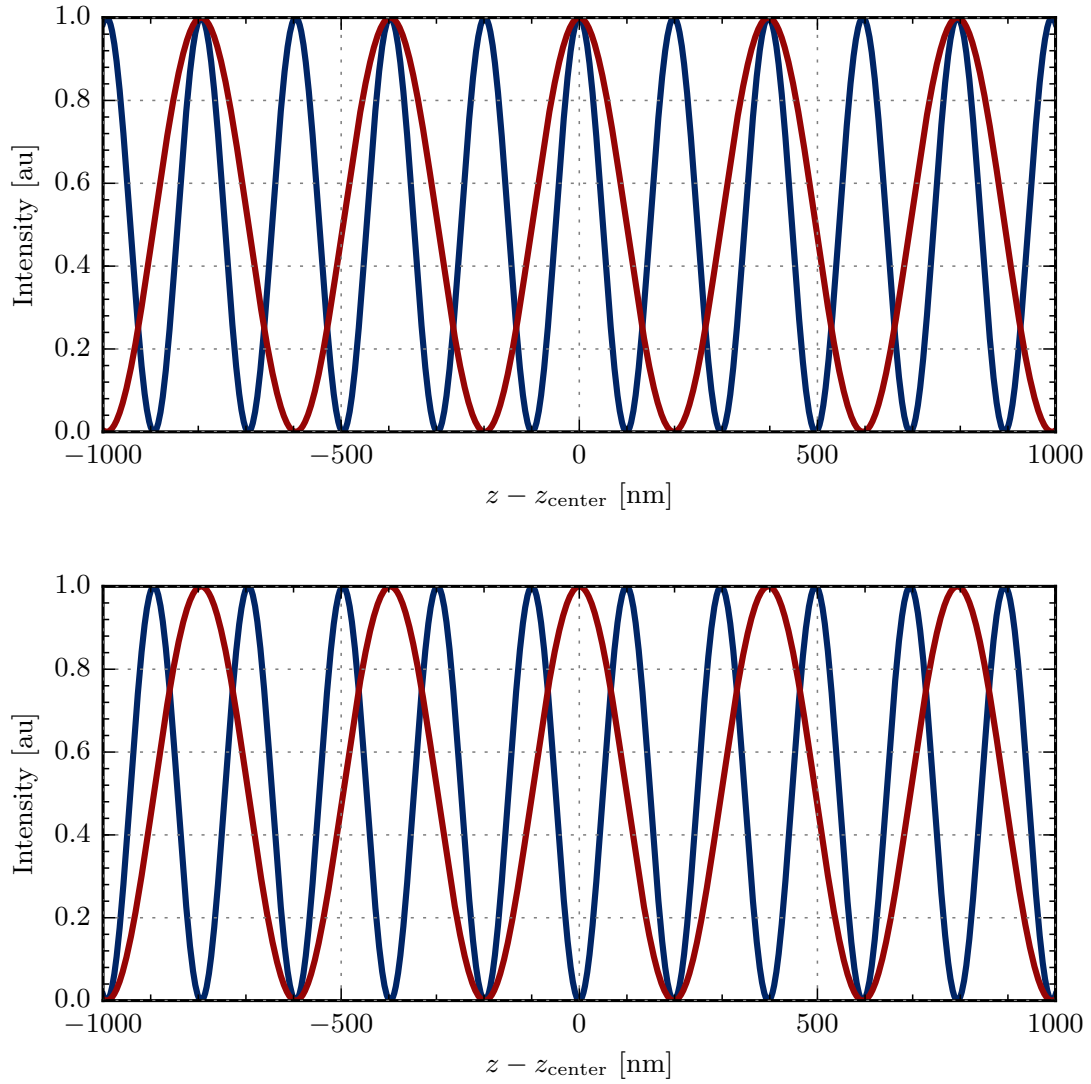


Figure 13.3: Top: A detailed view of the spatial variation of the intensity of the 794 nm (red) and 397 nm (blue) fields near the center of the cavity. Here  $L = 12.5$  mm,  $q_{794} = 31487$ ,  $q_{397} = 2q_{794} + 1 = 62975$ . Bottom: The same for  $q_{397} = 2q_{794}$ .

## 13.4 Simulation of friction at the atomic scale

### 13.4.1 Frenkel-Kontorova model of dry friction

The Frenkel-Kontorova model was developed in order to understand friction at the microscopic scale [112][110][114]. It can be compared to the relatively simple Prandtl-Tomlinson (PT) model which is used to describe dry friction phenomena such as static friction and the onset of kinetic friction [110]. The PT model considers a single point mass moving in a sinusoidal potential. Since only a point mass is simulated, this model will not model heating, and thus not dissipation of energy, in the system. The Frenkel-Kontorova (FK) model is more refined in that it describes a chain of masses interconnected with springs moving in a sinusoidal potential. This means that friction can give rise to energy being distributed among the degrees of freedom of the individual particles.

Friction is in general an effect occurring in 3D space between 2D surfaces, but the friction of *real materials* is exceedingly hard to probe and control at the microscopic level [115]. For this reason system governed by simple model Hamiltonians are sought. These can then work as analogues of the system in question, but with better control and more detailed understanding. These are then applied as models for simulations and direct confirmation of models such as PT and FK.

The one dimensional Frenkel-Kontorova model describes [114][110], a sinusoidal potential with period  $a_s$ , interacting with a chain of identical particles with mass  $m$ , connected with ideal springs<sup>1</sup> of spring constant  $k_s$  and where  $a_0$  is the equilibrium distance of the springs. The amplitude of the periodic potential is  $K$  and the total Hamiltonian is

$$H = \sum_i \left[ \frac{p_i^2}{2m} + \frac{1}{2}k_s(z_i - z_{i-1} - a_0)^2 + K \cos\left(\frac{2\pi z_i}{\lambda}\right) \right], \quad (13.6)$$

where  $z_i$  and  $p_i$  are the position and momentum of the  $i$ th particle.

We consider the case where  $a$  and  $\lambda$  are incommensurate and thus the ratio  $a/\lambda$  is an irrational number. We would like to distinguish between two separate phases of the system: Stick-slip and sliding. The sliding phase occurs for  $K$  zero or very small. In this case the force required to move the chain,  $F_d^{\delta x}$ , vanishes due to the translational symmetry of the Hamiltonian. Thus the smallest push will move the chain. For small, but finite,  $K < K_c$ , where  $K_c$  is called the critical value, we would naively expect resistance to movement because of the corrugation of the potential. But, due to the infinite chains and incommensurate periods, the net potential felt by the particles will average out. This can be understood as the particle positions being primarily determined by the springs. Any translation of the whole chain will thus not feel a potential gradient from the periodic potential and  $F_d^{\delta x}$  remains zero.

At  $K > K_c$  a phase transition occurs [110][113], where the particle positions will be pinned to the minima of the periodic potential. The periodic potential effect no longer averages out and  $F_x^{\delta x}$  becomes finite. This phase transition is called the Aubry transition. Above the Aubry transition the phase is called stick-slip since the ions "sticking" to their potential minima until a point where

<sup>1</sup>Since all bound states are, in some limit, ideal springs, this is a useful model in many low excitation cases.

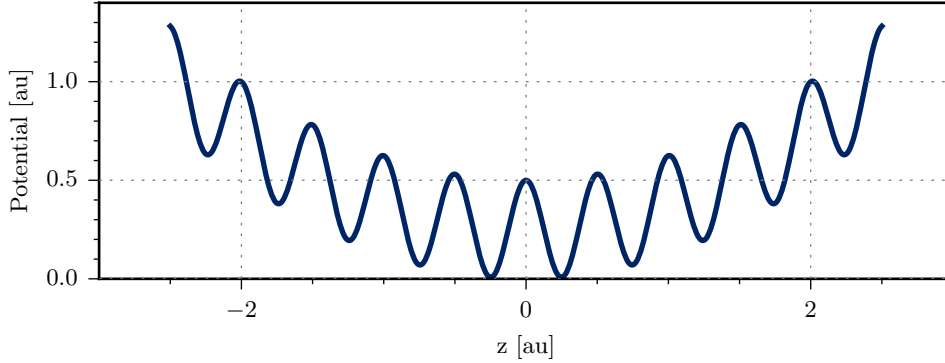


Figure 13.4: The external potential of the FKI model with ions in lattices. In addition to the optical and electrical potential there is also the Coulomb repulsion of the ions (not shown).

the force  $F_d^{\delta x}$  overcomes the optical potential and all the whole chains moves together. In this movement energy is dissipated, and the ions will again stick until enough force is built up to move them again.

### 13.4.2 Simulating the Frenkel-Kontorova model with ions in lattices (FKI)

Recently proposals have been made that suggest testing the Frenkel-Kontorova model using ions (FKI) trapped in Paul traps with the periodic potential supplied by optical lattices [110]. Very recently, first experiments have been performed by the group of Vlado Vuletić [115][116].

The FKI model is not a perfect analogue for the FK model. In the FKI model a finite chain of ions are held by a linear Paul trap in a string along the axis of the trap. The Coulomb repulsion along with the harmonic confinement yields equilibrium positions for the ions [129] about which they will, to first order, oscillate harmonically.

The periodic potential is an optical lattice generated by a far detuned cavity field (or a very intense standing wave) which generates an optical potential as in section 6. Figure 13.4 shows the resulting potential.

The Hamiltonian of the FKI model is

$$H = \sum_i \left[ \frac{p_i^2}{2m} + \frac{1}{2} m \omega_z^2 x_i^2 + K \cos \left( \frac{2\pi x_i}{\lambda} \right) \right] + \sum_{i < j} \left[ \frac{e^2}{4\pi\epsilon_0 |x_j - x_i|} \right], \quad (13.7)$$

where the first sum runs over the number of ions and the second sum runs over all pairs of ions without double-counting.

Comparing eq. 13.7 with eq. 13.6 we note that there are several deviations from the simple FK model. Firstly, there is a long range, an-harmonic interaction between the ions and, secondly, there is the overall harmonic potential of the trap which confines the ions. The distances between ions will not be uniform, but the ions can still be assumed to sample each phase of the lattice since the lattice is periodic.

The lack of translational symmetry due to the harmonic confinement suggests that the FKI model should not have the same characteristics as the FK model. It turns out however that the FKI model shows a similar phase transition, where at the critical point the restoring force on the chain of ions goes to zero before increasing monotonically above the critical point [111]. The ideal FK model suggests a flat zero restoring force until the critical point.

### 13.4.3 FKI in practice

To actually perform this type of experiment, initial laser cooling is necessary. In our setup it is possible to use the 397 nm transition from  $S_{1/2}$  to  $P_{1/2}$  of the calcium ion with a laser detuned several nanometers from the atomic resonance to limit the scattering. Alternatively we can address the same transition, but with the *very* far detuned 794 nm laser from which 397 nm light is generated, see section 10.5 for details. The cavity of our experiment is coated for both wavelengths and the finesse is higher for 794 nm.

The simplest way of measuring the effect of the FKI friction mode is to apply a static electric field to one end of the Paul trap. This constitutes the  $F_d^{\delta x}$  displacement force. In this case the imaging system, see section 11.3.3, can be used to detect the position of the ions as the force is increased. The ions will have to move over several maxima for the result to be resolvable on the CCD.

Alternatively detection schemes based on measuring the position dependent light shift due to the lattice are used in e.g. [115] giving sub-lattice-site resolution.

### 13.4.4 Further applications of the FKI model

In addition to measuring the mode spectrum and depinning force in the FKI model several other applications have been proposed [115][110]. One application is the study of energy transport in systems like e.g light harvesting molecules.

In the case of molecules it is difficult to control the large number of parameters of the system. In the FKI system though, most parameters can be directly controlled. This can be done through the trap parameters, the strength of the lattice, and by driving parts of the chain with light fields. By using the light fields cooling or heating can be applied. It is then possible to prepare parts of the ion chain in various phonon states using light pulses [229] or coherent state manipulation [163]. In the case of classical motion of the ions one can use a pulsed light field to increase the energy of specific ions in the chain. The number of ions touched is adjustable by e.g. the size of the waist of the beam used.

After exciting chain motion the dynamics of the relaxation can be observed over time and the temperature can be probed using measurements of the dipole transition linewidth or using techniques like the free space qubit laser technique or potentially a cavity thermometry scheme as discussed in section 9.2, though this would require resolved sidebands.

## Chapter 14

# Conclusion

In this thesis we have explained the basic theory ion trapping, laser cooling, and cavity optomechanics, and we have described experiments investigating the interaction between ions and light fields in optical resonators. We have also presented simulations, which suggest that a pulsed Doppler cooling scheme can potentially improve the cooling of ions in the presence of micromotion.

In part 2, experiments performed at MIT with single  $^{88}\text{Sr}^+$  ions in a linear Fabry-Perot resonator were presented. A novel method for measuring the temperature of a single, laser cooled ion using the scattering into a narrow linewidth optical resonator was investigated and compared to standard sideband spectroscopy methods. This new method has potential applications in more complex systems, e.g. molecules. The results of sub-Doppler resolved sideband cavity cooling along the cavity axis were presented. These results improve on those presented in [102], using the same setup in a modified configuration, and complement the results of [103], which are not done in the Lamb-Dicke regime.

In part 3, the design and construction of a new linear Paul trap with an integrated optical resonator, the Blue Cavity trap, was presented. Alignment and assembly has been performed, and the cavity has been characterized. Initial trapping of ions was reported along with preparations for performing pulsed Doppler cooling experiments. Other potential applications of the Blue Cavity trap include investigations and control of the structure of so-called ion Coulomb crystals, and investigations of the dynamics of ions in intracavity generated optical potentials.

## Part IV

# Appendices

# Appendix A

## The calcium ion

Here, we present data on singly ionized calcium (calcium II) used in the experiments performed in Aarhus.

### A.1 Abundance of Ca-isotopes

The abundances of natural calcium are given in table below. Values are those listed as *IUPAC Representative isotopic composition* in [230] so that the uncertainty reflects the range likely encountered in laboratory settings.

Isotope	Abundance
40	96.941(156) %
42	0.647(23) %
43	0.135(10) %
44	2.086(110) %
46	0.004(3) %
48	0.187(21) %

### A.2 Transitions in the $^{40}\text{Ca}^+$ ion

The isotope shifts for the  $S \leftrightarrow P$  transitions (397nm, 393 nm) and the  $D \leftrightarrow P$  transitions (850 nm, 854 nm, 866 nm) are listed here:

Transition	$^{40}\text{Ca}^+$	$^{42}\text{Ca}^+$	$^{43}\text{Ca}^+$	$^{44}\text{Ca}^+$	$^{46}\text{Ca}^+$	$^{48}\text{Ca}^+$
$S \leftrightarrow P$	0	425	688	842	1287	1696
$D \leftrightarrow P$	0	-2350	-3465	-4495	-6478	-8288

Table A.1: Isotope shifts in  $^{40}\text{Ca}^+$  in MHz. Values are taken from Ref. [211].

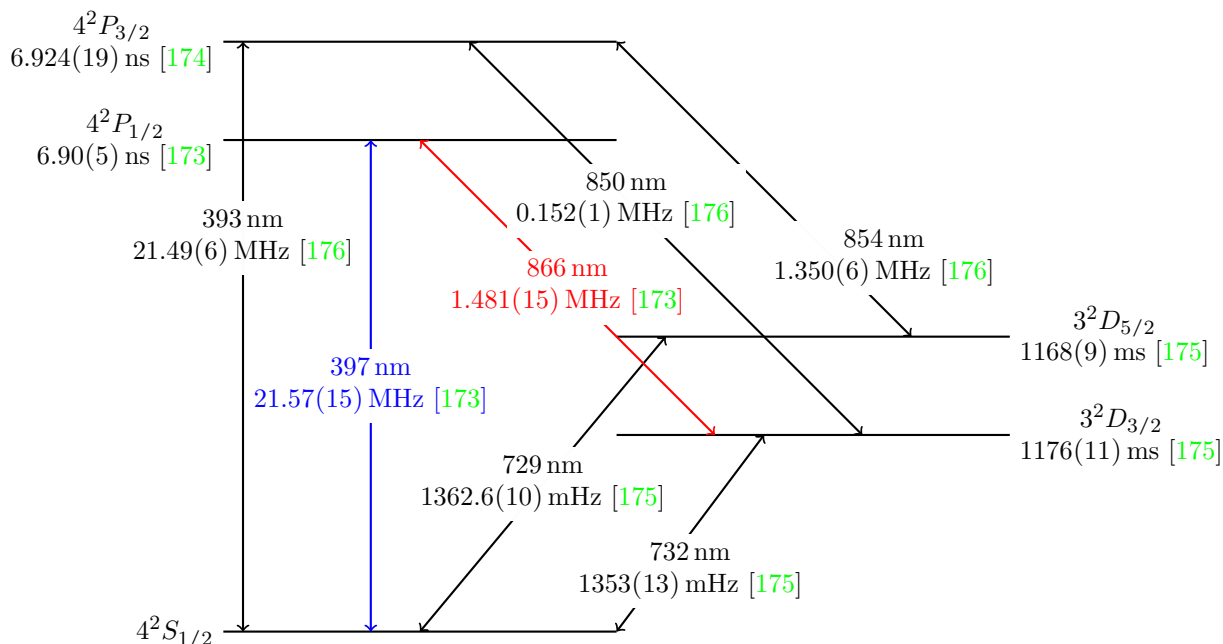


Figure A.1: The level structure of the calcium-40 ion with decay rates, life times, and transition wavelengths. References are given in brackets.

Figure A.2: Tabulated transition data for  $^{40}\text{Ca}^+$ . Wavelengths are measured in vacuum unless stated otherwise. References for all numbers are given in brackets after the number. No reference means that it was measured using the wavemeter in our lab. One value was truncated for space.

Transition	Wavelength [nm]	Frequency [THz]	$\Gamma/2\pi$
$4^2S_{1/2} - 4^2P_{1/2}$	396.958 978 8(9) [231]	755.222 766 2(17) [231]	21.57(15) MHz [173]
$4^2S_{1/2} - 4^2P_{3/2}$	393.477 471 6(3) [232]	761.905 012 7(5) [232]	21.49(6) MHz [176]
$3^2D_{3/2} - 4^2P_{1/2}$	866.214 (air) [233]	346.000 155 [234]	1.481(15) MHz [173]
$3^2D_{3/2} - 4^2P_{3/2}$	849.802 (air) [233]	352.684 [233]	1.481(15) MHz [173]
$3^2D_{5/2} - 4^2P_{3/2}$	854.209 (air) [233]	350.862 351	1.350(6) MHz [176]
$4^2S_{1/2} - 3^2D_{5/2}$	729.347 276 8...	411.042 129 776 393 2(10) [15]	1.3626(10) Hz [175]
$4^2S_{1/2} - 3^2D_{3/2}$	732.389 (air) [233]	409.224 [233]	1.353(13) Hz [175]

The following tables are reproduced from [133]. To determine the coupling strength between dipole allowed transitions between the various Zeeman substates one needs the Clebsch-Gordan coefficients and the corresponding decay rate. These are listed in table A.1 and in tables A.2–A.4. The Clebsch-Gordan coefficients are also defined in e.g. [146].

	$4S_{1/2}, -1/2$	$4S_{1/2}, +1/2$
$4P_{1/2}, -1/2$	$-\sqrt{1/3}$	$\sqrt{2/3}$
$4P_{1/2}, +1/2$	$-\sqrt{2/3}$	$\sqrt{1/3}$
$4P_{3/2}, -3/2$	1	-
$4P_{3/2}, -1/2$	$\sqrt{2/3}$	$\sqrt{1/3}$
$4P_{3/2}, +1/2$	$\sqrt{1/3}$	$\sqrt{2/3}$
$4P_{3/2}, +3/2$	-	1

Table A.2: Clebsch-Gordan coefficients for transitions between the  $4S_{1/2}$  state and the  $4P_{1/2}$  and  $4P_{3/2}$  states.

	$3D_{3/2}, -3/2$	$3D_{3/2}, -1/2$	$3D_{3/2}, +1/2$	$3D_{3/2}, +3/2$
$4P_{1/2}, -1/2$	$\sqrt{1/2}$	$-\sqrt{1/3}$	$\sqrt{1/6}$	-
$4P_{1/2}, +1/2$	-	$\sqrt{1/6}$	$-\sqrt{1/3}$	$\sqrt{1/2}$
$4P_{3/2}, -3/2$	$-\sqrt{3/5}$	$\sqrt{2/5}$	-	-
$4P_{3/2}, -1/2$	$-\sqrt{2/5}$	$-\sqrt{1/15}$	$\sqrt{8/15}$	-
$4P_{3/2}, +1/2$	-	$-\sqrt{8/15}$	$\sqrt{1/15}$	$\sqrt{2/5}$
$4P_{3/2}, +3/2$	-	-	$-\sqrt{2/5}$	$\sqrt{3/5}$

Table A.3: Clebsch-Gordan coefficients for transitions between the  $3D_{3/2}$  state and the  $4P_{1/2}$  and  $4P_{3/2}$  states.

	$4P_{3/2}, -3/2$	$4P_{3/2}, -1/2$	$4P_{3/2}, +1/2$	$4P_{3/2}, +3/2$
$3D_{5/2}, -5/2$	$\sqrt{2/3}$	-	-	-
$3D_{5/2}, -3/2$	$-\sqrt{4/15}$	$\sqrt{2/5}$	-	-
$3D_{5/2}, -1/2$	$\sqrt{1/15}$	$-\sqrt{2/5}$	$\sqrt{1/5}$	-
$3D_{5/2}, +1/2$	-	$\sqrt{1/5}$	$-\sqrt{2/5}$	$\sqrt{1/15}$
$3D_{5/2}, +3/2$	-	-	$\sqrt{2/5}$	$-\sqrt{4/15}$
$3D_{5/2}, +5/2$	-	-	-	$\sqrt{2/3}$

Table A.4: Clebsch-Gordan coefficients for transitions between the  $3D_{5/2}$  state and the  $4P_{3/2}$  state.

## Appendix B

### The strontium ion

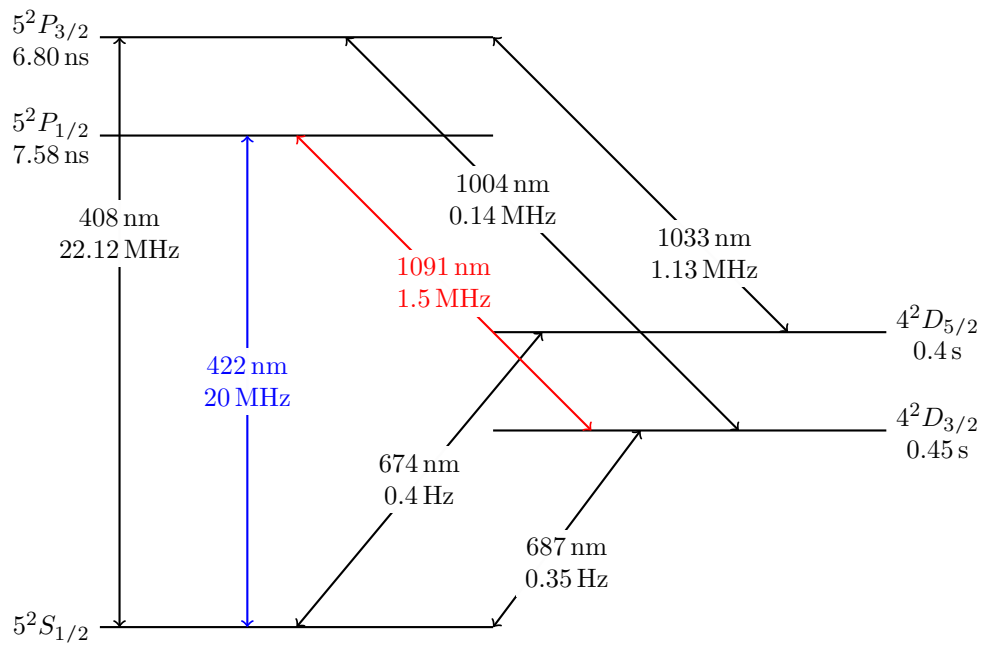


Figure B.1: The level structure of the  $^{88}\text{Sr}^+$  ion with decay rates. All values are from [185] and references therein.

## Appendix C

### The barium ion

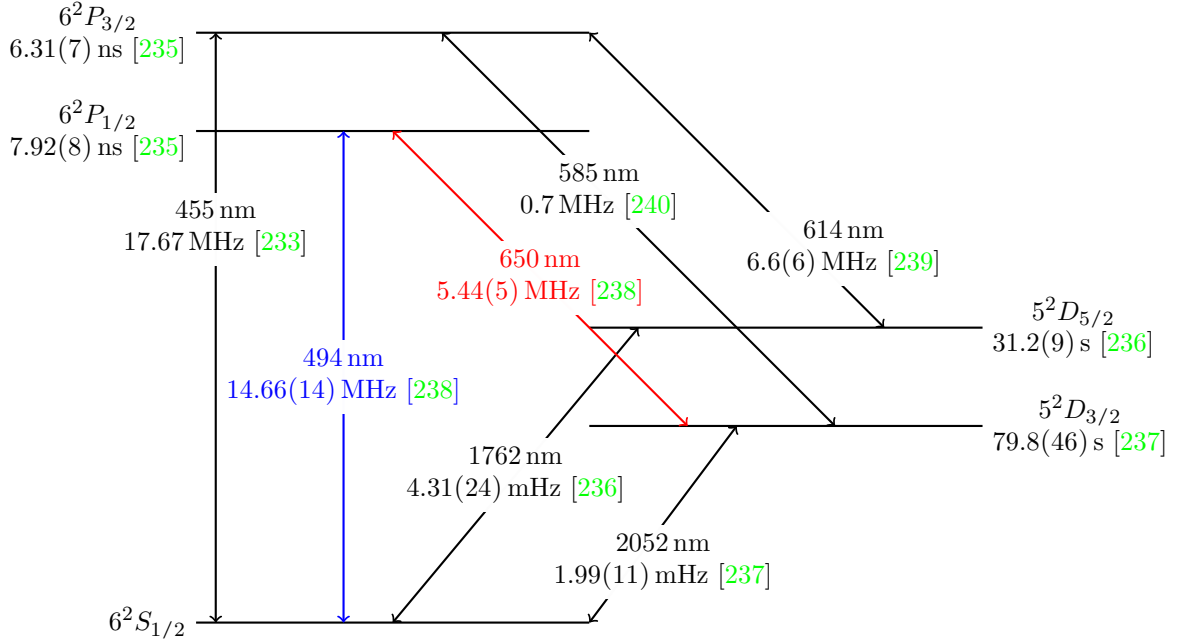
Barium is the 5th element of in Group 2 of the periodic table of the elements ( $A = 56$ ).

#### C.1 Abundance of Ba-isotopes

The abundances of natural barium are given in table below. Values are those listed as *IUPAC Representative isotopic composition* in [230] so that the uncertainty reflects the range likely encountered in laboratory settings.

Isotope	Abundance
130	0.1058(2) %
132	0.1012(2) %
134	2.417(3) %
135	6.592(2) %
136	7.853(4) %
137	11.232(4) %
138	71.699(7) %

#### C.2 Transitions in the $^{138}\text{Ba}^+$ ion

Figure C.1: The level structure of the  $^{138}\text{Ba}^+$  ion with decay rates.

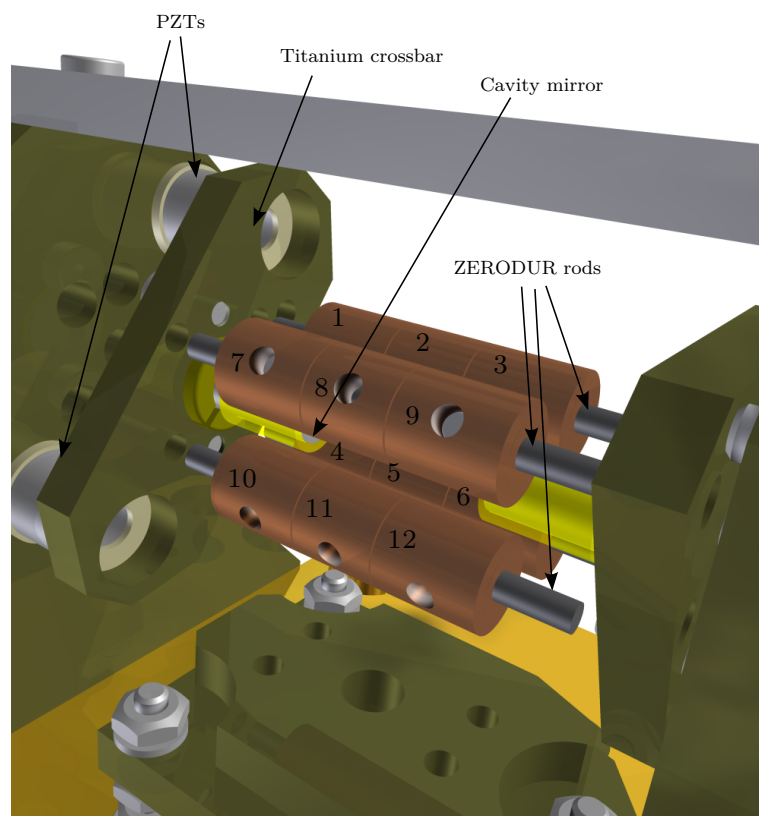
Transition	Wavelength [nm]	f [THz]	$\Gamma/2\pi$
$6^2S_{1/2} - 6^2P_{1/2}$	493.545 433 4 [241]	607.426 262 5(2) [241]	14.66(14) MHz [238]
$6^2S_{1/2} - 6^2P_{3/2}$	455.4033 (air) [233]	658.9415 [233]	17.67 MHz [233]
$5^2D_{3/2} - 6^2P_{1/2}$	649.869 365 98(14) [241]	461.311 878 5(1) [241]	5.44(5) MHz [238]
$5^2D_{3/2} - 6^2P_{3/2}$	585.3675 (air) [233]	512.640 62 [233]	0.95 MHz [233], 0.7 MHz [240]
$5^2D_{5/2} - 6^2P_{3/2}$	614.1713 (air) [239]	488.598 28 [239]	6.6(6) MHz [239]
$5^2D_{3/2} - 5^2D_{5/2}$	12 485.096 [233]	24.012 03 [233]	0.79(13) mHz [236]
$6^2S_{1/2} - 5^2D_{5/2}$	1762.1745 [233]	170.126 43 [233]	4.31(24) mHz [236]
$6^2S_{1/2} - 5^2D_{3/2}$	2051.765 540 1(14) [241]	146.114 384 0(1) [241]	1.99(11) mHz [237]

Figure C.2: Tabulated transition data for  $^{138}\text{Ba}^+$ . Wavelengths are measured in vacuum unless stated otherwise. References for all numbers are given in brackets after the number. References from the NIST Atomic spectra database are listed without uncertainties. Conversions to frequency have used the Ciddor equation [233].

## Appendix D

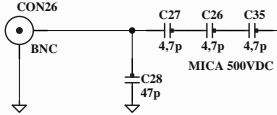
### Additional trap data

Shown below is a close-up of the trap with indication of the numbering scheme used for the electrodes. In this image, the MACOR housing has been suppressed for a better view. The yellow parts are the dielectric cylinders around the cavity mirrors (which are visible through the cylinders). Middle electrode is 5 mm long for scale.



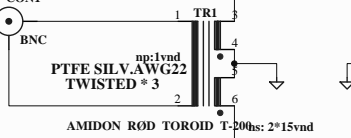
The following page includes a schematic of the rf-dc mixer circuit. A simplified version of this is discussed in chapter 10.

BNC 100:1 Monitor out



RF INPUT 4Mhz

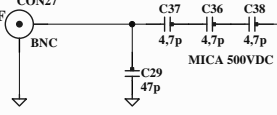
0-> 45W



AIR COOLED

BNC 100:1 Monitor out

CABLE CAP : 110pF

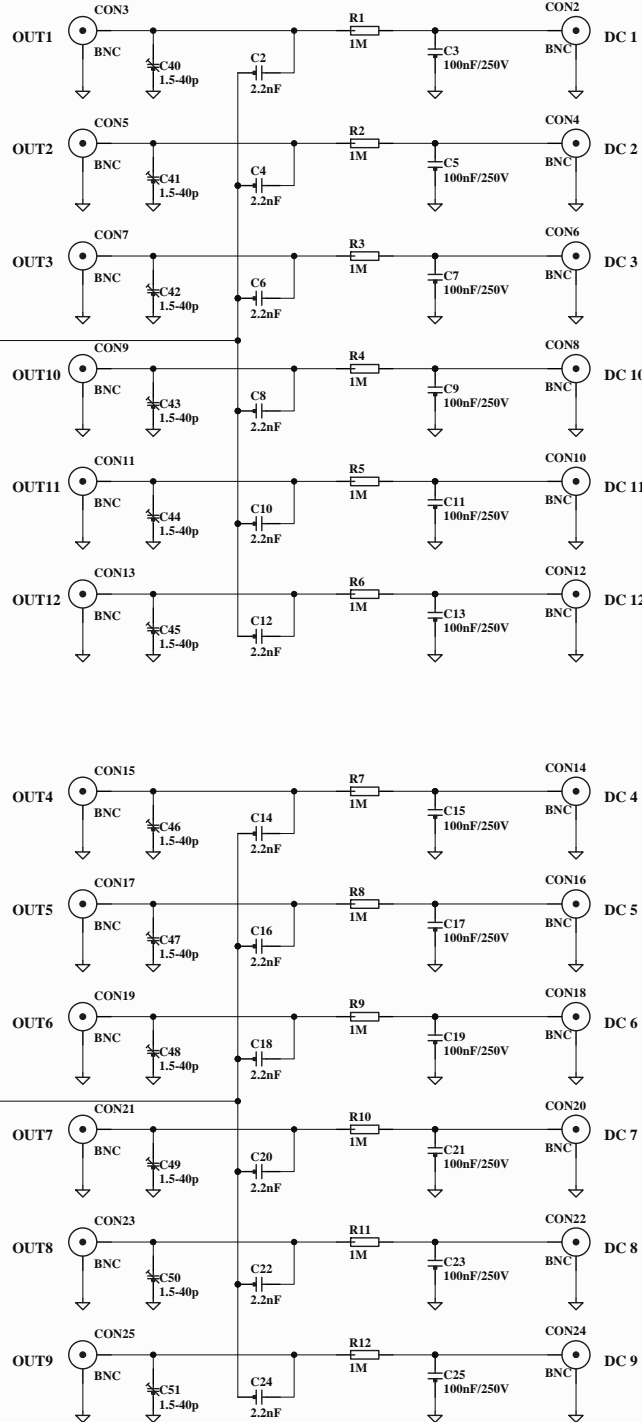


MIXED OUTPUTS

MIXED OUTPUTS

MIXED OUTPUTS

MIXED OUTPUTS



INPUTS

INPUTS

IFA

Title			TRAP CONTROLLER RF 4MHz and DC		
Size	Number	Revision			
A3	DIA669A PC4646A				
Date:	13-05-2015	Sheet	of		
File:	J:\es\99 sch\dia669a\dia669a.sch	Drawn	By: ESO		

# Bibliography

- [1] Brown R. Hanbury and R. Q. Twiss. “Correlation between Photons in two Coherent Beams of Light”. In: *Nature* 177.4497 (Jan. 1956), pp. 27–29. ISSN: 0028-0836. DOI: [10.1038/177027a0](https://doi.org/10.1038/177027a0).
- [2] Jürgen Eschner et al. “Laser cooling of trapped ions”. In: *J. Opt. Soc. Am. B* 20.5 (May 2003), pp. 1003–1015. DOI: [10.1364/JOSAB.20.001003](https://doi.org/10.1364/JOSAB.20.001003). URL: <http://josab.osa.org/abstract.cfm?URI=josab-20-5-1003>.
- [3] Y. B. Zel'Dovich. “Cooling with the aid of high-frequency energy”. In: *ZhETF Pisma Redaktsiiu* 19 (Mar. 1974), p. 120.
- [4] D. Wineland and Hans Dehmelt. “Proposed  $10^{14} \Delta\nu < \nu$  laser fluorescence spectroscopy on  $Tl^+$  mono-ion oscillator III”. In: *Bulletin of the American Physical Society*. Vol. 20. 4. 1975, pp. 637–637.
- [5] T. W. Hansch and A. L. Schawlow. “Cooling of gases by laser radiation”. In: *Optics Communications* 13 (Jan. 1975), p. 68. DOI: [10.1016/0030-4018\(75\)90159-5](https://doi.org/10.1016/0030-4018(75)90159-5).
- [6] D. J. Wineland, R. E. Drullinger, and F. L. Walls. “Radiation-Pressure Cooling of Bound Resonant Absorbers”. In: *Physical Review Letters* 40.25 (June 1978), pp. 1639–1642. ISSN: 0031-9007. DOI: [10.1103/PhysRevLett.40.1639](https://doi.org/10.1103/PhysRevLett.40.1639). URL: <http://dx.doi.org/10.1103/PhysRevLett.40.1639>.
- [7] W. Neuhauser et al. “Optical-Sideband Cooling of Visible Atom Cloud Confined in Parabolic Well”. In: *Physical Review Letters* 41.4 (July 1978), pp. 233–236. ISSN: 0031-9007. DOI: [10.1103/PhysRevLett.41.233](https://doi.org/10.1103/PhysRevLett.41.233). URL: <http://dx.doi.org/10.1103/PhysRevLett.41.233>.
- [8] Nobelprize.org. “*The Nobel Prize in Physics 1997*”. Nobelprize.org. 1997. URL: [http://www.nobelprize.org/nobel\\_prizes/physics/laureates/1997/](http://www.nobelprize.org/nobel_prizes/physics/laureates/1997/).
- [9] F. Diedrich et al. “Laser Cooling To The Zero-Point Energy Of Motion”. In: *Physical Review Letters* 62.4 (Jan. 1989), pp. 403–406. URL: [http://prola.aps.org/abstract/PRL/v62/p403\\_1](http://prola.aps.org/abstract/PRL/v62/p403_1).
- [10] D. Hanneke, S. Fogwell, and G. Gabrielse. “New Measurement of the Electron Magnetic Moment and the Fine Structure Constant”. In: *Physical Review Letters* 100.12 (Mar. 2008). ISSN: 1079-7114. DOI: [10.1103/PhysRevLett.100.120801](https://doi.org/10.1103/PhysRevLett.100.120801). URL: <http://dx.doi.org/10.1103/PhysRevLett.100.120801>.

- [11] The ACME Collaboration et al. “Order of Magnitude Smaller Limit on the Electric Dipole Moment of the Electron”. In: *Science* 343.6168 (2014), pp. 269–272. DOI: [10.1126/science.1248213](https://doi.org/10.1126/science.1248213). eprint: <http://www.sciencemag.org/content/343/6168/269.full.pdf>. URL: <http://www.sciencemag.org/content/343/6168/269.abstract>.
- [12] P. O. Schmidt et al. “Spectroscopy using quantum logic”. In: *Science* 309.5735 (July 2005), pp. 749–752. URL: <http://www.sciencemag.org/cgi/content/abstract/sci;309/5735/749?maxtoshow=&hits=10&RESULTFORMAT=&fulltext=P.O.Schmidt&searchid=1&FIRSTINDEX=0&resourcetype=HWCIT>.
- [13] T. Rosenband et al. “Frequency Ratio of Al+ and Hg+ Single-Ion Optical Clocks; Metrology at the 17th Decimal Place”. In: *Science* 319 (2008), pp. 1808–1812. URL: <http://www.sciencemag.org/cgi/content/abstract/319/5871/1808>.
- [14] C. W. Chou et al. “Frequency Comparison of Two High-Accuracy Al<sup>+</sup> Optical Clocks”. In: *Phys. Rev. Lett.* 104.7 (Feb. 2010), pp. 070802–. URL: <http://link.aps.org/doi/10.1103/PhysRevLett.104.070802>.
- [15] M. Chwalla et al. “Absolute Frequency Measurement of the <sup>40</sup>Ca<sup>+</sup> 4s <sup>2</sup>S<sub>1/2</sub> – 3d <sup>2</sup>D<sub>5/2</sub> Clock Transition”. In: *Phys. Rev. Lett.* 102 (2 Jan. 2009), p. 023002. DOI: [10.1103/PhysRevLett.102.023002](https://doi.org/10.1103/PhysRevLett.102.023002).
- [16] Nobelprize.org. “*The Nobel Prize in Physics 1989*”. Nobelprize.org. 1989. URL: [http://www.nobelprize.org/nobel\\_prizes/physics/laureates/1989/](http://www.nobelprize.org/nobel_prizes/physics/laureates/1989/).
- [17] Nobelprize.org. “*The Nobel Prize in Physics 2001*”. Nobelprize.org. 2001. URL: [http://www.nobelprize.org/nobel\\_prizes/physics/laureates/2001/](http://www.nobelprize.org/nobel_prizes/physics/laureates/2001/).
- [18] Nobelprize.org. “*The Nobel Prize in Physics 2009*”. Nobelprize.org. 2009. URL: [http://www.nobelprize.org/nobel\\_prizes/physics/laureates/2009/](http://www.nobelprize.org/nobel_prizes/physics/laureates/2009/).
- [19] Nobelprize.org. “*The Nobel Prize in Physics 2012*”. Nobelprize.org. 2012. URL: [http://www.nobelprize.org/nobel\\_prizes/physics/laureates/2012/](http://www.nobelprize.org/nobel_prizes/physics/laureates/2012/).
- [20] Bureau International des Poids et Mesures. *SI Brochure: The International System of Units (SI) [8th edition, 2006; updated in 2014]*. BIPM SI units. 2014. URL: <http://www.bipm.org/en/publications/si-brochure/>.
- [21] Richard P. Feynman. “There’s plenty of room at the bottom”. English. In: *Resonance* 16.9 (2011). Transcript published in 2011. The original talk is from 1959., pp. 890–905. ISSN: 0971-8044. DOI: [10.1007/s12045-011-0109-x](https://doi.org/10.1007/s12045-011-0109-x). URL: <http://dx.doi.org/10.1007/s12045-011-0109-x>.
- [22] Richard P. Feynman. “Simulating physics with computers”. In: *Int. J. Theor. Phys.* 21.6-7 (June 1982), pp. 467–488. ISSN: 1572-9575. DOI: [10.1007/bf02650179](https://doi.org/10.1007/bf02650179). URL: <http://dx.doi.org/10.1007/BF02650179>.

- [23] S. Lloyd. “Universal Quantum Simulators”. In: *Science* 273.5278 (Aug. 1996), pp. 1073–1078. ISSN: 1095-9203. DOI: [10.1126/science.273.5278.1073](https://doi.org/10.1126/science.273.5278.1073). URL: <http://dx.doi.org/10.1126/science.273.5278.1073>.
- [24] J. Ignacio Cirac and Peter Zoller. “Goals and opportunities in quantum simulation”. In: *Nature Physics* 8.4 (Apr. 2012), pp. 264–266. ISSN: 1745-2481. DOI: [10.1038/nphys2275](https://doi.org/10.1038/nphys2275). URL: <http://dx.doi.org/10.1038/nphys2275>.
- [25] D. Deutsch. “Quantum Theory, the Church-Turing Principle and the Universal Quantum Computer”. In: *Proceedings of the Royal Society of London A: Mathematical, Physical and Engineering Sciences* 400.1818 (1985), pp. 97–117. ISSN: 0080-4630. DOI: [10.1098/rspa.1985.0070](https://doi.org/10.1098/rspa.1985.0070).
- [26] Lieven M. K. Vandersypen et al. “Experimental realization of Shor’s quantum factoring algorithm using nuclear magnetic resonance”. In: *Nature* 414.6866 (Dec. 2001), pp. 883–887. ISSN: 0028-0836. DOI: [10.1038/414883a](https://doi.org/10.1038/414883a). URL: <http://dx.doi.org/10.1038/414883a>.
- [27] P. W. Shor. “Polynomial-Time Algorithms for Prime Factorization and Discrete Logarithms on a Quantum Computer”. In: *SIAM Review* 41 (Jan. 1999). Paper originally from 1994. Revised in 1997 and electronically published in 1999., pp. 303–332. DOI: [10.1137/S0036144598347011](https://doi.org/10.1137/S0036144598347011).
- [28] L. K. Grover. “Quantum mechanics helps in searching for a needle in a haystack”. In: *Physical Review Letters* 79.2 (July 1997), pp. 325–328. URL: [http://prola.aps.org/abstract/PRL/v79/i2/p325\\_1](http://prola.aps.org/abstract/PRL/v79/i2/p325_1).
- [29] Isaac L. Chuang et al. “Experimental realization of a quantum algorithm”. In: *Nature* 393.6681 (May 1998), pp. 143–146. ISSN: 0028-0836. DOI: [10.1038/30181](https://doi.org/10.1038/30181). URL: <http://dx.doi.org/10.1038/30181>.
- [30] M. A. Nielsen and I. L. Chuang. *Quantum Computation and Quantum Information*. Cambridge University Press, 2000.
- [31] R. Blatt and D. Wineland. “Entangled states of trapped atomic ions”. In: *Nature* 453.7198 (June 2008), pp. 1008–1015. URL: <http://www.nature.com/nature/journal/v453/n7198/abs/nature07125.html>.
- [32] David J. Wineland. “Nobel Lecture: Superposition, entanglement, and raising Schrödinger’s cat”. In: *Rev. Mod. Phys.* 85.3 (July 2013), pp. 1103–1114. ISSN: 1539-0756. DOI: [10.1103/revmodphys.85.1103](https://doi.org/10.1103/revmodphys.85.1103). URL: <http://dx.doi.org/10.1103/RevModPhys.85.1103>.
- [33] Warren Nagourney, Jon Sandberg, and Hans Dehmelt. “Shelved optical electron amplifier: Observation of quantum jumps”. In: *Physical Review Letters* 56.26 (June 1986), pp. 2797–2799. ISSN: 0031-9007. DOI: [10.1103/physrevlett.56.2797](https://doi.org/10.1103/physrevlett.56.2797). URL: <http://dx.doi.org/10.1103/PhysRevLett.56.2797>.
- [34] Th. Sauter et al. “Observation of Quantum Jumps”. In: *Physical Review Letters* 57.14 (Oct. 1986), pp. 1696–1698. ISSN: 0031-9007. DOI: [10.1103/physrevlett.57.1696](https://doi.org/10.1103/physrevlett.57.1696). URL: <http://dx.doi.org/10.1103/PhysRevLett.57.1696>.

- [35] J. C. Bergquist et al. “Observation of Quantum Jumps in a Single Atom”. In: *Physical Review Letters* 57.14 (Oct. 1986), pp. 1699–1702. ISSN: 0031-9007. DOI: [10.1103/physrevlett.57.1699](https://doi.org/10.1103/physrevlett.57.1699). URL: <http://dx.doi.org/10.1103/PhysRevLett.57.1699>.
- [36] F.M. Penning. “Die glimmentladung bei niedrigem druck zwischen koaxialen zylindern in einem axialen magnetfeld”. In: *Physica* 3.9 (1936), pp. 873–894. ISSN: 0031-8914. DOI: [10.1016/S0031-8914\(36\)80313-9](https://doi.org/10.1016/S0031-8914(36)80313-9). URL: <http://www.sciencedirect.com/science/article/pii/S0031891436803139>.
- [37] Wolfgang Paul. “Nobel Lecture: Electromagnetic Traps for Charged and Neutral Particles”. In: ed. by Gösta Ekspång. Nobelprize.org, 1989. URL: [http://www.nobelprize.org/nobel\\_prizes/physics/laureates/1989/paul-lecture.html](http://www.nobelprize.org/nobel_prizes/physics/laureates/1989/paul-lecture.html).
- [38] W. Paul and H. Steinwedel. “Ein Neues Massenspektrometer Ohne Magnetfeld”. In: *Zeitschrift Fur Naturforschung Section A-A Journal Of Physical Sciences* 8.7 (1953), pp. 448–450.
- [39] J. D. Prestage, G. J. Dick, and L. Maleki. “New ion trap for frequency standard applications”. In: *Journal of Applied Physics* 66.3 (1989), p. 1013. ISSN: 0021-8979. DOI: [10.1063/1.343486](https://doi.org/10.1063/1.343486). URL: <http://dx.doi.org/10.1063/1.343486>.
- [40] J. I. Cirac and P. Zoller. “Quantum Computations With Cold Trapped Ions”. In: *Physical Review Letters* 74.20 (May 1995), pp. 4091–4094. URL: [http://prl.aps.org/abstract/PRL/v74/i20/p4091\\_1](http://prl.aps.org/abstract/PRL/v74/i20/p4091_1).
- [41] Klaus Mølmer and Anders Sørensen. “Multiparticle Entanglement of Hot Trapped Ions”. In: *Phys. Rev. Lett.* 82.9 (Mar. 1999), pp. 1835–. URL: <http://link.aps.org/doi/10.1103/PhysRevLett.82.1835>.
- [42] F. Schmidt-Kaler et al. “Realization of the Cirac-Zoller controlled-NOT quantum gate”. In: *Nature* 422.6930 (Mar. 2003), pp. 408–411. URL: <http://www.nature.com/nature/journal/v422/n6930/abs/nature01494.html>.
- [43] D. Leibfried et al. “Experimental demonstration of a robust, high-fidelity geometric two ion-qubit phase gate”. In: *Nature* 422.6930 (Mar. 2003), pp. 412–415. URL: <http://www.nature.com/nature/journal/v422/n6930/abs/nature01492.html>.
- [44] J. Benhelm et al. “Towards fault-tolerant quantum computing with trapped ions”. In: *Nature Physics* 4 (2008), pp. 463–466. URL: <http://www.nature.com/nphys/journal/v4/n6/abs/nphys961.html>.
- [45] T. Monz et al. “Realization of the Quantum Toffoli Gate with Trapped Ions”. In: *Physical Review Letters* 102.4 (Jan. 2009). ISSN: 1079-7114. DOI: [10.1103/physrevlett.102.040501](https://doi.org/10.1103/physrevlett.102.040501). URL: <http://dx.doi.org/10.1103/PhysRevLett.102.040501>.
- [46] Ch. Roos et al. “Quantum State Engineering on an Optical Transition and Decoherence in a Paul Trap”. In: *Phys. Rev. Lett.* 83.23 (Dec. 1999), pp. 4713–4716. URL: <http://link.aps.org/doi/10.1103/PhysRevLett.83.4713>.

- [47] C. F. Roos et al. “Bell states of atoms with ultralong lifetimes and their tomographic state analysis”. In: *Physical Review Letters* 92.22 (June 2004), p. 220402. URL: <http://prola.aps.org/abstract/PRL/v92/i22/e220402>.
- [48] D. Leibfried et al. “Creation of a six-atom ‘Schrödinger cat’ state”. In: *Nature* 438 (2005), pp. 639–642. URL: <http://www.nature.com/nature/journal/v438/n7068/abs/nature04251.html>.
- [49] M. Riebe et al. “Deterministic quantum teleportation with atoms”. In: *Nature* 429 (2004), pp. 734–737. URL: <http://www.nature.com/nature/journal/v429/n6993/abs/nature02570.html>.
- [50] M. D. Barrett et al. “Deterministic quantum teleportation of atomic qubits”. In: *Nature* 429 (2004), pp. 737–739. URL: <http://www.nature.com/nature/journal/v429/n6993/abs/nature02608.html>.
- [51] S. Gulde et al. “Implementation of the Deutsch-Jozsa algorithm on an ion-trap quantum computer”. In: *Nature* 421.6918 (Jan. 2003), pp. 48–50. URL: <http://www.nature.com/nature/journal/v421/n6918/abs/nature01336.html>.
- [52] J. Chiaverini et al. “Implementation of the semiclassical quantum Fourier transform in a scalable system”. In: *Science* 308.5724 (May 2005), pp. 997–1000. URL: <http://proquest.umi.com/pqdlink?Ver=1&Exp=09-08-2013&FMT=7&DID=842609411&RQT=309>.
- [53] H. Häffner et al. “Scalable multiparticle entanglement of trapped ions”. In: *Nature* 438 (2005), pp. 643–646. URL: <http://www.nature.com/nature/journal/v438/n7068/abs/nature04279.html>.
- [54] Thomas Monz et al. “14-Qubit Entanglement: Creation and Coherence”. In: *Physical Review Letters* 106.13 (Mar. 2011). ISSN: 1079-7114. DOI: [10.1103/physrevlett.106.130506](https://doi.org/10.1103/physrevlett.106.130506). URL: <http://dx.doi.org/10.1103/PhysRevLett.106.130506>.
- [55] D. Nigg et al. “Quantum computations on a topologically encoded qubit”. In: *Science* 345.6194 (June 2014), pp. 302–305. ISSN: 1095-9203. DOI: [10.1126/science.1253742](https://doi.org/10.1126/science.1253742). URL: <http://dx.doi.org/10.1126/science.1253742>.
- [56] R. Blatt and C. F. Roos. “Quantum simulations with trapped ions”. In: *Nat. Phys.* 8.4 (Apr. 2012), pp. 277–284. ISSN: 1745-2481. DOI: [10.1038/nphys2252](https://doi.org/10.1038/nphys2252). URL: <http://dx.doi.org/10.1038/nphys2252>.
- [57] Ch. Schneider, Diego Porras, and Tobias Schaetz. “Experimental quantum simulations of many-body physics with trapped ions”. In: *Reports on Progress in Physics* 75.2 (Jan. 2012), p. 024401. ISSN: 1361-6633. DOI: [10.1088/0034-4885/75/2/024401](https://doi.org/10.1088/0034-4885/75/2/024401). URL: <http://dx.doi.org/10.1088/0034-4885/75/2/024401>.
- [58] A. Friedenauer et al. “Simulating a quantum magnet with trapped ions”. In: *Nature Physics* 4.10 (July 2008), pp. 757–761. ISSN: 1745-2481. DOI: [10.1038/nphys1032](https://doi.org/10.1038/nphys1032). URL: <http://dx.doi.org/10.1038/nphys1032>.

- [59] Joseph W. Britton et al. “Engineered two-dimensional Ising interactions in a trapped-ion quantum simulator with hundreds of spins”. In: *Nature* 484.7395 (Apr. 2012), pp. 489–492. ISSN: 1476-4687. DOI: [10.1038/nature10981](https://doi.org/10.1038/nature10981). URL: <http://dx.doi.org/10.1038/nature10981>.
- [60] Philip Richerme et al. “Non-local propagation of correlations in quantum systems with long-range interactions”. In: *Nature* 511.7508 (July 2014), pp. 198–201. ISSN: 1476-4687. DOI: [10.1038/nature13450](https://doi.org/10.1038/nature13450). URL: <http://dx.doi.org/10.1038/nature13450>.
- [61] P. Richerme et al. “Quantum Catalysis of Magnetic Phase Transitions in a Quantum Simulator”. In: *Physical Review Letters* 111.10 (Sept. 2013). ISSN: 1079-7114. DOI: [10.1103/physrevlett.111.100506](https://doi.org/10.1103/physrevlett.111.100506). URL: <http://dx.doi.org/10.1103/PhysRevLett.111.100506>.
- [62] P. Jurcevic et al. “Quasiparticle engineering and entanglement propagation in a quantum many-body system”. In: *Nature* 511.7508 (July 2014), pp. 202–205. ISSN: 1476-4687. DOI: [10.1038/nature13461](https://doi.org/10.1038/nature13461). URL: <http://dx.doi.org/10.1038/nature13461>.
- [63] R. Islam et al. “Emergence and Frustration of Magnetism with Variable-Range Interactions in a Quantum Simulator”. In: *Science* 340.6132 (May 2013), pp. 583–587. ISSN: 1095-9203. DOI: [10.1126/science.1232296](https://doi.org/10.1126/science.1232296). URL: <http://dx.doi.org/10.1126/science.1232296>.
- [64] S. Ulm et al. “Observation of the Kibble-Zurek scaling law for defect formation in ion crystals”. In: *Nat. Comms.* 4 (Aug. 2013). ISSN: 2041-1723. DOI: [10.1038/ncomms3290](https://doi.org/10.1038/ncomms3290). URL: <http://dx.doi.org/10.1038/ncomms3290>.
- [65] K. Pyka et al. “Topological defect formation and spontaneous symmetry breaking in ion Coulomb crystals”. In: *Nat. Comms.* 4 (Aug. 2013). ISSN: 2041-1723. DOI: [10.1038/ncomms3291](https://doi.org/10.1038/ncomms3291). URL: <http://dx.doi.org/10.1038/ncomms3291>.
- [66] Sam Genway et al. “Generalized Dicke Nonequilibrium Dynamics in Trapped Ions”. In: *Physical Review Letters* 112.2 (Jan. 2014). ISSN: 1079-7114. DOI: [10.1103/physrevlett.112.023603](https://doi.org/10.1103/physrevlett.112.023603). URL: <http://dx.doi.org/10.1103/PhysRevLett.112.023603>.
- [67] S. Korenblit et al. “Quantum simulation of spin models on an arbitrary lattice with trapped ions”. In: *New Journal of Physics* 14.9 (Sept. 2012), p. 095024. ISSN: 1367-2630. DOI: [10.1088/1367-2630/14/9/095024](https://doi.org/10.1088/1367-2630/14/9/095024). URL: <http://dx.doi.org/10.1088/1367-2630/14/9/095024>.
- [68] S. Haroche and J. M. Raimond. *Exploring the quantum: atoms, cavities, and photons*. Oxford University Press, 2006.
- [69] H. J. Kimble. “Strong interactions of single atoms and photons in cavity QED”. In: *Phys. Scripta* T76 (1998), pp. 127–137. URL: <http://www.iop.org/EJ/abstract/1402-4896/1998/T76/019>.
- [70] R. G. Hulet, E. S. Hilfer, and D. Kleppner. “Inhibited Spontaneous Emission By A Rydberg Atom”. In: *Physical Review Letters* 55.20 (1985), pp. 2137–2140. URL: [http://prola.aps.org/abstract/PRL/v55/i20/p2137\\_1](http://prola.aps.org/abstract/PRL/v55/i20/p2137_1).

- [71] F. Demartini et al. “Anomalous Spontaneous Emission Time In A Microscopic Optical Cavity”. In: *Physical Review Letters* 59.26 (Dec. 1987), pp. 2955–2958. URL: [http://prola.aps.org/abstract/PRL/v59/i26/p2955\\_1](http://prola.aps.org/abstract/PRL/v59/i26/p2955_1).
- [72] D. J. Heinzen et al. “Enhanced And Inhibited Visible Spontaneous Emission By Atoms In A Confocal Resonator”. In: *Physical Review Letters* 58.13 (Mar. 1987), pp. 1320–1323. URL: [http://prola.aps.org/abstract/PRL/v58/i13/p1320\\_1](http://prola.aps.org/abstract/PRL/v58/i13/p1320_1).
- [73] Daniel Kleppner. “Inhibited Spontaneous Emission”. In: *Physical Review Letters* 47.4 (July 1981), pp. 233–236. ISSN: 0031-9007. DOI: [10.1103/physrevlett.47.233](https://doi.org/10.1103/physrevlett.47.233). URL: <http://dx.doi.org/10.1103/PhysRevLett.47.233>.
- [74] A. Boca et al. “Observation of the Vacuum Rabi Spectrum for One Trapped Atom”. In: *Phys. Rev. Lett.* 93.23 (Dec. 2004), pp. 233603–. URL: <http://link.aps.org/doi/10.1103/PhysRevLett.93.233603>.
- [75] J. McKeever et al. “Deterministic generation of single photons from one atom trapped in a cavity”. In: *Science* 303.5666 (Mar. 2004), pp. 1992–1994. URL: <http://www.sciencemag.org/cgi/content/abstract/303/5666/1992>.
- [76] J. McKeever et al. “Experimental realization of a one-atom laser in the regime of strong coupling”. In: *Nature* 425.6955 (Sept. 2003), pp. 268–271. ISSN: 1476-4679. DOI: [10.1038/nature01974](https://doi.org/10.1038/nature01974). URL: <http://dx.doi.org/10.1038/nature01974>.
- [77] P. F. Herskind et al. “Realization of collective strong coupling with ion Coulomb crystals in an optical cavity”. In: *Nature Phys.* 5.7 (July 2009), pp. 494–498. URL: <http://www.nature.com/nphys/journal/v5/n7/full/nphys1302.html>.
- [78] Magnus Albert, Aurelien Dantan, and Michael Drewsen. “Cavity electromagnetically induced transparency and all-optical switching using ion Coulomb crystals”. In: *Nat. Photon.* 5.10 (Oct. 2011), pp. 633–636. ISSN: 1749-4885. URL: <http://dx.doi.org/10.1038/nphoton.2011.214>.
- [79] Peter F. Herskind et al. “Microfabricated surface ion trap on a high-finesse optical mirror”. In: *Opt. Lett.* 36.16 (2011), p. 3045. ISSN: 1539-4794. DOI: [10.1364/ol.36.003045](https://doi.org/10.1364/ol.36.003045). URL: <http://dx.doi.org/10.1364/OL.36.003045>.
- [80] Matthias Steiner et al. “Single Ion Coupled to an Optical Fiber Cavity”. In: *Physical Review Letters* 110.4 (Jan. 2013). ISSN: 1079-7114. DOI: [10.1103/physrevlett.110.043003](https://doi.org/10.1103/physrevlett.110.043003). URL: <http://dx.doi.org/10.1103/PhysRevLett.110.043003>.
- [81] Hiroki Takahashi et al. “An integrated fiber trap for single-ion photonics”. In: *New J. Phys.* 15.5 (May 2013), p. 053011. ISSN: 1367-2630. DOI: [10.1088/1367-2630/15/5/053011](https://doi.org/10.1088/1367-2630/15/5/053011). URL: <http://dx.doi.org/10.1088/1367-2630/15/5/053011>.
- [82] B. Brandstätter et al. “Integrated fiber-mirror ion trap for strong ion-cavity coupling”. In: *Review of Scientific Instruments* 84.12 (2013), p. 123104. ISSN: 0034-6748. DOI: [10.1063/1.4838696](https://doi.org/10.1063/1.4838696). URL: <http://dx.doi.org/10.1063/1.4838696>.

- [83] G. R. Guthohrlein et al. “A single ion as a nanoscopic probe of an optical field”. In: *Nature* 414.6859 (Nov. 2001), pp. 49–51. URL: <http://www.nature.com/nature/journal/v414/n6859/abs/414049a0.html>.
- [84] M. Keller et al. “Continuous generation of single photons with controlled waveform in an ion-trap cavity system”. In: *Nature* 431.7012 (Oct. 2004), pp. 1075–1078. URL: <http://www.nature.com/nature/journal/v431/n7012/full/nature02961.html>.
- [85] A. B. Mundt et al. “Coupling a single atomic quantum bit to a high finesse optical cavity”. In: *Phys. Rev. Lett.* 89.10 (Sept. 2002), p. 103001. URL: <http://prola.aps.org/abstract/PRL/v89/i10/e103001>.
- [86] A. Kreuter et al. “Spontaneous emission lifetime of a single trapped Ca<sup>+</sup> ion in a high finesse cavity”. In: *Physical Review Letters* 92.20 (May 2004), p. 203002. URL: <http://prola.aps.org/abstract/PRL/v92/i20/e203002>.
- [87] Francois Dubin et al. “Quantum to classical transition in a single-ion laser”. In: *Nat. Phys.* 6.5 (May 2010), pp. 350–353. ISSN: 1745-2473. URL: <http://dx.doi.org/10.1038/nphys1627>.
- [88] A. Stute et al. “Tunable ion-photon entanglement in an optical cavity”. In: *Nature* 485.7399 (May 2012), pp. 482–485. ISSN: 0028-0836. URL: <http://dx.doi.org/10.1038/nature11120>.
- [89] B. Casabone et al. “Enhanced Quantum Interface with Collective Ion-Cavity Coupling”. In: *Physical Review Letters* 114.2 (Jan. 2015). ISSN: 1079-7114. DOI: [10.1103/physrevlett.114.023602](https://doi.org/10.1103/physrevlett.114.023602). URL: <http://dx.doi.org/10.1103/PhysRevLett.114.023602>.
- [90] T. E. Northup and R. Blatt. “Quantum information transfer using photons”. In: *Nature Photon* 8.5 (Apr. 2014), pp. 356–363. ISSN: 1749-4893. DOI: [10.1038/nphoton.2014.53](https://doi.org/10.1038/nphoton.2014.53). URL: <http://dx.doi.org/10.1038/nphoton.2014.53>.
- [91] A. Stute et al. “Quantum-state transfer from an ion to a photon”. In: *Nature Photon* 7.3 (Feb. 2013), pp. 219–222. ISSN: 1749-4893. DOI: [10.1038/nphoton.2012.358](https://doi.org/10.1038/nphoton.2012.358). URL: <http://dx.doi.org/10.1038/nphoton.2012.358>.
- [92] V. Vuletic and S. Chu. “Laser Cooling of Atoms, Ions, or Molecules by Coherent Scattering”. In: *Physical Review Letters* 84 (2000), pp. 3787–3790. URL: [http://prola.aps.org/abstract/PRL/v84/i17/p3787\\_1](http://prola.aps.org/abstract/PRL/v84/i17/p3787_1).
- [93] Peter Horak et al. “Cavity-Induced Atom Cooling in the Strong Coupling Regime”. In: *Physical Review Letters* 79.25 (Dec. 1997), pp. 4974–4977. ISSN: 1079-7114. DOI: [10.1103/physrevlett.79.4974](https://doi.org/10.1103/physrevlett.79.4974). URL: <http://dx.doi.org/10.1103/PhysRevLett.79.4974>.
- [94] K. Murr et al. “Three-dimensional cavity cooling and trapping in an optical lattice”. In: *Physical Review A* 73.6 (June 2006). ISSN: 1094-1622. DOI: [10.1103/physreva.73.063415](https://doi.org/10.1103/physreva.73.063415). URL: <http://dx.doi.org/10.1103/PhysRevA.73.063415>.

- [95] K. Murr. “Large Velocity Capture Range and Low Temperatures with Cavities”. In: *Physical Review Letters* 96.25 (June 2006). ISSN: 1079-7114. DOI: [10.1103/physrevlett.96.253001](https://doi.org/10.1103/physrevlett.96.253001). URL: <http://dx.doi.org/10.1103/PhysRevLett.96.253001>.
- [96] Stefano Zippilli and Giovanna Morigi. “Cooling Trapped Atoms in Optical Resonators”. In: *Physical Review Letters* 95.14 (Sept. 2005). ISSN: 1079-7114. DOI: [10.1103/physrevlett.95.143001](https://doi.org/10.1103/physrevlett.95.143001). URL: <http://dx.doi.org/10.1103/PhysRevLett.95.143001>.
- [97] Marc Bienert and Giovanna Morigi. “Cooling the motion of a trapped atom with a cavity field”. In: *Physical Review A* 86.5 (Nov. 2012). ISSN: 1094-1622. DOI: [10.1103/physreva.86.053402](https://doi.org/10.1103/physreva.86.053402). URL: <http://dx.doi.org/10.1103/PhysRevA.86.053402>.
- [98] Vladan Vuletić, Hilton W. Chan, and Adam T. Black. “Three-dimensional cavity Doppler cooling and cavity sideband cooling by coherent scattering”. In: *Physical Review A* 64.3 (Aug. 2001). ISSN: 1094-1622. DOI: [10.1103/physreva.64.033405](https://doi.org/10.1103/physreva.64.033405). URL: <http://dx.doi.org/10.1103/PhysRevA.64.033405>.
- [99] P. Maunz et al. “Cavity cooling of a single atom”. In: *Nature* 428.6978 (Mar. 2004), pp. 50–52. ISSN: 0028-0836. URL: <http://dx.doi.org/10.1038/nature02387>.
- [100] Andreas Reiserer et al. “Ground-State Cooling of a Single Atom at the Center of an Optical Cavity”. In: *Physical Review Letters* 110.22 (May 2013). ISSN: 1079-7114. DOI: [10.1103/physrevlett.110.223003](https://doi.org/10.1103/physrevlett.110.223003). URL: <http://dx.doi.org/10.1103/PhysRevLett.110.223003>.
- [101] Peter Horak and Helmut Ritsch. “Dissipative dynamics of Bose condensates in optical cavities”. In: *Physical Review A* 63.2 (Jan. 2001). ISSN: 1094-1622. DOI: [10.1103/physreva.63.023603](https://doi.org/10.1103/physreva.63.023603). URL: <http://dx.doi.org/10.1103/PhysRevA.63.023603>.
- [102] D. R. Leibbrandt et al. “Cavity Sideband Cooling of a Single Trapped Ion”. In: *Phys. Rev. Lett.* 103.10 (Sept. 2009), p. 103001. URL: <http://prl.aps.org/abstract/PRL/v103/i10/e103001>.
- [103] Boon Leng Chuah et al. “Sub-Doppler cavity cooling beyond the Lamb-Dicke regime”. In: *Phys. Rev. A* 87 (4 Apr. 2013), p. 043420. DOI: [10.1103/PhysRevA.87.043420](https://doi.org/10.1103/PhysRevA.87.043420). URL: <http://link.aps.org/doi/10.1103/PhysRevA.87.043420>.
- [104] R. Grimm, M. Weidemüller, and Y. B. Ovchinnikov. “Optical Dipole Traps for Neutral Atoms”. In: *Advances in Atomic Molecular and Optical Physics* 42 (2000), pp. 95–170. DOI: [10.1016/S1049-250X\(08\)60186-X](https://doi.org/10.1016/S1049-250X(08)60186-X). eprint: <http://arxiv.org/abs/physics/9902072>.
- [105] Ch. Schneider et al. “Optical trapping of an ion”. In: *Nature Photon* 4.11 (Oct. 2010), pp. 772–775. ISSN: 1749-4893. DOI: [10.1038/nphoton.2010.236](https://doi.org/10.1038/nphoton.2010.236). URL: <http://dx.doi.org/10.1038/nphoton.2010.236>.
- [106] Thomas Huber et al. “A far-off-resonance optical trap for a Ba<sup>+</sup> ion”. In: *Nat. Comms.* 5 (Nov. 2014), p. 5587. ISSN: 2041-1723. DOI: [10.1038/ncomms6587](https://doi.org/10.1038/ncomms6587). URL: <http://dx.doi.org/10.1038/ncomms6587>.

- [107] Rasmus B. Linnet et al. “Pinning an Ion with an Intracavity Optical Lattice”. In: *Phys. Rev. Lett.* 109 (23 Dec. 2012), p. 233005. DOI: [10.1103/PhysRevLett.109.233005](https://doi.org/10.1103/PhysRevLett.109.233005). URL: <http://link.aps.org/doi/10.1103/PhysRevLett.109.233005>.
- [108] Martin Enderlein et al. “Single Ions Trapped in a One-Dimensional Optical Lattice”. In: *Physical Review Letters* 109.23 (Dec. 2012). ISSN: 1079-7114. DOI: [10.1103/physrevlett.109.233004](https://doi.org/10.1103/physrevlett.109.233004). URL: <http://dx.doi.org/10.1103/PhysRevLett.109.233004>.
- [109] Marko Cetina et al. “One-dimensional array of ion chains coupled to an optical cavity”. In: *New J. Phys.* 15.5 (May 2013), p. 053001. ISSN: 1367-2630. DOI: [10.1088/1367-2630/15/5/053001](https://doi.org/10.1088/1367-2630/15/5/053001). URL: <http://dx.doi.org/10.1088/1367-2630/15/5/053001>.
- [110] Thaned Pruttivarasin et al. “Trapped ions in optical lattices for probing oscillator chain models”. In: *New Journal of Physics* 13.7 (2011), p. 075012. URL: <http://stacks.iop.org/1367-2630/13/i=7/a=075012>.
- [111] I. García-Mata, O. V. Zhirov, and D. L. Shepelyansky. “Frenkel-Kontorova model with cold trapped ions”. English. In: *The European Physical Journal D* 41.2 (2007), pp. 325–330. ISSN: 1434-6060. DOI: [10.1140/epjd/e2006-00220-2](https://doi.org/10.1140/epjd/e2006-00220-2). URL: <http://dx.doi.org/10.1140/epjd/e2006-00220-2>.
- [112] Ya. I. Frenkel and T. Kontorova. “The model of dislocation in solid body”. In: *Zh. Eksp. Teor. Fiz* 8.1340 (1938).
- [113] Serge Aubry. “The twist map, the extended Frenkel-Kontorova model and the devils staircase”. In: *Physica D: Nonlinear Phenomena* 7.1–3 (1983), pp. 240–258. ISSN: 0167-2789. DOI: [10.1016/0167-2789\(83\)90129-X](https://doi.org/10.1016/0167-2789(83)90129-X). URL: <http://www.sciencedirect.com/science/article/pii/016727898390129X>.
- [114] Oleg M. Braun and Yuri S. Kivshar. “Nonlinear dynamics of the Frenkel-Kontorova model”. In: *Physics Reports* 306.1-2 (Dec. 1998), pp. 1–108. ISSN: 0370-1573. DOI: [10.1016/S0370-1573\(98\)00029-5](https://doi.org/10.1016/S0370-1573(98)00029-5). URL: [http://dx.doi.org/10.1016/S0370-1573\(98\)00029-5](http://dx.doi.org/10.1016/S0370-1573(98)00029-5).
- [115] Alexei Bylinskii, Dorian Gangloff, and Vladan Vuletic. “Tuning friction atom-by-atom in an ion-crystal simulator”. In: *Science* 348.6239 (2015), pp. 1115–1118. DOI: [10.1126/science.1261422](https://doi.org/10.1126/science.1261422). eprint: <http://www.sciencemag.org/content/348/6239/1115.full.pdf>. URL: <http://www.sciencemag.org/content/348/6239/1115.abstract>.
- [116] D. Gangloff et al. “Velocity tuning of friction with two trapped atoms”. In: *ArXiv e-prints* (May 2015). arXiv: [1505.01828](https://arxiv.org/abs/1505.01828) [[physics.atom-ph](https://arxiv.org/abs/1505.01828)].
- [117] E. L. Raab et al. “Trapping of Neutral Sodium Atoms with Radiation Pressure”. In: *Physical Review Letters* 59.23 (Dec. 1987), pp. 2631–2634. ISSN: 0031-9007. DOI: [10.1103/physrevlett.59.2631](https://doi.org/10.1103/physrevlett.59.2631). URL: <http://dx.doi.org/10.1103/PhysRevLett.59.2631>.
- [118] Samuel Earnshaw. “On the Nature of the Molecular Forces which Regulate the Constitution of the Luminiferous Ether”. In: *Transactions of the Cambridge Philosophical Society* 7 (Mar. 1839). Published in 1842, p. 97. URL: <http://www.mit.edu/~kardar/research/seminars/Casimir2010/pdf/EarnshawPaper.pdf>.

- [119] K. Blaum, Y. Novikov, and G. Werth. “Penning traps as a versatile tool for precise experiments in fundamental physics”. In: *Contemporary Physics* 51 (Mar. 2010), pp. 149–175. DOI: [10.1080/00107510903387652](https://doi.org/10.1080/00107510903387652). arXiv: [0909.1095](https://arxiv.org/abs/0909.1095) [physics.atom-ph].
- [120] Lowell S. Brown and Gerald Gabrielse. “Geonium theory: Physics of a single electron or ion in a Penning trap”. In: *Rev. Mod. Phys.* 58.1 (Jan. 1986), pp. 233–311. ISSN: 0034-6861. DOI: [10.1103/revmodphys.58.233](https://doi.org/10.1103/revmodphys.58.233). URL: <http://dx.doi.org/10.1103/RevModPhys.58.233>.
- [121] M. Drewsen and A. Brøner. “Harmonic linear Paul trap: Stability diagram and effective potentials”. In: *Physical Review A* 6204.4 (Oct. 2000), p. 045401. URL: <http://prola.aps.org/abstract/PRA/v62/i4/e045401>.
- [122] D. J. Berkeland et al. “Minimization of ion micromotion in a Paul trap”. In: *Journal of Applied Physics* 83.10 (1998), p. 5025. ISSN: 0021-8979. DOI: [10.1063/1.367318](https://doi.org/10.1063/1.367318). URL: <http://dx.doi.org/10.1063/1.367318>.
- [123] D. R. Denison. “Operating Parameters of a Quadrupole in a Grounded Cylindrical Housing”. In: *Journal of Vacuum Science & Technology* 8.1 (1971), pp. 266–269. DOI: [10.1116/1.1316304](https://doi.org/10.1116/1.1316304).
- [124] M Abramowitz and I. A. Stegun. *Handbook of Mathematical Functions With Formulas, Graphs, and Mathematical Tables*. National Bureau of Standards, 1964.
- [125] Daniel H. E. Dubin and T. M. O’Neil. “Trapped nonneutral plasmas, liquids, and crystals (the thermal equilibrium states)”. In: *Rev. Mod. Phys.* 71.1 (Jan. 1999), pp. 87–172. ISSN: 1539-0756. DOI: [10.1103/revmodphys.71.87](https://doi.org/10.1103/revmodphys.71.87). URL: <http://dx.doi.org/10.1103/RevModPhys.71.87>.
- [126] Michael Drewsen. “Ion Coulomb crystals”. In: *Physica B: Condensed Matter* 460 (2015). Special Issue on Electronic Crystals (ECRYs-2014), pp. 105–113. ISSN: 0921-4526. DOI: [10.1016/j.physb.2014.11.050](https://doi.org/10.1016/j.physb.2014.11.050). URL: <http://www.sciencedirect.com/science/article/pii/S0921452614008849>.
- [127] Stefan Willitsch et al. “Chemical applications of laser- and sympathetically-cooled ions in ion traps”. In: *Phys. Chem. Chem. Phys.* 10 (48 2008), pp. 7200–7210. DOI: [10.1039/B813408C](https://doi.org/10.1039/B813408C).
- [128] J. P. Schiffer. “Phase transitions in anisotropically confined ionic crystals”. In: *Physical Review Letters* 70.6 (Feb. 1993), pp. 818–821. ISSN: 0031-9007. DOI: [10.1103/physrevlett.70.818](https://doi.org/10.1103/physrevlett.70.818).
- [129] D. F. V. James. “Quantum dynamics of cold trapped ions with application to quantum computation”. In: *Applied Physics B-Lasers And Optics* 66.2 (Feb. 1998), pp. 181–190. URL: <http://www.springerlink.com/content/01e0nug5v1v9dta2/>.
- [130] D. G. Enzer et al. “Observation of Power-Law Scaling for Phase Transitions in Linear Trapped Ion Crystals”. In: *Physical Review Letters* 85.12 (Sept. 2000), pp. 2466–2469. ISSN: 1079-7114. DOI: [10.1103/physrevlett.85.2466](https://doi.org/10.1103/physrevlett.85.2466). URL: <http://dx.doi.org/10.1103/PhysRevLett.85.2466>.

- [131] M. Mielenz et al. “Trapping of Topological-Structural Defects in Coulomb Crystals”. In: *Physical Review Letters* 110.13 (Mar. 2013). ISSN: 1079-7114. DOI: [10.1103/physrevlett.110.133004](https://doi.org/10.1103/physrevlett.110.133004). URL: <http://dx.doi.org/10.1103/PhysRevLett.110.133004>.
- [132] H. Landa et al. “Modes of oscillation in radiofrequency Paul traps”. In: *New Journal of Physics* 14.9 (Sept. 2012), p. 093023. ISSN: 1367-2630. DOI: [10.1088/1367-2630/14/9/093023](https://doi.org/10.1088/1367-2630/14/9/093023). URL: <http://dx.doi.org/10.1088/1367-2630/14/9/093023>.
- [133] Peter Herskind. “Cavity Quantum Electrodynamics with Ion Coulomb Crystals”. PhD thesis. University of Aarhus, Sept. 2008. URL: [http://phys.au.dk/fileadmin/site\\_files/publikationer/phd/Peter\\_Herskind.pdf](http://phys.au.dk/fileadmin/site_files/publikationer/phd/Peter_Herskind.pdf).
- [134] L. Hornekær et al. “Structural properties of two-component Coulomb crystals in linear Paul traps”. In: *Physical Review Letters* 86.10 (Mar. 2001), pp. 1994–1997. URL: [http://prola.aps.org/abstract/PRL/v86/i10/p1994\\_1](http://prola.aps.org/abstract/PRL/v86/i10/p1994_1).
- [135] L. Turner. “Collective Effects On Equilibria Of Trapped Charged Plasmas”. In: *Physics Of Fluids* 30.10 (Oct. 1987), pp. 3196–3203. DOI: [10.1063/1.866495](https://doi.org/10.1063/1.866495). URL: <http://dx.doi.org/10.1063/1.866495>.
- [136] Daniel H. E. Dubin and J. P. Schiffer. “Normal modes of cold confined one-component plasmas”. In: *Phys. Rev. E* 53 (5 May 1996), pp. 5249–5267. DOI: [10.1103/PhysRevE.53.5249](https://doi.org/10.1103/PhysRevE.53.5249). URL: <http://link.aps.org/doi/10.1103/PhysRevE.53.5249>.
- [137] A. Mortensen et al. “Observation of three-dimensional long-range order in small ion Coulomb crystals in an rf trap”. In: *Physical Review Letters* 96.10 (Mar. 2006), p. 103001. URL: <http://dx.doi.org/10.1103/PhysRevLett.96.103001>.
- [138] A. Mortensen et al. “Radio frequency field-induced persistent long-range ordered structures in two-species ion Coulomb crystals”. In: *Journal Of Physics B-Atomic Molecular And Optical Physics* 40.15 (Aug. 2007), F223–F229. URL: <http://www.iop.org/EJ/abstract/0953-4075/40/15/F01>.
- [139] J. P. Schiffer. “Melting of Crystalline Confined Plasmas”. In: *Physical Review Letters* 88.20 (May 2002). ISSN: 1079-7114. DOI: [10.1103/physrevlett.88.205003](https://doi.org/10.1103/physrevlett.88.205003). URL: <http://dx.doi.org/10.1103/PhysRevLett.88.205003>.
- [140] D. J. Wineland et al. “Atomic-Ion Coulomb Clusters In An Ion Trap”. In: *Physical Review Letters* 59.26 (Dec. 1987), pp. 2935–2938. URL: [http://prola.aps.org/abstract/PRL/v59/i26/p2935\\_1](http://prola.aps.org/abstract/PRL/v59/i26/p2935_1).
- [141] F. Diedrich et al. “Observation Of A Phase-Transition Of Stored Laser-Cooled Ions”. In: *Physical Review Letters* 59.26 (Dec. 1987), pp. 2931–2934. URL: [http://prola.aps.org/abstract/PRL/v59/i26/p2931\\_1](http://prola.aps.org/abstract/PRL/v59/i26/p2931_1).

- [142] Kasper R. Zangenberg, Aurélien Dantan, and Michael Drewsen. “Spatial mode effects in a cavity EIT-based quantum memory with ion Coulomb crystals”. In: *Journal of Physics B: Atomic, Molecular and Optical Physics* 45.12 (June 2012), p. 124011. ISSN: 1361-6455. DOI: [10.1088/0953-4075/45/12/124011](https://doi.org/10.1088/0953-4075/45/12/124011). URL: <http://dx.doi.org/10.1088/0953-4075/45/12/124011>.
- [143] A. Mortensen. “Aspects of Ion Coulomb Crystal based Quantum Memory for Light”. PhD thesis. University of Aarhus, 2005. URL: [http://phys.au.dk/fileadmin/site\\_files/forskning/iontrap/pdfs/PhD\\_Mortensen\\_2005.pdf](http://phys.au.dk/fileadmin/site_files/forskning/iontrap/pdfs/PhD_Mortensen_2005.pdf).
- [144] Kyle Arnold et al. “Prospects for atomic clocks based on large ion crystals”. In: (July 2015). eprint: <http://arxiv.org/abs/1507.02028>.
- [145] P. A. M. Dirac. “A new notation for quantum mechanics”. In: *Proceedings of the Cambridge Philosophical Society* 35 (1939), p. 416. DOI: [10.1017/S0305004100021162](https://doi.org/10.1017/S0305004100021162).
- [146] B. H. Bransden and C. J. Joachain. *Physics of Atoms and Molecules*. second. Prentice Hall, 2003.
- [147] J. J. Sakurai. *Modern Quantum Mechanics*. Ed. by S. F. Tuan. Addison-Wesley, 1994.
- [148] C. W. Gardiner and Peter Zoller. *Quantum noise*. 2nd. Springer, Berlin, 2000.
- [149] G. Lindblad. “On the generators of quantum dynamical semigroups”. In: *Communications in Mathematical Physics* 48 (June 1976), pp. 119–130. DOI: [10.1007/BF01608499](https://doi.org/10.1007/BF01608499).
- [150] Howard M. Wiseman and Gerard J. Milburn. *Quantum Measurement and Control*. Cambridge: Cambridge University Press, 2010.
- [151] Christopher C. Gerry and Peter L. Knight. *Introductory Quantum Optics*. Cambridge University Press, 2005.
- [152] D. Braak. “Integrability of the Rabi Model”. In: *Phys. Rev. Lett.* 107 (10 Aug. 2011), p. 100401. DOI: [10.1103/PhysRevLett.107.100401](https://doi.org/10.1103/PhysRevLett.107.100401).
- [153] C. Cohen-Tannoudji, J. Dupont-Roc, and G. Grynberg. *Atom-photon interactions*. John Wiley, New York, 1992.
- [154] P. Lebedev. “The experimental study of the pressure of the light”. In: *Ann. Phys.* 6 (1901), p. 433.
- [155] E. F. Nichols and G. F. Hull. “A Preliminary Communication on the Pressure of Heat and Light Radiation”. In: *Physical Review (Series I)* 13.5 (Nov. 1901), pp. 307–320. ISSN: 1536-6065. DOI: [10.1103/PhysRevSeriesI.13.307](https://doi.org/10.1103/PhysRevSeriesI.13.307). URL: <http://dx.doi.org/10.1103/PhysRevSeriesI.13.307>.
- [156] Albert Einstein. “Über die Entwicklung unserer Anschauungen über das Wesen und die Konstitution der Strahlung”. In: *Physik Journal* 25.9 (1969), pp. 386–391. ISSN: 1521-3722. DOI: [10.1002/phbl.19690250902](https://doi.org/10.1002/phbl.19690250902).

- [157] C. Cohen-Tannoudji. “Atomic motion in laser light”. In: *Fundamental Systems in Quantum Optics, Proceedings of the Les Houches Summer School, Session LIII*. Ed. by J. Dalibard, J.-M. Raimond, and J. Zinn-Justin. Elsevier Science Publishers B.V., North-Holland, 1992. Chap. 1.
- [158] D. J. Wineland and Wayne M. Itano. “Laser cooling of atoms”. In: *Phys. Rev. A* 20 (4 Oct. 1979), pp. 1521–1540. DOI: [10.1103/PhysRevA.20.1521](https://doi.org/10.1103/PhysRevA.20.1521).
- [159] H. J. Metcalf and P. van der Straten. *Laser Cooling and Trapping*. Springer, 2002.
- [160] D.J. Wineland et al. “Experimental Issues in Coherent Quantum-State Manipulation of Trapped Atomic Ions”. In: (1998).
- [161] Stig Stenholm. “The semiclassical theory of laser cooling”. In: *Rev. Mod. Phys.* 58 (3 July 1986), pp. 699–739. DOI: [10.1103/RevModPhys.58.699](https://doi.org/10.1103/RevModPhys.58.699).
- [162] V. S. Letokhov, V. G. Minogin, and B. D. Pavlik. “Cooling and capture of atoms and molecules by a resonant light field”. In: *Soviet Journal of Experimental and Theoretical Physics* 45 (Apr. 1977), p. 698.
- [163] D. Leibfried et al. “Quantum dynamics of single trapped ions”. In: *Rev. Mod. Phys.* 75.1 (Mar. 2003), pp. 281–324. URL: <http://link.aps.org/doi/10.1103/RevModPhys.75.281>.
- [164] Christian Doppler. *Über das farbige Licht der Doppelsterne und einiger anderer Gestirne des Himmels: Versuch einer das Bradley’sche Aberrations-Theorem als integrierenden Theil in sich schliessenden allgemeineren Theorie*. Borrosch & André, 1842.
- [165] Michael Plischke and Birger Bergersen. *Equilibrium statistical physics*. Third. World Scientific, 2006.
- [166] J. I. Cirac et al. “Laser cooling of trapped ions in a standing wave”. In: *Phys. Rev. A* 46 (5 Sept. 1992), pp. 2668–2681. DOI: [10.1103/PhysRevA.46.2668](https://doi.org/10.1103/PhysRevA.46.2668). URL: <http://link.aps.org/doi/10.1103/PhysRevA.46.2668>.
- [167] C. B. Zhang et al. “Molecular-dynamics simulations of cold single-species and multispecies ion ensembles in a linear Paul trap”. In: *Phys. Rev. A* 76 (1 July 2007), p. 012719. DOI: [10.1103/PhysRevA.76.012719](https://doi.org/10.1103/PhysRevA.76.012719).
- [168] R. G. DeVoe, J. Hoffnagle, and R. G. Brewer. “Role of laser damping in trapped ion crystals”. In: *Physical Review A* 39.9 (May 1989), pp. 4362–4365. ISSN: 0556-2791. DOI: [10.1103/physreva.39.4362](https://doi.org/10.1103/physreva.39.4362). URL: <http://dx.doi.org/10.1103/PhysRevA.39.4362>.
- [169] R. Blümel et al. “Chaos and order of laser-cooled ions in a Paul trap”. In: *Physical Review A* 40.2 (July 1989), pp. 808–823. ISSN: 0556-2791. DOI: [10.1103/physreva.40.808](https://doi.org/10.1103/physreva.40.808). URL: <http://dx.doi.org/10.1103/PhysRevA.40.808>.
- [170] Klaus Mølmer. “Limits of Doppler cooling in pulsed laser fields”. In: *Phys. Rev. Lett.* 66 (18 May 1991), pp. 2301–2304. DOI: [10.1103/PhysRevLett.66.2301](https://doi.org/10.1103/PhysRevLett.66.2301).

- [171] J. P. Schiffer et al. “Temperature, ordering, and equilibrium with time-dependent confining forces”. In: *Proceedings of the National Academy of Sciences of the United States of America* 97.20 (Sept. 2000), pp. 10697–10700. URL: <http://www.jstor.org/stable/view/123189>.
- [172] T. Schätz, U. Schramm, and D. Habs. “Crystalline ion beams”. In: *Nature* 412.6848 (Aug. 2001), pp. 717–720. ISSN: 0028-0836. DOI: [10.1038/35089045](https://doi.org/10.1038/35089045). URL: <http://dx.doi.org/10.1038/35089045>.
- [173] M. Hettrich et al. “Measurement of dipole matrix elements with a single trapped ion”. In: *ArXiv e-prints* (May 2015). arXiv: [1505.02574](https://arxiv.org/abs/1505.02574) [quant-ph]. URL: <http://arxiv.org/abs/1505.02574>.
- [174] Jian Jin and D. A. Church. “Precision lifetimes for the  $\text{Ca}^{+4} p^2 P$  levels: Experiment challenges theory at the 1% level”. In: *Phys. Rev. Lett.* 70 (21 May 1993), pp. 3213–3216. DOI: [10.1103/PhysRevLett.70.3213](https://doi.org/10.1103/PhysRevLett.70.3213).
- [175] A. Kreuter et al. “Experimental and theoretical study of the  $3d^2D$ -level lifetimes of  $^{40}\text{Ca}^{+}$ ”. In: *Phys. Rev. A* 71 (3 Mar. 2005), p. 032504. DOI: [10.1103/PhysRevA.71.032504](https://doi.org/10.1103/PhysRevA.71.032504).
- [176] R. Gerritsma et al. “Precision measurement of the branching fractions of the  $4p^2P_{3/2}$  decay of  $\text{Ca II}$ ”. English. In: *The European Physical Journal D* 50.1 (2008), pp. 13–19. ISSN: 1434-6060. DOI: [10.1140/epjd/e2008-00196-9](https://doi.org/10.1140/epjd/e2008-00196-9).
- [177] D. J. Berkeland and M. G. Boshier. “Destabilization of dark states and optical spectroscopy in Zeeman-degenerate atomic systems”. In: *Physical Review A* 65.3 (Mar. 2002), p. 033413. URL: <http://journals.aps.org/prabstract/10.1103/PhysRevA.65.033413>.
- [178] Christian Felix Roos. “Controlling the quantum state of trapped ions”. PhD thesis. University of Innsbruck, 2000. URL: [http://heart-c704.uibk.ac.at/publications/dissertation/roos\\_diss.pdf](http://heart-c704.uibk.ac.at/publications/dissertation/roos_diss.pdf).
- [179] David R. Leibbrandt. “Integrated chips and optical cavities for trapped ion quantum information processing”. PhD thesis. Massachusetts Institute of Technology, June 2009. URL: <http://web.mit.edu/~cua/www/quanta/LeibbrandtThesis.pdf>.
- [180] P.W. Milonni and J.H. Eberly. *Lasers*. John Wiley & Sons, Inc., New York, 1988.
- [181] H. Kogelnik and T. Li. “Laser Beams And Resonators”. In: *Applied Optics* 5.10 (1966). URL: <http://ao.osa.org/abstract.cfm?uri=ao-5-10-1550>.
- [182] Magnus Albert. “A light-matter interface based on ion Coulomb crystals in an optical cavity”. PhD thesis. Danish National Research Foundation Center for Quantum Optics - Quantop Department of Physics and Astronomy, Aarhus University, 2010. URL: [http://phys.au.dk/fileadmin/site\\_files/forskning/iontrap/pdfs/PhD\\_Albert\\_2010.pdf](http://phys.au.dk/fileadmin/site_files/forskning/iontrap/pdfs/PhD_Albert_2010.pdf).

- [183] Haruka Tanji-Suzuki et al. “Chapter 4 - Interaction between Atomic Ensembles and Optical Resonators: Classical Description”. In: *Advances in Atomic, Molecular, and Optical Physics*. Ed. by P.R. Berman E. Arimondo and C.C. Lin. Vol. 60. Advances In Atomic, Molecular, and Optical Physics. Academic Press, 2011, pp. 201–237. DOI: [10.1016/B978-0-12-385508-4.00004-8](https://doi.org/10.1016/B978-0-12-385508-4.00004-8). URL: <http://www.sciencedirect.com/science/article/pii/B9780123855084000048>.
- [184] David J. Griffiths. *Introduction to Quantum Mechanics*. Second. Upper Saddle River, NJ 07458: Pearson Prentice Hall, 2005.
- [185] D. R. Leibbrandt et al. “Demonstration Of A Scalable, Multiplexed Ion Trap For Quantum Information Processing”. In: *Quantum Information & Computation* 9.11-12 (Nov. 2009), pp. 901–919. URL: <http://arxiv.org/abs/0904.2599>.
- [186] Tadashi Furukawa et al. “Design and Characteristic Measurement of Miniature Three-Segment Linear Paul Trap”. In: *Japanese Journal of Applied Physics* 44.10 (2005), pp. 7619–7624. DOI: [10.1143/JJAP.44.7619](https://doi.org/10.1143/JJAP.44.7619). URL: <http://jjap.jsap.jp/link?JJAP/44/7619/>.
- [187] K. Vant et al. “Photoionization of strontium for trapped-ion quantum information processing”. In: (2007). eprint: <http://arxiv.org/abs/quant-ph/0607055>.
- [188] M. Brownnutt et al. “Controlled photoionization loading of Sr-88(+) for precision ion-trap experiments”. In: *Applied Physics B-Lasers And Optics* 87.3 (May 2007), pp. 411–415. URL: <http://www.springerlink.com/content/377526u074jh0641/>.
- [189] Jaroslaw Labaziewicz. “High Fidelity Quantum Gates with Ions in Cryogenic Microfabricated Ion Traps”. PhD thesis. Massachusetts Institute of Technology, 2008. URL: <http://web.mit.edu/~cua/www/quanta/LabaziewiczThesis.pdf>.
- [190] Carl E. Wieman and Leo Hollberg. “Using diode lasers for atomic physics”. In: *Review of Scientific Instruments* 62.1 (1991), p. 1. ISSN: 0034-6748. DOI: [10.1063/1.1142305](https://doi.org/10.1063/1.1142305). URL: <http://dx.doi.org/10.1063/1.1142305>.
- [191] Roger Barlow. *Statistics: A Guide to the Use of Statistical Methods in the Physical Sciences*. Wiley, 1989. URL: <https://barlow.web.cern.ch/barlow/book.html>.
- [192] E. D. Black. “An introduction to Pound-Drever-Hall laser frequency stabilization”. In: *American Journal Of Physics* 69.1 (Jan. 2001), pp. 79–87. URL: <http://scitation.aip.org/content/aapt/journal/ajp/69/1/10.1119/1.1286663>.
- [193] Daniel Adam Steck. “Quantum and Atom Optics”. 2015. URL: <http://atmoptics-nas.uoregon.edu/~dsteck/teaching/quantum-optics/>.
- [194] A. K. Hansen et al. “Efficient rotational cooling of Coulomb-crystallized molecular ions by a helium buffer gas”. In: *Nature* 508.7494 (Mar. 2014), pp. 76–79. ISSN: 1476-4687. DOI: [10.1038/nature12996](https://doi.org/10.1038/nature12996). URL: <http://dx.doi.org/10.1038/nature12996>.

- [195] B. G. Norton et al. “Millikelvin spatial thermometry of trapped ions”. In: *New Journal of Physics* 13.11 (2011), pp. 113022–. ISSN: 1367-2630. URL: <http://stacks.iop.org/1367-2630/13/i=11/a=113022>.
- [196] S. Knunz et al. “Sub-millikelvin spatial thermometry of a single Doppler-cooled ion in a Paul trap”. In: *Phys. Rev. A* 85.2 (Feb. 2012), pp. 023427–. URL: <http://link.aps.org/doi/10.1103/PhysRevA.85.023427>.
- [197] L. Slodicka et al. “Interferometric thermometry of a single sub-Doppler-cooled atom”. In: *Phys. Rev. A* 85.4 (Apr. 2012), p. 043401. URL: <http://link.aps.org/doi/10.1103/PhysRevA.85.043401>.
- [198] Hans Harhoff Andersen et al. “Single-ion thermometry with an optical resonator”. 2015.
- [199] A. Bermudez, M. Bruderer, and M. B. Plenio. “Controlling and Measuring Quantum Transport of Heat in Trapped-Ion Crystals”. In: *Phys. Rev. Lett.* 111 (4 July 2013), p. 040601. DOI: [10.1103/PhysRevLett.111.040601](https://doi.org/10.1103/PhysRevLett.111.040601). URL: <http://link.aps.org/doi/10.1103/PhysRevLett.111.040601>.
- [200] Thomas Lauprêtre et al. “Localization of ions within one-, two- and three-dimensional Coulomb crystals by a standing wave optical potential”.
- [201] P. Herskind et al. “Loading of large ion Coulomb crystals into a linear Paul trap incorporating an optical cavity”. In: *Applied Physics B: Lasers and Optics* 93 (2008), pp. 373–379. URL: <http://dx.doi.org/10.1007/s00340-008-3199-8>.
- [202] M. Brownnutt et al. “Ion-trap measurements of electric-field noise near surfaces”. In: *ArXiv e-prints* (Sept. 2014). arXiv: [1409.6572](https://arxiv.org/abs/1409.6572) [quant-ph].
- [203] Sumanth B Chikkamaranahalli et al. “Damping mechanisms for precision applications in UHV environment”. In: *NIST* (2006). URL: <http://citeseerx.ist.psu.edu/viewdoc/download?doi=10.1.1.486.7126&rep=rep1&type=pdf>.
- [204] A. I. Oliva, M. Aguilar, and Victor Sosa. “Low- and high-frequency vibration isolation for scanning probe microscopy”. In: *Meas. Sci. Technol.* 9.3 (Mar. 1998), pp. 383–390. ISSN: 1361-6501. DOI: [10.1088/0957-0233/9/3/011](https://doi.org/10.1088/0957-0233/9/3/011). URL: <http://dx.doi.org/10.1088/0957-0233/9/3/011>.
- [205] Olivier Legrand. “Localization spectroscopy of a single ion in an optical lattice”. PhD thesis. Ny Munkegade 120, DK-8000 Aarhus C: Aarhus University, July 2015. URL: <http://phys.au.dk/forskning/forskningsomraader/amo/the-ion-trap-group/publications/theses/>.
- [206] F. K. Jensen. “Laser frequency stabilization for use in stirap experiments”. MA thesis. University of Aarhus, 2004.
- [207] T. W. Hänsch and B. Couillaud. “Laser Frequency Stabilization By Polarization Spectroscopy Of A Reflecting Reference Cavity”. In: *Optics Communications* 35.3 (1980), pp. 441–444. URL: [http://dx.doi.org/10.1016/0030-4018\(80\)90069-3](http://dx.doi.org/10.1016/0030-4018(80)90069-3).

- [208] G. Rempe et al. “Measurement of ultralow losses in an optical interferometer”. In: *Opt. Lett.* 17.5 (1992), p. 363. ISSN: 1539-4794. DOI: [10.1364/ol.17.000363](https://doi.org/10.1364/ol.17.000363). URL: <http://dx.doi.org/10.1364/OL.17.000363>.
- [209] Dorian Gangloff et al. “Preventing and reversing vacuum-induced optical losses in high-finesse tantalum (V) oxide mirror coatings”. In: *Opt. Express* 23.14 (July 2015), pp. 18014–18028. DOI: [10.1364/OE.23.018014](https://doi.org/10.1364/OE.23.018014). URL: <http://www.opticsexpress.org/abstract.cfm?URI=oe-23-14-18014>.
- [210] N. Kjærgaard et al. “Isotope selective loading of an ion trap using resonance-enhanced two-photon ionization”. In: *Applied Physics B-Lasers And Optics* 71.2 (Aug. 2000), pp. 207–210. URL: <http://www.springerlink.com/content/24an4atvqmnfwtc6/>.
- [211] D. M. Lucas et al. “Isotope-selective photoionization for calcium ion trapping”. In: *Physical Review A* 69.1 (Jan. 2004), p. 012711. URL: <http://prola.aps.org/abstract/PRA/v69/i1/e012711>.
- [212] A. Mortensen et al. “Isotope shifts of the 4s(2) S-1(0)-> 4s5p P-1(1) transition and hyperfine splitting of the 4s5p P-1(1) state in calcium”. In: *Physical Review A* 69.4 (Apr. 2004), p. 042502. URL: <http://prola.aps.org/abstract/PRA/v69/i4/e042502>.
- [213] Ralph Hultgren et al. *Selected values of the thermodynamic properties of the elements*. Tech. rep. DTIC Document, 1973.
- [214] P. Herskind et al. “Second-harmonic generation of light at 544 and 272 nm from an ytterbium-doped distributed-feedback fiber laser”. In: *Optics Letters* 32.3 (Feb. 2007), pp. 268–270. URL: <http://ol.osa.org/abstract.cfm?uri=ol-32-3-268>.
- [215] R. W. P. Drever et al. “Laser Phase And Frequency Stabilization Using An Optical-Resonator”. In: *Applied Physics B-Photophysics And Laser Chemistry* 31.2 (1983), pp. 97–105. URL: <http://www.springerlink.com/content/rgg2823656435593/>.
- [216] Yves Colombe et al. “Single-mode optical fiber for high-power, low-loss UV transmission”. In: *Opt. Express* 22.16 (Aug. 2014), pp. 19783–19793. DOI: [10.1364/OE.22.019783](https://doi.org/10.1364/OE.22.019783). URL: <http://www.opticsexpress.org/abstract.cfm?URI=oe-22-16-19783>.
- [217] F. Gebert et al. “Damage-free single-mode transmission of deep-UV light in hollow-core PCF”. In: *Opt. Express* 22.13 (June 2014), pp. 15388–15396. DOI: [10.1364/OE.22.015388](https://doi.org/10.1364/OE.22.015388). URL: <http://www.opticsexpress.org/abstract.cfm?URI=oe-22-13-15388>.
- [218] R. J. Hendricks et al. “An all-optical ion-loading technique for scalable microtrap architectures”. In: *Applied Physics B-Lasers And Optics* 88.4 (Sept. 2007), pp. 507–513. URL: <http://www.springerlink.com/content/1k76j29052377knh/>.
- [219] Gregers Poulsen. “Sideband Cooling of Atomic and Molecular Ions”. PhD thesis. Danish National Research Foundation Center for Quantum Optics - Quantop Department of Physics and Astronomy, Aarhus University, 2011. URL: [http://phys.au.dk/fileadmin/site\\_files/forskning/iontrap/pdfs/PhD\\_Poulsen\\_2012.pdf](http://phys.au.dk/fileadmin/site_files/forskning/iontrap/pdfs/PhD_Poulsen_2012.pdf).

- [220] P. F. Herskind et al. “Positioning of the rf potential minimum line of a linear Paul trap with micrometer precision”. In: *Journal Of Physics B-Atomic Molecular And Optical Physics* 42.15 (Aug. 2009), p. 154008. URL: <http://iopscience.iop.org/0953-4075/42/15/154008/>.
- [221] Martin Sand Nielsen. “Indfangning og laserkøling af calciumioner mhp. dannelse af Coulombkrystaller vha. pulseret laserkøling”. Not available online. MA thesis. Ny Munkegade 120, 8000 Aarhus C, Denmark.: Aarhus University, June 2015.
- [222] Henry Wallman. “Transient response and the central limit theorem of probability”. In: *Proc. Symposia Appl. Math.* Vol. 2. 1950, p. 91.
- [223] D. M. Stamper-Kurn. “Cavity optomechanics with cold atoms”. In: *ArXiv e-prints* (Apr. 2012). arXiv: [1204.4351](https://arxiv.org/abs/1204.4351) [quant-ph].
- [224] Peter Horak, Aurelien Dantan, and Michael Drewsen. “Optically induced structural phase transitions in ion Coulomb crystals”. In: *Phys. Rev. A* 86 (2012), p. 043435. DOI: [10.1103/PhysRevA.86.043435](https://doi.org/10.1103/PhysRevA.86.043435). URL: <http://link.aps.org/doi/10.1103/PhysRevA.86.043435>.
- [225] A. Dantan et al. “Non-invasive vibrational mode spectroscopy of ion Coulomb crystals through resonant collective coupling to an optical cavity field”. In: *Physical Review Letters* 105.10 (2010), pp. 103001+. URL: <http://dx.doi.org/10.1103/PhysRevLett.105.103001>.
- [226] R.W Hasse and J.P Schiffer. “The structure of the cylindrically confined Coulomb lattice”. In: *Annals of Physics* 203.2 (1990), pp. 419–448. ISSN: 0003-4916. DOI: [10.1016/0003-4916\(90\)90177-P](https://doi.org/10.1016/0003-4916(90)90177-P). URL: <http://www.sciencedirect.com/science/article/pii/000349169090177P>.
- [227] Leon Karpa et al. “Suppression of Ion Transport due to Long-Lived Subwavelength Localization by an Optical Lattice”. In: *Physical Review Letters* 111.16 (Oct. 2013). ISSN: 1079-7114. DOI: [10.1103/physrevlett.111.163002](https://doi.org/10.1103/physrevlett.111.163002). URL: <http://dx.doi.org/10.1103/PhysRevLett.111.163002>.
- [228] T. A. Savard, K. M. O’Hara, and J. E. Thomas. “Laser-noise-induced heating in far-off resonance optical traps”. In: *Phys. Rev. A* 56 (2 Aug. 1997), R1095–R1098. DOI: [10.1103/PhysRevA.56.R1095](https://doi.org/10.1103/PhysRevA.56.R1095). URL: <http://link.aps.org/doi/10.1103/PhysRevA.56.R1095>.
- [229] Michael Ramm, Thaned Pruttivarasin, and Hartmut Häffner. “Energy transport in trapped ion chains”. In: *New J. Phys.* 16.6 (June 2014), p. 063062. ISSN: 1367-2630. DOI: [10.1088/1367-2630/16/6/063062](https://doi.org/10.1088/1367-2630/16/6/063062). URL: <http://dx.doi.org/10.1088/1367-2630/16/6/063062>.
- [230] Michael Berglund and Michael E. Wieser. “Isotopic compositions of the elements 2009 (IUPAC Technical Report)”. In: *Pure and Applied Chemistry* 83.2 (Jan. 2011). ISSN: 0033-4545. DOI: [10.1351/pac-rep-10-06-02](https://doi.org/10.1351/pac-rep-10-06-02).
- [231] A. L. Wolf et al. “Frequency metrology on the  $4s^2S_{1/2}4p^2P_{1/2}$  transition in  $^{40}\text{Ca}^+$  for a comparison with quasar data”. In: *Phys. Rev. A* 78 (3 Sept. 2008), p. 032511. DOI: [10.1103/PhysRevA.78.032511](https://doi.org/10.1103/PhysRevA.78.032511).

- [232] A. L. Wolf et al. “Direct Frequency Comb Spectroscopy of Trapped Ions”. In: *Phys. Rev. Lett.* 102 (22 June 2009), p. 223901. DOI: [10.1103/PhysRevLett.102.223901](https://doi.org/10.1103/PhysRevLett.102.223901).
- [233] A. Kramida et al. NIST Atomic Spectra Database (ver. 5.2), [Online]. Available: <http://physics.nist.gov/asd> [2015, July 8]. National Institute of Standards and Technology, Gaithersburg, MD. 2014. URL: <http://physics.nist.gov/asd>.
- [234] Ion Trap Group. “Measurements of Transitions of  $^{40}\text{Ca}^+$ ”. Own measurements performed with HighFinesse WS-U wavemeter. 2015.
- [235] P. Kuske et al. “Lifetime measurements by pulsed laser excitation of fast ion beams”. In: *Physics Letters A* 64.4 (Jan. 1978), pp. 377–380. ISSN: 0375-9601. DOI: [10.1016/0375-9601\(78\)90271-2](https://doi.org/10.1016/0375-9601(78)90271-2). URL: [http://dx.doi.org/10.1016/0375-9601\(78\)90271-2](http://dx.doi.org/10.1016/0375-9601(78)90271-2).
- [236] Carolyn Auchter et al. “Measurement of the branching fractions and lifetime of the  $5\text{D}_{5/2}$  level of  $\text{Ba}^+$ ”. In: *Physical Review A* 90.6 (Dec. 2014). ISSN: 1094-1622. DOI: [10.1103/PhysRevA.90.060501](https://doi.org/10.1103/PhysRevA.90.060501). URL: <http://dx.doi.org/10.1103/PhysRevA.90.060501>.
- [237] N. Yu, W. Nagourney, and H. Dehmelt. “Radiative Lifetime Measurement of the  $\text{Ba} +$  Metastable  $\text{D } 3 / 2$  State”. In: *Physical Review Letters* 78.26 (June 1997), pp. 4898–4901. ISSN: 1079-7114. DOI: [10.1103/physrevlett.78.4898](https://doi.org/10.1103/physrevlett.78.4898). URL: <http://dx.doi.org/10.1103/PhysRevLett.78.4898>.
- [238] D. De Munshi et al. “Precision measurement of branching fractions of  $^{138}\text{Ba}^+$ : Testing many-body theories below the 1% level”. In: *Phys. Rev. A* 91.4 (Apr. 2015). ISSN: 1094-1622. DOI: [10.1103/physreva.91.040501](https://doi.org/10.1103/physreva.91.040501). URL: <http://dx.doi.org/10.1103/PhysRevA.91.040501>.
- [239] J. J. Curry. “Compilation of Wavelengths, Energy Levels, and Transition Probabilities for  $\text{Ba I}$  and  $\text{Ba II}$ ”. In: *Journal of Physical and Chemical Reference Data* 33.3 (2004), p. 725. ISSN: 0047-2689. DOI: [10.1063/1.1643404](https://doi.org/10.1063/1.1643404). URL: <http://www.nist.gov/data/PDFfiles/jpcrd659.pdf>.
- [240] B. K. Sahoo et al. “Theoretical studies of the  $6s^2S_{1/2} \rightarrow 5dD_{3/2}$  parity-nonconserving transition amplitude in  $\text{Ba}^+$  and associated properties”. In: *Phys. Rev. A* 75.3 (Mar. 2007). ISSN: 1094-1622. DOI: [10.1103/physreva.75.032507](https://doi.org/10.1103/physreva.75.032507). URL: <http://dx.doi.org/10.1103/PhysRevA.75.032507>.
- [241] E. A. Dijck et al. “Determination of transition frequencies in a single  $^{138}\text{Ba}^+$  ion”. In: *Phys. Rev. A* 91 (6 June 2015), p. 060501. DOI: [10.1103/PhysRevA.91.060501](https://doi.org/10.1103/PhysRevA.91.060501).